ENGINEERING THE BIOMECHANICS OF PVA/GELATIN CRYOGELS FOR CORONARY ARTERY TISSUE REPLACEMENTS

by

KATIE L. FEGAN

A thesis submitted to the
University of Birmingham
for the degree of
DOCTOR OF PHILOSOPHY



Physical Sciences for Health
School of Chemistry
College of Engineering and Physical Sciences
University of Birmingham
MAY 2023

UNIVERSITY OF
BIRMINGHAM

University of Birmingham Research Archive

e-theses repository

This unpublished thesis/dissertation is copyright of the author and/or third parties. The intellectual property rights of the author or third parties in respect of this work are as defined by The Copyright Designs and Patents Act 1988 or as modified by any successor legislation.

Any use made of information contained in this thesis/dissertation must be in accordance with that legislation and must be properly acknowledged. Further distribution or reproduction in any format is prohibited without the permission of the copyright holder.

ABSTRACT

With coronary artery disease remaining the leading cause of death worldwide, the design and manufacture of clinically-viable synthetic coronary artery grafts remains a fundamental healthcare challenge. It is widely accepted that vascular mimicking materials (VMMs) should emulate the heterogeneous biomechanical and biological functions of the multi-layered artery wall to ensure long-term patency post-implantation. However, few VMMs can adequately meet these complex design requirements. Poly(vinyl alcohol) (PVA)/gelatin cryogels are prospective VMMs owing to their combined mechanical (PVA) and biointegrative (gelatin) features, but their development thus far has been limited to homogenous constructs. This thesis aimed to combine the mechanical characterisation of PVA/gelatin cryogel with the finite element modelling of heterogeneous coronary artery grafts to inform the design of biomimetic synthetic grafts – an approach that is critically underused in the field of cardiovascular tissue engineering.

In addition to exhibiting a hyperelastic stiffening response when loaded up to 50% strain, the linear elastic (E = 144.4–334.4 kPa at 15–20% strain) and dynamic viscoelastic (E' = 182.9–444.4 kPa and E'' = 24.8–39.5 kPa between 0–10 Hz) parameters of PVA/gelatin cryogel fell within the ranges reported for coronary arteries. These findings not only extend current understanding of PVA/gelatin mechanics, but further perpetuate its use as a mechanically-relevant VMM.

The biomechanics of four multi-layered, laminated PVA/gelatin cryogel graft designs were explored at systolic pressure using a hyperelastic finite element (FE) framework. FE analysis was used to match the transmural stress and strain distributions of PVA/gelatin grafts to the coronary intima, media and adventitia through layer-specific variation of cryogel. While the magnitudes of stress, strain

and absolute compliance of all PVA/gelatin grafts exceeded that of the coronary artery, this thesis demonstrated for the first time the potential of FE analysis to design stress- and compliance-matched coronary artery grafts; this work not only supports the development of PVA/gelatin grafts, but supports the development of all hyperelastic VMMs intended for use as coronary artery grafts.

Finally, this thesis investigated a previously unexplored research theme in cardiovascular tissue engineering: the role of interface design on achieving bioinspired, functionally-graded coronary artery grafts. The FE framework was extended to assess the impact of interface radius, amplitude and frequency of an elastic lamallae-inspired sinusoidal interface on stress distribution and graft compliance. While the radius had the largest influence on compliance, larger amplitudes also increased the mean compliance by increasing the extent of non-uniform radial deformation around the lumen. Critically, transmural stress patterns were continuously graded ('phased') as a function of interface amplitude and frequency, illustrating a novel approach to designing biomimetic, functionally graded synthetic grafts. By qualitatively assessing the impact that interface-induced stress may have on endothelialisation, this thesis has taken a novel and important step towards bridging the gap between the mechanical and biological characterisation of heterogeneous PVA/gelatin grafts.

ACKNOWLEDGEMENTS

I must start by thanking my primary supervisor, Dr Lauren Thomas-Seale, for her unwavering support throughout my PhD journey and for believing that a chemist could do a biomechanical engineering PhD. Lauren, this project would not have been possible without your mentorship and encouragement, and for that I cannot thank you enough.

To Dr Asif Iqbal and Dr Melanie Britton, thank you for welcoming me into your labs and opening my eyes to the world of interdisciplinary science. My special thanks go to Dr Naomi Green for not only stepping in as an interim supervisor during my second year, but for showing me the value of science communication. I would also like to acknowledge the financial support I received from the EPSRC as part of the Physical Sciences for Health Doctoral Training Programme (EP/L016346/1).

I am extremely grateful to have worked with some incredible people throughout my time in Birmingham. Joe, it's my turn to thank you for keeping me sane, and for the countless (needed!) trips to Bacchus and beyond. Sanj, thank you for the life coaching and top football banter over the years. James, thank you for your friendship throughout the MSc and PhD. To the 2017 Sci Phy cohort, not only are you all great scientists, but you are also fantastic people. To the biomedical engineering group, it's been a pleasure working with you over the last five years.

To the friends who have cheered me on while I have mumbled and grumbled about PhD life, you are all saints. To my wonderful colleagues at Helios Medical Communications, thank you for your support during my write-up period.

To Mum and Dad, Nan and Grandad, Matthew and Vickie, Elaine and Martin. A simple 'thank you' just doesn't cut it – your belief in me throughout my many

years of studying means the absolute world. I could not ask for a more supportive family.

And finally, to my wonderful fiancé. Ed, thank you for celebrating every high and commiserating every low with me throughout my PhD years – I can't wait to see where life takes us next.

I dedicate this thesis to Ed and my family

NOVEL CONTRIBUTIONS

PRINCIPAL AUTHOR

Data from the following paper are presented in Chapters 3 and 4 of this thesis; Statement of Contributions are included prior to both chapters.

Fegan, K. L., Green, Naomi C., Britton, Melanie M., Iqbal, Asif J. & Thomas-Seale, L. E. J. Design and simulation of the biomechanics of multi-layered composite poly(vinyl alcohol) coronary artery grafts. *Frontiers in Cardiovascular Medicine* **9**, 883179 (2022). DOI: 10.3389/fcvm.2022.883179

SECOND AUTHOR

Miramini, S., **Fegan, K. L.**, Green, Naomi C., Espino, D. M., Zhang, L. & Thomas-Seale, L. E. J. The status and challenges of replicating the mechanical properties of connective tissues using additive manufacturing. *Journal of the Mechanical Behavior of Biomedical Materials* **103**, 103544 (2020). DOI: 10.1016/j.jmbbm.2019.103544

CONFERENCES

Fegan, K. L., Crolla, J. P., Homer-Vanniasinkam, S. Britton, M. M., Iqbal, A. J., Thomas-Seale, L. E. J. Replicating the behaviour of the arterial wall through multimaterial design of vessel mimicking materials. *25th Congress of the European Society of Biomechanics* (July 2019)

Contents

LIST OF FIGURES **xii**

LIST OF TABLES **xxiii**

ACRONYMS AND KEY PARAMETERS **xxviii**

1 INTRODUCTION **1**

1.1 Aims and Objectives 3

1.2 Thesis Structure 4

2 BACKGROUND **7**

2.1 The Cardiovascular System 7

2.1.1 Introducing the Cardiovascular System 7

2.1.2 The Coronary Arteries 8

2.2 The Anatomy of Arteries 9

2.2.1 Artery Wall Structure 9

2.2.2 The Endothelium 10

2.2.3 Vascular ECM 11

2.2.4 Artery Classification 13

2.3 Coronary Artery Disease and Atherosclerosis 14

2.3.1 Disease Development 14

2.3.2 Treatment Methods for Coronary Artery Disease 16

2.4 The Mechanics of Materials 18

2.4.1 Overview . . . 18
2.4.2 Stress and Strain . . . 19
2.4.3 Linear Elasticity . . . 20
2.4.4 Hyperelasticity . . . 21
2.4.5 Viscoelasticity . . . 24
2.5 The Mechanical Environment of Arteries . . . 27
2.5.1 Haemodynamic Forces . . . 27
2.5.2 ECM Stiffness . . . 30
2.5.3 Mechanotransduction . . . 31
2.5.4 Significance for Coronary Artery Grafts . . . 33
2.6 Vascular Mimicking Materials . . . 36
2.6.1 Synthetic Graft Requirements . . . 36
2.6.1.1 Mechanical Properties . . . 37
2.6.1.2 Haemocompatibility . . . 37
2.6.1.3 Ease of Manufacture . . . 38
2.6.2 Hydrogels . . . 38
2.6.3 Poly(vinyl alcohol) (PVA) Cryogels . . . 40
2.6.3.1 Composite PVA Cryogels . . . 43
2.6.3.2 PVA/Gelatin Cryogels . . . 44
2.7 Design, Manufacture and Validation of Multi-Layered Coronary Artery Grafts . . . 47
2.7.1 Overview . . . 47
2.7.2 Heterogeneous Graft Design Through Functional Grading . . . 48
2.7.3 Manufacture of Multi-Layered Grafts . . . 51
2.7.3.1 Manufacture of PVA Cryogel-based Grafts . . . 55
2.7.4 Graft Validation Through Computational Modelling: The Finite Element Method . . . 57

2.7.4.1 Finite Element Analysis of Small Diameter Artery Grafts 60
2.8 Research Hypothesis 61

STATEMENT OF CONTRIBUTIONS I **63**

3 MECHANICAL CHARACTERISATION OF PVA/GELATIN CRYOGELS **64**

3.1 Introduction 64
3.1.1 Aims and Objectives 69
3.2 Method 70
3.2.1 Chemicals and Materials 70
3.2.2 Preparation of PVA/Gelatin Cryogels 71
3.2.3 Density Measurements 72
3.2.4 Ramp Testing 72
3.2.5 Dynamic Mechanical Analysis 73
3.2.6 Curve Fitting of Hyperelastic Strain Energy Density Functions 74
3.2.7 Data Analysis 77
3.3 Results 78
3.3.1 Linear Elastic Response of PVA/Gelatin Cryogel 78
3.3.2 Dynamic Mechanical Analysis of PVA/Gelatin Cryogel 81
3.3.3 Hyperelastic Constitutive Modelling of PVA/Gelatin 88
3.3.4 Validation of Yeoh and Ogden Constitutive Parameters for FE Modelling 91
3.4 Discussion 93
3.4.1 Linear Elastic Behaviour 93
3.4.2 Viscoelastic Behaviour 96
3.4.3 Hyperelastic Behaviour 100

3.5 Conclusion 102

STATEMENT OF CONTRIBUTIONS II **104**

4 FINITE ELEMENT MODELLING OF HYPERELASTIC PVA/GELATIN GRAFTS **105**

4.1 Introduction 105

4.1.1 Aims and Objectives 108

4.2 Method 111

4.2.1 Overview 111

4.2.2 FE Model 112

4.2.2.1 Geometry 112

4.2.2.2 Boundary Conditions 113

4.2.2.3 Mesh 115

4.2.2.4 Material Properties 116

4.2.3 Field Variable Extraction for Stress/Strain Analyses 117

4.2.4 Relative Difference Calculation 119

4.3 Results 120

4.3.1 Comparison of Coronary Artery Transmural Biomechanics . . 120

4.3.2 PVA/Gelatin Graft Design Validation 123

4.4 Discussion 132

4.4.1 Simulating the Biomechanics of the Coronary Artery Wall . . 132

4.4.2 Comparison of Coronary Artery and PVA/Gelatin Graft Biomechanics 134

4.4.3 Study Limitations and Next Steps 136

4.5 Conclusion 138

5 HETEROGENEOUS DESIGN OF FUNCTIONALLY GRADED CORONARY ARTERY GRAFTS 140

5.1 Introduction . . . 140

5.1.1 Aims and Objectives . . . 143

5.2 Method . . . 145

5.2.1 Overview . . . 145

5.2.2 FE Model . . . 147

5.2.2.1 Geometry . . . 147

5.2.2.2 Boundary Conditions . . . 148

5.2.2.3 Mesh . . . 149

5.2.2.4 Material Properties . . . 150

5.2.3 Compliance Analysis . . . 151

5.2.4 Analysis of the Variation of Lumen Radii . . . 154

5.2.5 Discretisation Analysis . . . 155

5.2.6 Data Analysis . . . 156

5.3 Results . . . 157

5.3.1 Overview . . . 157

5.3.2 Modelling the Contact Between Interdigitated Surfaces . . . 157

5.3.3 Impact of Interface Radius on Graft Biomechanics . . . 164

5.3.3.1 Varying Interface Radius: Stress Distribution . . . 164

5.3.3.2 Varying Interface Radius: Compliance . . . 165

5.3.4 Impact of Interface Amplitude on Graft Biomechanics . . . 166

5.3.4.1 Varying Interface Amplitude: Stress Distribution . . . 166

5.3.4.2 Varying Interface Amplitude: Compliance . . . 171

5.3.5 Impact of Interface Frequency on Graft Biomechanics . . . 175

5.3.5.1 Varying Interface Frequency: Stress Distribution . . . 175

5.3.5.2 Varying Interface Frequency: Compliance . . . 180

5.3.6 Combining Interface Radius and Amplitude: Compliance . . . 181
5.4 Discussion . . . 184
5.4.1 Modelling the Contact Between Interdigitated Surfaces . . . 186
5.4.2 Analysis of Sine Wave Parameters on Graft Biomechanics . . . 188
5.5 Conclusion . . . 194

6 GENERAL DISCUSSION AND CONCLUSIONS 196
6.1 Thesis Summary . . . 196
6.2 Impact, Novelty and Contribution to the Field . . . 197
6.3 Limitations . . . 200
6.4 Future Work . . . 204

REFERENCES 207

APPENDIX A 237

APPENDIX B 246

APPENDIX C 251

List of Figures

FIGURE 2.1: Anterior view of the coronary arterial system and its branches. Reprinted from [24] with permission from Elsevier Science & Technology Journals. 8

FIGURE 2.2: Idealised wall structure of a healthy elastic artery, consisting of the intima (I), media (M) and adventitia (A). Reprinted from [27] with permission from The Royal Society (UK). 9

FIGURE 2.3: Atherosclerosis disease development. RLP, remnant-like particle; LDL, low-density lipoprotein; ox-LDL, oxidised low-density lipoprotein; CRP, C-reactive protein. Note that EPA (eicosapentaenoic acid) is not relevant to the progression of atherosclerosis and can be ignored. Figure reproduced from [66] under CC-BY-NC-ND 4.0 (https://creativecommons.org/licenses/by-nc-nd/4.0/). 14

FIGURE 2.4: Uniaxial compression of a cylinder, showing the relationship between the applied force (F), initial length (L_0) and compressed length (L). 19

FIGURE 2.5: **(A)** Example non-linear hyperelastic stress–strain curve. The shaded area is represented by U; **(B)** strain tensor for a 3D material. 21

FIGURE 2.6: Applied sinusoidal load and corresponding displacement waveform of a viscoelastic material, plotted as a function of time t. 25

FIGURE 2.7: Using δ, E^* can be solved for E' and E''. 27

FIGURE 2.8: Haemodynamic forces acting on an idealised artery wall. . . 28

FIGURE 2.9: Types of mechanosensor structures that form the EC mechanosensory system. 32

FIGURE 2.10: Examples of transcription factors (KLF2, Nrf2, NF-κB and AP-1) and their downstream products under atheroprotective and atherogenic flow. 34

FIGURE 2.11: Key requirements of VMMs for use in cardiovascular grafts. . 36

FIGURE 2.12: **(A)** The structure of PVA crosslinks formed using freeze–thaw (FT) cycling. Examples of pendant hydroxyl and acetate groups are highlighted in orange and blue, respectively. Hydrogen bonds are represented by dashed lines; **(B)** The semi-crystalline structure of PVA cryogel. The solid polymer network is represented in black; bulk water fills the interstitial space between the polymer network, represented in light grey. 40

FIGURE 2.13: **(A)** Discontinuous FGBMs achieve grading through stepwise changes in composition and/or microstructure; **(B)** continuous FGBMs achieve grading through smooth transitions in composition and/or microstructure. **(C)** While a discontinuous boundary is observed between the coronary media and adventitia, collagen (red) and elastin (green) orientation and distribution vary throughout the adventitia. Figure 2.13C reproduced from [227] with permission from Elsevier. 49

FIGURE 2.14: Discretisation of coronary artery wall, plaque, balloon and stent for the simulation of PCI. Reprinted from [20] with permission from Elsevier. 57

FIGURE 3.1: Flow chart outlining the hyperelastic curve fitting procedure and Abaqus uniaxial compression model used to validate hyperelastic coefficients. 77

FIGURE 3.2: Engineering stress–strain curves for pure PVA cryogels compressed to 20% strain. The strain region used to calculate E is shaded in blue. 78

FIGURE 3.3: Engineering stress–strain curves for PVA/gelatin cryogels compressed to 20% strain. The strain region used to calculate E is shaded in blue. 79

FIGURE 3.4: Variation in E as a function of gelatin addition. $^*P = 0.036$ 80

FIGURE 3.5: Effect of M_w PVA and cryogel coagulation on the E' of **(A)** pure PVA and **(B)** PVA/gelatin cryogels. Error bars show 95% confidence intervals (CIs). 81

FIGURE 3.6: Effect of M_w PVA and cryogel coagulation on the E'' of **(A)** pure PVA and **(B)** PVA/gelatin cryogels. Error bars show confidence intervals (CIs). 82

FIGURE 3.7: $tan\delta$ of **(A)** pure PVA and **(B)** PVA/gelatin cryogels. Error bars show confidence intervals (CIs). 83

FIGURE 3.8: Representative curve fit of stable hyperelastic models to uniaxial

compression data, taken from an individual P_9G_1-A-C sample. Compressive stress and strain are shown as absolute values. 89

FIGURE 3.9: Simulated compressive stress–strain response using averaged Yeoh (solid blue line) and first order Ogden (solid orange) parameters of PVA/gelatin cryogels compared with experimental test data (grey dashed lines). Compressive stresses and strains are shown as absolute values. 92

FIGURE 4.1: Workflow used to create tri-layered FE models. Dashed lines represent data obtained from the literature, while dotted lines represent the steps performed in Chapter 3. 110

FIGURE 4.2: Discretised three-layer coronary artery wall. A cylindrical coordinate system was adopted using the three-dimensional coordinates r (radial), θ (circumferential) and z (axial). Each layer was meshed with seven layers of elements through the radial thickness; the nodal analysis path used to extract field variable values from the model is highlighted by the red dotted line. 112

FIGURE 4.3: Boundary condition convergence study performed at systolic pressure using first order Ogden P_9G_1-A-C coefficients for all three tissue layers (tissue interfaces are represented by grey dashed lines). **(A)** σ_θ and **(B)** σ_r profiles through the thickness of the wall; **(C)** Convergence of luminal σ_θ; **(D)** Convergence of σ_r at the adventitia–tissue interface. 114

FIGURE 4.4: Mesh convergence study performed using third order Ogden coronary artery coefficients at systolic pressure. Convergence was achieved when the luminal stress increased less than 2% relative to the previous mesh size (dashed lines). 115

FIGURE 4.5: Schematic of the nodal analysis path used to extract stress and strain values with respect to wall thickness. Representative node labels are shown in red; dashed lines represent the boundaries between tissue layers. 118

FIGURE 4.6: Example schematic of the individual and mean stress–pressure curves obtained for the medial layer of the Ogden-derived coronary artery model. 119

FIGURE 4.7: Mean ϵ_θ of the coronary intima between **(A)** 0–120 mmHg pressure and **(B)** 80–120 mmHg pressure (dashed lines show the SD for each model). 121

FIGURE 4.8: Mean ϵ_r of the coronary intima between **(A)** 0–120 mmHg pressure and **(B)** 80–120 mmHg pressure (dashed lines show the SD for each model). 122

FIGURE 4.9: **(A)** σ_θ and **(B)** σ_r profiles for each coronary artery model at systolic pressure. Grey dashed lines represent the intima–media and media–adventitia interfaces. 123

FIGURE 4.10: σ_θ contour maps of each PVA/gelatin graft using Ogden parameters. Analogous Yeoh σ_θ contour maps are displayed in Figure B.3. 125

FIGURE 4.11: The circumferential biomechanics of PVA/gelatin grafts at systolic pressure. **(A)** The mean ϵ_θ of the PVA/gelatin graft intima between 0–120 and 80–120 mmHg pressure (error bars have been omitted for clarity), modelled using Ogden (solid lines) and Yeoh (dashed lines) hyperelastic parameters. **(B)** σ_θ and ϵ_θ profiles through the radial thickness of each PVA/gelatin graft design. Grey dashed lines represent the intima–media and media–adventitia interfaces. . . 126

FIGURE 4.12: The radial biomechanics of PVA/gelatin grafts at systolic pressure. **(A)** σ_r and ϵ_r profiles through the radial thickness of each PVA/gelatin graft design, modelled using Ogden (solid lines) and Yeoh (dashed lines) hyperelastic parameters. Grey dashed lines represent the intima–media and media–adventitia interfaces; **(B)** Compliance of PVA/gelatin grafts compared with coronary artery models. 127

FIGURE 4.13: The relative difference (%) in **(A)** σ_θ, **(B)** σ_r, **(C)** ϵ_θ and **(D)** ϵ_r between tri-layered PVA/gelatin grafts and the Ogden coronary artery model. The solid and dotted lines represent PVA/gelatin grafts modelled using Ogden and Yeoh hyperelastic parameters, respectively. Grey dashed lines represent the intima—media and media–adventitia interfaces. 129

FIGURE 4.14: The relative difference (%) in **(A)** σ_θ, **(B)** σ_r, **(C)** ϵ_θ and **(D)** ϵ_r between tri-layered PVA/gelatin grafts and the polynomial coronary artery model. The solid and dotted lines represent PVA/gelatin grafts modelled using Ogden and Yeoh hyperelastic parameters, respectively. Grey dashed lines represent the intima—media and media–adventitia interfaces. 130

FIGURE 4.15: The relative difference (%) in **(A)** σ_θ, **(B)** σ_r, **(C)** ϵ_θ and **(D)** ϵ_r between bi-layered PVA/gelatin graft PG–4 and the reduced polynomial coronary artery model. The solid and dotted lines represent PVA/gelatin grafts modelled using Ogden and Yeoh hyperelastic parameters, respectively. Grey dashed lines represent the intima—media and media-–adventitia interfaces. 131

FIGURE 5.1: Micromechanics of elastic lamellae. **(A)** Transverse cross-sectional images of mouse carotid artery elastic lamellae when loaded up to systolic pressure and **(B)** Schematic of three elastic lamellae layers in the arterial wall. Both figures reprinted from [351] with permission from The Royal Society (UK). 144

FIGURE 5.2: Workflow of Chapter 5. 146

FIGURE 5.3: Example of a sinusoidally-interdigitated graft model and its mesh. 147

FIGURE 5.4: Examples of nodal analysis paths (red dotted lines) taken at ϕ = **(A)** 0°, **(B)** 90° and **(C)** 270°. In the left panel, grey dotted vertical lines represent a circumferential mesh density of 36 elements/wave. 152

FIGURE 5.5: Interfaces comprised of different ω were out of phase. Arc lengths are shown in orange and and arc angles are shown in blue. . . 153

FIGURE 5.6: Node path corresponding to stress analyses along the interface. The stress at the nodes in red were plotted either as a function of ϕ or as a function of graft arc angle. 153

FIGURE 5.7: The lumen diameter was assessed as a function of ϕ to calculate $\overline{CC}$. 154

FIGURE 5.8: r_{lumen} was used to map the surface profile of the lumen; the blue arrow represents the peak-to-trough height profile of the lumen surface. Note that arc angle or arc length can be used in place of ϕ to map the luminal surface profile. 155

FIGURE 5.9: Example reconstruction of a graft sector in Fusion 360, shown for an interdigitated graft where $A = 0.25$ mm, $\omega = 10$ and $r = 1.815$ mm. Circumferential segments are numbered from 1–10. 156

FIGURE 5.10: Comparison of friction, rough friction and tied contact formulations on a bi-layered non-interdigitated graft, where the IM and adventitia were modelled using the same PVA/gelatin composition (IM = adventitia; P_9G_1-A-C) and different PVA/gelatin compositions (IM > adventitia; IM = P_9G_1-A-C; adventitia = P_9G_1-B-NC). 158

FIGURE 5.11: σ_θ distributions for three contact formulations (tied / μ_F = 0.04 / $\mu_F = \infty$) when the IM and adventitia were modelled using the same PVA/gelatin composition (P_9G_1-A-C). Layer boundaries are represented by grey dashed lines. 161

FIGURE 5.12: σ_θ distributions for three contact formulations (tied / μ_F = 0.04 / $\mu_F = \infty$) when the IM (P_9G_1-A-C) was stiffer than the adventitia (P_9G_1-B-NC). Layer boundaries are represented by grey dashed lines. 162

FIGURE 5.13: **(A)** x_θ and **(B)** σ_θ of the rough friction coefficient model; **(C)** x_θ and **(D)** σ_θ of the 0.04 friction coefficient model (IM = P_9G_1-A-C, adventitia = P_9G_1-B-NC). In the x_θ plots, red and blue signify clockwise and anticlockwise displacement, respectively. In the σ_θ plots, tensile stress concentrations are highlighted by black dotted circles and compressive stress concentrations are highlighted by white dotted circles. Data for the tied model are displayed in Figure C.3. . . . 163

FIGURE 5.14: σ_θ distribution at systolic pressure at an IM:adventitia ratio of 1:2, 1:1 and 2:1. Dashed lines show the interface boundary (r). . . 164

FIGURE 5.15: The impact of varying the IM:adventitia ratio on the CC of the graft. 165

FIGURE 5.16: σ_θ distribution at A = 0.05 mm (left) and A = 0.25 mm (right) at systolic pressure. 167

FIGURE 5.17: Transmural σ_θ distribution at systolic pressure with varying A at **(A)** $\phi = 0°$, **(B)** $\phi = 90°$ and **(C)** $\phi = 270°$. Dashed lines show the interface at each ϕ. 168

FIGURE 5.18: Contact pressures observed at the interface of all amplitude models at systolic pressure. 169

FIGURE 5.19: σ_θ along the interface as a function of ϕ at systolic pressure. Dashed lines show the locations of minimum and maximum σ_θ. 170

FIGURE 5.20: The impact of varying A on the $\overline{CC}$ ($\pm$ SD) of PVA/gelatin grafts. 171

FIGURE 5.21: The impact of varying A on the **(A)** r_{lumen} at systolic pressure and **(B)** interface depth of PVA/gelatin grafts. Both **(A)** and **(B)** are presented as a function of ϕ. 174

FIGURE 5.22: σ_θ distribution at systolic pressure when ω = 6, 10, 20 and 30.175

FIGURE 5.23: Transmural σ_θ distribution at systolic pressure with varying ω at **(A)** $\phi = 0°$, **(B)** $\phi = 90°$ and **(C)** $\phi = 270°$. Dashed lines show the interface at each ϕ. 176

FIGURE 5.24: Contact pressures observed at the interface of all amplitude models at systolic pressure. 177

FIGURE 5.25: σ_θ along the interface at systolic pressure as a function of **(A)** ϕ of the interface and **(B)** graft arc angle. Dotted and dashed lines in **(B)** show arc angles corresponding to $\phi = 90°$ and $\phi = 270°$, respectively. 178

FIGURE 5.26: The impact of varying ω on the $\overline{CC}$ ($\pm$ SD) of PVA/gelatin grafts. *P<0.05; **P<0.01 180

FIGURE 5.27: The impact of varying ω on r_{lumen} at systolic pressure with respect to graft arc angle. 181

FIGURE 5.28: The impact of varying the r and A of bi-layered interdigitated PVA/gelatin grafts. (A) $\overline{CC}$ $\pm$ SD; **(B)** r_{lumen} at systolic pressure. In all cases, ω = 10. 182

FIGURE 6.1: Anticipated future trajectory of this thesis. The boxes with solid outlines represent the starting points for the experimental (aqua) and computational (blue) workstreams; if at any point undesirable biomechanical or haemocompatible behaviours surface, the research should circle back to both starting points. 204

FIGURE 6.2: Sub-zero AM has been used to fabricate functionally graded PVA cryogel lattice structures with variable sinusoidal wavelengths. Reprinted from [371] with permission from the author. 205

FIGURE A.1: Individual stress–strain curves (test data) for P_9G_1-A-NC, P_9G_1-A-C, P_9G_1-B-NC and P_9G_1-B-C. 238

FIGURE B.1: The mean ϵ_θ (top row) and ϵ_r (bottom row) of the coronary media between 0–120 and 80–120 mmHg pressure. Dashed lines show the SD of each model. 246

FIGURE B.2: The mean ϵ_θ (top row) and ϵ_r (bottom row) of the coronary adventitia between 0–120 and 80–120 mmHg pressure. Dashed lines show the SD of each model. 247

FIGURE B.3: σ_θ contour maps of each PVA/gelatin graft using Yeoh parameters. 248

FIGURE B.4: The mean ϵ_θ (top row) and ϵ_r (bottom row) of PVA/gelatin graft media between 0–120 and 80–120 mmHg pressure, modelled using Ogden (solid lines) and Yeoh (dashed lines) hyperelastic parameters. Error bars have been omitted for clarity. 249

FIGURE B.5: The mean ϵ_θ (top row) and ϵ_r (bottom row) of PVA/gelatin graft adventitia between 0–120 and 80–120 mmHg pressure, modelled using Ogden (solid lines) and Yeoh (dashed lines) hyperelastic parameters. Error bars have been omitted for clarity. 250

FIGURE C.1: Custom Python script used to create a sinusoidal interface in Abaqus. In this example, $r = 1.815$ mm, $A = 0.10$ mm and $\omega = 10$. 252

FIGURE C.2: Lumen diameter varies as a function of ϕ. In this example, $r = 1.815$ mm, $A = 0.25$ mm and $\omega = 10$. 253

FIGURE C.3: x_θ (left) and σ_θ (right) in the tied surface model (IM = P_9G_1-A-C, adventitia = P_9G_1-B-NC) at systolic pressure. In the x_θ plots, red and blue signify clockwise and anticlockwise displacement, respectively. In the σ_θ plots, tensile stress concentrations are highlighted by black dotted circles and compressive stress concentrations are highlighted by white dotted circles. 254

FIGURE C.4: Contact pressures observed at the interface at systolic pressure for rough friction and friction coefficient models. 254

List of Tables

TABLE 2.1: Comparison of manufacturing methods used to fabricate multi-layer artery grafts. Table developed from [9, 237, 245–253]. 53

TABLE 3.1: Key mechanical testing literature characterising the impact of formulation and processing parameters on the linear elastic, hyperelastic and viscoelastic properties of pure PVA cryogel. ↑ signifies increasing values, while ↓ signifies decreasing values. 67

TABLE 3.2: Key mechanical testing literature characterising the impact of formulation and processing parameters on the linear elastic, hyperelastic and viscoelastic properties of PVA/gelatin cryogel. ↑ signifies increasing values, while ↓ signifies decreasing values. UTS = ultimate tensile testing. 68

TABLE 3.3: PVA/gelatin cryogel compositions. P_xG_y signifies the w/w ratio of PVA:gelatin, A/B denotes the M_w of PVA (A = 146–186 kDa, B = 89–98 kDa) and C/NC signifies whether coagulation treatment (C) or no coagulation treatment (NC) was employed during cryogel manufacture. 70

TABLE 3.4: E (mean ± SD) between 15–20% strain for all cryogel compositions. 80

TABLE 3.5: E' (mean ± SD) for all PVA(/gelatin) compositions at 0.5 Hz and 10 Hz. P-values represent the statistical significance between the minimum (0.5 Hz) and maximum (10 Hz) frequencies for each composition. For full frequency data, the reader is referred to Table A.2. 85

TABLE 3.6: E'' (mean ± SD) for all PVA(/gelatin) compositions at 0.5 Hz and 10 Hz. P-values represent the statistical significance between the minimum (0.5 Hz) and maximum (10 Hz) frequencies for each composition. For full frequency data, the reader is referred to Table A.3. 86

TABLE 3.7: Comparison of E' (mean ± SD) upon addition of gelatin to all PVA cryogel compositions at 0.5 Hz and 10 Hz. P-values represent the statistical significance between the minimum (0.5 Hz) and maximum (10 Hz) frequencies for each composition. 87

TABLE 3.8: Stability of hyperelastic models during curve fitting. Coefficients fulfilling Drucker's stability criteron were deemed stable ('yes'), while those which failed were deemed unstable ('no'). 88

TABLE 3.9: First order Ogden and Yeoh constitutive parameters fitted to PVA/gelatin compression data and densities of all PVA/gelatin cryogel compositions (mean ± SD). 90

TABLE 3.10: Correlation matrices showing the effect of M_w PVA and coagulation treatment on μ_0 of PVA/gelatin cryogel. NS = not statistically significant ($P > 0.05$); * = $P \leq 0.05$; ** = $P \leq 0.01$; *** = $P \leq 0.001$. 91

TABLE 4.1: Layer-specific hyperelastic material coefficients obtained from the literature, derived from hyperelastic isotropic constitutive models fitted to coronary arterial tissue. 116

TABLE 4.2: First order Ogden and Yeoh constitutive parameters fitted to PVA/gelatin compression data and densities of all PVA/gelatin cryogel compositions in Chapter 3 (mean ± SD). 117

TABLE 4.3: PVA/gelatin (PG) compositions used in the four iterations of the PVA/gelatin tri-layered FE model. 124

TABLE 5.1: Design matrix of sine wave parameters for amplitude and frequency studies. The blue row represents the variation of ω at a fixed A of 0.10 mm; the red column represents the variation in A at a fixed ω of 10; the purple cell represents overlap between the two studies. In all cases, r was fixed to 1.815 mm. 148

TABLE 5.2: Material parameters used in all Chapter 5 experiments (mean ± SD). ν = Poisson's ratio. 151

TABLE 5.3: Peak-to-trough height profiles at the lumen surface as a function of A at systolic pressure. 172

TABLE 5.4: The ratio of IM:adventitia through each circumferential segment as a function of A. The relative areas of the IM and adventitia are normalised to the total area of the corresponding segment. Segment 1 is closest to the lumen, while segment 10 is furthest away from the lumen. 173

TABLE 5.5: Magnitude of the decrease in σ_θ across the IM–adventitia interface at the extremes of ϕ (0°, 90° and 270°) and ω (6 and 30) at systolic pressure. 177

TABLE 5.6: Peak-to-trough height profiles at the lumen surface as a function of ω at systolic pressure. 181

TABLE 5.7: Peak-to-trough height profiles at the lumen surface as a function of A and IM:adventitia ratio at systolic pressure. 183

TABLE 5.8: Compliance of bi-layered interdigitated PVA/gelatin grafts compared with human and porcine coronary arteries. 184

TABLE A.1: First order Ogden parameters and r^2 values for individual PVA/gelatin samples. For P_9G_1-B-C, samples marked with $**$ yielded $\alpha_1 < 0$ and were excluded to allow averaging of α_1. For P_9G_1-A-C, P_9G_1-A-NC and P_9G_1-B-NC, samples marked with $**$ were excluded to keep the sample size consistent between compositions ($n = 6$). The $n = 6$ mean values were the hyperelastic constants used in subsequent FE models. 239

TABLE A.2: E' (mean $\pm$ SD) for all PVA(/gelatin) compositions tested between 0.5 Hz and 10 Hz. 240

TABLE A.3: E'' (mean $\pm$ SD) for all PVA(/gelatin) compositions tested between 0.5 Hz and 10 Hz. 240

TABLE A.4: The relative difference in E' of PVA cryogel between frequencies of 0.5–10 Hz as a function of M_w PVA (top) and coagulation treatment (bottom), calculated as the percentage difference between two compositions of interest. 241

TABLE A.5: The relative difference in E' of PVA/gelatin cryogel between frequencies of 0.5–10 Hz as a function of M_w PVA (top) and coagulation treatment (bottom), calculated as the percentage difference between two compositions of interest. 242

TABLE A.6: The relative difference in E'' of PVA cryogel between frequencies of 0.5–10 Hz as a function of M_w PVA (top) and coagulation treatment (bottom), calculated as the percentage difference between two compositions of interest. 243

TABLE A.7: The relative difference in E'' of PVA/gelatin cryogel between frequencies of 0.5–10 Hz as a function of M_w PVA (top) and coagulation treatment (bottom), calculated as the percentage difference between two compositions of interest. 244

TABLE A.8: Constitutive parameters of stable hyperelastic models fitted to PVA/gelatin compression data for all PVA/gelatin cryogel compositions (mean ± SD) 245

TABLE C.1: The areas of the IM and adventitia through circumferential segments 1–10 as a function of A. 255

ACRONYMS AND KEY PARAMETERS

AM	additive manufacturing
ANOVA	analysis of variance
CABG	coronary artery bypass grafting
CAD	coronary artery disease
CC	cross-sectional compliance
CI	confidence interval
CVD	cardiovascular disease
DMA	dynamic mechanical analysis
EC	endothelial cell
ECM	extracellular matrix
ePTFE	expanded polytetrafluoroethylene
FE	finite element
FEA	finite element analysis
FGBM	functionally graded biomaterial
FT	freeze–thaw
GAG	glycosaminoglycan
IM	intima–media
ITA	internal thoracic artery
LAD	left anterior descending
LCA	left coronary artery
LCX	left circumflex
(ox)-LDL	(oxidised)-low-density lipoprotein
PCI	percutaneous coronary intervention
PCL	polycaprolactone
PG	poly(vinyl alcohol)/gelatin

PLLA	poly-L-lactide
PVA	poly(vinyl alcohol)
RCA	right coronary artery
SV	saphenous vein
RGD	arginine–glycine–aspartate
SD	standard deviation
UTS	ultimate tensile testing
VMM	vascular mimicking material
VSMC	vascular smooth muscle cell
WSS	wall shear stress

$\boldsymbol{A}$	amplitude
$\boldsymbol{C_{ij}}$	hyperelastic material parameter
$\boldsymbol{E}$	Young's modulus
$\boldsymbol{E^*}$	complex modulus
$\boldsymbol{E'}$	storage modulus
$\boldsymbol{E''}$	loss modulus
$\boldsymbol{r^2}$	correlation coefficient
$\boldsymbol{U}$	strain energy density function
$\boldsymbol{\alpha_i}$	Ogden parameter of i^{th} order
$\boldsymbol{\delta}$	phase lag
$\boldsymbol{\epsilon}$	strain
$\boldsymbol{\epsilon_\theta}$	circumferential strain
$\boldsymbol{\epsilon_r}$	radial strain
$\boldsymbol{\mu_0}$	initial shear modulus
$\boldsymbol{\mu_F}$	friction coefficient
$\boldsymbol{\mu_i}$	Ogden parameter of i^{th} order
$\boldsymbol{\mu_\infty}$	infinite friction
$\boldsymbol{r}$	radius
$\boldsymbol{r_{lumen}}$	lumen radius
$\boldsymbol{\rho}$	density
$\boldsymbol{\sigma}$	stress
$\boldsymbol{\sigma_\theta}$	circumferential stress
$\boldsymbol{\sigma_r}$	radial stress
$\boldsymbol{\phi}$	phase
$\boldsymbol{\omega}$	frequency

Chapter One

INTRODUCTION

Cardiovascular disease (CVD) is the leading cause of death worldwide. Despite increasing awareness of the behavioural and metabolic risk factors associated with CVDs, they are responsible for almost a third of global deaths reported annually [1]. In Europe, they account for almost half [2]. Analysis of global CVD trends over the last three decades illustrates the immense scale of CVD-related disease burden [3]. Thanks to rising healthcare costs and increasing years lived with disability, treating CVD is listed as a major sustainable development goal by the United Nations and the World Health Organization [4, 5].

CVD is an umbrella term encompassing conditions relating to the heart and circulatory system. The common denominator shared by many CVDs is the narrowing and occlusion of vessels that supply blood to various regions of the body, such as the brain (cerebrovascular disease), arms and legs (peripheral artery disease) and heart (coronary artery disease). Of these, coronary artery disease (CAD) is the most prevalent, with an estimated 200 million people living with the disease worldwide [1]. Furthermore, CAD kills an estimated nine million people each year, accounting for approximately 1 in 6 deaths globally [1]. Patients with advanced CAD often

require bypass surgery to re-establish blood flow to the heart and prevent further downstream complications, including heart failure, heart attack and death.

Almost four decades have passed since the term *tissue engineering* was first introduced [6]. Since then, thousands of papers relating to cardiovascular tissue engineering – specifically, the development of novel biomaterials for the fabrication of synthetic bypass grafts – have been published worldwide. Yet, the search for clinically viable, small-diameter tissue-engineered grafts continues. Synthetic grafts must support the native biological functions of the coronary artery wall [7]. Mechanical mismatch between a graft and its host vessel has long been cited as a major cause of graft failure due to the complex interplay between vascular cells and their surrounding mechanical environment [8]. Although a variety of vascular mimicking materials (VMMs) have been developed as replacement vascular tissue, few have been rigorously characterised according to the hyperelastic, viscoelastic and/or anisotropic biomechanical behaviours exhibited by native vessels [9].

Hydrogels are promising VMMs due to their compositional similarity to soft tissue. Poly(vinyl alcohol) (PVA) cryogel is a biocompatible, hydrophilic VMM with tuneable mechanical properties and is thus a compelling biomaterial across a spectrum of tissue engineering applications [10, 11]. Significant effort has been made to manufacture PVA composites with improved biological integration; in cardiovascular tissue engineering, PVA/gelatin cryogel has demonstrated enhanced endothelialisation and haemocompatibility with respect to pure PVA [12, 13]. Nevertheless, as a VMM, PVA/gelatin has only been applied to the manufacture of homogeneous constructs. The artery wall is comprised of three tissue layers which each confer different mechanical and biological functions to the vessel. Synthetic grafts should therefore be designed to emulate the heterogeneous nature of the native wall. It follows that research into PVA/gelatin cryogel as a

VMM should progress into the realm of heterogeneous graft design, drawing on biomimetic concepts such as functional grading [14]. With the advent of advanced manufacturing techniques such as sub-zero additive manufacturing (AM) [15–17], more complex graft designs may be unlocked.

While computational modelling has become a staple tool in the haemodynamic assessment of arteries in terms of understanding the progression of atherosclerosis and designing stents for balloon angioplasty [18–22], its application to the design and manufacture of soft synthetic vascular grafts is comparatively limited. Specifically, finite element analysis (FEA) – a modelling technique used extensively in the design of hard tissue implants to evaluate the governing biomechanical interactions under physiological loading – is not routinely used in the assessment of novel VMMs. Given the need to emulate the physiological functions of native coronary arteries to prevent premature graft failure, FEA offers a complementary method to AM for tackling these design challenges and optimising the stress distribution and compliance of different graft designs [23].

1.1 Aims and Objectives

This thesis aims to mechanically characterise PVA/gelatin cryogels through variation of formulation parameters and further explore their potential as VMMs through the *in silico* design of heterogeneous multi-layered coronary artery grafts. The following overarching objectives are set:

- *Identify gaps in the mechanical characterisation of PVA/gelatin cryogel*: quantify the hyperelastic and viscoelastic properties as a function of M_w PVA and use of polymer coagulation treatment (Chapter 3);

- *Integrate PVA/gelatin mechanical characterisation data into computational models to inform the design of multi-layered coronary artery grafts*: employ FEA to analyse the stress/strain distributions and compliance of laminated PVA/gelatin graft designs relative to the native coronary artery wall (Chapter 4);

- *Expand heterogeneous graft design to explore biomimetic and interdigitated interfaces*: employ FEA to assess the impact of a bioinspired sinusoidal interface on the stress distribution and compliance of interdigitated PVA/gelatin grafts (Chapter 5).

1.2 Thesis Structure

Chapter 2 aims to guide the reader through the interdisciplinary research themes of this thesis by outlining the relevant background literature and theory. First, the cardiovascular system is introduced (Section 2.1) and the anatomy of the artery wall is dissected (Section 2.2). Then, in Section 2.3, the pathology behind CAD and atherosclerosis are described. This is followed by a review of the current approaches used to understand and treat CAD.

An overview of the mechanics of materials is provided in Section 2.4. This section is essential for understanding the constitutive laws that describe the mechanical environment of arteries, which are outlined in Section 2.5. The design requirements of synthetic grafts and VMMs in mimicking the mechanical and physiological environment of arteries are detailed in Section 2.6. In particular, the potential of PVA-based cryogels as VMMs is explored in relation to the design requirements set in the preceding sections.

Finally, the current status surrounding the design, manufacture and validation of multi-layered coronary artery grafts is reviewed in Section 2.7. By tying together these different disciplines, this chapter will set the scene for the research hypothesis specific to this thesis (Section 2.8).

Chapter 3 aims to address current knowledge gaps in the mechanical characterisation of PVA/gelatin cryogels. Specifically, Chapter 3 will present the linear elastic, dynamic viscoelastic and hyperelastic mechanical properties of PVA/gelatin cryogels as a function of M_w PVA and polymer coagulation treatment. Not only will the experimental data and their constitutive parameters provide further quantification of the mechanical behaviour of PVA/gelatin cryogel, the data will be used to inform the development of finite element (FE) models of PVA/gelatin grafts in Chapters 4 and 5 of this thesis.

Chapter 4 synergises the hyperelastic constitutive parameters of PVA/gelatin cryogel with FEA to probe the transmural biomechanics of four synthetic multi-layered graft designs under physiological pressure, relative to the coronary artery wall. While this thesis has investigated PVA/gelatin as the representative VMM, the proposed method is transferable to other hyperelastic biomaterials and is intended to guide the future validation of multi-layered grafts for the treatment of CAD.

Inspired by the waviness of the elastic laminae of arteries and the biomimetic interface design principles applied to hard tissue implants, Chapter 5 explores the potential of FEA to inform the design of functionally-graded vascular grafts with sinusoidal interfaces. The impact of sinusoid interface parameters on the transmural stress distribution and compliance of bi-layered PVA/gelatin grafts under physiological pressure is assessed.

Chapter 6 summarises the key conclusions from each research chapter in the

context of the aims and objectives of this thesis. The significance and limitations of the methods and results presented in each chapter are reviewed and potential future research trajectories are proposed.

Appendices A–C contain the supplementary material for each research chapter. These include (but are not limited to): constitutive fitting parameters; complementary simulations to those presented in the main body of the thesis; and the Python script developed to generate sinusoidal interfaces.

Chapter Two

BACKGROUND

2.1 The Cardiovascular System

2.1.1 Introducing the Cardiovascular System

The cardiovascular system is a network of blood vessels that circulates blood to every organ, tissue and cell in the body. Together with the heart, these vessels deliver the nutrients and respiratory gases essential for life. Likewise, they provide a disposal route for the metabolic waste produced by living organisms [25].

There are three major classes of blood vessels: arteries carry oxygenated blood away from the heart; veins return deoxygenated blood back to the lungs; and capillaries facilitate fluid exchange between the two. The collective network of vessels is often referred to as the vascular tree, reflecting the hierarchical branching observed between the large central arteries of the heart and the microscopic capillaries of bodily tissues [26].

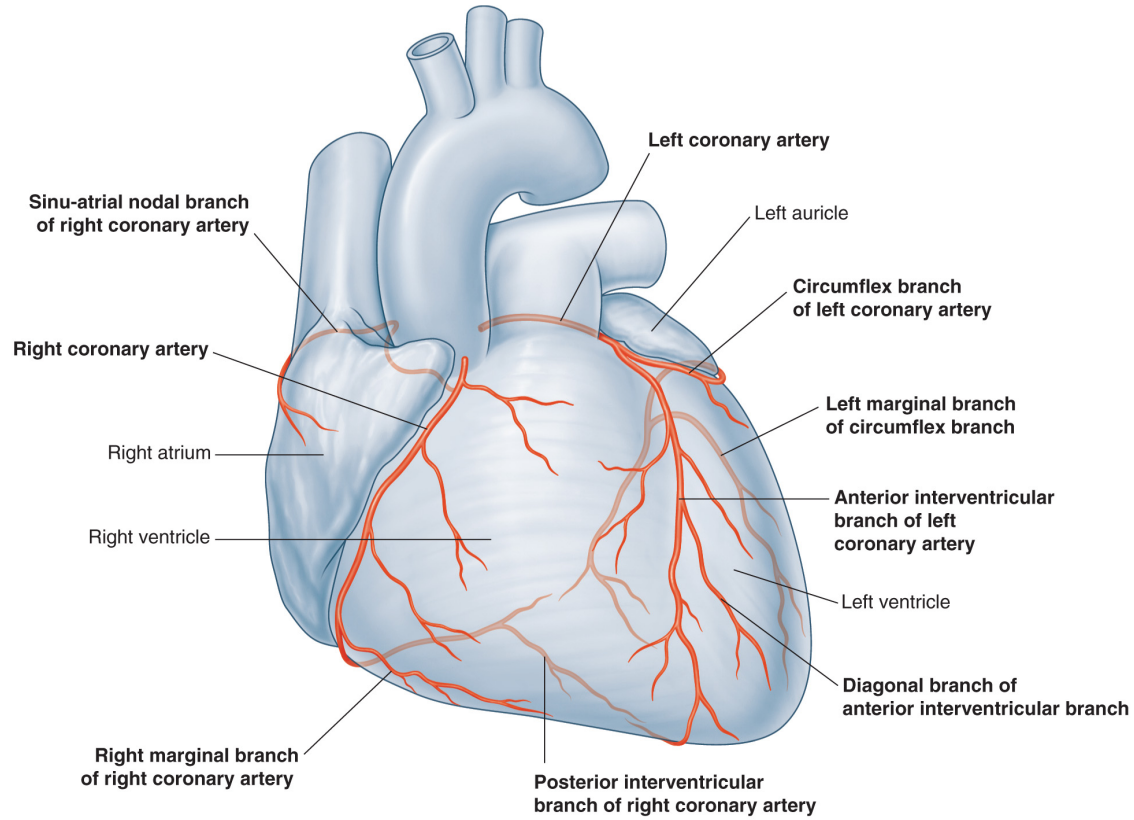


Figure 2.1: Anterior view of the coronary arterial system and its branches. Reprinted from [24] with permission from Elsevier Science & Technology Journals.

2.1.2 The Coronary Arteries

The coronary arteries supply oxygenated blood to the myocardium, the muscle layer of the heart. Originating from the aorta, the two main branches – the left (LCA) and right (RCA) coronary arteries – wrap around the epicardium, the surface layer of the heart (Figure 2.1). The LCA and its branches supply the left chambers of the heart, while the RCA and its branches supply the right chambers.

2.2 The Anatomy of Arteries

2.2.1 Artery Wall Structure

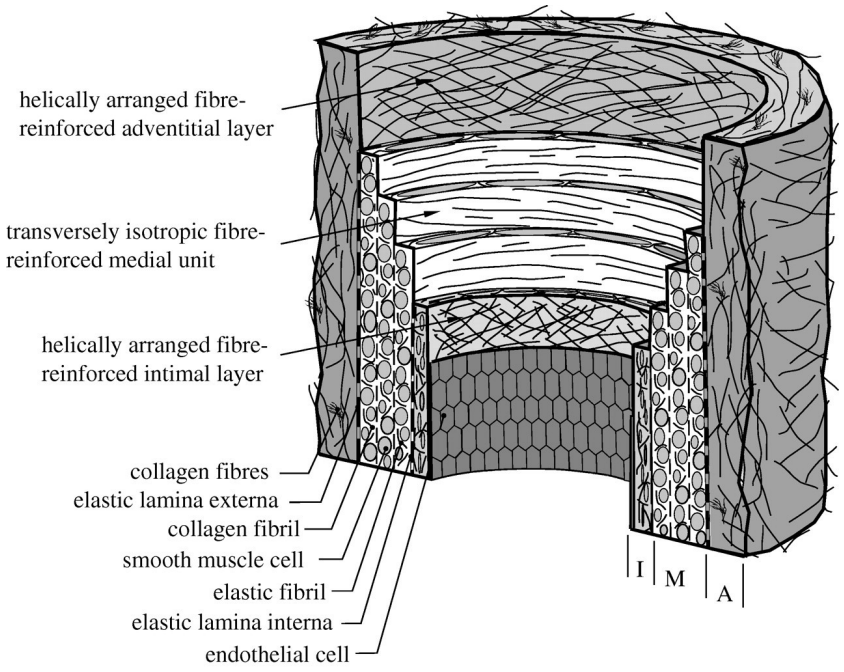


Figure 2.2: Idealised wall structure of a healthy elastic artery, consisting of the intima (I), media (M) and adventitia (A). Reprinted from [27] with permission from The Royal Society (UK).

Although the size and function of arteries varies throughout the vascular tree, they share the same heterogeneous wall structure. A healthy artery wall is comprised of three concentric tissue layers (Figure 2.2):

- *The tunica intima*: the blood-interfacing layer containing the endothelium and internal elastic lamina;
- *The tunica media*: the muscle-rich middle layer responsible for blood flow regulation and homeostasis;

- *The tunica adventitia*: the outer layer that provides structural support and integration with the surrounding tissues.

The organisation and orientation of constituent cells and extracellular matrix (ECM) proteins varies in each layer to confer specific biological and mechanical functions [28, 29]. Sections 2.2.2 and 2.2.3 will introduce these constituents and review their contribution to healthy and diseased-related vessel wall behaviour.

2.2.2 The Endothelium

The luminal surfaces of all blood vessels are lined with a monolayer of endothelial cells (ECs) called the endothelium. ECs are thin, flat cells approximately 50–70 µm long, 10–30 µm wide and 0.1–10 µm thick [30]. The endothelium functions as a permeable barrier through which molecules and cells are selectively transported between the bloodstream and the vessel wall [31, 32]. Importantly, the endothelium provides more than a selective physical barrier between the vessel and circulating blood. It regulates:

- Coagulation and thrombosis [33, 34];
- Immune cell trafficking and inflammation [35, 36];
- Vessel dilation and contraction (vasomotor tone) [37, 38];
- Growth of new blood vessels (angiogenesis) [39].

In a healthy vessel, the endothelium is quiescent, meaning that ECs do not proliferate (divide). However, this does not mean they are inert. Quiescent ECs are anticoagulant, antithrombogenic and anti-inflammatory [40]. Platelet adhesion

is suppressed through the production of antiplatelet agents such as nitric oxide and prostacyclin. Both agents are also potent vasodilators that help to maintain vasomotor tone [38]. Activation of anticoagulant pathways, for example the protein C/protein S pathway, prevents unnecessary blood clot formation by inactivating factors involved in the coagulation cascade [33]. If coagulation occurs, fibrin clots are dissolved through the upregulation of enzymes such as tissue-type plasminogen activator. For a more comprehensive overview of quiescent EC behaviour, the reader is directed to the recent review by Ricard *et al.* [41].

The observed physical and physiological characteristics of ECs (phenotype) varies across the vascular tree. This ensures homeostasis in the different organs and vessels of the body [33, 42, 43]. Not only are arterial ECs distinct to vascular and capillary ECs [44, 45], but ECs located near branch points and bifurcations will display higher proliferative behaviour than those located in straight segments of arteries [46]. Furthermore, ECs can adapt their phenotype in response to local chemical and biomechanical cues. ECs will switch to a pro-inflammatory and pro-thrombogenic phenotype when faced with vascular injury. Excessive phenotypic changes are associated with pathological remodelling of the cardiovascular system [42].

2.2.3 Vascular ECM

The vascular ECM is a specialised network of fibrous macromolecules embedded in ground substance, a hydrated gel comprised mostly of glycosaminoglycans (GAGs) and water [29, 47, 48]. It is secreted by resident ECs, vascular smooth muscle cells (VSMCs) and fibroblasts [48]. The ECM not only provides structural support to the artery wall, but plays a fundamental role in intercellular communication.

Although the specific mechanisms regulating vascular cell behaviour are complex, the ECM controls cell adhesion, proliferation, migration and differentiation – the basic functions needed for cell survival [49].

Collagen and elastin are the most abundant components of vascular ECM. Where collagen provides rigidity to the artery, elastin provides compliance. At low pressure, the mechanical behaviour of the artery wall is dictated by elastin; at high pressure, the crimping behaviour of collagen governs wall behaviour to prevent overdistension [50]. The organisation and orientation of collagen and elastin varies both across and within the different tissue layers of the artery wall (Figure 2.2) [27]. The impact of fibre dispersion in each layer on the mechanical functioning of arteries has been extensively studied [27, 51–53]. Notably, medial collagen is distributed circumferentially and demonstrates fibre engagement at all magnitudes of strain [51]. Meanwhile, the orientation of adventitial collagen is comparatively more varied at low or no strain, demonstrating fibre engagement after 20% strain [51, 52].

GAGs are highly hydrophilic polysaccharides that enable rapid diffusion of metabolites and nutrients through the ECM [49]. Proteoglycans are formed through the covalent bonding of GAG chains to core proteins. Proteoglycans are important components of the endothelial glycocalyx, a specialised form of ECM that lines the luminal surface of the endothelium [54]. Proteoglycans therefore regulate a number of cellular activities, from maintaining vascular permeability to binding cytokines, small signalling proteins that drive reactions with immune cells [55, 56]. In addition to modulating cellular interactions, proteoglycans (and GAGs) impact the mechanical and structural properties of the ECM through their interactions with collagen and elastin [57, 58]. Furthermore, their affinity for water and ability to maintain osmotic equilibrium serves as a mechanism for resisting compressive forces [58].

VSMCs regulate blood flow between arteries and tissues through contraction and relaxation. By changing the diameter (tone) of the vessel in response to mechanical (eg blood pressure) or metabolic (eg nitric oxide) stimulation, VSMCs help to maintain vasomotor tone [59]. Hence, VSMCs are an integral component of distributing arteries such as the coronary arteries. VSMCs also contribute to ECM protein synthesis [60]. In healthy arteries, VSMCs reside in the media and display a contractile and non-proliferative phenotype to maintain vascular tone. In damaged arteries, VSMCs switch to a synthetic and proliferative phenotype which supports the repair process through secretion of ECM-remodelling enzymes called matrix metalloproteinases [61]. In atherosclerotic arteries, synthetic VSMCs migrate to the intima in response to inflammation and contribute to atherosclerotic lesion formation [60].

2.2.4 Artery Classification

Arteries are classified as muscular or elastic depending on the relative tissue composition of the artery wall. The arteries closest to the heart, such as the aorta and pulmonary arteries, are elastic in order to accommodate high arterial pressures; elastic recoil during diastole propels blood further along the vascular tree [62]. Muscular arteries have a higher abundance of smooth muscle than their elastic counterparts, allowing them to regulate blood flow to the heart through vasodilation and vasoconstriction [63]. Though anatomically close to the heart, the coronary arteries supply blood to the myocardium and are muscular [64]. In general, the calibre (lumen diameter) of an artery indicates whether it is elastic or muscular: large calibre arteries (> 10 mm) are elastic, while medium to small calibre arteries (< 10 mm) are muscular [65].

2.3 Coronary Artery Disease and Atherosclerosis

2.3.1 Disease Development

CAD is a lipid-driven inflammatory disease that develops over the course of several decades. It is characterised by atherosclerosis, or the chronic narrowing and hardening (*sclerosis*) of the coronary arteries due to the accumulation of fatty lesions (*atheromas*) on the vessel wall. The progression of atherosclerosis is illustrated in Figure 2.3.

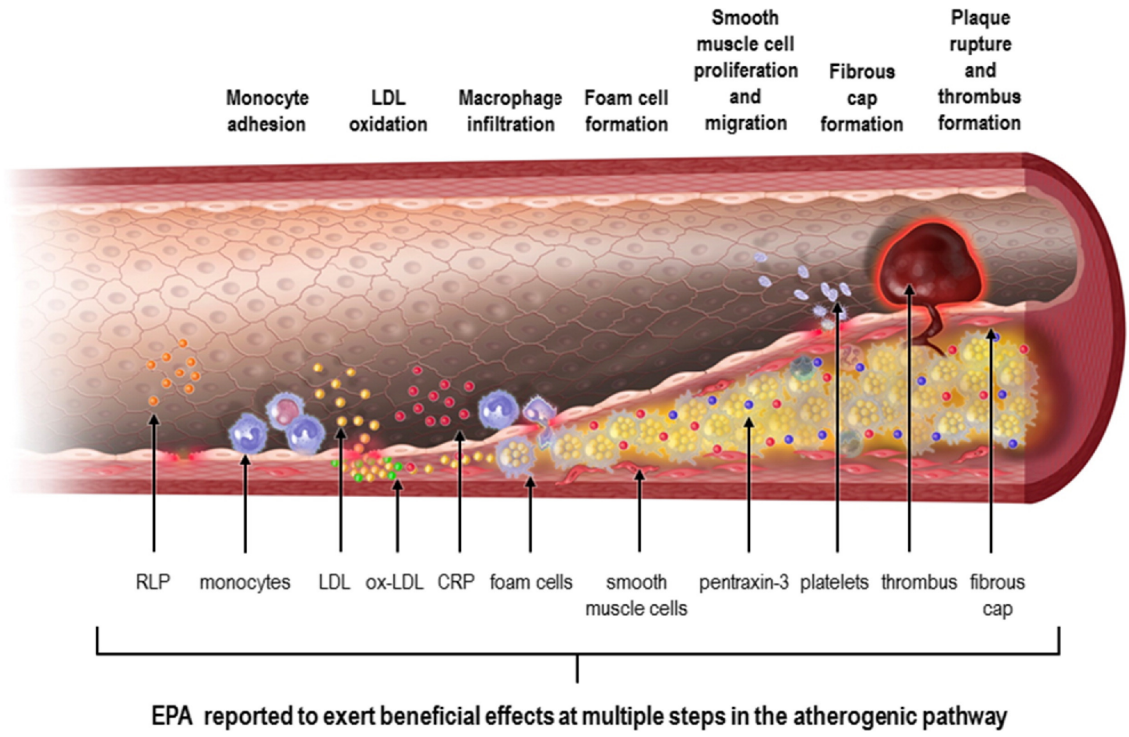


Figure 2.3: Atherosclerosis disease development. RLP, remnant-like particle; LDL, low-density lipoprotein; ox-LDL, oxidised low-density lipoprotein; CRP, C-reactive protein. Note that EPA (eicosapentaenoic acid) is not relevant to the progression of atherosclerosis and can be ignored. Figure reproduced from [66] under CC-BY-NC-ND 4.0 (https://creativecommons.org/licenses/by-nc-nd/4.0/).

The artery wall remodels in response to pro-inflammatory stimuli. These stimuli

are often linked to lifestyle-related stressors such as high blood pressure, smoking and poor diet [67]. Proteoglycans play an important role in early atherosclerosis, where endothelial dysfunction increases vascular permeability [56]. This facilitates the transendothelial migration of molecules responsible for lesion formation, including immune cells and cholesterol-containing low-density lipoproteins (LDLs) [68].

Activated ECs recruit white blood cells from the blood, namely circulating monocytes, by expressing inflammatory cytokines and surface adhesion molecules. Adhered monocytes infiltrate the subendothelial ECM, where they differentiate into lesional macrophages [69]. Not only do lesional macrophages oxidise LDLs [70], but they express scavenger receptors that preferentially engulf oxidised LDLs (ox-LDLs), a well-known class of inflammatory mediator [71, 72]. A positive feedback loop is generated: by producing ox-LDLs, macrophages contribute to further EC activation, macrophage recruitment and LDL modification [73]. Uncontrolled ox-LDL uptake and excessive cellular accumulation of cholesterol triggers foam cell formation [71].

Foam cells are present in fatty streaks, the earliest visible atherosclerotic lesions. While fatty streaks do not obstruct blood flow, they may mature into plaques that protrude into the lumen. When foam cells die, they release their lipid content to the surrounding intima; the debris aggregates to form a lipid-rich necrotic core [74]. Sustained inflammation causes VSMCs to switch to a synthetic phenotype, where they migrate to, and proliferate in, the intima [60]. This type of vascular remodelling is critical in the formation of advanced lesions. On the one hand, activated VSMCs display atheroprotective behaviour, synthesising ECM proteins to form a layer of connective tissue over the luminal surface of the plaque. This tissue, known as the fibrous cap, separates the necrotic core from the blood to prevent thrombosis [75]. On the other hand, macrophage-like VSMCs amplify inflammation by increasing ox-LDL retention, accelerating necrotic core growth [75].

In the latter stages of CAD, the lumen may narrow to the point of occlusion. If blood flow through the coronary arteries is compromised, the rate of oxygen delivery to the heart will not meet the metabolic requirements needed to pump blood efficiently [76]. This condition, known as myocardial ischaemia, is symptomatic of CAD and may lead to unstable angina (chest pain). In the event of an acute plaque rupture and subsequent thrombus formation, the coronary artery may be blocked completely, leading to myocardial infarction (heart attack).

2.3.2 Treatment Methods for Coronary Artery Disease

Preventing CAD is preferable to treating CAD. In 2019, more than 4 in 5 CVD-related deaths worldwide were associated with, or attributed to, modifiable risk factors such as hypertension, poor diet and high LDL cholesterol [77]. Numerous health organisations emphasise the importance of lifestyle changes to reduce risk [5, 77, 78].

For patients with advanced CAD, coronary revascularisation is performed to restore blood flow to the heart. Revascularisation is achieved using one of two methods: (1) stenoses are reduced using percutaneous coronary intervention (PCI); or (2) they are bypassed using coronary artery bypass grafting (CABG) surgery. PCI is a minimally-invasive procedure in which a balloon catheter is inserted into the lumen of an occluded artery and inflated. A drug-eluting metal stent is then placed to keep the artery patent [19]. CABG, on the other hand, is a surgical procedure that uses vascular grafts to create a new route through which blood can reach the myocardium [79]. The optimal strategy for revascularisation remains contentious. PCI mitigates the risk associated with open heart surgery, and advances in drug-eluting stent technology demonstrate reduced rates of restenosis compared with

their bare metal counterparts [80]. In 2019, 100,294 PCIs were performed in the UK compared with just over 14,000 CABG procedures [77]. However, several clinical studies indicate lower rates of rehospitalisation and improved long-term survival when using CABG to treat advanced CAD [81, 82]. This thesis is focused on CABG and the use of vascular grafts.

CABG was first performed over fifty years ago using blood vessels from the patient's own vasculature [79]. Since then, the saphenous vein (SV) and the internal thoracic artery (ITA), harvested from the leg and chest respectively, have become the gold standard conduits for CABG [83]. Nevertheless, several adverse outcomes have been documented when using these vessels. Firstly, veins do not make good artery substitutes. Mismatched calibre between SVs and coronary arteries leads to low patency rates, increasing the likelihood of graft failure and reoperation [84]. ITA grafts offer better 10-year patency rates than SV grafts [85, 86]; however, in cases where multiple bypasses are required, the ITA alone cannot provide enough tissue for grafting. By adding atherosclerotic vessels and vein varicosity into the mix, it is easy to see how the limitations associated with autologous vessels has fuelled interest into alternative coronary artery conduits [83].

Donor tissue is more readily available than autologous tissue. Furthermore, using donor tissue minimises the number of incision sites needed during surgery. However, the tissue recovery process is inefficient. A 20-year analysis from the European Homograft Bank revealed that 32% of arterial segments were discarded prior to preservation, citing morphology and bacterial contamination as the most common causes for rejection [87]. A more radical approach, and the one underpinning this thesis, is to tissue-engineer coronary artery grafts using synthetic VMMs. While polyester grafts have found reasonable success in repairing large arteries such as the aorta [88], the search for small calibre (<6 mm) synthetic grafts remains challenging

due to the intricate balance between EC behaviour, their surrounding mechanical environment and graft success [89, 90]. Section 2.4 will introduce theory needed to understand the mechanical environment of arteries (Section 2.5).

2.4 The Mechanics of Materials

2.4.1 Overview

So far, this thesis has introduced the cardiovascular system, the physiology of healthy and diseased coronary arteries, and the need to develop synthetic grafts for CABG. As well as discussing the biological activities of the artery wall, we must also understand the impact of mechanical forces in maintaining arterial homeostasis and initiating CAD. The *biomechanics* of the artery wall must therefore be factored into the graft design process.

Before we can understand the biomechanical behaviours of the artery wall – or design synthetic grafts that mimic them – we must first understand how materials deform when subjected to external forces. This field of study, called the mechanics of materials, is critical to predicting how a structure will perform under a prescribed load and the mechanism through which it will fail. Four fundamental concepts describing the deformation of soft biological tissues must be established:

- Stress and strain (Section 2.4.2);
- Linear elasticity and stiffness (Section 2.4.3);
- Hyperelasticity (Section 2.4.4);
- Viscoelasticity (Section 2.4.5).

2.4.2 Stress and Strain

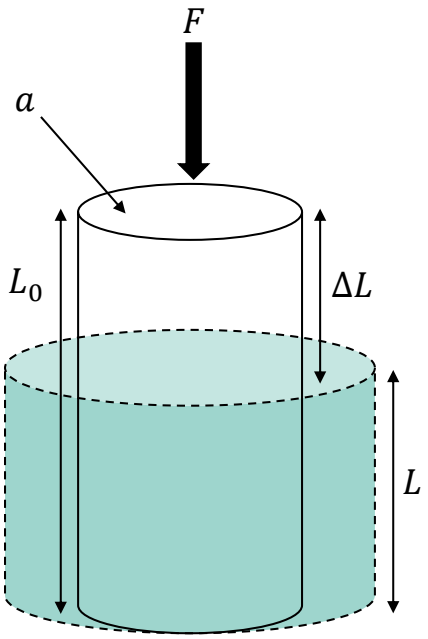


Figure 2.4: Uniaxial compression of a cylinder, showing the relationship between the applied force (F), initial length (L_0) and compressed length (L).

Consider a cylinder of length L_0, as displayed in Figure 2.4. Internal forces are generated within the cylinder in response to applied load F. The engineering stress, σ, is a measure of the internal resistance to compression per unit area (a) of the cylinder (Equation 2.1).

$$\sigma = \frac{F}{a} \tag{2.1}$$

The cylinder deforms in the direction of F by amount ΔL. Like stress, ΔL can be normalised to the sample's geometry. While ΔL provides an absolute measure of deformation, it is more useful to define shape change in terms of the relative change in length from the initial length. This unitless value is known as the engineering strain, ϵ (Equation 2.2).

$$\epsilon = \frac{L - L_0}{L_0} = \frac{\Delta L}{L_0} \tag{2.2}$$

Converting force and displacement into stress and strain sheds light on the intrinsic material properties of the cylinder. A stress–strain diagram is used to assess the relationship between stress and strain. The shape of the curve tells us whether a material is brittle or ductile, the stresses and strains at which elastic and plastic deformation occur, and ultimately when a material will fail. For further detail on stress and strain, the reader is directed to the textbook by Hibbeler [91].

2.4.3 Linear Elasticity

Many solid materials behave elastically. A material is perfectly elastic if it returns to its initial dimensions after an external load is removed. Consider the cylinder in Figure 2.4 once more. If the amount of force needed to compress the cylinder is directly proportional to the induced displacement (x), Hooke's law is instated:

$$F = -kx \tag{2.3}$$

where k is the proportionality constant. Converting force and displacement to stress and strain yields the Young's modulus of elasticity, E:

$$E = \frac{\sigma}{\epsilon} \tag{2.4}$$

While k is an extrinsic property of the cylinder, E is an intrinsic property of the constituent material. E is therefore a measure of material stiffness: the greater the value of E, the more stress that is needed to induce a specified strain. It should be noted that E is the elastic modulus in tension and compression; different elastic moduli exist for other modes of deformation. In reality, no material is perfectly elastic. Hooke's law (and therefore E) is only applicable for very small deformations. This translates to the linear elastic region of a stress–strain curve. Beyond this, plastic (permanent) deformation and failure occurs. For further detail on lin-

ear elasticity and stress–strain diagrams, the reader is directed to the textbook by Hibbeler [91].

2.4.4 Hyperelasticity

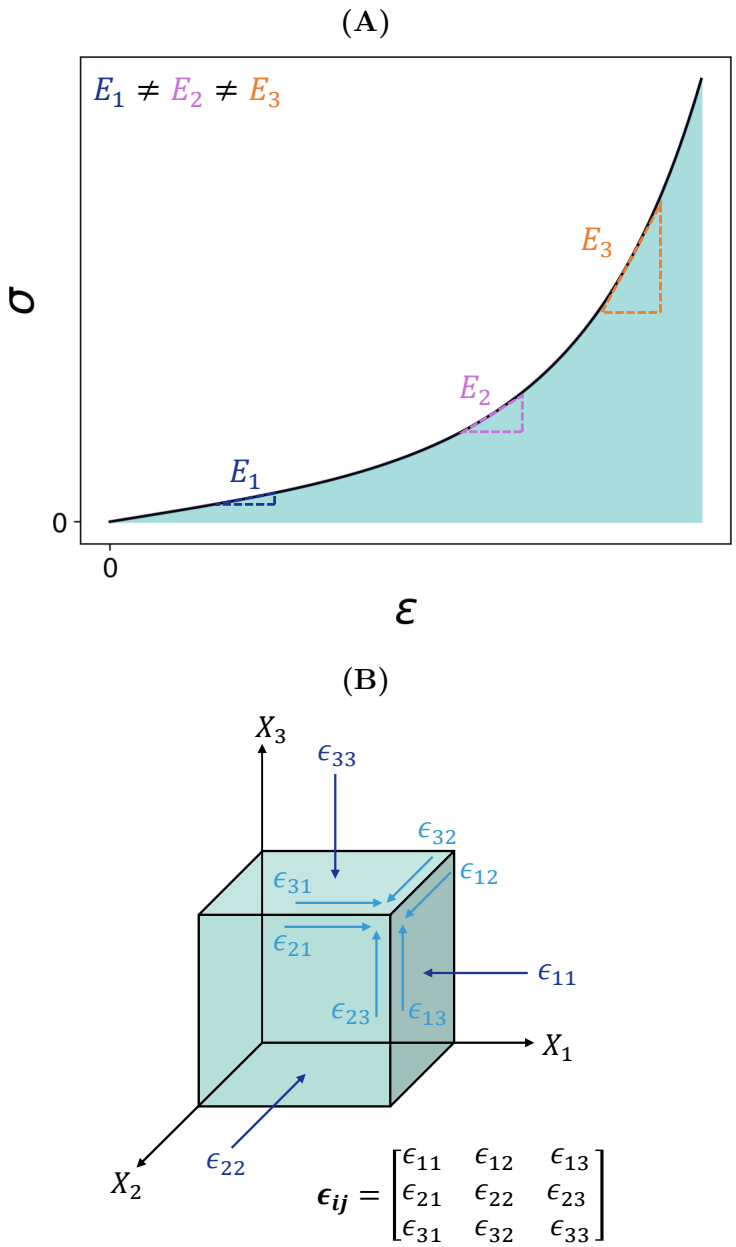


Figure 2.5: **(A)** Example non-linear hyperelastic stress–strain curve. The shaded area is represented by U; **(B)** strain tensor for a 3D material.

Hooke's law describes linear elastic behaviour, which is a fair assumption for many solid materials. For materials such as biological tissue and hydrogels, however, the elastic behaviour is highly non-linear (Figure 2.5A). Such materials are said to be hyperelastic. Although linear elastic theory can be used to model the elastic behaviour of these materials at low strain, more complex constitutive models are needed to accurately model elastic behaviour at larger strains [92].

Hyperelastic models use strain energy density functions, U, to relate the amount of energy needed per unit volume of material to induce a given deformation [93]. The strain energy is equal to the area under the stress–strain diagram. Several assumptions are made when formulating U: (1) the stress–strain relationship is strain-rate independent; (2) the material does not display hysteresis and all energy is recovered upon removal of load; and (3) the material is nearly or completely incompressible [93]. Isotropic hyperelastic models also assume the material is homogeneous [93]. Anisotropic formulations (notably the Holzapfel-Gasser-Ogden model [94]) have been developed to model the collagen fibre-reinforced behaviour of arterial tissue [95], but their theory go beyond the scope of this thesis. Hyperelastic models may be phenomenological (derived from experimental observations) or mechanistic (derived from an understanding of the underlying microscopic structure of the material, such as networks of idealised chain molecules) [96, 97]. As hyperelastic models will be fitted to experimental test data in later chapters, only the theory behind phenomenological models will be discussed.

Phenomenological models are formulated by fitting mathematical functions derived from mechanical principles to experimental test data obtained under uniaxial, biaxial and/or shear loading [92, 93]. Models are chosen based on their ability to accurately reproduce experimental data across all relevant loading modes. Additional factors influencing model choice include material type, ease of imple-

mentation and the number of constitutive parameters with unique solutions [93, 96, 98]. In practice, hyperelastic models containing the fewest parameters needed to accurately model the stress–strain response of the material are desired to increase model practicality, especially in terms of the number of experimental tests needed and computational cost [92, 98].

Two key types of isotropic phenomenological models have emerged. The first are expressed by principle stretches (λ_i). Considering Figure 2.4 once more, λ_i are given by the ratio of L and L_0 in dimension i. λ_i can be related to strain using Equation 2.5.

$$\lambda_i = \frac{L_i}{L_{0i}} = \frac{L_{0i} + \Delta L_i}{L_{0i}} = 1 + \frac{\Delta L_i}{L_{0i}} = 1 + \epsilon_i \tag{2.5}$$

The Ogden model is an example of a hyperelastic model based on principle stretches (Equation 3.13).

$$U\,(Ogden) = \sum_{i=1}^{N} \frac{2\mu_i}{\alpha_i^2}(\bar{\lambda}_1^{\alpha_i} + \bar{\lambda}_2^{\alpha_i} + \bar{\lambda}_3^{\alpha_i} - 3) \tag{2.6}$$

where $\overline{\lambda}_i$ are the principle stretch ratios and μ_i and α_i are material constants describing the shear behaviour.

The second common type of phenomenological models are expressed by the principal invariants of the strain tensor $\boldsymbol{\epsilon}$, I_i (Figure 2.5B, Equations 2.7–2.9).

$$I_1 = tr(\boldsymbol{\epsilon}) \tag{2.7}$$

$$I_2 = \frac{1}{2}[tr(\boldsymbol{\epsilon})^2 - tr(\boldsymbol{\epsilon}^2)] \tag{2.8}$$

$$I_3 = det(\boldsymbol{\epsilon}) \tag{2.9}$$

For incompressible materials, $I_3 = 1$; thus, U is a function only of I_1 and I_2 [99]. Polynomial-based strain energy functions are based on I_1 and I_2 (Equation 3.11).

$$U\,(polynomial) = \sum_{i+j=1}^{N} C_{ij}(\bar{I}_1 - 3)^i(\bar{I}_2 - 3)^j + \sum_{i=1}^{N} \frac{1}{D_i}(J_{el} - 1)^{2i} \tag{2.10}$$

where N is the order of the polynomial, J_{el} is the elastic volume ratio and C_{ij} and D_i are material constants that describe the shear (C_{ij}) and compressibility (D_i) behaviour of the material. For fully incompressible materials, $D_i = 0$ [98] and the compressibility term is subsequently eliminated to yield Equation 3.11.

$$U\,(polynomial) = \sum_{i+j=1}^{N} C_{ij}(\bar{I}_1 - 3)^i(\bar{I}_2 - 3)^j \tag{2.11}$$

If I_2 is omitted, the polynomial model degenerates into a reduced polynomial model of the general form shown in Equation 3.12.

$$U\,(reduced\,polynomial) = \sum_{i=1}^{N} C_{i0}(\bar{I}_1 - 3)^i \tag{2.12}$$

Specific forms of each model are obtained for specific choices of C_{ij}. For example, the Mooney-Rivlin form follows the first order polynomial model (Equation 2.13).

$$U\,(Mooney - Rivlin) = C_{10}(\overline{I}_1 - 3) + C_{01}(\overline{I}_2 - 3) \tag{2.13}$$

Meanwhile, when the order of the reduced polynomial model is set to 3, the Yeoh form is obtained (Equation 2.14).

$$U\,(Yeoh) = C_{10}(\overline{I}_1 - 3) + C_{20}(\overline{I}_1 - 3)^2 + C_{30}(\overline{I}_1 - 3)^3 \tag{2.14}$$

2.4.5 Viscoelasticity

A viscoelastic material exhibits both solid-like (elastic) and fluid-like (viscous) properties. If an applied stress is removed from a purely elastic material, the material will immediately recover its original shape. Conversely, a purely viscous material shows time-dependent deformation behaviour and will retain its new shape. This difference is attributed to each material's ability to dissipate energy. The elastic material stores all of the energy exerted upon it as elastic potential energy until the load is removed. Meanwhile, the viscous material irreversibly dissipates the energy.

Polymers, including the natural polymers comprising the vascular ECM, are viscoelastic. Long polymer chains stretch under mechanical loading to store energy elastically; the same polymer chains also reorganise over time to dissipate the induced stress [100]. The elastic response is characterised by the storage modulus, E', and the viscous response is characterised by the loss modulus, E''. The combination of elastic and viscous contributions is given by the dynamic modulus of elasticity, E^*:

$$E^* = E' + iE'' \tag{2.15}$$

The relative contributions of E' and E'' are strain rate dependent, meaning the viscoelastic response at short relaxation times (seconds and less) differs to that observed at long relaxation times (minutes to days) [101]. Long-term viscoelasticity is assessed using stress relaxation and creep tests. Stress relaxation measures the gradual decrease in stress of a material when held at a constant strain, while creep measures the gradual increase in strain of a material when held at a constant stress.

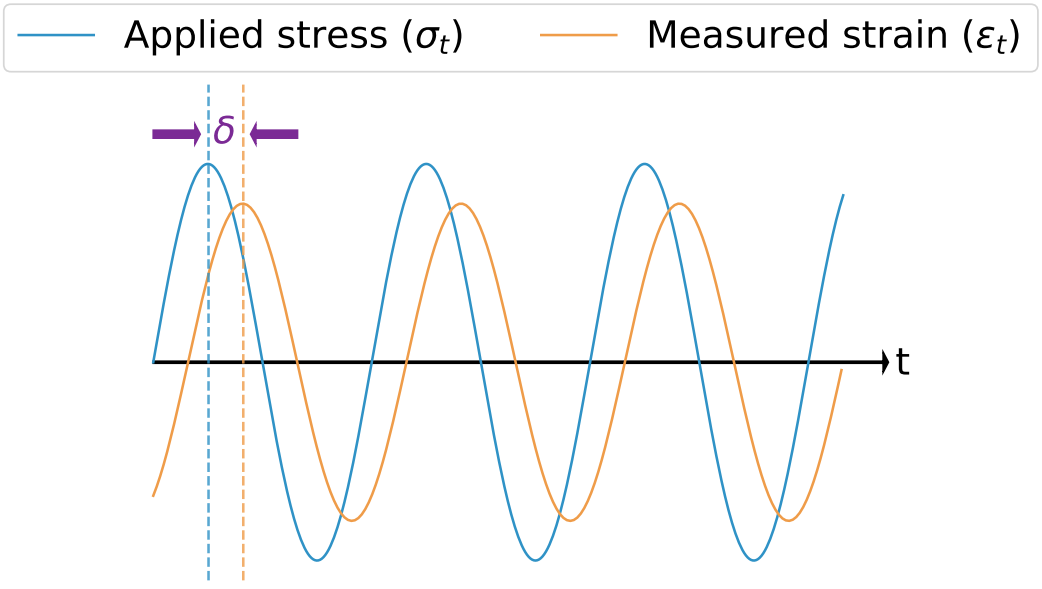


Figure 2.6: Applied sinusoidal load and corresponding displacement waveform of a viscoelastic material, plotted as a function of time t.

Long-term viscoelasticity is characterised using quasi-static loads. However, blood vessels are subjected to dynamic loads. The resting adult human heart beats roughly 65–75 times per minute [50]. Using a mechanical characterisation test that simulates the dynamic nature of pulsatile blood flow is therefore crucial to understanding the short-term viscoelastic response of the artery wall at physiologically relevant frequencies [102].

Dynamic mechanical analysis (DMA) characterises the short-term E^* of a material by applying a sinusoidal force F in the frequency range of interest and recording the resulting sinusoidal displacement response x or vice versa (Figure 2.6) [103–105]. To calculate E^* at a given frequency, F and x are first transformed from the time domain using a fast Fourier transform; the ratio of peak F to peak x gives the dynamic stiffness, k^* (Equation 2.16). Dividing k^* by the shape factor S of the sample, where S is calculated as the sample's volume, gives E^* (Equation 2.17).

$$k^* = \frac{F^*}{x^*} \tag{2.16}$$

$$E^* = \frac{k^*}{S} \tag{2.17}$$

The phase lag δ, calculated as the difference in phase angle between the two waves, reflects the material's tendency to recover elastic energy ($\delta \to 0°$) or flow ($\delta \to 90°$). Thus, the δ of a viscoelastic material falls between 0° and 90°, and the elastic (in phase) and viscous (out of phase) components of stress can be resolved from E^* using δ, as demonstrated in Figure 2.7.

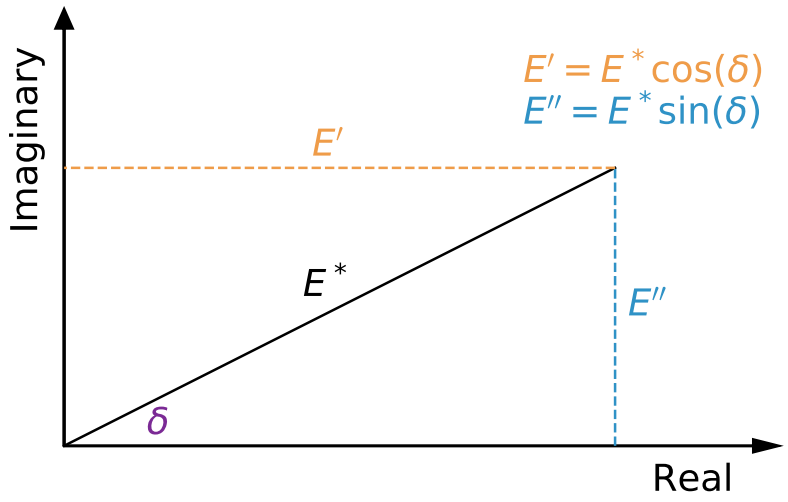


Figure 2.7: Using δ, E^* can be solved for E' and E''.

2.5 The Mechanical Environment of Arteries

2.5.1 Haemodynamic Forces

Section 2.4 provided the background theory for understanding the solid mechanics phenomena (linear elasticity, hyperelasticity and viscoelasticity) that are observed as a result of the artery wall structure outlined in Section 2.2. Understanding the mechanical environment of arteries is critical to deciphering the physiological functions of arteries *in vivo* and the requirements of synthetic grafts for CABG. The following sections will provide an overview of the relationship between ECs and their surrounding mechanical environment, and highlight mechanical considerations in the context of coronary artery graft development.

Blood circulation through the vasculature generates a complex array of interrelated mechanical forces [106]. Furthermore, these forces are transient, driven by changes in the cardiac cycle and subsequent propagation of the blood pressure

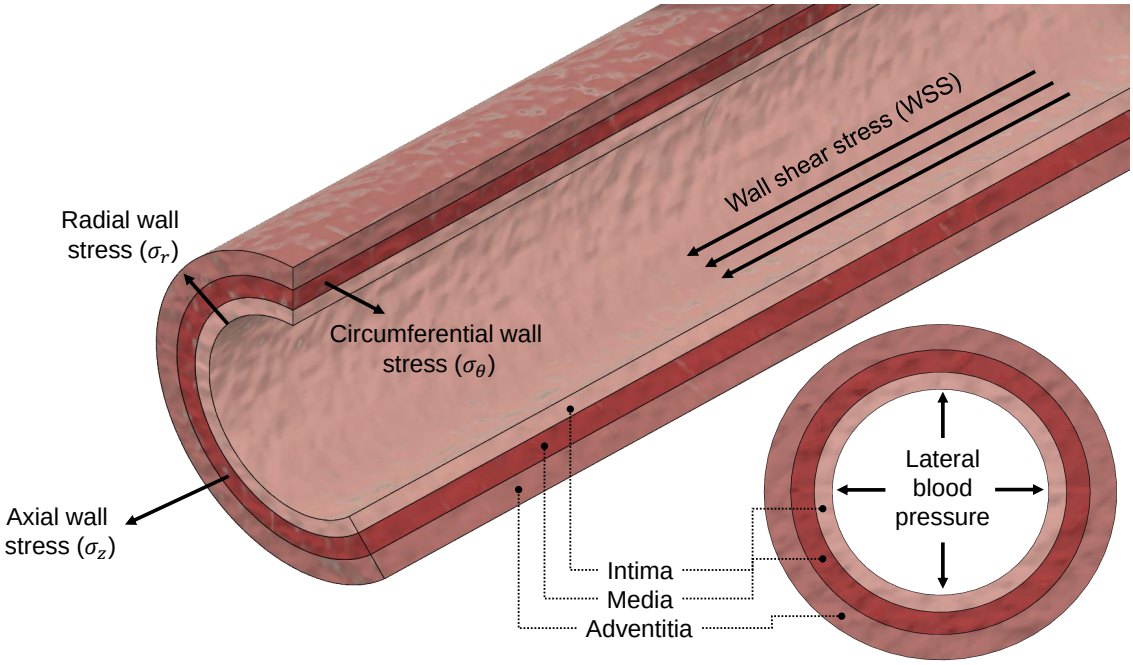


Figure 2.8: Haemodynamic forces acting on an idealised artery wall.

pulse [107]. As such, the endothelium is subjected to a combination of dynamic forces arising from fluid flow [106, 107]. These haemodynamic forces are depicted in Figure 2.8.

Haemodynamic forces act directly on ECs. Blood flow through the artery, for instance, creates frictional drag parallel to the luminal surface of the endothelium. This tangential force, commonly referred to as the wall shear stress (WSS), is highly sensitive to the vessel geometry [108]. Moreover, while blood flow through straight regions of the vasculature is laminar and unidirectional, bifurcated regions are associated with turbulent flow, flow separation and comparatively lower time-averaged WSS [108]. Differences in the average curvature [109] and torsion [110] of the three main human coronary arteries (the left descending anterior (LAD) artery, the left circumflex (LCX) and the RCA) as they wrap around the epicardium result in varying levels of WSS exposure, with low WSS defined as WSS <0.43–0.68 Pa and high WSS defined as WSS >0.86–1.30 Pa [111]. As low time-averaged WSS

is implicated in the progression of atherosclerotic plaque growth and constrictive remodelling in patients with CAD [111–113], high and low WSS are considered atheroprotective and atheroprone, respectively [114].

In addition to shear stress, pulsatile changes in blood pressure also exert a perpendicular force on the artery wall [115]. Internal stresses are generated in the wall to counteract wall distension under pressure. This phenomenon, known as cyclic stretch, is impacted by the vessel thickness, diameter and elasticity [116]. Internal wall stresses induced by cyclic stretch are several orders of magnitude larger than WSS [117].

Notably, the mechanical influence of circumferential stretch on EC and VSMC function represents a key research theme spanning several decades [118–121]. VSMCs, for example, produce more collagen under sustained high pressure to increase wall thickness and restore circumferential wall stress to homeostatic levels [122]. 5–10% EC stretch (with respect to the cell's original dimensions) is considered physiologic and is associated with an atheroprotective phenotype; EC stretch $\geq$18% is considered pathologic and is associated with an atherogenic phenotype [123, 124]. Compared with ECs cultured under static conditions (as may be observed *in vivo* due to stagnant flow), ECs subjected to cyclic stretch are elongated and oriented perpendicular to the stretch direction to reduce tension [125].

In vivo, the arterial pressure never drops to 0 mmHg; thus, the circumferential stress (σ_θ) field of the artery wall never reaches zero [62]. In addition, the existence of residual stresses within arteries (stresses that remain within the wall, even when free of all external loads) has been known for 40 years [126]. Residual stresses are believed to maintain homeostasis by controlling the stress gradient within and across the layers of the arterial wall [127], and pathological

changes in σ_θ can trigger vascular remodelling [128]. In CAD, regions of pressure-induced high σ_θ are believed to contribute to the localisation of atherosclerotic plaques [129] and plaque rupture [118, 130]. Therefore, understanding and measuring the σ_θ profile of the artery wall provides insight into the pathological events associated with CAD.

Although many studies investigate the relationship between cyclic stretch and circumferential stress and strain, the three-dimensionality of the wall also generates stresses and strains in the radial and axial directions [131, 132]. Research suggests that radial and axial displacement are coupled and mediated by the distending pressure waveform [131, 133]. Axial stresses are implicated in the progression of atherosclerosis, with stenoses increasing longitudinal wall stress proximal to the stenotic lesion [132].

2.5.2 ECM Stiffness

Alongside the haemodynamics forces associated with fluid flow, ECs are also subjected to contact forces derived from the underlying matrix stiffness and topology of the artery wall [106, 107, 134]. ECs adhered to the vessel wall exert contractile forces that deform the basal membrane to a magnitude proportional to the stiffness and thickness of the underlying tissue [135, 136]. It is thought that the collective forces transmitted by ECs are integrated over the endothelium, allowing cells to sense the effective stiffness of all three layers of the artery wall [136].

A large range of elastic moduli have been reported for coronary arteries, spanning from 0.09 MPa to 10 MPa [9]. The discrepancy between values is attributed to age, anatomical location, pathology and measurement method; notably, the stiffness of excised vessels differs to pressurised vessels due to their

hyperelasticity [134]. In addition, the elastic moduli of arteries measured using mechanical testing differs to that measured using atomic force microscopy, with the former measuring bulk stiffness and the latter measuring local stiffness [106]. Irrespective of these factors, arterial stiffness is predominantly determined by the relative composition of compliant elastin and rigid collagen [29]. The balance of elastin and collagen is layer-specific and is affected by age, disease and the haemodynamic environment outlined in Section 2.5.1. For instance, pathogenic cyclic stretch activates elastolytic enzymes responsible for elastin degradation in the media [137]. The regulatory impact of ECM stiffness on physiologic and pathogenic EC behaviour makes ECM stiffness a key contributor to the mechanical environment in coronary arteries.

2.5.3 Mechanotransduction

The endothelial processes outlined in Section 2.2.2, such as the maintenance of blood coagulation, immune response and vasomotor tone, are not only regulated by chemical mediators but also by haemodynamic forces [115]. ECs act as a sensor and transducer of the mechanical forces produced by the local microenvironment [107, 115, 138]. This process, known as mechanotransduction, allows ECs to convert mechanical signals into functional responses under both physiological and pathological conditions [107].

The general mechanotransduction process may be simplified as follows: a mechanosensor (a cellular structure expressed on the EC surface that is capable of sensing physical forces) detects a mechanical signal → the mechanosensor activates multiple complex signalling pathways within the cell → these signalling pathways activate transcription factors that modulate gene expression →

protein expression is subsequently triggered or suppressed [139]. The resulting up- or down-regulation of these proteins has short- and long-term atheroprotective or atherogenic effects on ECs. The mechanical environment therefore plays a pivotal role in determining vascular health.

ECs rapidly detect the haemodynamic forces and ECM-derived forces outlined in Sections 2.5.1 and 2.5.2. An enormous variety of mechanosensors have been identified (Figure 2.9) [140]. These include luminal mechanosensors (eg G-protein-coupled receptors and mechano-activated ion channels), junctional mechanosensors (eg the PECAM-1/VE-cadherin/VEGFR-2 complex [141]) and basal mechanosensors (eg integrins) [115]. Each mechanosensor plays a pivotal role in dictating EC growth, differentiation, migration and survival through regulation of mechanosensitive genes. Luminal and junctional mechanosensors are often involved in shear-mediated cell signalling, while basal mechanosensors sense ECM type and stiffness [115].

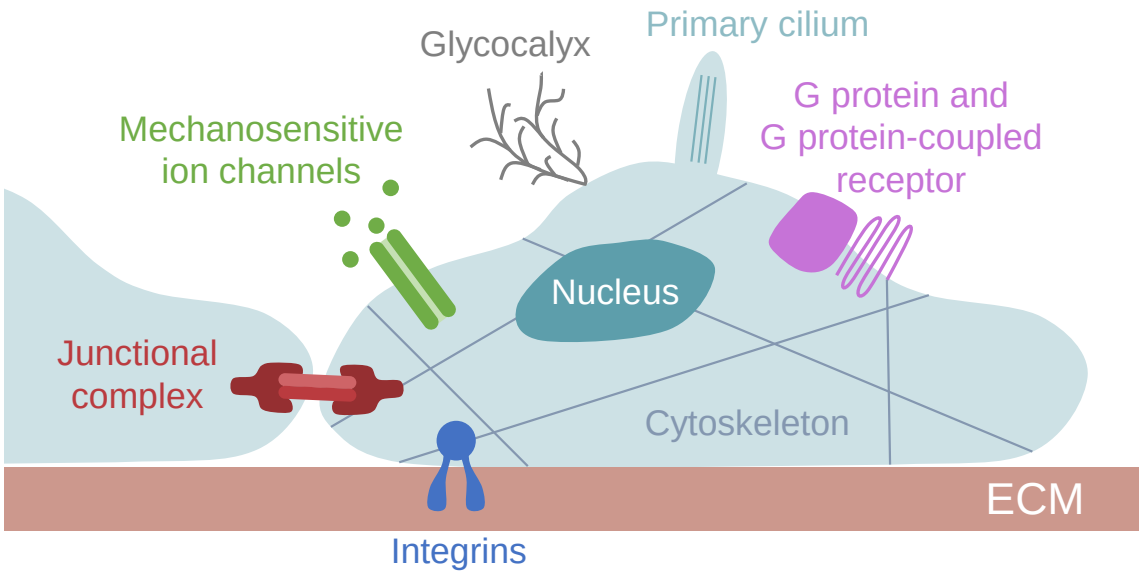


Figure 2.9: Types of mechanosensor structures that form the EC mechanosensory system.

It is unsurprising that WSS-mediated mechanotransduction has dominated the

literature due to the link between atherogenic flow and CAD progression. Figure 2.10 summarises the expression of several key transcription factors linked to atheroprotective and atherogenic flow [142]. The figure is intended only to give the reader a taste of EC mechanotransduction in response to mechanical stimulation – the transcription factor Nrf2, for example, regulates the expression of >1000 genes [143], and WSS has been linked to the transcription of hundreds of mechanosensitive genes [144]. However, mechanosensitive genes are also mediated by cyclic stretch, lateral pressure, and substrate stiffness and topology.

Cyclic stretch is known to alter both EC morphology and cellular signalling through mechano-activated ion channels and integrins [123, 124]. Our understanding of cyclic stretch-mediated mechanotransduction pathways is constantly evolving: the recent transcriptome analyses by Lai *et al*, for instance, mapped pathological stretch to four key endothelial responses driven by eight transcription factors [123]. They also identified transcription factors mediated by both physiological cyclic stretch/WSS (and pathological cyclic stretch/WSS), highlighting the synergy between the different domains of the mechanical environment to determine atheroprotective and atherogenic behaviours in arteries [123].

2.5.4 Significance for Coronary Artery Grafts

Understanding the mechanical environment of arteries and the interactions of ECs with their mechanical microenvironment is critical for the design of functional coronary artery grafts [107]. These grafts are intended to replace diseased sections of the coronary vasculature; once implanted, they are subjected to the dynamic forces of the cardiovascular system. Sections 2.5.1–2.5.3 highlighted the influence of mechanical stimuli on EC phenotype. It follows that, if the mechanical behaviour of

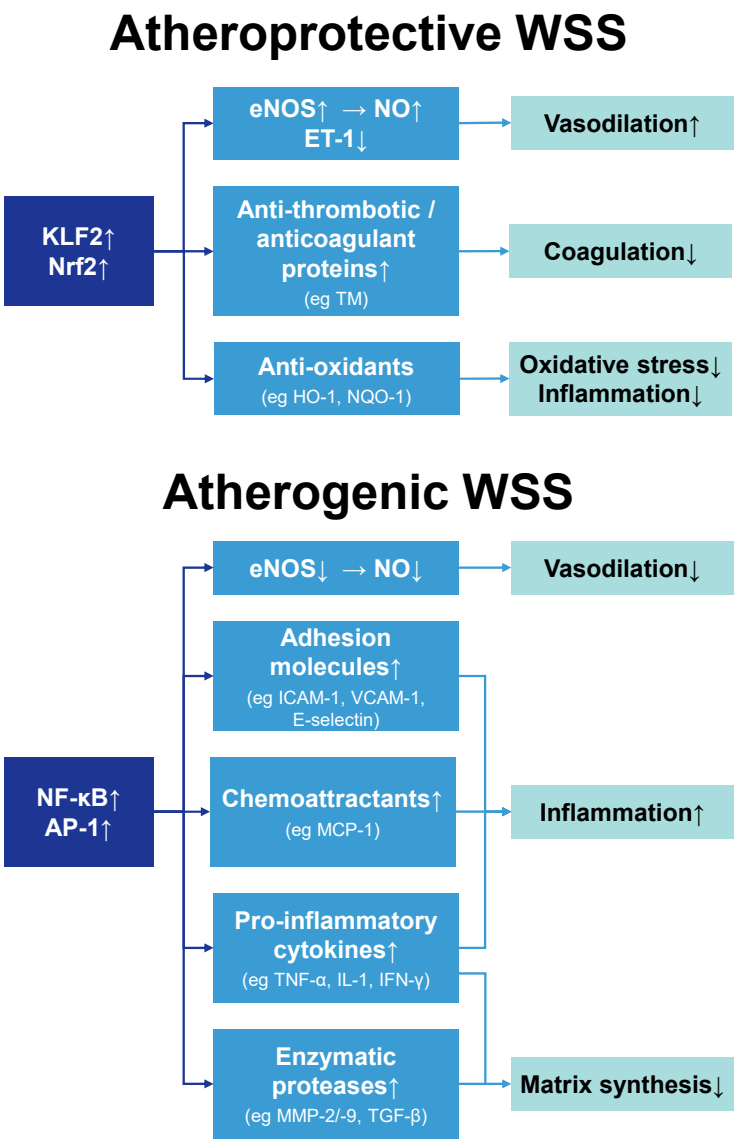


Figure 2.10: Examples of transcription factors (KLF2, Nrf2, NF-κB and AP-1) and their downstream products under atheroprotective and atherogenic flow.

a synthetic graft is sufficiently different to healthy arterial tissue, ECs will sense and translate abnormal mechanical cues into potentially pathogenic behaviours through activation of transcription factors related to vascular remodelling, triggering graft failure [145].

Consider the response of a rigid synthetic graft under pulsatile flow. Many of

the mechanotransduction pathways of grafted ECs are mediated by flow patterns created at the anastamoses (and thus the compliance difference between the graft and native vessel) [146]. Small calibre grafts, including those designed for CABG, often fail due to compliance mismatch between the synthetic graft and adjacent tissue [8, 89]. The reduced distensibility of rigid synthetic grafts disrupts the elastic recoil of adjacent arterial tissue during diastole [8, 147]. The reduced propagation of pulsatile energy at the graft–artery interface weakens the artery and is a known cause of anastomotic aneurysm formation [8].

In addition, the mismatch in material stiffness alters the anastomotic geometry, generating turbulent flow patterns around the anastamoses [8]. Disturbed flow promotes downstream platelet aggregation and thrombus formation; meanwhile, flow separation zones trigger release of growth factors which increase the proliferation of VSMCs and myofibroblasts [147]. Decreased mean WSS, increased oscillating WSS and suture line stresses have all been linked to increased EC injury and inflammation in vascular grafts [148]. Furthermore, studies on hydrogels exceeding the stiffness of subendothelial matrix of bovine carotid arteries have demonstrated that comparatively increased graft stiffness destabilises EC–EC junction integrity, increasing the permeability of the endothelium [149]. The combination of increased endothelial permeability and recruitment of inflammatory cells triggers a positive feedback loop for intimal hyperplasia, a major contributor to loss of graft patency [147].

Integrating biomimetic stiffness and related biomechanical behaviours into the graft design may therefore increase their success by negating aneurysm and neointima development [89, 106]. Section 2.6 will explore the requirements of synthetic grafts and VMMs in more detail and outline the potential of PVA cryogel to meet the mechanical environment of arteries.

2.6 Vascular Mimicking Materials

2.6.1 Synthetic Graft Requirements

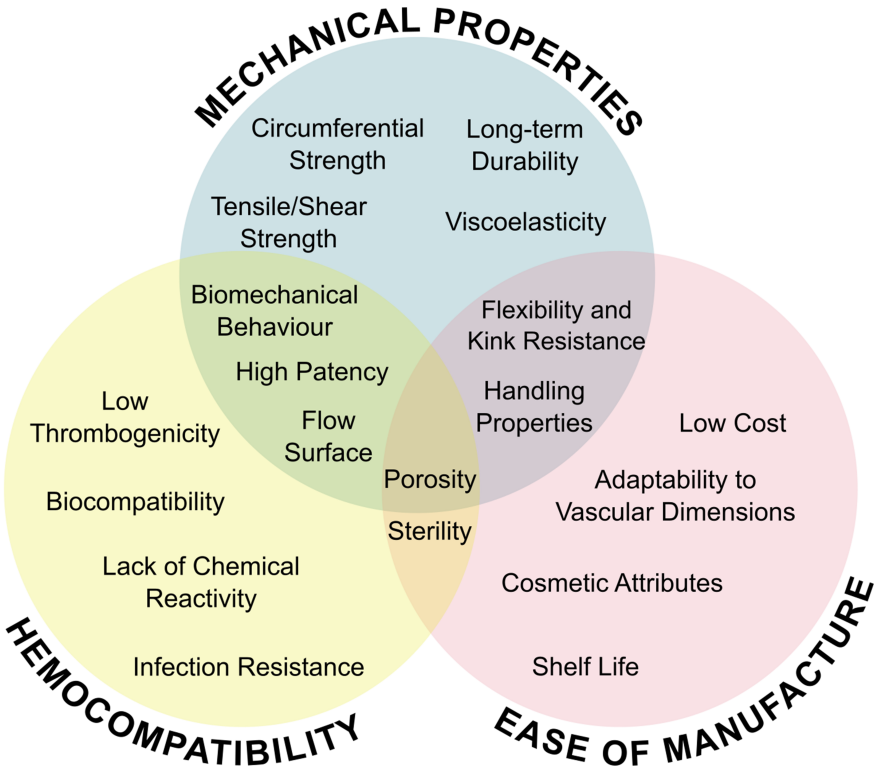


Figure 2.11: Key requirements of VMMs for use in cardiovascular grafts.

So far, this chapter has highlighted the importance of engineering synthetic coronary artery grafts that emulate the physiological functions of a healthy artery. The design challenges associated with doing so have been thoroughly reviewed over the last two decades [89, 90, 150–153], and are summarised in Figure 2.11: specifically, a VMM must demonstrate suitable haemocompatibility and mechanical properties and be easily manufacturable (Figure 2.11). The lack of clinically-approved small calibre synthetic grafts is therefore explained by the sheer number of properties a graft must possess in order to ensure long-term success in a low-flow environment.

Sections 2.6.1.1–2.6.1.3 will briefly summarise the key requirements outlined in Figure 2.11 in the context of commonly-used VMMs for bypass surgery.

2.6.1.1 Mechanical Properties

The strength, elasticity and fatigue response of a VMM should match that of healthy coronary arteries [151]. Expanded polytetrafluoroethylene (ePTFE) and Dacron, two synthetic grafts that display acceptable long-term patency in large calibre reconstructions, show poor patency in small calibre vessels. This is attributed to the rigidity of ePTFE (0.014–4 GPa [154, 155]) and Dacron (11 MPa [155]) grafts. The compliance of ePTFE (0.90 %/100 $mmHg^{-1}$ [156]) and Dacron (1.90 %/100 $mmHg^{-1}$ [156]) are subsequently lower than that reported for porcine coronary artery (6.69–8.02 %/100 $mmHg^{-1}$ [157]). Compliance mismatch, and the resulting disturbed blood flow through the graft, promotes neointimal hyperplasia. Neointimal hyperplasia shares a similar pathology to atherosclerosis, whereby VSMCs migrate and proliferate in the intima. Intimal thickening occurs as a result of fibrous tissue formation, leading to restenosis of the host vessel. Neointimal hyperplasia is a prominent cause of graft failure [8, 158]. Two-thirds of ePTFE grafts, for instance, fail within 2 years of implantation when used for CABG [152].

2.6.1.2 Haemocompatibility

Poor endothelialisation of a synthetic graft triggers thrombosis. In humans, endothelial outgrowth from adjacent arteries is limited to 1–2 cm from the anastomoses [159]. In addition, grafts may be stripped of their endothelium when exposed to shear stress *in vivo* [160]. A lack of midgraft endothelial coverage reduces the blood compatibility of the graft, increasing the risk of platelet activation and thrombus

formation [161]. Untreated Dacron and ePTFE are known thrombogenic materials with documented platelet activation and leukocyte adhesion properties [162–164]. Blood clot formation is a major cause of graft failure in small-diameter, low flow vessels [163].

Clearly, the haemocompatibility and mechanical properties of a VMM must be considered in tandem. At the most fundamental level, thrombosis will occur without a functional endothelium, and the endothelium will not survive arterial pressures without sufficient adherence to a graft of adequate strength. The graft must be able to support blood flow without bulging or bursting, and it must not induce turbulent flow or high stresses around the anastomoses with the host vessel [8].

2.6.1.3 Ease of Manufacture

From a clinical product standpoint, a VMM should be cheap, easy to manufacture according to the vascular dimensions of arteries, and remain stable when stored long-term. Practically speaking, the suturability and durability of a VMM during handling is important – which is partly determined by flexibility and porosity, factors which impact its biomechanical behaviour. The manufacturing process must be regulated, quality controlled, sterile and should not involve any steps or reagents that may trigger a negative immunogenic or cytotoxic response [152]. Manufacturing methods of interest in this thesis will be reviewed in more detail in Section 2.7.3.

2.6.2 Hydrogels

Hydrogels are crosslinked polymeric networks with compositional properties that can be engineered to resemble the mechanical and biochemical properties

of native ECM. They are hydrophilic, capable of absorbing water and other biological fluids up to several thousand % of their initial weight without dissolution [165]. Furthermore, their interconnected pore structure enables the diffusion of oxygen and nutrients to cells distributed throughout their volume. Hydrogels therefore meet many of the synthetic graft requirements outlined in Figure 2.11 and provide the 3D microenvironment needed to guide tissue regeneration [165–167].

A hydrogel can be classified according to any number of its properties, from its ionic charge to its physical appearance [167]. As the organisation of polymer chains on the micro- and nanoscale has a profound impact on many of a hydrogel's physical and mechanical properties, it is often convenient to classify hydrogels by the nature of their crosslinks [168]. Crosslinks are the intra- and intermolecular connections that hold the polymer chains in place; they are responsible for maintaining the structural integrity of the hydrogel under external load. (Photo)chemical crosslinking agents are commonly used to introduce permanent covalent bonds between chains. Alternatively, physical crosslinks may be created by exploiting reversible intermolecular interactions between chains, including molecular entanglements, crystallite formation and hydrogen (H)-bonding. For more detail on the chemical and physical crosslinking strategies commonly used to fabricate biomedical hydrogels, the reader is directed to the review by Hu *et al.* [166].

The simplest hydrogels comprise single monomer species. Poly(ethylene glycol) and poly(vinyl acetate), for example, are prepared through polymerisation of ethylene oxide and vinyl acetate, respectively. However, additives are often added to homopolymeric hydrogels to improve their functionality [169, 170]. An array of composite hydrogel systems have been developed for biomedical applications. In this thesis, polymer blends that combine two synthetic and/or natural polymer com-

ponents are of interest. More specifically, PVA-based blends that simultaneously enhance the biological activities and mechanical properties of PVA to mimic native ECM are covered in Section 2.6.3.

2.6.3 Poly(vinyl alcohol) (PVA) Cryogels

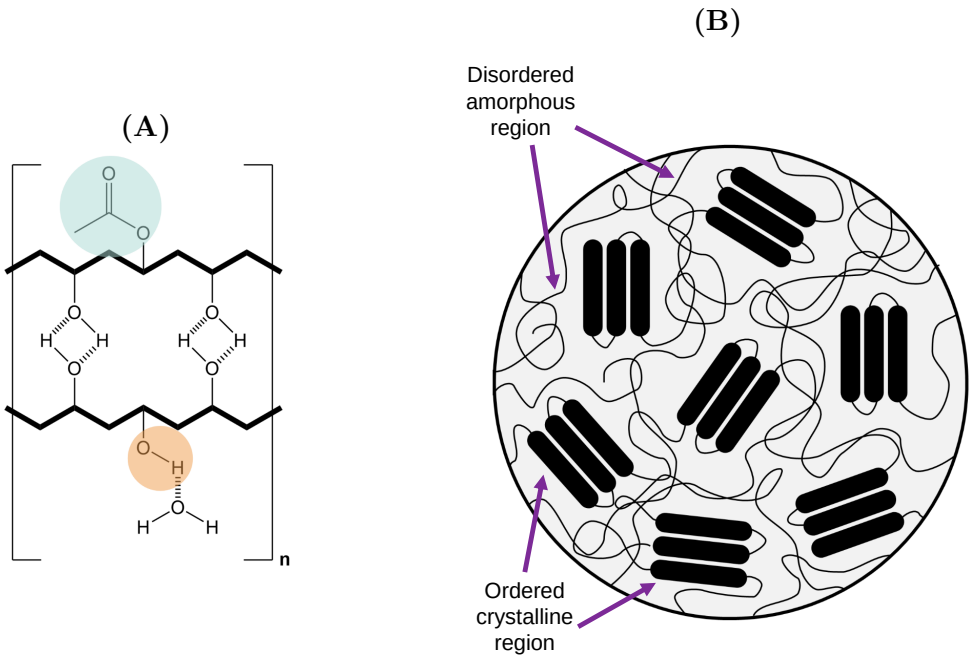


Figure 2.12: **(A)** The structure of PVA crosslinks formed using freeze–thaw (FT) cycling. Examples of pendant hydroxyl and acetate groups are highlighted in orange and blue, respectively. Hydrogen bonds are represented by dashed lines; **(B)** The semi-crystalline structure of PVA cryogel. The solid polymer network is represented in black; bulk water fills the interstitial space between the polymer network, represented in light grey.

PVA is a synthetic, semi-crystalline polymer. With the relatively simple molecular formula $[CH_2CH(OH)]_n$, it is synthesised industrially through the hydrolysis of poly(vinyl acetate). The degree of acetate to alcohol substitution is known as the degree of hydrolysis. While fully hydrolysed PVA is homopolymeric, a degree of hydrolysis of <100% renders PVA a copolymer of vinyl alcohol and vinyl acetate.

The pendant hydroxyl groups of PVA (Figure 2.12A) may be crosslinked to form hydrogels with specific porosity and variable mechanical properties. In the context of cardiovascular tissue engineering, PVA grafts have been manufactured using chemical [171–175] and physical [12, 176–180] crosslinking methods. The nature of crosslinking influences many aspects of graft performance, including biodegradability and blood compatibility. Notably, chemical crosslinkers such as glutaraldehyde can incite thrombus formation through increased platelet activation [181]. Unreacted crosslinker could also leach from the gel matrix after implantation. The ability to physically crosslink PVA through repetitive freeze–thaw (FT) cycles offers a simple and cost-effective method to manufacture hydrogels under comparatively milder experimental conditions.

Thermally crosslinked hydrogels are commonly referred to as *cryogels*, and will remain the focus of this thesis herein. The structure of PVA cryogel is depicted in Figure 2.12B. FT cycling exploits the phase separation of PVA solution at sub-zero (°C) temperatures and the subsequent crystallisation of polymer upon thawing to form a stable elastic gel [182]. During the freezing step, ice crystal formation drives the separation of PVA-rich and PVA-poor phases as PVA chains are expelled from the expanding ice. The high concentration and close proximity of polymer within the PVA-rich phase then facilitate crystallite growth through inter- and intrachain H-bonding. Interchain H-bonds are shown in Figure 2.12A. Once thawed, two phase domains prevail: a polymer-rich phase, consisting of crosslinked PVA crystallites and amorphous (uncrosslinked) PVA entanglements; and a bulk water phase, situated in the interstitial pores of the cryogel. Repeating the FT cycle reinforces the polymer-rich phase; multiple FT cycles are often used to increase crystallinity and thus the Young's modulus of the gel [183].

The inherent biocompatibility and hydrophilicity of PVA cryogel, combined

with the ability to refine mechanical properties through simple adjustments in manufacturing parameters, renders it an attractive candidate for a diverse range of biomedical and tissue engineering applications [10, 11]. PVA cryogel has not only been investigated as a VMM, but also as articular cartilage and meniscus tissue replacements [184, 185], intervertebral disc prostheses [186], artificial corneas [187], wound dressings [188, 189] and drug delivery agents [190]. As such, many studies have sought to quantify the impact of formulation and process parameters on the cryogelation of PVA. Key parameters include:

- The degree of hydrolysis [191, 192];
- The molecular weight, M_w, of the polymer [103, 193];
- The concentration, often expressed as weight per weight (w/w) or wt% [103, 180, 182, 183, 186, 192–194];
- The freezing/thawing temperature and/or rate [180, 195];
- The number and/or duration of FT cycles [13, 103, 180, 183, 193, 196, 197];
- Polymer coagulation treatment and salt addition [13, 198–200].

Each parameter affects the processability of PVA and determines the extent of polymer crystallisation. Highly concentrated PVA solutions (>30–40 wt%) have poor flowability due to their increased viscosity [10]. This restricts their use in applications where geometrical precision and/or material extrusion is required, such as in electrospinning [201, 202] and cryogenic 3D printing [15, 16]. Meanwhile, the presence of bulky hydrophobic acetate groups disrupts the formation of crystallites during the FT cycle. Subsequently, partially hydrolysed PVA cannot gelate at concentrations lower than 12 wt% [191]. The mechanical properties of PVA cryogel will be discussed further in Chapter 3.

2.6.3.1 Composite PVA Cryogels

Pure PVA cryogel often cannot provide the optimuum properties required for each of the biomedical applications highlighted in Section 2.6.2. Cartilage replacements, for instance, must demonstrate lubricating properties under high load conditions [184]. On the other hand, artificial corneas must maintain high optical transparency and demonstrate integration with surrounding ocular tissue [186]. As such, PVA may be combined with polymers, ceramics, biologic agents and nanomaterials to provide enhanced biological, chemical and mechanical properties [11].

The need for composite PVA cryogels is exemplified by the demands of cardiovascular grafts. Despite excellent biocompatibility, *in vitro* and *in vivo* culture of ECs on PVA hydrogels reveals poor biointegration of PVA grafts [173]. This is explained by the inherent hydrophilicity of PVA [203] and the lack of cell adhesive ligands required for integrin-mediated binding of ECs [204]. Surface wettability experiments have demonstrated maximised cell adhesion on moderately hydrophilic surfaces [205]. Hydrogen bonding between the hydrophilic hydroxyl groups of PVA and water forms a water hydration barrier, increasing surface wettability to the point of preventing protein adsorption [205, 206]. As cells adhere to biomaterials through cell adhesion proteins rather than directly onto the biomaterial surface [203], significant efforts to improve cellular adhesion have been documented in the literature, and are grouped into the following methods:

- Blending PVA with natural macromolecules such as gelatin [12, 13, 174, 207] and chitosan [208–210];
- Modifying the surface chemistry of PVA using techniques such as reactive ion plasma [204, 205, 211, 212], covalent conjugation of cell adhesion proteins [172,

173, 213, 214] and provision of topographical cues [212].

Each approach aims to introduce the functional groups required for peptide bonding with integrins, the adhesion receptors responsible for EC proliferation, differentiation and migration [215]. Crucially, none of these functional groups (amines, amides and carbonyls) are present in the chemical structure of unmodified PVA [204, 205].

2.6.3.2 PVA/Gelatin Cryogels

Blending PVA cryogel with gelatin has been shown to be an effective method to overcome the low bioactivity of the pure PVA [10]. The seminal study by Liu *et al.* found that EC proliferation rates on PVA/gelatin cryogel exceeded those on PVA/starch and PVA/chitosan cryogels, justifying the use of PVA/gelatin as a VMM over other PVA/biomacromolecule blends [13]. The cell-interactive properties of gelatin, a protein derived from denatured collagen, are well documented. Gelatin contains the arginine–glycine–aspartate (RGD) peptide sequence, a motif that serves as an attachment site for numerous cell types [216, 217].

From a commercial perspective, gelatin is cheap, readily available and performs many of the biomaterial functions of pure (and expensive) ECM proteins [218]. It is commonly extracted from porcine, bovine and fish skin; Type A and Type B forms are obtained through the acid- and base-catalysed partial hydrolysis of Type I collagen, respectively [219]. Gelatin is easy and cheap to store [220]. In addition, gelatin is highly soluble and does not induce toxicity and antigenicity in cells [218]. Gelatin therefore meets the VMM manufacturing requirements listed in Section 2.6.1 and has found use in numerous biomedical applications, most notably in wound healing and controlled drug release. Compared with collagen, however, gelatin lacks the

mechanical and thermal stability required for long-term applications. Thus, gelatin hydrogels are often chemically modified (eg gelatin methacryloyl [221]) and/or used in conjunction with synthetic polymers (eg PVA) to improve their physical and mechanical properties.

PVA cryogel shares many of the required mechanical traits of VMMs, including hyperelasticity [195] and dynamic viscoelasticity [103]. While the lack of mechanical characterisation of PVA/gelatin is a research gap that this thesis aims to address, the stress–strain responses of PVA/gelatin up to 40% suggest that PVA/gelatin performs similarly to pure PVA [13]. PVA/gelatin, in principle, meets all three VMM requirement pillars set in Figure 2.11: it is haemocompatible, easy to manufacture, and displays analogous mechanical properties to arteries. Although PVA and gelatin gels are both easy to manufacture, PVA gels lack haemocompatibility and gelatin gels lack stiffness; PVA/gelatin is expected to merge the advantages and overcome the disadvantages associated with the two biomaterials in isolation.

Several studies have investigated the ability to culture an endothelium on the surface of composite PVA/gelatin hydrogels *in vitro* [12, 13, 172, 174, 222]. However, a comprehensive parameter sweep investigating the impact of the formulation and process parameters described in Section 2.6.3 on the endothelialisation of PVA/gelatin cryogel has not, to the author's knowledge, been reported previously. Liu *et al.* were among the first to assess the potential of PVA/gelatin cryogels as VMMs [13]. They determined that collagen adsorption, used as a marker of protein adhesion to the biomaterial surface, and bovine vascular EC proliferation were higher on PVA/gelatin composites than on PVA/-chitosan and PVA/starch. In a later paper, they demonstrated how ramped shear stress conditions help to accelerate endothelialisation times [12]. Ino *et al.* investigated the thrombogenicity of sodium trimetaphosphate-crosslinked PVA/gelatin

films by studying static platelet adhesion and thrombin generation [174]. Both PVA and PVA/gelatin films exhibited a lower and slower onset of coagulation compared with Dacron [223].

Parikh *et al.* combined computational fluid dynamics with electrospinning to design helical PVA/gelatin scaffolds with improved responsiveness to WSS [222]. Thanks to the helical geometry of the scaffolds, human coronary artery ECs seeded onto the scaffolds were subject to spiral laminar flow, a predominant flow pattern in the circulatory system [224], yielding increased expression of EC adhesion molecules and mechanosensitive genes (eg Nrf-2) compared with conventional scaffolds [222]. ECs were more uniformly distributed on the helical scaffold and demonstrated an improved atheroprotective response compared with conventional electrospun scaffolds. While the authors noted that the nanotopology of the helical grafts was randomly oriented in a manner analogous to the ECM, the multi-layered nature of arteries was not accounted for during the design process.

Although each of these studies investigated aspects of the haemocompatibility of PVA/gelatin grafts, mechanical characterisation was comparatively more limited. Despite observing non-linear stress–strain behaviour up to 40% strain – a strain range chosen to mimic the *in vivo* strain of porcine aortic root – Liu *et al.* did not quantify hyperelastic constitutive parameters, reporting only the Young's modulus at 40% strain [13]. Vrana *et al.* acknowledged the viscoelasticity of PVA/gelatin cryogel through quantification of water content and surface hydrophilicity, but did not specifically characterise quasi-static or dynamic viscoelastic behaviour under physiological load [12]. Ino *et al.* determined the compliance, burst pressure and suture retention of their tubular scaffolds to assess suitability for implantation under *in vivo* haemodynamic strains [174]. However, the link between these mechanical properties and EC behaviour, such as atheroprotective and/or atherogenic gene

expression, was not investigated. While Parikh *et al.* reported the expression of nine mechanosensitive genes under WSS, the study focused solely on the impact of scaffold geometry on shear response. The PVA/gelatin composition and electrospinning parameters were both fixed, leaving room for further optimisation of shear stress responsiveness in future.

In 2018, Atlan *et al.* published the first report of a PVA/gelatin graft transplanted into an animal model [207]. The 1.4 mm-diameter tubular graft, manufactured using a hybrid chemical and physical crosslinking method, displayed *in situ* endothelialisation and 75% patency after 4 weeks in a rat aorta model. While the results were promising, they noted that increased thrombosis after 8–12 weeks highlights the importance of PVA/gelatin graft aging when considering long-term patency.

2.7 Design, Manufacture and Validation of Multi-Layered Coronary Artery Grafts

2.7.1 Overview

Section 2.2 introduced the three-layered structure of the artery wall. The multi-layered structure of arteries imparts complex mechanical properties; arteries are both heterogeneous and anisotropic, meaning their properties vary with both location and direction, respectively [225]. It is therefore reasonable to assume that a single-layer, isotropic vascular graft cannot sufficiently replicate the heterogeneity and anisotropy of native blood vessels. Replicating the *heterogeneity* of the artery wall through synthetic graft design is a key research theme in this thesis. Multi-

layered grafts can overcome the mechanical simplicity of homogeneous VMMs by mimicking the structure–function relationship of the intima, media and adventitia and have subsequently emerged as key next-generation synthetic grafts [150, 226].

The final background sections of this chapter will discuss the current status surrounding the design, manufacture and validation of multi-layered coronary artery grafts. Section 2.7.2 will introduce the concept of functionally graded biomaterials (FGBMs) and their applicability to mimicking the structural heterogeneity of the artery wall. Section 2.7.3 will then review the manufacturing techniques that enable multi-layered graft fabrication and Section 2.7.3.1 will discuss the opportunities these techniques provide toward the manufacture of PVA cryogel-based grafts. Finally, Section 2.7.4 will highlight the role that computational methods such as finite element analysis (FEA) can offer towards the design optimisation and validation of multi-layered coronary artery grafts.

2.7.2 Heterogeneous Graft Design Through Functional Grading

FGBMs are materials whose compositions and/or microstructures gradually change along at least one spatial direction [228]. The heterogeneity of these properties creates mechanical and/or biochemical gradients that the constituent phases cannot reproduce in isolation. FGBMs are classified according to the presence (discontinuous) or absence (continuous) of interfaces between regions of opposing properties (Figure 2.13). The global structure of the artery wall is discontinuous; the intima, media and adventitia form three distinct layers and are separated by the internal and external elastic lamina. However, local variations of cells and ECM proteins within each layer impart localised regions of continuous grading.

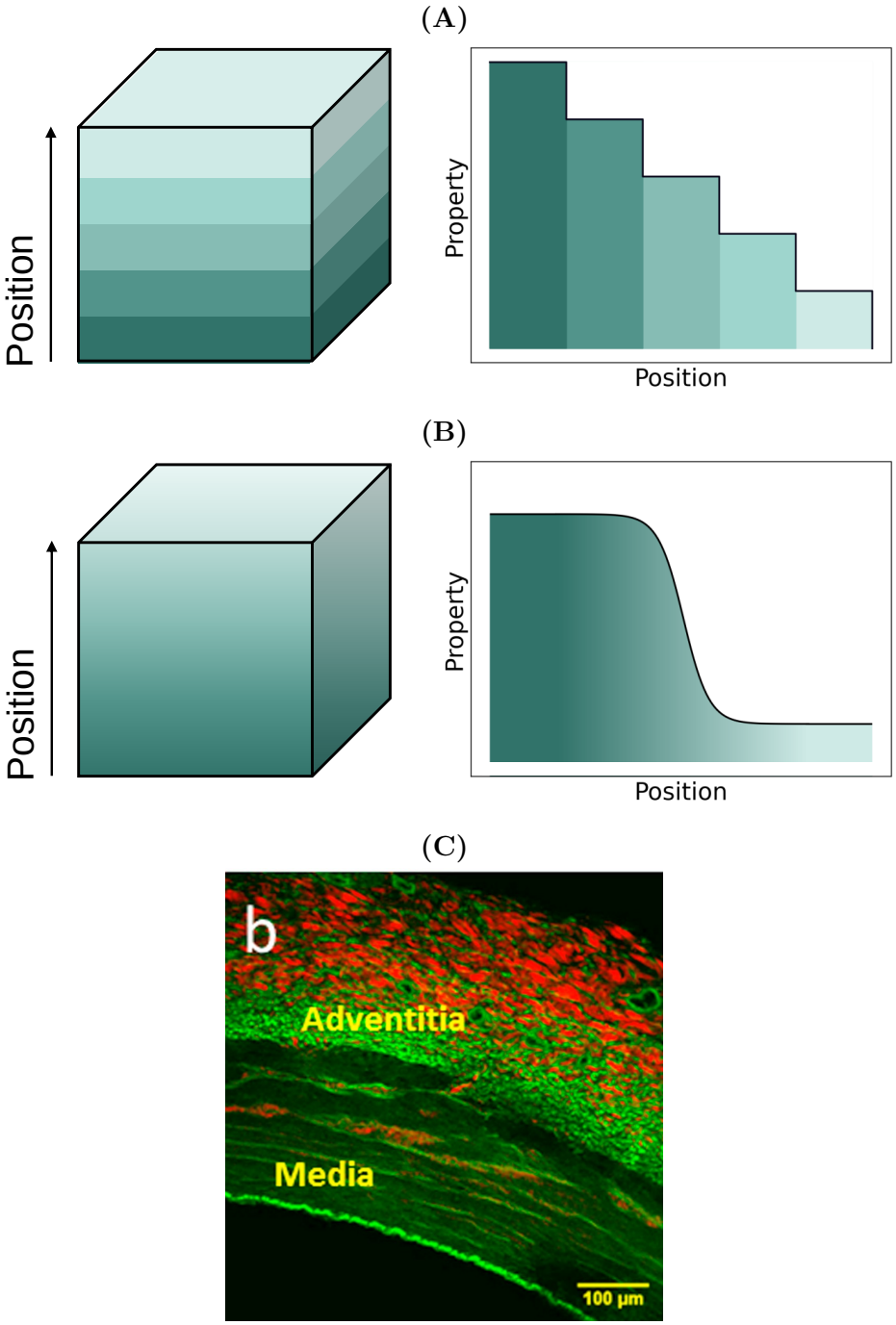


Figure 2.13: **(A)** Discontinuous FGBMs achieve grading through stepwise changes in composition and/or microstructure; **(B)** continuous FGBMs achieve grading through smooth transitions in composition and/or microstructure. **(C)** While a discontinuous boundary is observed between the coronary media and adventitia, collagen (red) and elastin (green) orientation and distribution vary throughout the adventitia. Figure 2.13C reproduced from [227] with permission from Elsevier.

For instance, morphometric analysis of the microstructure of the adventitia has revealed that the orientation and transmural distribution of elastin and collagen fibres varies between the inner and outer adventitia [229]. While dense concentric layers of collagen and elastin form at the inner adventitia, the width, area fraction and orientation randomness of collagen fibres increases towards the outer adventitia; meanwhile, elastin content decreases significantly (Figure 2.13C [227, 229]). These differences are thought to contribute to the different functions of the inner and outer adventitia, where the inner adventitia prevents overdistension at high transmural pressure and the outer adventitia anchors the coronary artery to the surrounding tissues [229]. Increased intralayer grading is also observed during both aging and the onset of CAD, where migration of VSMCs from the media to the intima creates regions of diffuse intimal thickening [230]. Furthermore, in early-stage atherosclerosis, lipid pools have been shown to form predominantly in the deepest subendothelial layers of the intima [231].

Thus, the artery wall can be considered a functionally graded structure, and functionally graded grafts can be designed to mimic the heterogeneity of the artery wall through gradual variation of the physical, mechanical and/or biological properties of the graft through space [232]. In the context of tissue engineering, the most studied functional gradients are composition, porosity, stiffness and biochemical concentration due to their ability to directly impact cell behaviour [233]. The comparative ease of implementing gradients in hard FGBMs through lattice design over soft FGBMs has resulted in FGBMs being applied predominantly in orthopaedic tissue engineering [234]. Nevertheless, the need for functional gradating has been acknowledged for soft tissues such as blood vessels [14], and advances in the manufacture of soft FGBMs are opening the possibility to engineer vascular grafts with controlled inter- and intralayer structural and compositional gradients. Section 2.7.3

will outline strategies to engineer multi-layered artery grafts.

2.7.3 Manufacture of Multi-Layered Grafts

Three key methods have emerged for the manufacture of multi-layered artery grafts:

- *Dip coating*: an immersion technique where a substrate is dipped into and withdrawn from a solution with controlled speed. The process may be repeated multiple times to generate multiple layers and/or to reach the desired outer diameter. A sacrificial core or glass mandrel is often used to manufacture tubular vascular grafts [235, 236];
- *Electrospinning*: a voltage-driven manufacturing method that produces a continuous stream of micro- and nanofibres. When applied to vascular grafts, the electrospun fibres are often collected on a rotating mandrel to produce a tubular graft [237]. Electrospinning yields grafts with high porosity and randomised nanofibrous morphology akin to the ECM [238];
- *AM*: a manufacturing method that deposits material(s), typically layer-by-layer, to create parts. Thanks to its integration with computer-aided design, AM offers rapid prototyping capabilities and can be combined with medical imaging to fabricate patient-specific grafts [239].

The design parameters and key benefits and limitations of each technique with respect to cardiovascular tissue engineering are listed in Table 2.1. There is a vast amount of literature exploring the application of dip coating, electrospinning and AM to the fabrication of cardiovascular grafts; herein, only papers investigating their implementation in the context of multi-layered artery grafts will be reviewed.

Dip coating provides a simple and cost-effective method to manufacture multi-layered artery grafts. For instance, Wang *et al.* manufactured tri-layered thermoplastic polyurethane grafts by controlling the number of immersion cycles of the intima, media and adventitia-mimicking layers [240]. Yet, few studies have used dip coating in isolation to create multi-layered grafts. Instead, dip coating is most commonly used to modify the surface characteristics of synthetic grafts to increase graft haemocompatibility [235, 241, 242].

Sequential electrospinning has been used to fabricate discontinuous grafts that mimic the matrix-tissue compositions of the intima, media and adventitia [238]. Overcoating layers of small diameter fibres (designed for optimised EC adhesion) with larger diameter fibres (designed for optimised mechanical stability) can be used to create electrospun constructs with microarchitectures reflecting the intima and combined media/adventitia, respectively [243]. However, while no delamination was observed between layers in the bi-layered electrospun grafts of de Valence *et al.* [243], these structures may be prone to delamination under loading as mechanical stresses are concentrated at the interface of layers [244]. Gradient electrospinning integrates the mechanical properties of each adjacent layer by gradually varying the fibre diameter between layers, such that the graft will function (and fail) as a unified structure [244]. Gradient electrospinning has also been used to incorporate chemical gradients through the artery wall. By gradually increasing the deposition of chitosan fibres toward the intimal surface of chitosan/polycaprolactone (PCL) electrospun grafts and selectively conjugating heparin to chitosan, Du *et al.* obtained grafts with enhanced endothelialisation and antithrombogenic properties compared with

Table 2.1: Comparison of manufacturing methods used to fabricate multi-layer artery grafts. Table developed from [9, 237, 245–253].

METHOD	DESIGN PARAMETERS	KEY BENEFITS	KEY LIMITATIONS
Dip coating	***Solution parameters*** • Viscosity • Concentration ***Production parameters*** • Dip angle • Immersion time • Withdrawal speed • Number of dipping cycles ***Ambient parameters*** • Temperature • Rate of solvent evaporation	• Simple setup • Low cost • Flexible material selection • Thin film coating suitable for modification of surface properties and drug-eluting stents	• Graft geometry limited by geometry of mandrel • Interface geometry fixed between dipping cycles • Poor control over layer uniformity, especially when layer thickness <0.5 mm
Electrospinning	***Solution parameters*** • Viscosity • Concentration • Conductivity • Surface tension • Polarity ***Polymer parameters*** • M_w • Solubility ***Ambient parameters*** • Temperature • Relative humidity • Vapour pressure ***Production parameters*** • Voltage • Feeding rate • Distance between needle tip/collector	• Flexible material selection • Multi-material capability using coaxial setup • Fabrication of aligned or random fibre meshes • Submicron to nanometre fibre diameter closely matches ECM fibre diameters • Deposition of living cells possible using cell-electrospinning setup	• High voltage apparatus needed • Fibre generation limited by viscosity • Toxic solvents may be required for synthetic polymers; residual solvent may affect cell viability • Graft geometry limited by geometry of mandrel • Limited control of pore structure; nanofibrous scaffolds suffer from limited cellular infiltration
AM	***Print parameters*** • Print toolpath • Extrusion pressure • Print speed • Strand diameter • Layer height • Part infill (density and design) ***Polymer parameters*** • Concentration • Viscosity • M_w	• Rich design space for the manufacture of complex geometries and interfaces • Compatible with several medical imaging modalities; ability to create patient-specific grafts • Flexible material selection • Multi-material capability using multi-material AM • Deposition of living cells possible with bioprinting	• 3D printing setup can be costly depending on modality • Limited print resolution restricts printing of sub-micron features • Bioink extrusion limited by viscosity • Lack of commercially available bioinks with sufficient bioactivity AND mechanical stiffness • Design for AM constraints lead to inefficient design and lack of creativity

uniform chitosan/PCL grafts [254].

In all of the above cases, the overall geometry of electrospun grafts was limited by the tubular geometry of the collection mandrel. This presents a key limitation toward the manufacture of patient-specific artery grafts. The design freedom and personalisation afforded by AM renders AM an attractive manufacturing technique across all domains of tissue engineering [255]. Moreover, elevated control of material geometry, mechanical properties and spatial localisation of biomolecular cues allows for rapid prototyping of tissue-engineered constructs resembling native tissues [255]. Numerous types of AM have been developed to print a diverse range of materials, including metals, ceramics, resins and hydrogels [256]; cardiovascular AM alone encompasses the creation of patient-specific anatomical models, surgical guides, vascular stents and vascular grafts [255]. In this thesis, hydrogel-compatible AM platforms for the creation of coronary artery grafts or phantoms are of interest.

Bioprinting involves the deposition of cells and hydrogels into predefined complex geometries; cell-laden hydrogels are often referred to as bioinks [257]. The polymer components of bioinks act as the ECM and may be comprised of synthetic (eg PVA), natural (eg gelatin) or combined elements. Multi-material bioprinting allows manufacture of multi-layered graft constructs [258]. Despite great progress towards the AM of artery grafts, AM grafts are still limited by the availability of compatible hydrogels and bioinks that provide the necessary balance between cell viability and mechanical stability and the resolution of AM platforms [259].

It is worth noting that multiple manufacturing methods can be combined to maximise the advantages of multiple techniques. Coupling the strengths of electrospinning (high resolution with fibres analogous to native ECM) and AM (controllable 3D geometry and mechanical integrity) presents an innovative way of mitigating the

weaknesses of electrospinning and AM in isolation [260]. This concept was first applied to PCL printed onto heparin-loaded electrospun poly-L-lactide (PLLA) tubular scaffolds [261]. The outer PCL layer increased the ultimate tensile strength of the graft while the heparin/PLLA layer provided an antithrombogenic surface optimised for cell attachment [261]. Meanwhile, in their proof-of-concept study, Guerra *et al.* combined the geometric capabilities of fused deposition modelling with dip coating and electrospinning to create a five-step method for fabricating bifurcated, bi-layered PCL grafts [262]. However, the authors noted that further studies are needed to test the scaffold's ability to maintain vascular pressure and support cells. Triple-layered grafts have also been fabricated using combined AM/electrospinning. For instance, PCL may be printed and electrospun to form three distinct layers, as verified by scanning electron microscopy images [263, 264].

2.7.3.1 Manufacture of PVA Cryogel-based Grafts

The simplest method of manufacturing PVA cryogel-based grafts is casting. Homogeneous tubular PVA/gelatin grafts have been fabricated by casting [207]. Casting has received ample attention in the development of PVA-based blood vessel phantoms, with many of these phantoms used to study optical or acoustic signals through the vessel wall [265, 266]. Tri-layer phantoms have been fabricated using an overmoulding process [267]. The intima is first injected into a mould and subjected to one FT cycle. By increasing the diameter of the mould after each FT cycle and injecting PVA solution into the resulting void, multi-layer grafts are obtained [267]. While the technique is effective at creating discontinuous FGBMs, it is limited to creating isotropic, homogeneous tissue layers.

Dip-coated tubular PVA cryogel grafts have also been fabricated as blood

vessel phantoms and preoperative models [245, 268]. A 3D-spin dip coating system, whereby the mandrel is spun after withdrawal from the PVA solution and before initiating the FT cycle, is needed to form layers of uniform thickness [245, 268]. By controlling the viscosity of PVA, number of dip cycles, withdrawal speed and mandrel diameter, homogeneous dip-coated PVA cryogel grafts have been manufactured with wall thicknesses between 30–250 µm (one dip) and 40–580 µm (four dips) [268]. In theory, a heterogeneous multi-layer graft can be obtained by varying the composition of PVA/gelatin solution between dip cycles. However, the reliance of layer thickness on viscosity, withdrawal velocity and the geometry of the mandrel present limiting factors to fabricating more complex graft designs. Stereo dip coating provides angular control over the dip coating process and presents an alternative route for the fabrication of dip-coated PVA cryogel grafts with tortuosity [245]. Nevertheless, the design of stereo dip-coated grafts is still inhibited by the geometry of the mandrel and, much like cast grafts, the interface behaviour cannot be controlled.

It is also possible to fabricate PVA cryogel-based grafts using electrospinning. Liu *et al.* cast PVA/gelatin into a mould lined with a fibrous electrospun PVA-styrylpyridinium mat before subjecting the mould to 1 FT, obtaining a composite graft with a fibre-reinforced 'intima' [269]. While electrospinning is highly effective at producing physiologically relevant surface topographies, the need for a mandrel or mould remains a key limitation toward the development of multi-layered vascular grafts.

Sub-zero AM, also referred to as cryobioprinting, offers an innovative way of fabricating PVA cryogel-based grafts with increasing geometric complexity. Sub-zero AM is an extrusion-based technique that employs a frozen print bed to freeze the extruded bioink upon contact. The *in situ* freezing step yields freeform structures

that retain their spatial geometry upon thawing. From a manufacturing perspective, the technique doubles as a cryopreservation method and therefore presents a compelling method for one-step fabrication and long-term storage of synthetic tissue scaffolds [270]. The sub-zero AM of PVA has been used to print a diverse range of soft and hard tissue scaffolds [15–17, 271]. To the author's knowledge, sub-zero AM has not yet been explicitly applied to the manufacture PVA cryogel-based vascular grafts; nevertheless, many of the concepts are applicable to the fabrication of vascular grafts and thus this thesis.

2.7.4 Graft Validation Through Computational Modelling: The Finite Element Method

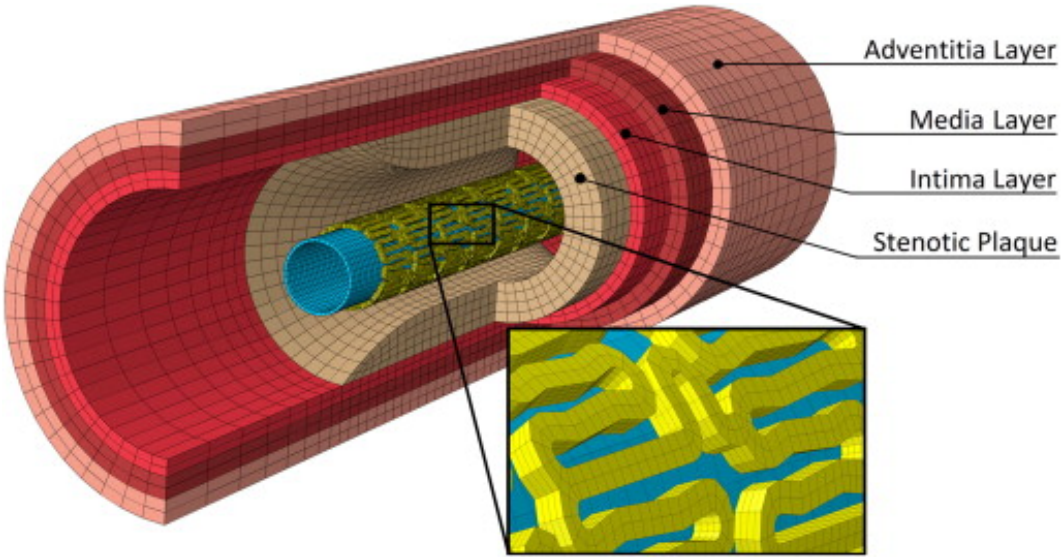


Figure 2.14: Discretisation of coronary artery wall, plaque, balloon and stent for the simulation of PCI. Reprinted from [20] with permission from Elsevier.

Sections 2.7.2 and 2.7.3 provided the justification for heterogeneous artery grafts and an overview of the manufacturing methods available enabling their manufacture, respectively. It follows that the mechanical and biological responses of different

heterogeneous graft designs must also be validated with respect to the specific artery they are designed to replace. Generally speaking, graft behaviour can be validated using *in vitro*, *in vivo* and/or *in silico* testing. The mechanical characterisation of (multi-layered) grafts, for example, is typically performed *in vitro* using methods such as uniaxial testing, burst pressure testing and suture retention testing [243]. Although these measurements provide insight into the overall strength and handling properties of the graft, the full mechanical response of synthetic grafts under physiological pressure, and the potential impact of this response on the function of adhered ECs, cannot be understood from *in vitro* test data alone. For instance, mechanical testing cannot measure how stress is internally distributed throughout the graft wall, nor can it relate these stresses to the mechanotransduction pathways of the endothelium.

Computational models derived from empirical data offer insight into the biomechanical behaviour of implants under physiological conditions. FEA is widely used in the design and analysis of orthopaedic implants [272–274] and cardiovascular stents [19–22]. It can also be used to inform cardiovascular graft design [23, 275]. These models aim to address the same questions: how does a synthetic graft perform under physiological pressure, constrained by physiologically relevant boundary conditions? Can we use computational models to identify which design parameters provide the desired biomechanical properties of an implant? It must be noted that a model is only as accurate as the data used to build it; all assumptions and simplifications will be amplified in the simulation [21]. Nevertheless, computational modelling can provide key insight in the arena of (coronary) artery graft design.

FEA is used by engineers to approximate the displacements, stresses and strains of a solid body under a defined set of loads and boundary conditions. It is worth noting that FEA is not limited to solid mechanics problems; computational fluid

dynamics is routinely used to investigate fluid flow, and the relationship between a deformable body and its adjacent flow can be coupled using fluid–structure interaction models. Both are widely used to model coronary artery biomechanics, but the theory behind them goes beyond the scope of this thesis. This section aims to concisely describe the workflow of the FE method and is informed by comprehensive texts dedicated to FEA [276, 277].

The FE method can be separated into three steps: (1) pre-processing, where the model is created according to its mesh and modelling assumptions; (2) processing, where the stiffness matrices are assembled and solved; and (3) post-processing, where the computed outputs are displayed graphically [276]. There are five main modelling assumptions to consider during the pre-processing step:

- *Geometry*: the continuous domain(s) of the object(s) under investigation;
- *Mesh*: the discretised domain(s) of the object(s) under investigation. FE meshes are comprised of a finite number of simple elements connected by nodes;
- *Material properties*: the constitutive laws governing the material behaviour of each object under investigation;
- *Load*: the type, magnitude, direction, distribution and time-dependency of the imposed force(s) on the system;
- *Boundary conditions*: the constraints required for solving the boundary value problem.

The internal distribution of stress and strain in a specified problem domain (eg the artery wall) can be represented mathematically as a boundary value problem,

or a system of partial differential equations. Where the geometry describes the continuous problem domain, the mesh discretises the domain using a finite number of simple, geometrically well-defined elements (Figure 2.14). Meshing is fundamental in FEA as it allows complex geometries – for which the governing equations cannot be solved – to be broken down into simpler 2D or 3D shapes with mathematically-defined volumes [278]. The displacement of each element is solved using interpolation shape functions. The global displacement field is then calculated by summing the contributions of each element; in this way, displacements and stresses at the element level can be combined to find the displacements and stresses of the complete object.

2.7.4.1 Finite Element Analysis of Small Diameter Artery Grafts

In the context of cardiovascular research, FEA is most commonly used to assess artery wall mechanics and to probe the underlying mechanisms of atherosclerotic plaque rupture [18, 279]. It is also used to assess vascular injury [22] and inform stent design [19–22] for PCI.

The concept of applying FEA to the analysis of compliance and stress distribution of synthetic grafts dates back to the 1990s [280]. In a linear elastic isotropic artery model, Chandran *et al.* demonstrated the presence of a hypercompliant zone on the arterial side of Dacron and PTFE grafts [280]. The authors highlighted the importance of studying the effects of compliance mismatch using FEA as a means to "suggest ways to improve the design of small diameter vascular grafts" [280]. Data from Castillo-Cruz *et al.* [156] and Byrne *et al.* [23] have since provided further justification for the use of FEA as a design tool in the manufacture of vascular grafts, with both using FEA to predict the compliance of grafts using synthetic grafts. Yet, FEA remains an underused resource in the assessment of novel VMMs and their

graft designs.

2.8 Research Hypothesis

The preceding sections of this Chapter have reviewed the key background pertaining to this thesis and are summarised as follows:

- The heterogeneous nature of the artery wall imparts complex biomechanical behaviours such as hyperelasticity and viscoelasticity; these behaviours are linked to EC behaviour through mechanotransduction and are subsequently key determinants of healthy and pathologic EC function;
- Synthetic VMMs are needed for CABG, a surgical procedure whereby stenotic regions of atherosclerotic arteries are replaced with grafts to restore blood flow;
- A single-layer vascular graft cannot sufficiently fulfil all of the mechanical and haemocompatible design requirements outlined in Section 2.6.1; multi-layered grafts could overcome the mechanical simplicity of homogeneous VMMs by mimicking the structure–function relationship of the intima, media and adventitia;
- PVA/gelatin cryogels are prospective VMMs for the manufacture of multi-layered grafts due to the ability to 'tune' the mechanical properties of PVA through variation of manufacturing parameters and the biointegrative properties of gelatin;
- Of the manufacturing methods suited to manufacturing heterogeneous coronary artery grafts, the sub-zero AM of PVA cryogel has demonstrated

potential for soft tissue engineering, yet it has not been explicitly applied to the manufacture of PVA cryogel-based coronary artery grafts;

- Despite the success of FEA in the design and validation of orthopaedic implants, similar design studies are needed to fully explore the potential of sub-zero AM to fabricate biomimetic vascular grafts.

Therefore, the hypothesis of this thesis is that PVA/gelatin cryogel can be used as a VMM to create heterogeneous biomimetic coronary artery grafts that replicate the mechanical properties of the three artery wall layers. To the author's knowledge, no studies thus far have investigated the biomechanics of multilayered PVA/gelatin constructs for any blood vessel replacement applications. While this thesis has not explicitly investigated the manufacture of multi-layered PVA/gelatin grafts, the synergy between the design optimisation capabilities of FEA and the rich geometric design space afforded by manufacturing techniques such as sub-zero AM calls for FE models that can inform the future design of multi-layered PVA/gelatin cryogel grafts.

Furthermore, it is hypothesised that the layer-specific mechanical properties of PVA/gelatin grafts can be optimised using FEA to induce healthy EC behaviours under physiological loading. While the endothelialisation and elastic properties of homogeneous PVA/gelatin cryogel have been explored separately prior to this thesis, the role that PVA/gelatin biomechanics play in modulating EC function is unknown, and few studies have used FEA to probe this relationship for any VMM. Despite the well-documented impact that artery wall biomechanics has on EC mechanotransduction in coronary arteries, the relationship between VMM biomechanics and EC mechanotransduction is seldom explored in cardiovascular tissue engineering; FEA has the potential to highlight graft stress distributions relevant to EC function.

STATEMENT OF CONTRIBUTIONS I

Chapter 3 includes novel research published in *Frontiers in Cardiovascular Medicine*, a peer-reviewed scientific journal, with myself as the principal author. The research was published as an open-access article with a full CC-BY 4.0 copyright license (https://creativecommons.org/licenses/by/4.0/), allowing for the reproduction of data within this thesis. The citation and statement of contributions from each author are as follows:

Fegan, K. L., Green, Naomi C., Britton, Melanie M., Iqbal, Asif J. & Thomas-Seale, L. E. J. Design and simulation of the biomechanics of multi-layered composite poly(vinyl alcohol) coronary artery grafts. *Frontiers in Cardiovascular Medicine* **9**, 883179 (2022). DOI: 10.3389/fcvm.2022.883179

- **KF** contributed to the conception, design and implementation of the research, to the analysis of the results, and to writing the original draft of the manuscript;
- NG supervised and contributed to the conception and design of the research;
- MB and AI supervised the research;
- LT-S supervised and contributed to the conception, design and implementation of the research.

All authors contributed to manuscript revision, read and approved the submitted version.

Chapter Three

MECHANICAL CHARACTERISATION OF PVA/GELATIN CRYOGELS

3.1 Introduction

For decades, cardiovascular tissue engineers have cited mechanical mismatch as a key determinant for premature graft failure [8, 151, 153, 281, 282]. On the one hand, a synthetic graft must possess sufficient strength to maintain structural integrity and avoid bulging and rupture [282]. On the other hand, rigid non-compliant grafts reduce elastic recoil and introduce excessive mechanical stresses at the graft-to-artery anastomoses [283]. Compliance mismatch induces turbulent flow and reduces the mean haemodynamic WSS exerted on ECs, promoting vascular injury and initiating neointimal hyperplasia [8, 283].

Mechanical mismatch is particularly problematic in small calibre vessels such as the coronary artery. Dacron and ePTFE, the gold-standard VMMs used in large

calibre reconstructions, demonstrate poor long-term patency when used in vessels <6 mm [284]. ePTFE grafts used for CABG, for example, offer a 2-year patency rate of 32% – >60% lower than autologous SV grafts [152]. Compliance correlates linearly with patency rate [8], and both Dacron and ePTFE are considerably less compliant than human coronary arteries under physiological pressure [285]. Thus, to reduce the likelihood of graft failure, synthetic grafts should be designed with compliance characteristics matching those of the coronary artery.

The mechanical properties of VMM(s) influence graft compliance. Synthetic grafts should possess anisotropic, hyperelastic and viscoelastic behaviour akin to the artery wall. Numerous studies have characterised the elastic [286, 287], hyperelastic [195, 288–293] and viscoelastic [102, 294] behaviour of coronary arteries using mechanical testing. Understanding the elastic and viscous properties of the artery wall under dynamic loading is of great value for the development of clinical treatments for CAD, including the design of stents and implants [102, 103, 288]. The mechanical properties of coronary arteries are also layer-specific; in arteries with non-atherosclerotic intimal thickening, the intima is the stiffest of the three tissue layers, while the adventitia demonstrates the highest ultimate tensile stress [288]. Material scientists must endeavour to engineer synthetic VMMs with locally and globally variable properties mirroring the mechanical heterogeneity of the artery wall [9]. Specifically, in order to harbour a confluent, anti-thrombogenic endothelium and remain patent, a synthetic graft should:

- Demonstrate comparable hyperelasticity, viscoelasticity and compliance;
- Withstand dynamic loading at physiologically relevant frequencies.

PVA cryogels are promising VMMs thanks to their biocompatibility and ease of manufacture [11]. Their high-water content and biphasic nature imparts vis-

coelastic properties compositionally similar to soft tissue. Moreover, unlike other highly hydrated gels, PVA cryogels exhibit hyperelastic exhibit stress–strain responses analogous to arterial tissue that can be easily manipulated through both formulation and cryogelation parameters. [295]. The extent of linear elasticity [13, 180, 183, 186, 196], hyperelasticity [195] and viscoelasticity [103, 186, 192, 200] of pure PVA cryogel can be tuned by varying the number and duration of FT cycles, polymer concentration, and use of polymer coagulation ("salting out") treatments (Table 3.1). In the context of cardiovascular tissue engineering, it has been shown that the number and duration of FT cycles can be optimised to yield stress–strain and stress–relaxation curves comparable to porcine aortic root [180], and porcine RCA and LCA [195]. The quantification of these constitutive parameters also allows researchers to validate different graft designs, and to assess their performance under physiological loads, using FEA. This has been demonstrated for PVA-based aortic valve prostheses [178].

While PVA displays desirable mechanical properties, it lacks the cell adhesion proteins needed to induce EC adhesion and proliferation [10]. Endothelialisation of the PVA graft surface, be it *in vitro* or *in situ*, is essential for long-term graft patency [151, 204, 281]. Loss or absence of a confluent endothelium may lead to thrombogenesis, pathological inflammation and neointimal hyperplasia [296]. The bioactivity of PVA can be improved by introducing gelatin, a natural polymer containing the integrin-mediating RGD peptide sequence [12, 13, 207]. PVA/gelatin is a low-cost, easy to manufacture VMM that has demonstrated superior EC proliferation rates compared with other PVA blends such as PVA/chitosan and PVA/starch [13, 295]. Of the three, PVA/gelatin has been identified as the best at simultaneously meeting the mechanical and biological requirements of a VMM [295].

Table 3.1: Key mechanical testing literature characterising the impact of formulation and processing parameters on the linear elastic, hyperelastic and viscoelastic properties of pure PVA cryogel. ↑ signifies increasing values, while ↓ signifies decreasing values.

LINEAR ELASTICITY				
Manufacturing Parameter	**Experimental Procedure**	**Modulus**	**Key Conclusions**	**From Study**
Concentration, number of FT cycles	Uniaxial compression testing (15% strain)	Compressive (1–5% strain)	↑ concentration: ↑ E; ↑ number of FT cycles: ↑ E, plateaus after 6 FT cycles.	[183]
Concentration, number of FT cycles	Uniaxial compression testing (25% strain)	Compressive (5% and 20% strain)	↑ concentration: ↑ E; ↑ number of FT cycles: ↑ E.	[186]
Number of FT cycles, coagulation treatment	Uniaxial tensile testing (60% strain)	Tensile (40% strain)	↑ number of FT cycles: ↑ E; E ↑ with use of coagulation treatment.	[13]
Number of FT cycles	Uniaxial tensile testing (unspecified strain)	Tensile (unspecified strain)	↑ number of FT cycles: ↑ E.	[196]
Number of FT cycles, freezing time, thawing rate	Uniaxial tensile testing (80% strain)	Tensile (20%, 40% and 50% strain)	↑ number of FT cycles: ↑ E; No significant difference in E using freezing times of 1 h and 6 h; ↓ thawing rate: ↑ E.	[180]
HYPERELASTICITY				
Manufacturing Parameter	**Experimental Procedure**	**Modulus**	**Key Conclusions**	**From Study**
Number of FT cycles, thawing rate	Uniaxial tensile testing	N/A	↑ number of FT cycles: ↑ hyperelastic coefficients and Cauchy stress; ↓ freezing rate: ↑ hyperelastic coefficients.	[195]
VISCOELASTICITY				
Manufacturing Parameter	**Experimental Procedure**	**Modulus**	**Key Conclusions**	**From Study**
Concentration, M_w, number of FT cycles	DMA (ω = 0–10 Hz)	Storage, loss	↑ concentration: ↑ E' and E'' for all frequencies; ↑ M_w: ↑ E' and E'' for all frequencies; ↑ number of FT cycles: ↑ E' and E'' for all frequencies.	[103]
Concentration, degree hydrolysis	DMA (ω = 1 Hz)	Storage, loss	↑ concentration: ↑ G' and G''; ↑ degree hydrolysis: ↑ G' and G''.	[192]
Concentration, number of FT cycles	Stress relaxation and creep (25% strain)	N/A	↑ concentration: ↑ instantaneous and steady state stress relaxation/creep rates; ↑ number of FT cycles: ↑ instantaneous and steady state stress relaxation/creep rates.	[186]
Addition of salting-out agents	Rheometry (ω = 0.1–10 Hz)	Storage, loss	G' and G'' ↑: PVA+Na_2SO_4 > PVA > PVA+NaCl > PVA+$NaNO_3$ for all frequencies.	[200]

Table 3.2: Key mechanical testing literature characterising the impact of formulation and processing parameters on the linear elastic, hyperelastic and viscoelastic properties of PVA/gelatin cryogel. ↑ signifies increasing values, while ↓ signifies decreasing values. UTS = ultimate tensile testing.

LINEAR ELASTICITY					
Manufacturing Parameter	**PVA:Gelatin Ratio**	**Experimental Procedure**	**Modulus**	**Key Conclusions**	**From Study**
Number of FT cycles, coagulation treatment	9:1	Uniaxial tensile testing (60% strain)	Tensile (40% strain)	↑ number of FT cycles: ↑ E; E ↑ with use of coagulation treatment.	[13]
Number of FT cycles, coagulation treatment	9:1	Uniaxial tensile testing (to failure)	UTS	↑ number of FT cycles: ↑ UTS; UTS ↑ with coagulation treatment for 1 FT, but not for 3 FT.	[199]
Number of FT cycles	15:1	Uniaxial tensile and compression testing	Tensile (20–40% strain), compressive (0–20% strain)	↑ number of FT cycles: ↑ E in tension and compression.	[297]
M_w	15:1	Uniaxial compression testing	Compressive	↑ M_w: ↑ E;	[298]
HYPERELASTICITY					
Manufacturing Parameter	**PVA:Gelatin Ratio**	**Experimental Procedure**	**Modulus**	**Key Conclusions**	**From Study**
N/A	N/A	N/A	N/A	N/A	N/A
VISCOELASTICITY					
Manufacturing Parameter	**PVA:Gelatin Ratio**	**Experimental Procedure**	**Modulus**	**Key Conclusions**	**From Study**
Number of FT cycles, coagulation treatment	9:1	Low strain rheometry (ω = 1 Hz)	Storage	↑ number of FT cycles: ↑ G'; G' ↑ with coagulation treatment for 1 FT, but not for 3 FT.	[199]

However, compared with pure PVA cryogel, the mechanical characterisation of PVA/gelatin cryogel is considerably more limited (Table 3.2). Most studies have focused on characterising the linear elastic properties of PVA/gelatin as a function of processing parameters [13, 199, 297, 298]. The impact of cryogelation on the hyperelastic and dynamic viscoelastic response of these cryogels has not yet been explored. Not only would these measurements provide insight into the fundamental mechanics of PVA/gelatin cryogels, but such measurements would facilitate the development of PVA/gelatin-based FE models with increasing material complexity. In doing so, these results could be used to complement the clinical translation of PVA/gelatin cryogel as a viable VMM.

3.1.1 Aims and Objectives

This chapter aims to address current gaps in the literature surrounding the mechanical characterisation of PVA and PVA/gelatin cryogels. There is a need for constitutive parameters that can be used as material parameters in computational models, including the FE models developed in Chapters 4 and 5 of this thesis. The impact of cryogel composition and post-cryogelation treatment on linear elastic, dynamic viscoelastic and hyperelastic parameters was evaluated using the following objectives:

- Calculate and compare the elastic moduli of PVA and PVA/gelatin cryogels as a function of M_w PVA and polymer coagulation treatment;
- Determine the dynamic viscoelastic behaviour, specifically the storage and loss moduli, of PVA/gelatin cryogels as a function of M_w PVA, polymer coagulation and gelatin addition;

- Using uniaxial compression test data, obtain hyperelastic parameters for PVA/gelatin cryogels, evaluating the stability and suitability of a range of phenomenological isotropic hyperelastic models.

3.2 Method

3.2.1 Chemicals and Materials

Table 3.3: PVA/gelatin cryogel compositions. P_xG_y signifies the w/w ratio of PVA:gelatin, A/B denotes the M_w of PVA (A = 146–186 kDa, B = 89–98 kDa) and C/NC signifies whether coagulation treatment (C) or no coagulation treatment (NC) was employed during cryogel manufacture.

COMPOSITION	M_w PVA (kDa)	COAGULATION TREATMENT?
$P_{10}G_0$-A-NC	146–186	No
$P_{10}G_0$-A-C	146–186	Yes
P_9G_1-A-NC	146–186	No
P_9G_1-A-C	146–186	Yes
$P_{10}G_0$-B-NC	89–98	No
$P_{10}G_0$-B-C	89–98	Yes
P_9G_1-B-NC	89–98	No
P_9G_1-B-C	89–98	Yes

PVA (89–98 kDa and 146–186 kDa), gelatin (Type B from bovine skin) and sodium sulphate (Na_2SO_4) were acquired from Merck Life Science (Dorset, UK). Potassium hydroxide (KOH, 85%) was acquired from Alfa Aesar (Lancashire, UK). Deionised water from a Purite Millipore tank (<18 MΩ, Milli-Q) was used for all experiments unless otherwise stated.

3.2.2 Preparation of PVA/Gelatin Cryogels

10 wt% PVA/gelatin cryogels were prepared according to the compositions outlined in Table 3.3. The following nomenclature is used: P_xG_y denotes a w/w ratio of PVA:gelatin of x:y; A/B denotes the M_w of PVA (A = 146–186 kDa, B = 89–98 kDa); and C/NC denotes coagulation (C) versus no coagulation (NC) treatment. For example, P_9G_1-A-C represents a 10 wt% cryogel with a PVA:gelatin ratio of 9:1, comprised of 146–186 kDa PVA, that has been put through coagulation treatment.

PVA solutions were prepared by autoclaving PVA in Milli-Q for 1 h at 121 °C. Meanwhile, gelatin was dissolved in water at 50 °C under magnetic stirring for 1 h. Composite PVA/gelatin solutions were obtained by combining 18 wt% PVA and 2 wt% gelatin in a 1:1 ratio. To prevent aggregation of the polymer chains, the final solution was mixed at 50 °C for 1 h followed by 1 h at room temperature (22.5 ± 1 °C). The solution was then poured into 20 × 10 mm cylindrical molds and subjected to 3 FT cycles at −20 °C and room temperature, respectively.

Once formed, half of the cryogels were immersed in a non-solvent (1 M KOH/ 1 M Na_2SO_4, coagulation treatment) for 1 h to promote further crosslinking of PVA. Coagulation treatment has been shown to influence the mechanical properties of both PVA and PVA/gelatin cryogel [13, 198, 199]. By exchanging bulk water with the non-solvent, amorphous PVA is precipitated out and the polymer microstructure is reinforced. Na_2SO_4 further aids PVA precipitation by decreasing the solubility of the polymer, a phenomenon known as the Hofmeister effect [198, 299]. All cryogels were stored in Milli-Q for 3–4 days before mechanical testing to ensure equilibrium swelling was reached [13].

3.2.3 Density Measurements

In preparation for the FEA of PVA/gelatin grafts in Chapters 4 and 5, the density (ρ) of each PVA/gelatin composition was measured by relating the volume, V, of each cylindrical sample to its mass, m (Equation 3.1). Each sample was dried of surface water before its mass was recorded using a mass balance.

$$\rho = \frac{m}{V} = \frac{4m}{\pi d^2 L} \tag{3.1}$$

3.2.4 Ramp Testing

Unconfined uniaxial compression tests were performed in air and at room temperature using a Bose Electroforce 3200 testing machine running WinTest software (Bose Corporation, ElectroForce Systems Group, Minnesota, USA; now TA instruments, Delaware USA) equipped with a 220 N load cell. For determination of Young's moduli (E), samples were compressed to low (20%) strain at a strain rate of 0.1 mm s^{-1}; for determination of hyperelastic parameters, samples were compressed to high (50%) strain using the same strain rate. To account for stress softening of the polymer chains [300], all samples were subjected to preconditioning cycles to improve test reproducibility. The force–displacement data were converted to engineering stress (σ_e) and engineering strain (ϵ_e) using Equations 3.2 and 3.3, where a is the cross-sectional area of the cryogel (measured using a Vernier calliper), L_0 is the initial height of the sample and ΔL is the change in length. E was calculated as the ratio of stress to strain (Equation 3.4).

$$\sigma_e = \frac{F}{a} \tag{3.2}$$

$$\epsilon_e = \frac{\Delta L}{L_0} \tag{3.3}$$

$$E = \frac{\sigma_e}{\epsilon_e} \tag{3.4}$$

In this thesis, all compressive stresses and strains are presented as their absolute values.

3.2.5 Dynamic Mechanical Analysis

DMA was performed using the same testing machine described in Section 3.2.4. A sinusoidal displacement loading protocol was run over a frequency sweep of 0.5–10 Hz to reflect the frequency range experienced by the coronary arteries of the left ventricle (<1 Hz = bradycardia; 1–3 Hz = exercise, >4 Hz = tachycardia [102, 301, 302]). A fast Fourier transform was implemented in WinTest to analyse the measured force and displacement waves. The dynamic stiffness (k^*) was calculated by dividing the peak load magnitude, F^*, by the peak displacement magnitude, d^* (Equation 3.5). Using the phase lag (δ) between the force and displacement waves, the storage and loss stiffnesses (k' and k'') were calculated from k^* (Equations 3.6 and 3.7). By relating k' and k'' to the shape factor of the cylindrical samples (Equation 3.8), the storage (E') and loss (E'') moduli were then determined (Equations 3.9 and 3.10).

$$k^* = \frac{F^*}{d^*} \tag{3.5}$$

$$k' = k^* cos(\delta) \tag{3.6}$$

$$k'' = k^* sin(\delta) \tag{3.7}$$

$$S = \frac{\pi D^2}{4L} \tag{3.8}$$

$$E' = \frac{k'}{S} \tag{3.9}$$

$$E'' = \frac{k''}{S} \tag{3.10}$$

Samples were compressed between 15–20% of their initial height using a dynamic amplitude of $\pm 0.025 L_0$. Like many biological soft tissues, the stress–strain curve of PVA is "J"-shaped when compressed to high strain (hyperelasticity will be further outlined in Section 3.3.3). This strain range covers the linear region before the transition point, and corresponds to the method used to characterise the dynamic viscoelasticity of the LAD coronary artery [102] and pure PVA cryogel [103]. A 60 s preconditioning cycle of 10 Hz was used to counteract the effects of stress relaxation [103].

3.2.6 Curve Fitting of Hyperelastic Strain Energy Density Functions

The hyperelastic curve fitting procedure is outlined in Figure 3.1. The large strain ramp test data were fitted to a number of phenomenological isotropic hyperelastic constitutive models in Abaqus/CAE 2021 (Dassault Systèmes, SIMULIA Corp., Johnston, RI, USA) using a non-linear regression routine. These models use strain energy density functions, U, to relate the amount of energy needed to deform a unit volume of a material to the imposed strain at that volume. For more detail on strain energy density functions, the reader is directed to Section 2.4.4. In this thesis, variations of the incompressible polynomial (Equation 3.11), reduced polynomial (Equation 3.12) and Ogden (Equation 3.13) strain energy functions were investigated:

$$U\,(polynomial) = \sum_{i+j=1}^{N} C_{ij}(\bar{I}_1 - 3)^i(\bar{I}_2 - 3)^j \tag{3.11}$$

$$U\,(reduced\,polynomial) = \sum_{i=1}^{N} C_{i0}(\bar{I}_1 - 3)^i \tag{3.12}$$

$$U\,(Ogden) = \sum_{i=1}^{N} \frac{2\mu_i}{\alpha_i^2}(\bar{\lambda}_1^{\alpha} + \bar{\lambda}_2^{\alpha} + \bar{\lambda}_3^{\alpha} - 3) \tag{3.13}$$

Specific forms of each model are obtained for specific choices of C_{ij}: the Mooney-Rivlin form follows the first order polynomial model; removing the second deviatoric strain invariant gives the first order reduced polynomial (neo-Hookean) model; and increasing the order of the neo-Hookean model from 1 to 3 yields the Yeoh model.

The parameters of each model were fitted to the test data using a least squares optimisation procedure. Owing to the resolution of the load cell used to collect stress–strain curves, the test data contained inherent noise. As noise reduced the quality of the curve fitting process, the data were smoothed such that the stress varied smoothly with strain. This was achieved by sampling stress–strain pairs in intervals of 40 between 0 and 25% strain. An interval of 20 was used between 25 and 50% strain to better capture the upturn of the stress–strain graphs. The order of the hyperelastic models was varied up to N=6; the stability of each model was then assessed using the Drucker stability criterion, which states that stress must continuously increase for increasing strain (and vice versa) [303, 304]. Unstable models were discounted from further analyses. The correlation between the test data and each stable hyperelastic model, or "goodness of fit", was established using Pearson's correlation coefficient, r^2:

$$r^2 = \left(\frac{\sum_{i=1}^{N}(\sigma_{i,exp} - \overline{\sigma}_{exp})(\sigma_{i,model} - \overline{\sigma}_{model})}{\sqrt{\sum_{i=1}^{N}(\sigma_{i,exp} - \overline{\sigma}_{exp})^2 \sum_{i=1}^{N}(\sigma_{i,model} - \overline{\sigma}_{model})^2}}\right)^2 \tag{3.14}$$

where, for N stress–strain pairs, $\sigma_{i,exp}$ is the experimental stress and $\sigma_{i,model}$ is the stress derived from the stress–strain relation of each strain energy function. Derivation of these stress–strain relations is described in detail elsewhere [305]. The hyperelastic parameters for each cryogel composition were averaged to provide single material constants for FEA (see Section 3.2.7).

To allow direct comparison of hyperelastic parameters from different hyperelastic models, a common parameter that could be derived from all constitutive models was needed. The initial shear modulus, μ_0, of polynomial, reduced polynomial and Ogden models were calculated using Equations 3.15–3.17.

$$\mu_0\,(polynomial) = 2(C_{10} + C_{01}) \tag{3.15}$$

$$\mu_0\,(reduced\,polynomial) = 2C_{10} \tag{3.16}$$

$$\mu_0\,(Ogden) = \frac{1}{2}\sum_{i=1}^{N} \mu_i \alpha_i \tag{3.17}$$

A displacement-driven uniaxial compression FE model matching the experimental setup was simulated using a quasi-static implicit analysis in Abaqus/CAE 2021 and the averaged constants. The dimensions of the platens matched their experimental counterparts (31.5 mm × 10 mm). The mean height and diameter of each PVA/gelatin cryogel composition were used to inform the geometry of the cryogel in each respective simulation (P_9G_1-A-C: 17.5 mm × 8.7 mm; P_9G_1-A-NC: 18.0 mm × 8.8 mm; P_9G_1-B-C: 18.1 mm × 9.0 mm; P_9G_1-B-NC: 18.0 mm × 8.4 mm). The cryogel was discretised using solid linear hexahedral (C3D8RH) elements.

Hybrid (H) elements were used to prevent volumetric locking, while reduced integration (R) elements were chosen to account for geometric nonlinearity. The platens were assumed to be rigid and were meshed using discrete rigid (R3D4) elements. The resulting mesh contained a total of 21,666 cryogel elements with an approximate edge length of 0.5 mm, and 6156 platen elements with an approximate edge length of 1 mm. The contact surfaces between cryogel and platen were modelled using surface-to-surface interactions with hard penalty contact constraints and a friction coefficient of 0.04, matching the average friction coefficient of PVA cryogel against titanium alloy [306]. The resulting stress–strain responses were then compared with the individual test data (Figure 3.1).

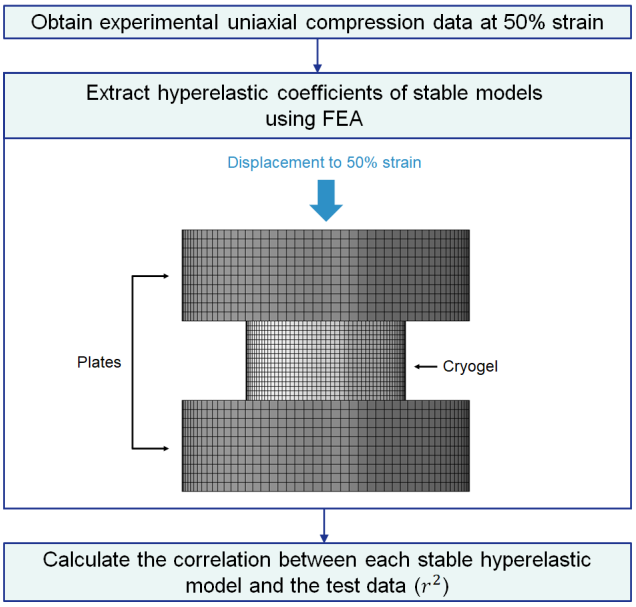


Figure 3.1: Flow chart outlining the hyperelastic curve fitting procedure and Abaqus uniaxial compression model used to validate hyperelastic coefficients.

3.2.7 Data Analysis

A total of eight samples were tested per cryogel composition. The effects of M_w and coagulation treatment on E, E', E'' and C_{ij} of PVA/gelatin cryogels were analysed in SigmaPlot 14.5 (Systat Software Inc, San Jose, CA, United States) using one-way ANOVA.

All hyperelastic constitutive parameters are presented as mean ± SD. Although single sets of optimal Ogden constitutive parameters were obtained for three of the compositions, two sets were obtained for P_9G_1-B-C: for one set, $\alpha_1 > 0$, and for the other, $\alpha_1 < 0$. Both sets are equally valid combinations of coefficients and yielded similar r^2 values (Table A.1). To allow averaging of the Ogden coefficients, samples where $\alpha_1 < 0$ were excluded from the dataset. The sample size was subsequently reduced to n=6 for all PVA/gelatin compositions and for the calculation of mean ± SD of all other stable constitutive models.

3.3 Results

3.3.1 Linear Elastic Response of PVA/Gelatin Cryogel

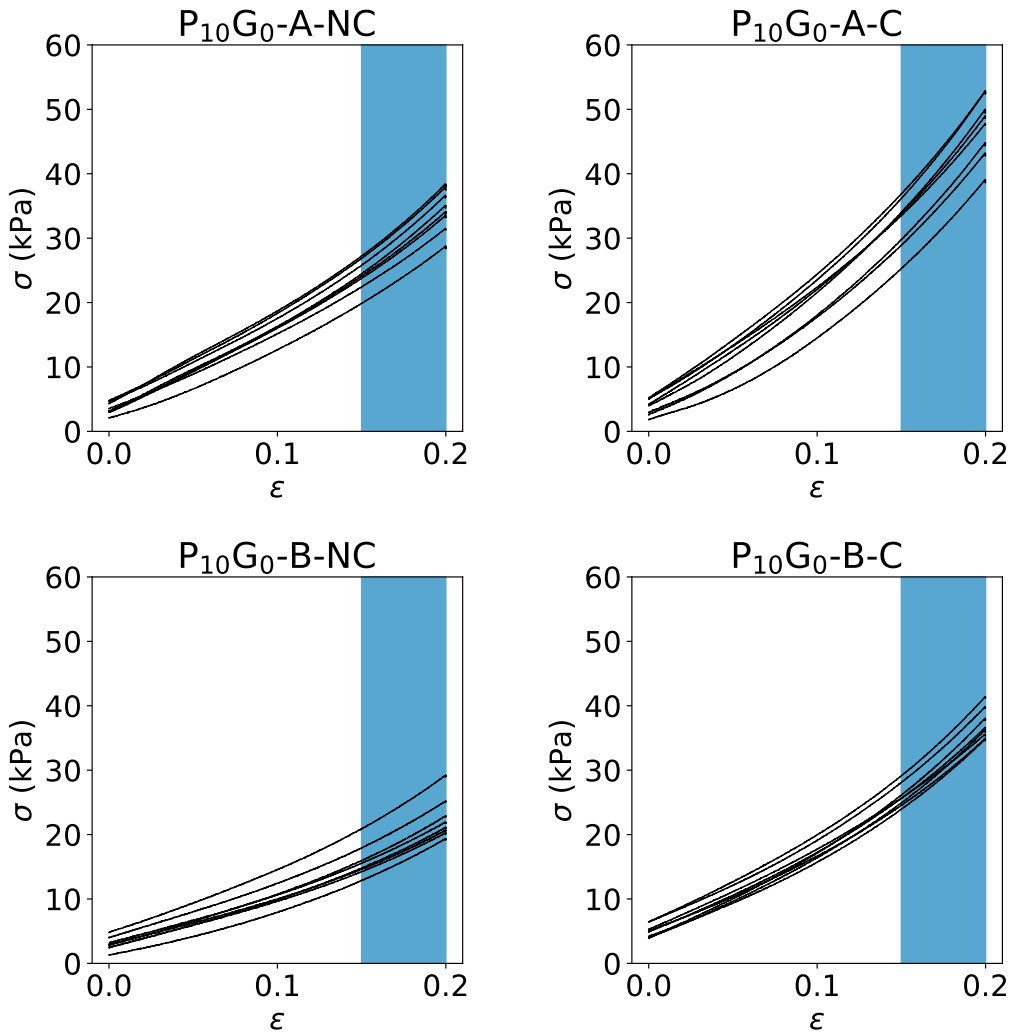


Figure 3.2: Engineering stress–strain curves for pure PVA cryogels compressed to 20% strain. The strain region used to calculate E is shaded in blue.

Figures 3.2 and 3.3 show the effect of M_w PVA and coagulation on the stress-strain responses of pure PVA (Figure 3.2) and PVA/gelatin (Figure 3.3) cryogels between 0–20% compressive strain, respectively. For all cryogel

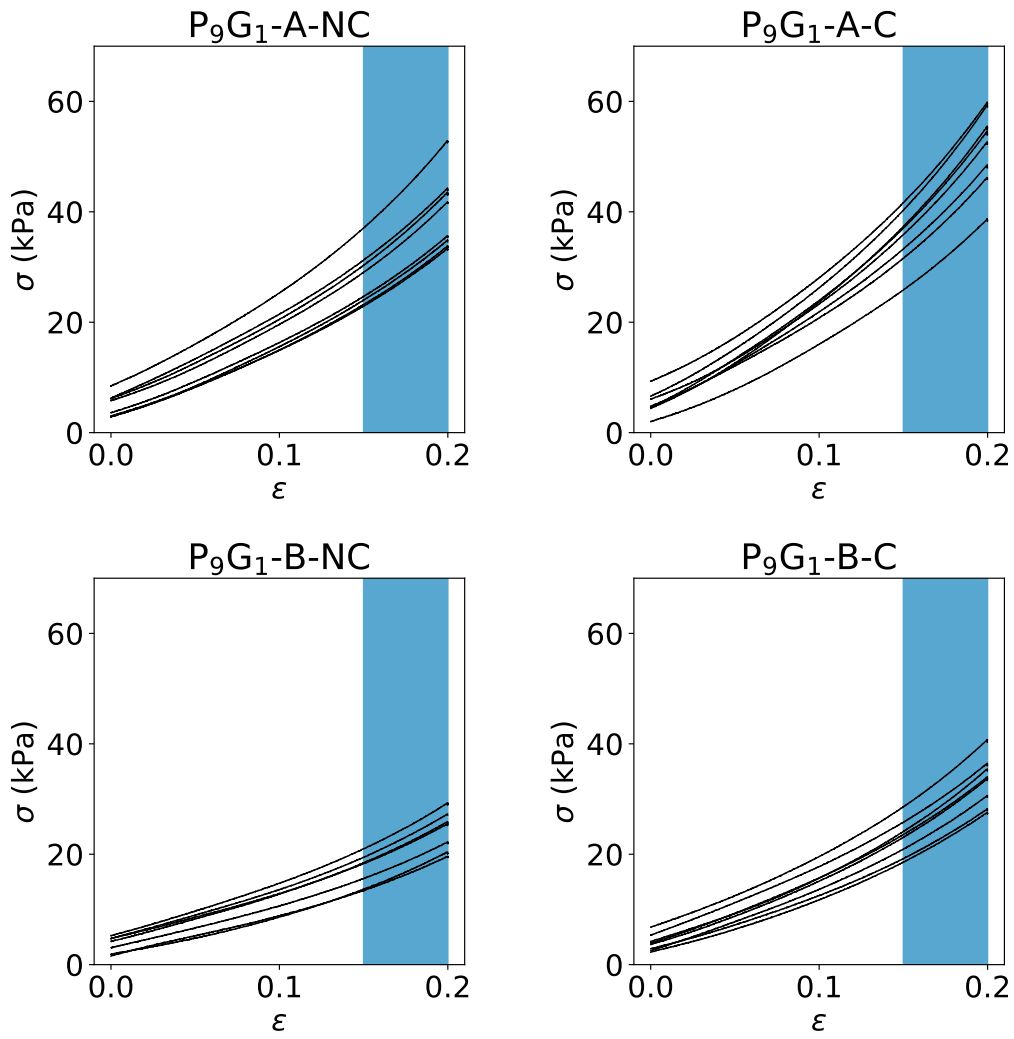


Figure 3.3: Engineering stress–strain curves for PVA/gelatin cryogels compressed to 20% strain. The strain region used to calculate E is shaded in blue.

compositions, E was calculated between 15–20% strain to match the dynamic amplitudes used for dynamic viscoelastic characterisation (Section 3.3.2). In all cases, the stress–strain responses were linear within this strain range; E values are reported in Table 3.4.

E ranged between 135.7 ± 15.5 kPa ($P_{10}G_0$-B-NC) and 334.4 ± 43.2 kPa (P_9G_1-A-C). E increased with increasing M_w PVA ($P < 0.001$) and use of coagulation treatment ($P < 0.001$). However, while $E_{P_9G_1-A-NC}$ increased

relative to $E_{P_{10}G_0-A-NC}$ ($P = 0.036$), no significant difference in stiffness was found upon addition of gelatin to $P_{10}G_0$-A-C, $P_{10}G_0$-B-NC or $P_{10}G_0$-B-C ($P > 0.05$, Figure 3.4).

Table 3.4: E (mean ± SD) between 15–20% strain for all cryogel compositions.

COMPOSITION	E (kPa)
$P_{10}G_0$-A-NC	205.8 ± 18.8
$P_{10}G_0$-A-C	307.5 ± 20.6
$P_{10}G_0$-B-NC	135.7 ± 15.5
$P_{10}G_1$-B-C	227.0 ± 16.2
P_9G_1-A-NC	246.7 ± 36.5
P_9G_1-A-C	334.4 ± 43.2
P_9G_1-B-NC	144.4 ± 14.7
P_9G_1-B-C	209.3 ± 22.6

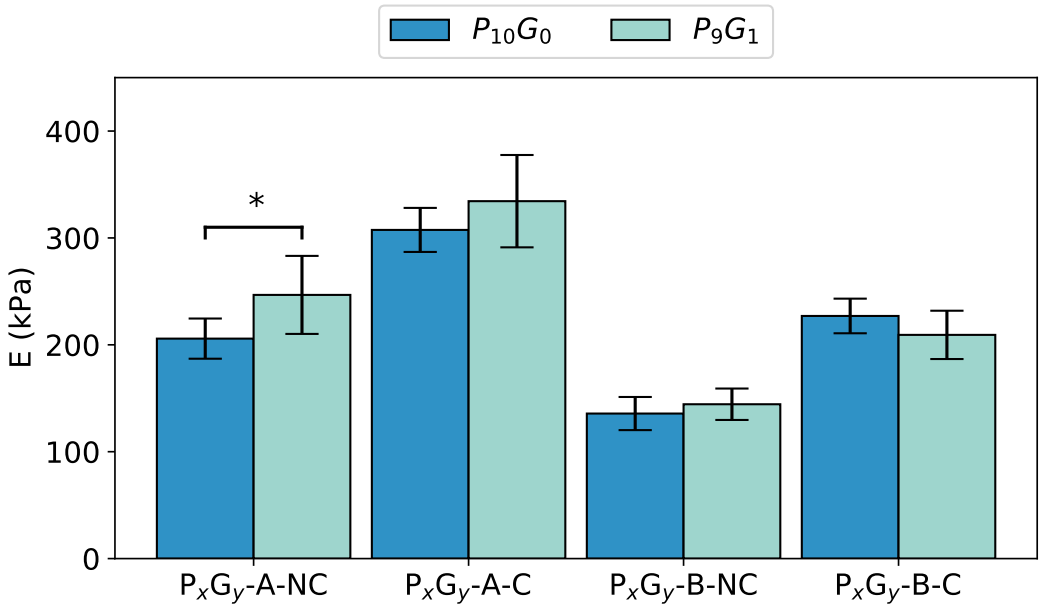


Figure 3.4: Variation in E as a function of gelatin addition. $^*P = 0.036$

3.3.2 Dynamic Mechanical Analysis of PVA/Gelatin Cryogel

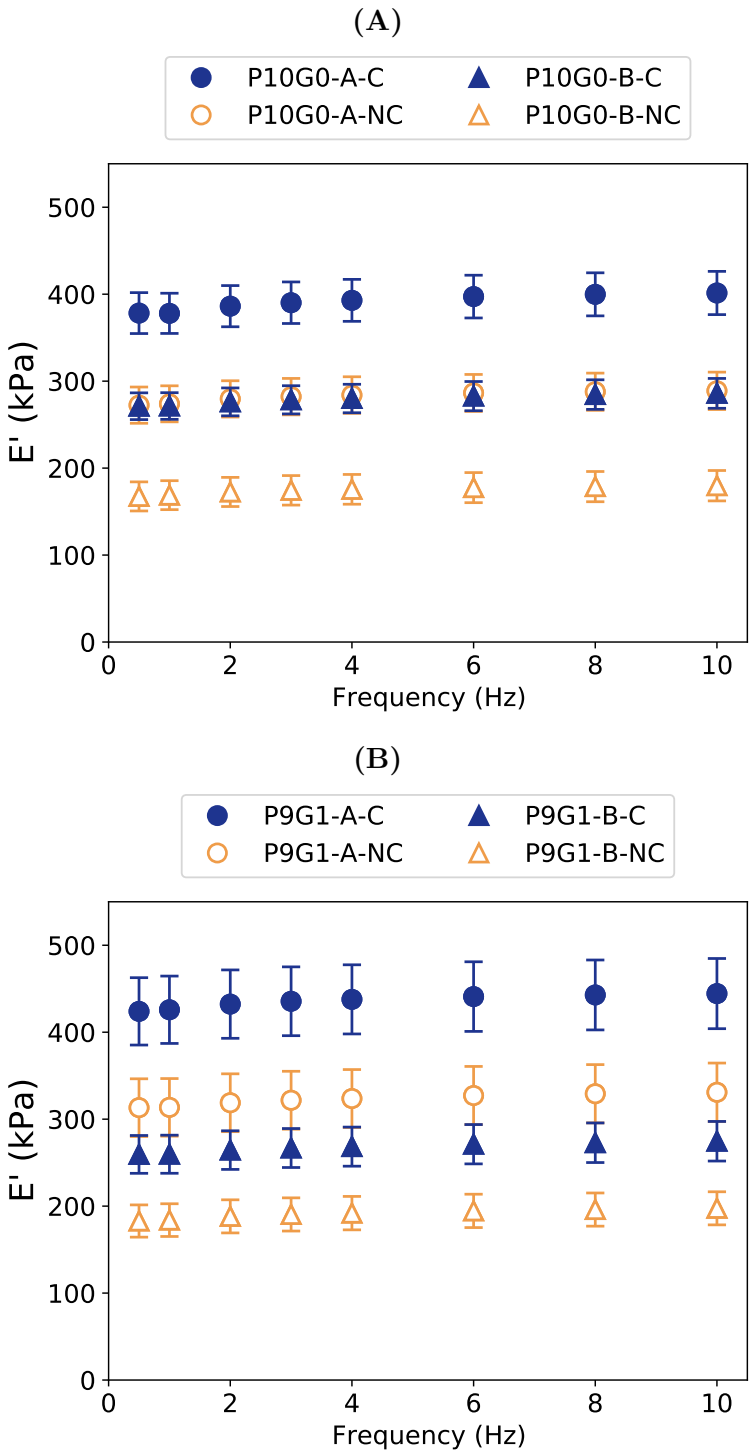


Figure 3.5: Effect of M_w PVA and cryogel coagulation on the E' of **(A)** pure PVA and **(B)** PVA/gelatin cryogels. Error bars show 95% confidence intervals (CIs).

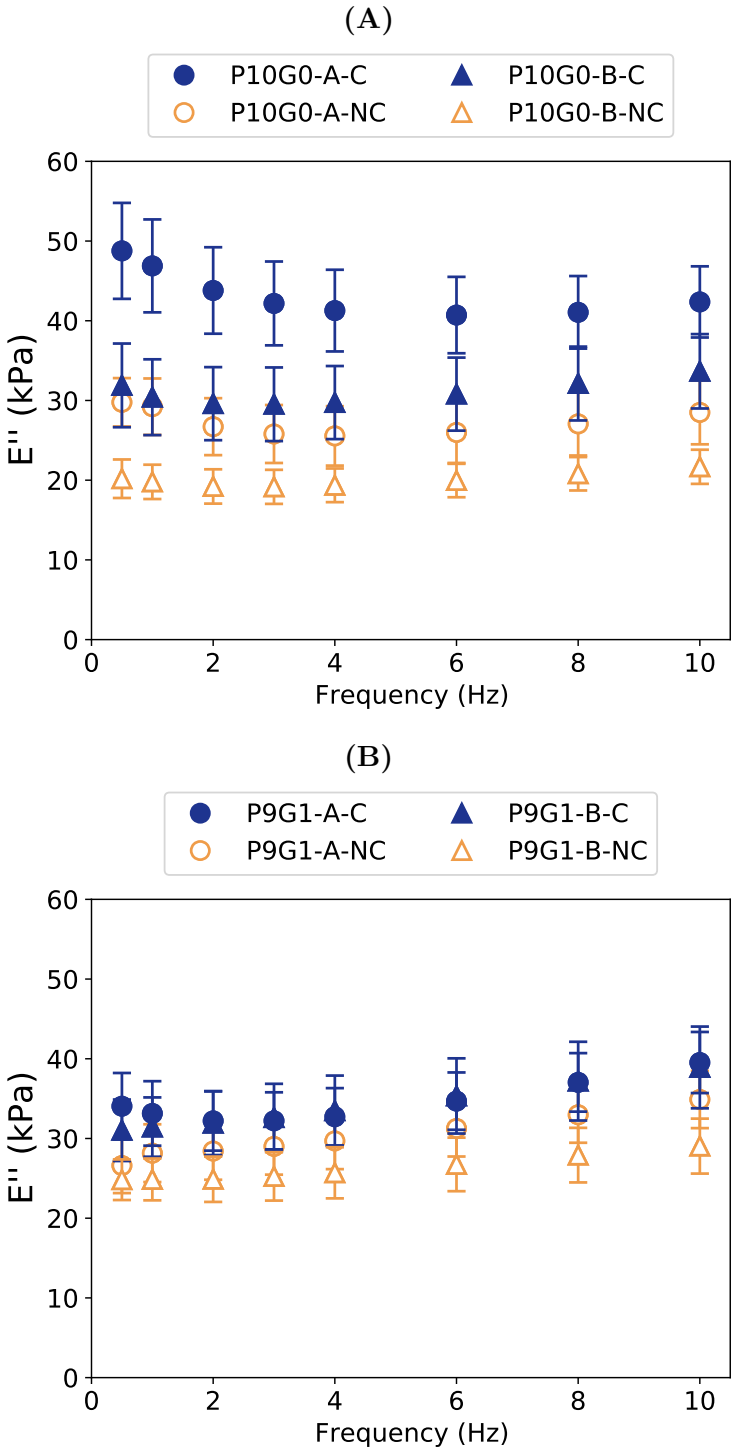


Figure 3.6: Effect of M_w PVA and cryogel coagulation on the E'' of **(A)** pure PVA and **(B)** PVA/gelatin cryogels. Error bars show confidence intervals (CIs).

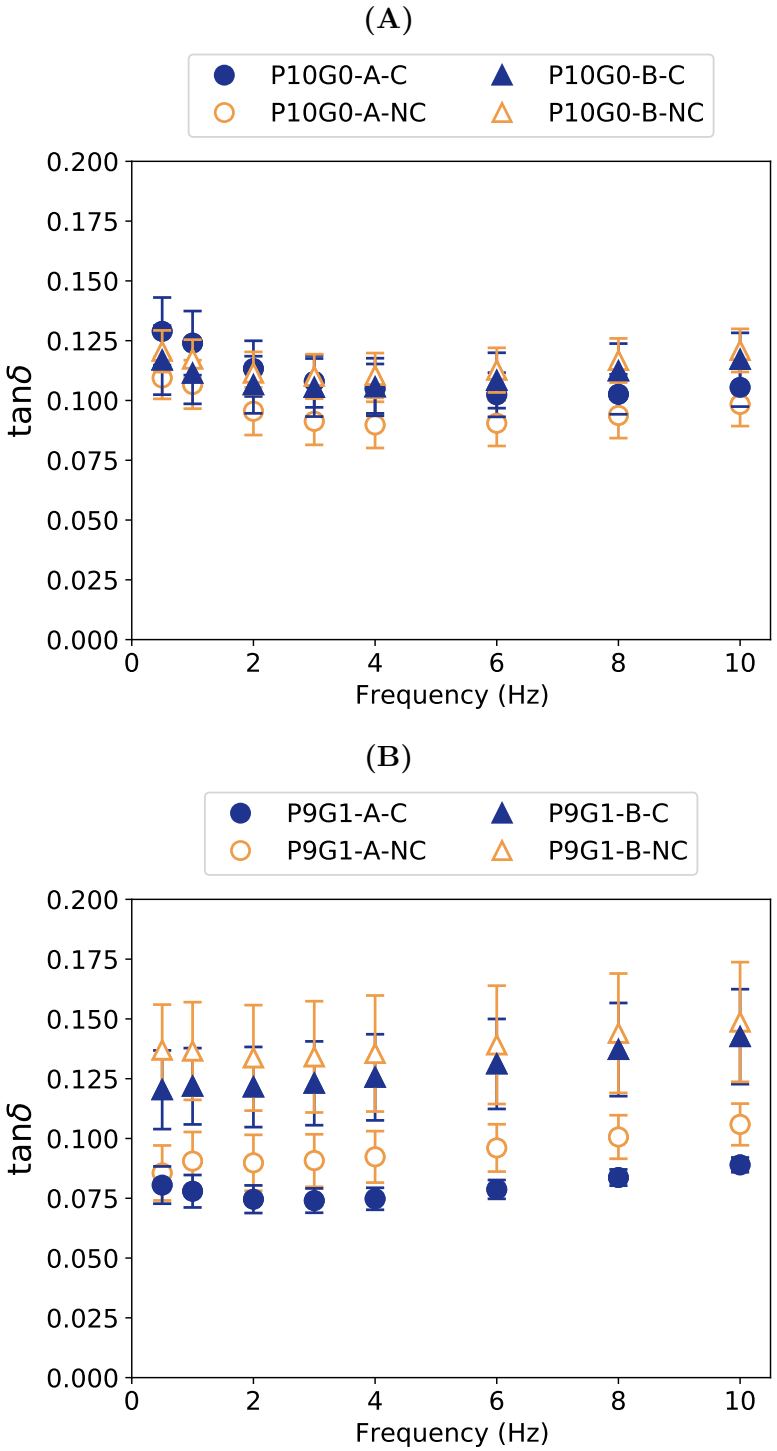


Figure 3.7: *tanδ* of **(A)** pure PVA and **(B)** PVA/gelatin cryogels. Error bars show confidence intervals (CIs).

For both M_w PVA used, irrespective of gelatin addition and coagulation treatment, E' were approximately an order of magnitude higher than E'' across all w/w ratios and frequencies tested (Figures 3.5 and 3.6). For instance, at a test frequency of 0.5 Hz, $E'_{P_{10}G_0-A-NC} = 272.4 \pm 24.9$ kPa and $E''_{P_{10}G_0-A-NC} = 29.8 \pm 3.6$ kPa (Figures 3.5A and 3.6A). At the same test frequency:

- $E'_{P_{10}G_0-B-NC} = 167.4 \pm 20.0$ kPa and $E''_{P_{10}G_0-B-NC} = 20.2 \pm 2.9$ kPa (lower M_w; Figures 3.5A and 3.6A)
- $E'_{P_{10}G_0-A-C} = 378.3 \pm 28.1$ kPa and $E''_{P_{10}G_0-A-C} = 48.8 \pm 7.2$ kPa (use of coagulation treatment; Figures 3.5A and 3.6A)
- $E'_{P_9G_1-A-NC} = 313.2 \pm 39.7$ kPa and $E''_{P_9G_1-A-NC} = 26.6 \pm 4.1$ kPa (addition of gelatin; Figures 3.5B and 3.6B)

By considering the ratio of E'':E', or $tan\delta$, the damping behaviour of each cryogel was further quantified (Figure 3.7). For all PVA/gelatin cryogel compositions tested, $tan\delta \ll 1$.

Numerically, E' increased with increasing frequency for all compositions (Table 3.5). However, the increase in E' between 0.5 and 10 Hz – the minimum and maximum frequencies tested – for all compositions was not statistically significant ($P > 0.05$). Thus, E' was found to be frequency-independent at the frequency range tested.

The frequency dependency of E'' could not be consistently determined for all cryogel compositions (Table 3.6). For pure PVA cryogels, no statistical difference was found in E'' between 0.5 and 10 Hz ($P > 0.05$). E'' was numerically lower at 10 Hz compared with 0.5 Hz for $P_{10}G_0$-A-C and $P_{10}G_0$-A-NC; yet, for pure PVA cryogels comprising lower M_w PVA, E'' was larger at 10 Hz. For all PVA/gelatin

compositions, E'' was larger at 10 Hz than at 0.5 Hz, and for all compositions except P_9G_1-B-C, this increase was statistically significant ($P < 0.05$).

The E' of pure PVA cryogel increased with increasing M_w PVA (Figure 3.5A). This trend was observed for all test frequencies: $E'_{P_{10}G_0-A-NC}$ (M_w PVA = 146–186 kDa) was, on average, 61.7% higher than $E'_{P_{10}G_0-B-NC}$ (M_w PVA = 89–98 kDa, Table A.4) at any given frequency. Coagulation treatment yielded a similar incremental effect: $E'_{P_{10}G_0-B-C}$ increased an average 59.9% relative to $E'_{P_{10}G_0-B-NC}$ across the frequency range (Table A.4). Analogous trends were observed for PVA/gelatin cryogel (Figure 3.5B). $E'_{P_9G_1-A-NC}$ was, on average, 69.1% higher than $E'_{P_9G_1-B-NC}$ and $E'_{P_9G_1-B-C}$ was, on average, 40.2% higher than $E'_{P_9G_1-B-NC}$ (Table A.5).

Table 3.5: E' (mean ± SD) for all PVA(/gelatin) compositions at 0.5 Hz and 10 Hz. P-values represent the statistical significance between the minimum (0.5 Hz) and maximum (10 Hz) frequencies for each composition. For full frequency data, the reader is referred to Table A.2.

	E' (kPa)			
	$P_{10}G_0$-A-C	**$P_{10}G_0$-A-NC**	**$P_{10}G_0$-B-C**	**$P_{10}G_0$-B-NC**
0.5 Hz	378.3 ± 28.1	272.4 ± 24.9	271.2 ± 18.4	167.4 ± 20.0
10 Hz	401.4 ± 29.7	288.9 ± 25.7	286.0 ± 20.5	179.8 ± 20.9
***P*-value**	0.130	0.234	0.151	0.161
	P_9G_1-A-C	**P_9G_1-A-NC**	**P_9G_1-B-C**	**P_9G_1-B-NC**
0.5 Hz	424.0 ± 46.3	313.2 ± 39.7	259.5 ± 26.0	182.9 ± 20.0
10 Hz	444.4 ± 48.3	330.9 ± 40.2	274.6 ± 27.2	197.5 ± 20.6
***P*-value**	0.402	0.207	0.275	0.203

Table 3.6: E'' (mean ± SD) for all PVA(/gelatin) compositions at 0.5 Hz and 10 Hz. P-values represent the statistical significance between the minimum (0.5 Hz) and maximum (10 Hz) frequencies for each composition. For full frequency data, the reader is referred to Table A.3.

	E'' (kPa)			
	$P_{10}G_0$-A-C	**$P_{10}G_0$-A-NC**	**$P_{10}G_0$-B-C**	**$P_{10}G_0$-B-NC**
0.5 Hz	48.8 ± 7.2	29.8 ± 3.6	31.9 ± 6.3	20.2 ± 2.9
10 Hz	42.4 ± 5.3	28.5 ± 4.8	33.7 ± 5.6	21.7 ± 2.6
***P*-value**	0.063	0.559	0.561	0.291
	P_9G_1-A-C	**P_9G_1-A-NC**	**P_9G_1-B-C**	**P_9G_1-B-NC**
0.5 Hz	34.0 ± 5.0	26.6 ± 4.1	31.0 ± 4.6	24.8 ± 2.8
10 Hz	39.5 ± 4.6	34.9 ± 4.3	38.9 ± 6.1	29.0 ± 3.7
***P*-value**	0.038	0.002	0.275	0.033

The E'' of pure PVA cryogel also increased at all test frequencies with increasing M_w PVA and use of coagulation treatment (Figure 3.6A). $E''_{P_{10}G_0-A-NC}$, for instance, increased an average 36.6% relative to $E''_{P_{10}G_0-B-NC}$, and $E''_{P_{10}G_0-B-C}$ increased an average 54.7% relative to $E''_{P_{10}G_0-B-NC}$ (Table A.6). These trends were observed for PVA/gelatin cryogels on a smaller, and in some cases non-significant, magnitude: $E''_{P_9G_1-A-NC}$ increased an average 15.0% relative to $E''_{P_9G_1-B-NC}$, and $E''_{P_9G_1-A-C}$ increased an average 1.5% relative to $E''_{P_{10}G_0-B-C}$ (Table A.7).

The addition of gelatin induced a statistically significant (albeit minor) increase in E' for higher M_w cryogels both with and without use of coagulation treatment, but not for lower M_w cryogels (Table 3.7).

Table 3.7: Comparison of E' (mean ± SD) upon addition of gelatin to all PVA cryogel compositions at 0.5 Hz and 10 Hz. P-values represent the statistical significance between the minimum (0.5 Hz) and maximum (10 Hz) frequencies for each composition.

	E' (kPa)	
	0.5 Hz	**10 Hz**
$P_{10}G_0$-A-C	378.3 ± 28.1	401.4 ± 29.7
P_9G_1-A-C	424.0 ± 46.3	444.0 ± 48.3
***P*-value**	0.042	0.050
	0.5 Hz	**10 Hz**
$P_{10}G_0$-A-NC	272.4 ± 24.9	288.9 ± 25.7
P_9G_1-A-NC	313.2 ± 39.7	330.9 ± 40.2
***P*-value**	0.027	0.026
	0.5 Hz	**10 Hz**
$P_{10}G_0$-B-C	271.2 ± 18.4	286.0 ± 20.5
P_9G_1-B-C	259.5 ± 26.0	274.6 ± 27.2
***P*-value**	0.317	0.363
	0.5 Hz	**10 Hz**
$P_{10}G_0$-B-NC	167.4 ± 20.0	179.8 ± 20.9
P_9G_1-B-NC	182.9 ± 20.0	197.5 ± 20.6
***P*-value**	0.160	0.123

3.3.3 Hyperelastic Constitutive Modelling of PVA/Gelatin

Table 3.8: Stability of hyperelastic models during curve fitting. Coefficients fulfilling Drucker's stability criteron were deemed stable ('yes'), while those which failed were deemed unstable ('no').

HYPERELASTIC MODEL	STABLE?
Reduced polynomial (N=1, neo-Hookean)	Yes
Reduced polynomial (N=2)	Yes
Reduced polynomial (N=3, Yeoh)	Yes
Reduced polynomial (N=4)	No
Reduced polynomial (N=5)	Yes
Reduced polynomial (N=6)	No
Polynomial (N=1, Mooney-Rivlin)	No
Ogden (N=1)	Yes
Ogden (N=2)	No
Ogden (N=3)	No

Hyperelastic data were collected for PVA/gelatin cryogels. When compressed to large (50%) compressive strains, each PVA/gelatin composition exhibited a characteristic "J"-shaped hyperelastic stress–strain response to loading. The stress–strain curves for individual samples are included in Figure A.1.

The Mooney-Rivlin model demonstrated limited success; while the model provided a stable fit for some samples, it yielded instabilities in others at the strain range tested (Drucker stability required the incremental strain to increase with incremental stress [304]). The neo-Hookean model, on the other hand, was unconditionally stable, as were the first order Ogden and second, third (Yeoh) and fifth order reduced polynomial models (Table 3.8 and Figure 3.8). The correlations between each stable model and the test data were close to unity ($1 < r^2 > 0.9$, Table A.8). Nevertheless, the neo-Hookean model underestimated stress at large strains, yielding

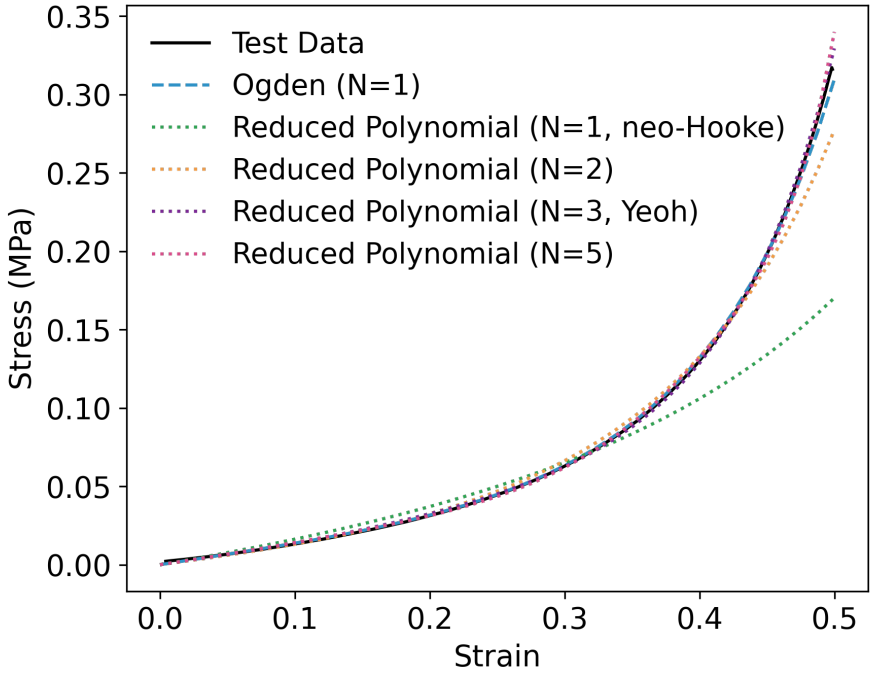


Figure 3.8: Representative curve fit of stable hyperelastic models to uniaxial compression data, taken from an individual P_9G_1-A-C sample. Compressive stress and strain are shown as absolute values.

the weakest correlation for all PVA/gelatin compositions ($r^2 \approx 0.93$). The approximation of stress at higher strains was improved by increasing the number of terms in the reduced polynomial model, as evidenced by increasing r^2 values; however, similar r^2 values were observed between the Yeoh and fifth order reduced polynomial models ($r^2 > 0.99$). Meanwhile, a single-term Ogden model was sufficient to capture the strain-stiffening behaviour of PVA/gelatin cryogel ($r^2 > 0.99$). The average Ogden and Yeoh constitutive parameters were taken forward for validation in Section 3.3.4 and are presented in Table 3.9.

Statistical analysis of the reduced polynomial parameter C_{10}, interpreted as $\frac{1}{2}\mu_0$, revealed a significant increase in stiffness as a function of M_w PVA for the Yeoh model ($P < 0.05$), but not as a result of coagulation treatment ($P > 0.05$,

Table 3.9: First order Ogden and Yeoh constitutive parameters fitted to PVA/gelatin compression data and densities of all PVA/gelatin cryogel compositions (mean ± SD).

FIRST ORDER OGDEN CONSTITUTIVE PARAMETERS				
	P_9G_1-A-C	**P_9G_1-A-NC**	**P_9G_1-B-C**	**P_9G_1-B-NC**
μ_1 **(MPa)**	0.0444 ± 0.0060	0.0374 ± 0.0042	0.0276 ± 0.0010	0.0227 ± 0.0025
α_1	7.116 ± 0.528	6.553 ± 0.276	7.765 ± 0.493	7.311 ± 0.581
μ_0 **(MPa)**	0.157 ± 0.016	0.122 ± 0.012	0.107 ± 0.009	0.083 ± 0.011
r^2	0.9994 ± 0.0004	0.9988 ± 0.0008	0.9994 ± 0.0003	0.9988 ± 0.0008
YEOH CONSTITUTIVE PARAMETERS				
	P_9G_1-A-C	**P_9G_1-A-NC**	**P_9G_1-B-C**	**P_9G_1-B-NC**
C_{10} **(MPa)**	0.0205 ± 0.0035	0.0180 ± 0.0024	0.0126 ± 0.0006	0.0108 ± 0.0014
C_{20} **(MPa)**	0.0015 ± 0.0028	−0.0015 ± 0.0019	0.0015 ± 0.0014	−0.0007 ± 0.0007
C_{30} **(MPa)**	0.0042 ± 0.0017	0.0044 ± 0.012	0.0032 ± 0.0006	0.0033 ± 0.0009
μ_0 **(MPa)**	0.0410 ± 0.0070	0.0360 ± 0.0049	0.0252 ± 0.0012	0.0217 ± 0.0027
r^2	0.9994 ± 0.0008	0.9984 ± 0.0009	0.9997 ± 0.0002	0.9985 ± 0.0007
DENSITY				
	P_9G_1-A-C	**P_9G_1-A-NC**	**P_9G_1-B-C**	**P_9G_1-B-NC**
ρ **(kg m^{-3})**	1080 ± 36	1190 ± 16	1070 ± 37	1120 ± 38

Table 3.10). Conversely, a statistically significant increase in the Ogden parameter μ_1 was observed as a function of M_w PVA or use of coagulation treatment. The same trend was observed for μ_0 (Table 3.10). For all compositions, $|\alpha_1| > 2$. This reflects the stiffening effect observed at higher strain [307]. However, the only statistically significant change in α_1 when varying the manufacturing parameters was between P_9G_1-A-NC and P_9G_1-B-C ($P = 0.02$).

Table 3.10: Correlation matrices showing the effect of M_w PVA and coagulation treatment on μ_0 of PVA/gelatin cryogel. NS = not statistically significant ($P > 0.05$); * = $P \leq 0.05$; ** = $P \leq 0.01$; *** = $P \leq 0.001$.

FIRST ORDER OGDEN: μ_0				
	P_9G_1-A-C	**P_9G_1-A-NC**	**P_9G_1-B-C**	**P_9G_1-B-NC**
P_9G_1-A-C	-	***	***	***
P_9G_1-A-NC	***	-	*	***
P_9G_1-B-C	***	*	-	**
P_9G_1-B-NC	***	***	**	-
YEOH: μ_0				
	P_9G_1-A-C	**P_9G_1-A-NC**	**P_9G_1-B-C**	**P_9G_1-B-NC**
P_9G_1-A-C	-	NS	***	***
P_9G_1-A-NC	NS	-	**	***
P_9G_1-B-C	***	**	-	NS
P_9G_1-B-NC	***	***	NS	-

3.3.4 Validation of Yeoh and Ogden Constitutive Parameters for FE Modelling

The Yeoh and first order Ogden models were taken forward to represent the hyperelastic behaviour of PVA/gelatin cryogel in all FE models. The mean stress–strain responses, yielded by the mean values of each model's constitutive parameters, were obtained using a displacement-driven uniaxial compression FE model and compared to the experimental stress–strain responses of individual samples (Figure 3.9). This method successfully generated master curves reflecting the

mean mechanical properties of each cryogel composition, with strain-stiffening behaviour analogous to the test data.

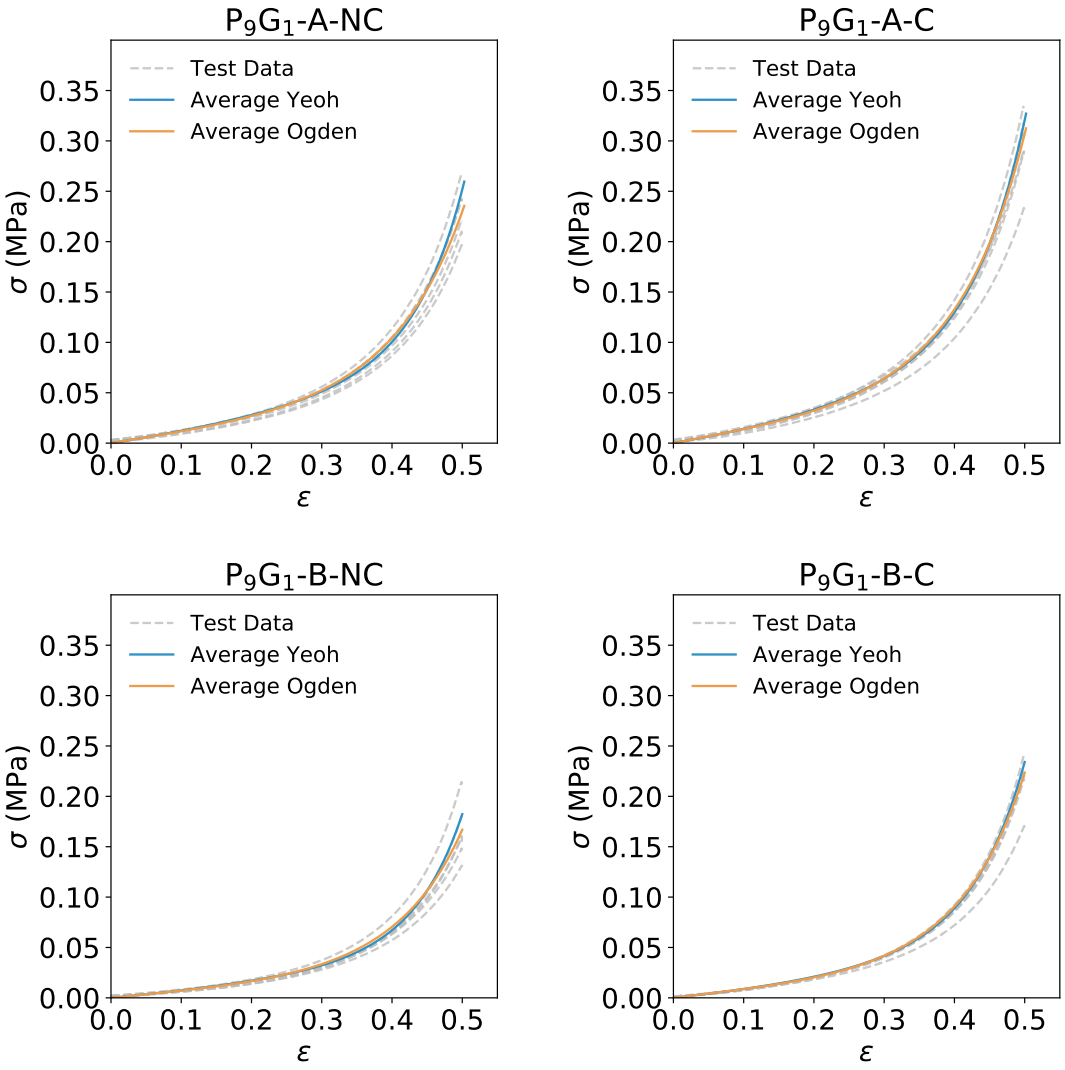


Figure 3.9: Simulated compressive stress–strain response using averaged Yeoh (solid blue line) and first order Ogden (solid orange) parameters of PVA/gelatin cryogels compared with experimental test data (grey dashed lines). Compressive stresses and strains are shown as absolute values.

3.4 Discussion

Thorough characterisation of the mechanical properties of PVA/gelatin cryogels is needed to explore their potential as VMMs. Moreover, the need to engineer VMMs with analogous mechanical heterogeneity to the artery wall reflects the need for a VMM whose mechanical properties can be varied within a desired range through manipulation of formulation parameters. This chapter evaluated the effect of two key formulation and process parameters – the M_w of PVA and use of polymer coagulation treatment – on the linear elastic, dynamic viscoelastic and hyperelastic properties of PVA/gelatin cryogels. Constitutive parameters have been determined for each and are summarised in the context of existing literature in Sections 3.4.1–3.4.3.

3.4.1 Linear Elastic Behaviour

Prior studies have characterised the linear elastic behaviour of PVA/gelatin cryogel as a function of the cryogelation process, namely number and duration of FT cycles [199, 297]. Post-cryogelation treatment (polymer coagulation) has also been explored as a method to vary the mechanical properties of PVA/gelatin cryogels through precipitation of amorphous PVA, which increases the amount of crystalline PVA available for crosslinking [13, 199]. Of the attributes related to the structure of PVA itself, the impact of M_w on the linear elasticity of PVA/gelatin cryogel is limited to PVA/gelatin theta-cryogels (where a theta-gel is a hydrogel formed with a porogen, a chemical designed to make pores, to create rigid macroporous structures [308]) [298]. While these studies provide insight into the underlying mechanics of PVA/gelatin cryogel, each assessed the impact of their respective parameter in isolation; a parameter sweep simultaneously assessing the impact of multiple parameters

on the linear elasticity of PVA/gelatin is lacking from the literature. Section 3.3.1 quantified the impact of M_w and coagulation treatment, both in isolation and in combination, on the Young's modulus of pure PVA and PVA/gelatin cryogels.

The range of E values (135.7 ± 15.5 kPa – 334.4 ± 43.2 kPa) obtained in this study highlights the dependence of compressive mechanical properties on M_w PVA and coagulation treatment. Increasing the M_w of PVA from 89–98 kDa to 146–186 kDa increased E, resulting in a stiffer cryogel. This is in agreement with the compressive data reported for PVA/gelatin theta-cryogels of matching M_w [298]. Increasing the chain length of PVA increases the lamellar thickness of PVA crystallites and allows for a higher degree of physical entanglement [193]. In addition, the increased viscosity of high M_w PVA further restricts the molecular motion of PVA chains during the freezing step. While Lozinksy *et al.* hypothesised that increased viscosity in the amorphous region lowers the efficiency of intermolecular interactions [309], Hassan and Peppas demonstrated increased (albeit minor) secondary crystallite formation with increasing M_w PVA [310]. The statistically significant increase in stiffness between $P_{10}G_0$-B-NC → $P_{10}G_0$-A-NC and P_9G_1-B-NC → P_9G_1-A-NC suggests that, at the two M_w PVA tested, the latter mechanism dominates. Ideally, this theory should be tested on PVA with a M_w > 146–186 kDa; however, such PVA is not readily available commercially. Hence, if a greater variation in E is desired for a given application, alternative polymer characteristics should be targeted in addition to chain length.

The ability to tailor the mechanical properties of PVA-based cryogels via salt addition has been documented by several groups [13, 198–200]. Kosmotropic anions, such as the SO_4^{2-} anions used in this study, reinforce the PVA microstructure through precipitation of amorphous PVA. A recent study by Hua *et al.* showed that kosmotropic anions expel the hydration water between amorphous PVA chains to

yield densified microfibres [198]. The higher the "salting out" power of the anion, the greater the densification and tensile stress of the cryogel [198]. However, in a preliminary experiment performed for this study, it was noted that sodium citrate – the most kosmotropic salt tested by Hua *et al.* [198] – resulted in considerable sample shrinkage (data not recorded). As a key goal of this thesis was to investigate the influence of mesoscale design principles on vascular graft behaviour, this shrinkage was deemed unacceptable and no further analyses were conducted using sodium citrate. For both M_w PVA tested in this thesis, immersing PVA and PVA/gelatin cryogels in 1 M KOH/1 M Na_2SO_4 increased E. As such, the M_w of PVA and polymer coagulation can be used in tandem to increase the stiffness of PVA/gelatin cryogel reported in this thesis.

With the exception of $P_{10}G_0$-A-NC $\rightarrow$ P_9G_1-A-NC, no statistically significant difference in E was observed upon addition of gelatin to the cryogel matrix. It can therefore be concluded that the compressive properties of PVA/gelatin cryogel are predominantly determined by the PVA matrix and that gelatin does not disrupt PVA crystallite formation. Charron *et al.* hypothesised that, as the M_w of PVA is increased, greater chain entanglement and ionic interactions between PVA and gelatin may result in a stiffer cryogel [298]. This may explain the statistically significant increase in E between $P_{10}G_0$-A-NC $\rightarrow$ P_9G_1-A-NC, but it is noted that the increase observed in this study was small, and 1 wt% gelatin addition should not be viewed as a dominant parameter to vary cryogel stiffness.

It should be stressed that E by itself is insufficient to describe the complex mechanical behaviour of the artery wall under physiological loading. In the strategic plan proposed by Camasão *et al.*, characterisation of E is deemed suitable for the initial stages of VMM development as it offers a simple way of assessing the magnitude of mechanical stiffness relative to the target vessel [311]. However, as-

suming the magnitudes of E are similar between the two, more complex mechanical testing methods (DMA, burst pressure and dynamic compliance tests) are needed thereafter. The range of E values reported for PVA and PVA/gelatin cryogel in this thesis falls within the lower end of the spectrum of values reported for coronary arteries, although it is noted that differences in test setup (eg uniaxial versus biaxial characterisation, extent of prestretch or preload) and tissue source (human versus animal, specimen age, disease progression, location along arterial branch) will influence E [290, 291, 293, 302, 311]. For instance, Kural *et al.* determined the equibiaxial moduli of non-calcified human coronary arteries to be between 7.9 and 89.9 kPa depending on strain region and load direction [290]. On the other hand, research into the uniaxial tensile behaviour of porcine coronary arteries yielded E values between 0.76–10 MPa [291, 293]. Stepniak *et al.* reported the average physiological E of porcine coronary artery under uniaxial loading to be 0.16 ± 0.04 MPa, which aligns more closely with the E of PVA and PVA/gelatin cryogel.

3.4.2 Viscoelastic Behaviour

The impact of cryogel composition on the dynamic viscoelastic response of PVA/gelatin has been investigated using frequency-domain DMA. Previous studies have explored the quasi-static viscoelastic response of PVA composite cryogels in terms of stress relaxation [186, 312] and creep [186]. While these studies offer insight into the long-term time-dependent deformation of PVA cryogel, they do not provide an understanding of its deformation under dynamic loading conditions. The mechanical behaviour of a VMM should replicate the distension and recoil behaviour of the host artery with each heartbeat [311]. DMA allows the quantification of viscoelastic behaviour at physiologically-relevant frequencies such as the heartbeat – a design consideration that is often overlooked when characteris-

ing the mechanical properties of VMMs.

Viscoelasticity is characterised by E' and E'', which describe how energy is stored and dissipated under loading within a sample, respectively. If the elastic and viscous contributions during cyclic deformation are equal – that is, if the ratio of energy lost (E'') to energy stored (E') are equivalent – $tan\delta = 1$. For all PVA and PVA/gelatin cryogel compositions tested, $tan\delta \ll 1$. Hence, more energy was stored during cyclic deformation than dissipated and the cryogels were predominately elastic in structure.

Research into the poro-viscoelastic properties of PVA has demonstrated that PVA can be described as a biphasic material [313]. PVA cryogel consists of a porous polymer network through which fluid can flow. Increasing the M_w of PVA and using polymer coagulation treatment increased the E' of PVA and PVA/gelatin cryogels across all frequencies. Not only do these data agree with the linear elasticity trends reported in Section 3.3.1, but they are in agreement with the dynamic viscoelastic parameters reported for PVA cryogels of increasing PVA concentration [103] and can be attributed to a similar hypothesis. Achieved via two distinct mechanisms, increasing the M_w of PVA and using coagulation treatment (separately or in tandem) yielded denser network structures with reduced pore size. This increased the mechanical stiffness of the cryogel. Furthermore, the addition of gelatin may contribute to further chain entanglement, as evidenced by an increase in E' of high M_w PVA/gelatin cryogels compared with the E' of high M_w PVA cryogels of matching coagulation status. However, no statistically significant difference was observed between the E' of low M_w PVA and PVA/gelatin cryogels of matching coagulation status; this finding further supports the linear elastic stiffness trends discussed in Section 3.4.1.

The biphasic model suggests that a reduction in pore size will hinder energy dissipation as fluid will flow less freely under an applied load. Research has shown that the creep and stress relaxation responses of PVA decrease with increasing PVA concentration, supporting this theory [313]. While no significant change in $tan\delta$ was observed as a function of M_w or coagulation treatment for pure PVA cryogel, the $tan\delta$ of PVA/gelatin cryogel decreased with increasing M_w. It is thought that the steric bulk of gelatin, combined with increased PVA chain length, may lead to a higher degree of chain entanglement [298]. This may restrict fluid flow throughout the polymer network and reduce viscous damping. While this study has demonstrated that gelatin concentration affects the damping capacity of PVA/gelatin cryogels, this hypothesis would need to be tested on a wider range of gelatin concentrations to determine an empirical trend.

For all compositions of PVA/gelatin cryogel, E' was approximately an order of magnitude higher than E''. These results match the relative magnitudes of E' and E'' reported for 10–20 wt% PVA cryogel [103]. Physiologically, a similar trend has been reported for the E' and E'' of porcine LAD coronary arteries [102, 302]. The magnitudes of E' and E'' reported in this study (10^1–10^2 kPa) were lower than those reported by Burton *et al.* (10^0–10^1 MPa) [102]. While this indicates that the compositions of PVA/gelatin tested in this study are less stiff than arterial tissue, it should be noted that Burton *et al.* used a large preload ($\approx 3.6L_0$) to overcome tissue slack due to dissection [102]. This is supported by data from Stepniak *et al.*, who reported the mean E' of porcine LAD, LCX and RCA to be between 0.012 MPa and 0.030 MPa at a frequency of 1.25 Hz [302]; however, the authors did not report the preload used to negate tissue slack. Freij *et al.* determined the mean low strain modulus (at a tensile stretch $<1.53L_0$) of porcine LAD coronary artery to be 0.67–0.85 MPa [293]. Therefore, it may be appropriate to aim for cryogel stiffness

on the order of 10^2 kPa, as achieved in this study.

The E' of PVA/gelatin cryogel was frequency-independent between 0.5–10 Hz. In the absence of dynamic viscoelastic data on human coronary arteries, this finding must be compared with the viscoelastic properties measured in studies of other arteries. Mavrilis *et al.* determined that the E' of human IMA and SV grafts were frequency-independent at low frequencies (<0.5 Hz); however, E' peaked between 0.5–1 Hz and decreased between 1–10 Hz [301]. Burton *et al.* found that the E' of porcine LAD coronary artery decreased between 0–10 Hz and concluded that the reduction in E' corresponds to a diminished capacity for elastic recoil with increasing heart rate [102]. However, statistical significance was only reported between 0.5 and 10 Hz; the authors did not indicate whether the reduction in E' was statistically significant at physiologically healthy frequencies (eg 0.5–3 Hz, or 30–180 bpm). On the contrary, Stepniak *et al.* determined that the E' of porcine LAD, LCX and RCA increased between 0.5 and 3.5 Hz and that no significant difference in E'/E'' was found between the three arterial branches [302]. Unfortunately, they also did not note whether this trend was statistically significant. Taken together, these results reflect that the elastic properties of different arteries have different frequency dependencies [301]. Thus, the dynamic mechanical properties of a VMM should be evaluated against the dynamic mechanical properties of the target vessel. The dynamic viscoelastic properties of PVA/gelatin cryogel must be compared with the dynamic viscoelastic properties of healthy human coronary arteries, once such data become available.

3.4.3 Hyperelastic Behaviour

Like arteries, hydrogels are nearly incompressible and demonstrate a non-linear response to loading. Thus, a hyperelastic model was needed to emulate the quasi-static mechanical behaviour of PVA/gelatin grafts. In this chapter, the hyperelasticity of four PVA/gelatin cryogel compositions were characterised according to a number of isotropic models used to empirically describe rubbery materials. Pure PVA cryogels have previously been fitted to first [195, 314] and second [315] order polynomial, Yeoh and Ogden [316] models. Here, the hyperelastic response of PVA/gelatin cryogels has been calibrated to polynomial, reduced polynomial and Ogden models of varying order, using data obtained under uniaxial compression.

For a hyperelastic model to be efficient, it should contain as few terms as possible. This ensures that each coefficient describes some part of the mechanical response of the material and minimises the number of experimental tests needed to fit them [92, 98]. The model must also be stable across the strain region of interest, where the Drucker stability condition requires incremental changes in strain to increase with respect to incremental changes in stress ($d\sigma{:}d\epsilon > 0$) [304]. Stability is especially important when characterising a synthetic graft material because the FE model must accurately predict its behaviour when subjected to multi-axial stress states, such as those experienced in a pressurised artery. The curve fitting procedure in Abaqus assesses stability under uniaxial, biaxial and planar shear; in this thesis, the stability of PVA/gelatin cryogel under biaxial and planar shear was considered qualitatively using the material constants obtained under uniaxial compression, as neither biaxial nor shear tests were performed experimentally. This approach has been implemented in the characterisation of other hyperelastic materials [317].

The Mooney-Rivlin model failed to consistently predict the hyperelastic

behaviour of each cryogel composition; it yielded Drucker instabilities under uniaxial, biaxial and planar compression and tension. Removing the second strain invariant overcame these instabilities. However, while the neo-Hookean model is suited to limited test data [98], it could not capture the strain hardening effect observed at high (>30%) strain. This was reflected in the correlation coefficient, which was notably lower than the other stable models for all cryogel compositions. Increasing the order of the reduced polynomial improved the approximation of the stiffening response of PVA/gelatin cryogel at high strain. The third order reduced polynomial (Yeoh) model provided the necessary accuracy at high strain while keeping the order of the strain energy density function as low as possible.

The first order Ogden model provided a good fit using only two coefficients: μ_1, with units of pressure, and α_1, a dimensionless quantity that determines the non-linearity of the stress–strain plot. Together, they describe the shear modulus of the cryogel. The Ogden model has been used to capture the hyperelastic behaviour of many soft strain-hardening materials, including gelatin gels [318]. Second and third order Ogden models need test data from multiple deformation modes for a stable fit; however, other studies have demonstrated that the first order model can properly characterise hydrogels under compression [318, 319].

Analysis of PVA/gelatin Ogden parameters showed that increasing the M_w of PVA or using coagulation treatment increased μ_1 and thus the stiffness of the cryogel ($p < 0.05$). This agrees with the elastic and dynamic complex moduli reported in Sections 3.3.1 and 3.3.2 as well as previous literature, where higher elastic [13, 199] and dynamic complex [103] moduli have been linked to changes in the gel microstructure caused by the cryogelation process. No statistical significance in α_1 was observed as either a function of M_w PVA or use of coagulation treatment. This indicates that the curvature of the stress–strain plot was independent of both

manufacturing parameters and each composition exhibited the same overall trend in stress–stiffening response over 50% strain.

Interestingly, the Yeoh model did not highlight a statistically significant increase in its stiffness parameter C_{10} when using coagulation treatment. This discrepancy may be explained by considering that $C_{10} = \frac{1}{2}\mu_0$ and thus describes only the initial region of the stress–strain curve, which does not vary significantly with use of coagulation treatment. However, μ_1 is influenced by the non-linearity of the curve at higher strain ($\mu_1 = \frac{2\mu_0}{\alpha_1}$). Importantly, the simulated stress–strain responses of each PVA/gelatin composition under compression, obtained using the mean values of the hyperelastic parameters of both constitutive models, compare well with the experimental test data. Despite the differences in constitutive parameters, both the first order Ogden and Yeoh models were appropriate for modelling the quasi-static hyperelastic behaviour of PVA/gelatin cryogel under compression.

3.5 Conclusion

The aim of this chapter was to expand existing knowledge on the manufacturing-specific mechanical properties of PVA/gelatin cryogel; this was achieved through quantification of linear elastic, dynamic viscoelastic and hyperelastic parameters of PVA/gelatin cryogels as a function of M_w PVA and polymer coagulation treatment. To the author's knowledge, this chapter marks the first time that dynamic viscoelastic and hyperelastic parameters have been reported for PVA/gelatin cryogel. More broadly to this thesis, the parameters generated from each mechanical test were intended to facilitate the development of computational models of PVA/gelatin-based coronary artery grafts and thus aid the design and clinical translation of PVA/gelatin cryogel as a viable VMM. The following conclusions are drawn:

- Increasing the M_w of PVA and/or using a 1 M KOH/1 M Na_2SO_4 coagulation bath to reinforce the cryogel microstructure increased the stiffness of PVA and PVA/gelatin cryogel, as evidenced by an increase in E, E'/E'' and $\mu_1/\mu_0/C_{10}$;

- For some high M_w compositions, the addition of 1 wt% gelatin induced a minor yet statistically significant increase in stiffness compared with pure PVA cryogel. It is concluded that gelatin does not disrupt PVA cryogel formation and may act to increase chain entanglement when high M_w PVA is used;

- In lieu of dynamic viscoelastic data on human coronary arteries, the dynamic viscoelastic parameters of PVA/gelatin cryogel were compared with porcine coronary arteries. The $tan\delta$ of PVA and PVA/gelatin cryogel was comparable to porcine coronary arteries; furthermore, the magnitudes of E' and E'' fell between the minimum and maximum values reported in the literature. However, PVA/gelatin cryogel and showed contrasting frequency-dependency trends between 0–10 Hz compared with porcine coronary arteries;

- The first order Ogden and Yeoh hyperelastic models are suitable for modelling the hyperelastic behaviour of cast (isotropic) PVA/gelatin cryogel.

STATEMENT OF CONTRIBUTIONS II

Chapter 4 includes novel research published in *Frontiers in Cardiovascular Medicine*, a peer-reviewed scientific journal, with myself as the principal author. The research was published as an open-access article with a full CC-BY 4.0 copyright license (https://creativecommons.org/licenses/by/4.0/), allowing for the reproduction of data within this thesis. The citation and statement of contributions from each author are as follows:

Fegan, K. L., Green, Naomi C., Britton, Melanie M., Iqbal, Asif J. & Thomas-Seale, L. E. J. Design and simulation of the biomechanics of multi-layered composite poly(vinyl alcohol) coronary artery grafts. *Frontiers in Cardiovascular Medicine* **9**, 883179 (2022). DOI: 10.3389/fcvm.2022.883179

- **KF** contributed to the conception, design and implementation of the research, to the analysis of the results, and to writing the original draft of the manuscript;
- NG supervised and contributed to the conception and design of the research;
- MB and AI supervised the research;
- LT-S supervised and contributed to the conception, design and implementation of the research.

All authors contributed to manuscript revision, read and approved the submitted version.

Chapter Four

FINITE ELEMENT MODELLING OF HYPERELASTIC PVA/GELATIN GRAFTS

4.1 Introduction

Chapter 3 demonstrated the impact of formulation and processing parameters on the mechanical properties of PVA/gelatin cryogel. The ability to tune key mechanical behaviours such as hyperelasticity and viscoelasticity through choice of manufacturing parameters makes PVA-based cryogels appealing targets for multi-layered coronary artery grafts. This chapter will build upon the growing body of experimental data supporting PVA/gelatin cryogel as a viable VMM – including the mechanical data presented in Chapter 3 – through the quasi-static simulation of four hyperelastic tri-layered PVA/gelatin coronary artery grafts under systolic and diastolic pressure. The simulated response of each PVA/gelatin-based graft will be assessed in relation to simulations of the coronary artery wall.

Designing synthetic grafts to replace diseased blood vessels remains a critical field of biomedical research [89, 151, 235]. A Web of Science literature search reveals that 1904 papers containing the words "small diameter vascular graft" or "small diameter artery graft" were published between 2000–2022. Yet, few grafts ever make it to the clinical trial stage.

For a graft to remain viable *in vivo*, it must replicate the native functions of the host artery that it intends to replace. This relies on the intrinsic characteristics of the biomaterial(s) used [320]. These characteristics are often grouped into four categories: (1) the ability to maintain a healthy endothelium on the biomaterial surface; (2) blood compatibility; (3) biocompatibility and biodegradability; and (4) matched mechanical properties [7]. Importantly, the success of a graft depends on satisfying all four categories simultaneously. A healthy endothelium displays a quiescent non-thrombogenic phenotype to prevent blood clot formation; this phenotype is mediated in part by the biomechanical forces exerted upon it. Arteries expand and contract in response to blood pressure, generating stress and strain within the vessel wall [119]. Cyclic stretch activates downstream signalling pathways through mechanotransduction, impacting EC phenotype [124]. The magnitude of stress and strain is partly determined by the wall stiffness, which in turn influences vessel compliance, defined as the change in arterial volume relative to the change in pressure. Compliance impacts blood flow through the vessel and subsequently the WSS exerted at the blood–endothelium interface [53, 321]. The biomechanics of coronary artery grafts should therefore emulate that of the native coronary artery wall in order to support healthy EC function.

Many VMMs have been developed over the last few decades, yet few have been characterised with the constitutive equations needed to capture the complex mechanical behaviour of the artery wall [9]. Arteries are hyperelastic, viscoelastic

and anisotropic [62, 225, 322]. Their response to loading under pulsatile blood flow is both strain-dependent and direction dependent; the stiffness not only increases at large strain, but is higher along the longitudinal direction of the vessel. This behaviour is driven by the arrangement of stiff (collagen) and elastic (elastin) fibrils in the three layers of the artery wall. Each layer fulfils a specific task. As the luminal layer, the intima supports the endothelium. It is generally thought that the media is responsible for arterial wall properties at physiological pressure [28, 323, 324]. However, studies in aged human coronary arteries suggest that the intima bears more load in arteries with non-atherosclerotic intimal thickening [288]. Meanwhile, the outermost layer, the adventitia, prevents overdistension.

It is reasonable to assume that a single-layer, homogeneous vascular graft could not sufficiently replicate all of the complex properties of the artery wall. Instead, multi-layered grafts could overcome the mechanical simplicity of homogeneous VMMs by mimicking the structure–function relationship of the individual artery wall layers [150]. Tri-layered artery grafts have been manufactured and tested *in vitro* [325] and *in vivo* [240, 326, 327]. For instance, biomimetic vascular scaffolds with enhanced tensile strength and burst pressure response have been obtained by supporting porous medial layers with adventitia-mimicking VMMs such as PCL [326] and polyurethane [327]. PCL and polyurethane have high ultimate stresses and provide mechanical stability to the outer wall of the graft. Meanwhile, by changing the thickness of the medial layer of triple-layered polyurethane scaffolds, the compliance can be tailored to match that of sheep carotid artery [240].

Tubular tri-layered PVA cryogel-based vascular grafts have been manufactured through casting [267] and dip-coating [245, 268]. Interestingly, despite PVA/gelatin cryogel being acknowledged as a VMM with improved haemocompatibility compared with pure PVA cryogel, no multi-layered PVA/gelatin grafts could be identified in

the literature. Taking inspiration from PVA cryogel grafts, casting and dip-coating could be used to manufacture of analogous multi-layered PVA/gelatin grafts. Alternatively, the design freedom afforded by sub-zero AM is well-suited to engineering grafts with structural complexity, including the three layers of the artery wall [15–17, 271].

Regardless of the manufacturing route chosen, there is scope for complementary computational design studies that predict which cryogel parameters can be optimised to target specific properties of the coronary artery wall. FEA is a versatile method for predicting the mechanical behaviour of arteries and prototype graft designs in a haemodynamic environment, allowing researchers to compute stress distributions through grafts and understand how material stresses are transmitted to the endothelium relative to native tissue [328, 329]. Thus, FEA has the potential to streamline the design of small diameter vascular grafts [280]. Computational optimisation schemes have been proposed in the design of other biopolymer-based vascular grafts to yield compliance-matched graft constructs [330, 331]. However, at present, no literature studies have used FEA to study the layer-specific biomechanics of PVA/gelatin grafts, nor modelled the compliance of PVA/gelatin grafts under physiological pressure. *In silico* studies of multi-layered PVA/gelatin grafts would provide insight into the transmural biomechanics of these grafts under physiological loads, as well as facilitate prediction of the mechanical behaviour of different coronary artery graft designs.

4.1.1 Aims and Objectives

This chapter aims to simulate the quasi-static biomechanical response of a hyperelastic, tri-layered FE model of a coronary artery graft, informed from the

experimental characterisation of PVA/gelatin cryogel performed in Chapter 3. These grafts could, in theory, be manufactured using sub-zero AM or casting techniques. The following objectives were set:

- Build a tri-layered, coronary artery FE model using hyperelastic parameters sourced from the literature;
- Assess the impact of different hyperelastic constitutive models on the simulated biomechanics of the coronary artery wall;
- Build a tri-layered, PVA/gelatin FE graft model using the Ogden and Yeoh parameters fitted in Chapter 3;
- Validate the transmural stress, transmural strain and compliance of multiple PVA/gelatin graft designs under physiological pressure against the native wall.

This research not only looks to expand the current literature surrounding PVA-based arterial grafts, but also presents a computational method that complements the experimental characterisation of hyperelastic VMMs for soft tissue engineering. In both cases, it is anticipated that FE modelling could extend current understanding of how stress, strain and compliance may alter the haemodynamic environment experienced by ECs, thereby helping guide the future design, manufacture and validation of tri-layered graft constructs for the treatment of coronary artery disease.

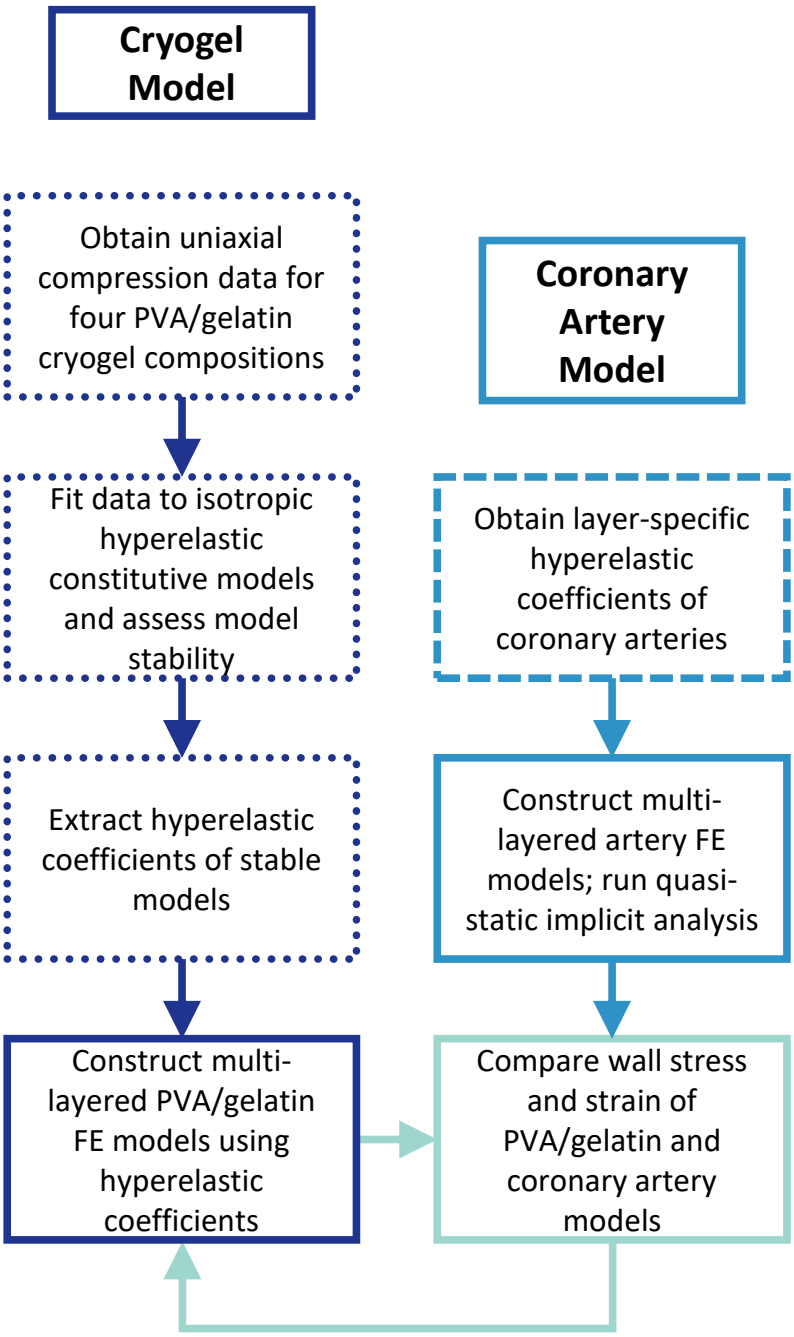


Figure 4.1: Workflow used to create tri-layered FE models. Dashed lines represent data obtained from the literature, while dotted lines represent the steps performed in Chapter 3.

4.2 Method

4.2.1 Overview

All multi-layer FE models were constructed in Abaqus/CAE 2021 (Dassault Systèmes, SIMULIA Corp., Johnston, RI, USA) using quasi-static implicit analyses. An overview of the computational workflow is given in Figure 4.1.

The hyperelastic behaviour of PVA/gelatin cryogel was previously determined using uniaxial compression test data from Chapter 3. The first order Ogden and Yeoh hyperelastic coefficients of four PVA/gelatin cryogel compositions were chosen for all subsequent FE analyses.

A control experiment replicating the native coronary artery wall was first performed to provide a benchmark for PVA/gelatin graft behaviour under physiological load. The layer-specific hyperelastic behaviour of human coronary arteries with non-atherosclerotic intimal thickening was determined experimentally by Holzapfel *et al*. [288]. This data has since been fitted to polynomial [332], reduced polynomial [333] and Ogden [334] models for the simulation of coronary artery biomechanics. However, the rationale behind choosing a specific hyperelastic model to describe the wall layers is not commonly reported. To reflect the variety of hyperelastic models used in the literature, and to investigate the resulting differences in transmural stress and strain between them, three multi-layered FE models of the artery wall, one for each constitutive model, were constructed according to these literature values (Table 4.1). The results of transmural stress and strain were taken as nodal analysis paths through the thickness of the wall, as shown in Figure 4.2; the stress and strain distribution of the multi-layered PVA/gelatin constructs were

then compared to those of the three artery models.

4.2.2 FE Model

4.2.2.1 Geometry

The coronary artery was idealised as a straight cylindrical vessel partitioned into three concentric tissue layers. The thicknesses of the intima, media and adventitia were chosen according to experimental data on human coronary arteries (0.23, 0.30 and 0.34 mm, respectively) [288]. The artery was then embedded within a representative block of soft tissue to represent the surrounding connective tissues.

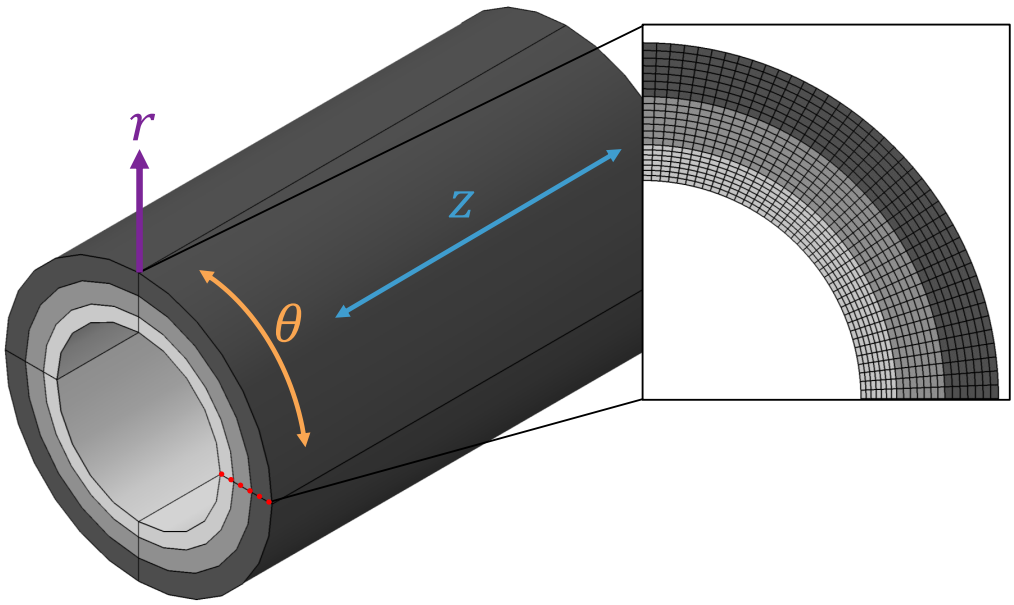


Figure 4.2: Discretised three-layer coronary artery wall. A cylindrical coordinate system was adopted using the three-dimensional coordinates r (radial), θ (circumferential) and z (axial). Each layer was meshed with seven layers of elements through the radial thickness; the nodal analysis path used to extract field variable values from the model is highlighted by the red dotted line.

4.2.2.2 Boundary Conditions

Using radial (r), circumferential (θ) and axial (z) cylindrical coordinates (Figure 4.2), the outer circumferential surface of the soft tissue was constrained in all six degrees of freedom (encastre). The inlets of the soft tissue and each tissue layer were also constrained axially. This allowed the artery to expand freely in both the radial and circumferential directions. The load was applied radially to the luminal surface of the model using two analysis steps: an 80 mmHg pressure load was first applied to represent diastolic blood pressure, and an additional 40 mmHg was applied to reach a systolic blood pressure of 120 mmHg.

A convergence study was performed to ensure that the values of wall stress and strain remained independent of the encastre boundary conditions. Shown for stress in Figure 4.3, the ratio of soft tissue diameter, D_{tissue}, to artery diameter, D_{artery}, was varied from 3:1 to 96:1. A D_{tissue}:D_{artery} ratio of 24:1 was used going forward ($D_{\text{tissue}} = 108$ mm and $D_{\text{artery}} = 4.5$ mm) to strike the balance between convergence and physiological relevance.

To replicate the behaviour between heterogeneous tissue and material boundaries (as opposed to a homogeneous construct), the following interface constraints were applied. The contact between each tissue layer was modelled using surface-to-surface interactions with hard penalty contact constraints. Under the quasi-static luminal pressures applied in these simulations, there will be no relative radial motion between the interfacing surfaces assuming these constraints. To enable circumferential motion, yet also prevent unconstrained sliding, static friction coefficients were used to model the behaviour between interfacing arterial tissue and PVA/gelatin layers. There is very limited research exploring the interactions between the surfaces of artery wall layers, the surfaces of hydrogels

and the surfaces between soft tissues and hydrogels. In their balloon angioplasty analysis, Mortier *et al.* [335] applied a friction coefficient of 0.2 between all contact pairs. While the friction between interfacing PVA layers has not been reported, the biotribological behaviour of PVA and titanium alloy yielded a friction coefficient of ≈ 0.04 [306]. These estimated values were applied herein.

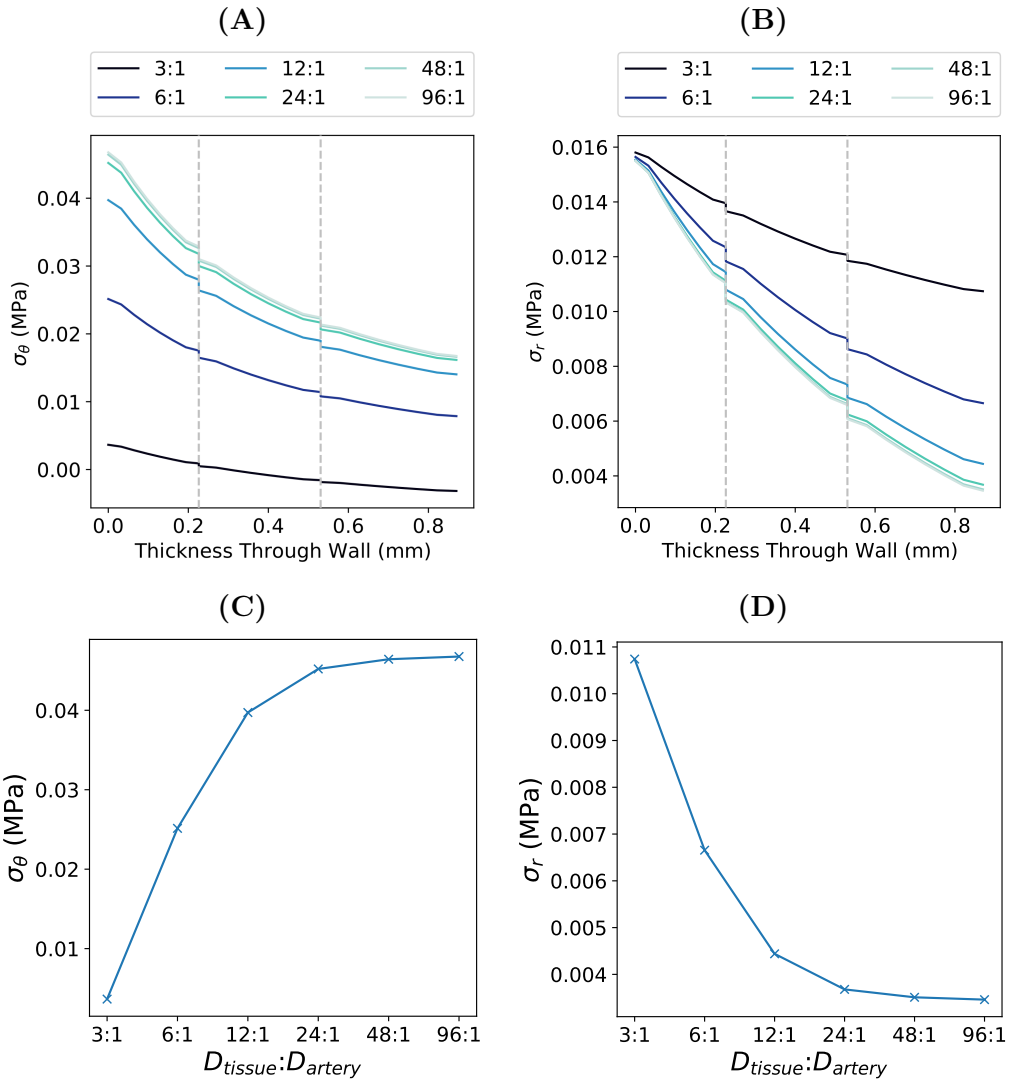


Figure 4.3: Boundary condition convergence study performed at systolic pressure using first order Ogden P_9G_1-A-C coefficients for all three tissue layers (tissue interfaces are represented by grey dashed lines). **(A)** σ_θ and **(B)** σ_r profiles through the thickness of the wall; **(C)** Convergence of luminal σ_θ; **(D)** Convergence of σ_r at the adventitia–tissue interface.

4.2.2.3 Mesh

The artery and surrounding soft tissue were discretised using solid linear hexahedral (C3D8RH) elements. Hybrid (H) element were used to prevent volumetric locking, while reduced integration (R) elements were chosen to account for geometric non-linearity. A mesh convergence study was conducted to ensure that the values of stress obtained were independent of mesh density (Figure 4.4). The resulting mesh contained a total of 171,200 elements, with an edge length of 0.36 mm, for the wall layers. Each layer contained seven layers of elements through the radial thickness (Figure 4.2).

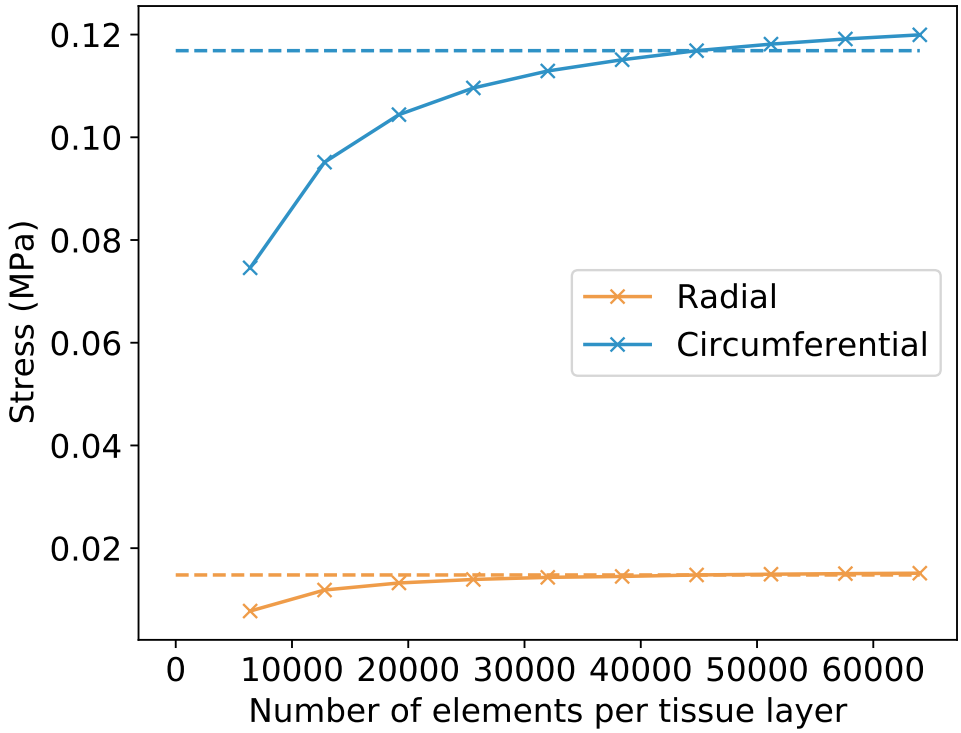


Figure 4.4: Mesh convergence study performed using third order Ogden coronary artery coefficients at systolic pressure. Convergence was achieved when the luminal stress increased less than 2% relative to the previous mesh size (dashed lines).

4.2.2.4 Material Properties

Table 4.1: Layer-specific hyperelastic material coefficients obtained from the literature, derived from hyperelastic isotropic constitutive models fitted to coronary arterial tissue.

MATERIAL PARAMETERS				
Material Model	**Intima**	**Media**	**Adventitia**	**From Study**
Polynomial	$C_{10} = -0.204$ MPa	$C_{10} = -0.117$ MPa	$C_{10} = -0.189$ MPa	[332]
	$C_{01} = 0.223$ MPa	$C_{01} = 0.128$ MPa	$C_{01} = 0.202$ MPa	
	$C_{20} = 1.37$ MPa	$C_{20} = 0.224$ MPa	$C_{20} = 0.459$ MPa	
	$C_{11} = -3.71$ MPa	$C_{11} = -0.672$ MPa	$C_{11} = -1.38$ MPa	
	$C_{02} = 2.67$ MPa	$C_{02} = 0.569$ MPa	$C_{02} = 1.34$ MPa	
Reduced Polynomial	$C_{10} = 6.79\times10^{-3}$ MPa	$C_{10} = 6.52\times10^{-3}$ MPa	$C_{10} = 8.27\times10^{-3}$ MPa	[333]
	$C_{20} = 0.54$ MPa	$C_{20} = 4.89\times10^{-2}$ MPa	$C_{20} = 1.20\times10^{-2}$ MPa	
	$C_{30} = -1.11$ MPa	$C_{30} = 9.26\times10^{-3}$ MPa	$C_{30} = 0.52$ MPa	
	$C_{40} = 10.65$ MPa	$C_{40} = 0.76$ MPa	$C_{40} = -5.63$ MPa	
	$C_{50} = -7.27$ MPa	$C_{50} = -0.43$ MPa	$C_{50} = 21.44$ MPa	
	$C_{60} = 1.63$ MPa	$C_{60} = 8.69\times10^{-2}$ MPa	$C_{60} = 0$ MPa	
Ogden	$\mu_1 = -5.70$ MPa	$\mu_1 = -1.84$ MPa	$\mu_1 = -1.99$ MPa	[334]
	$\mu_2 = 3.58$ MPa	$\mu_2 = 1.12$ MPa	$\mu_2 = 1.20$ MPa	
	$\mu_3 = 2.17$ MPa	$\mu_3 = 0.73$ MPa	$\mu_3 = 0.81$ MPa	
	$\alpha_1 = 24.43$	$\alpha_1 = 21.71$	$\alpha_1 = 24.61$	
	$\alpha_2 = 25.00$	$\alpha_2 = 22.00$	$\alpha_2 = 25.00$	
	$\alpha_3 = 23.24$	$\alpha_3 = 21.20$	$\alpha_3 = 23.90$	
	$D_1 = 0.85$	$D_1 = 4.11$	$D_1 = 3.92$	

Layer-specific hyperelastic coefficients of human coronary arteries were obtained from the literature and are listed in Table 4.1. The surrounding soft tissue was modelled as a Hookean linearly elastic material with a Young's modulus of 0.05 MPa and a Poisson's ratio of 0.49 [336]. Both the artery wall layers and the surrounding tissue were modelled using an average value of density for soft tissue (1040 kg m^{-3}) according to a previous study [336].

The hyperelastic coefficients and densities of P_9G_1-A-C, P_9G_1-A-NC, P_9G_1-B-C and P_9G_1-B-NC were taken from Chapter 3; for convenience, the material properties are reprinted in Table 4.2. A Poisson's ratio of 0.49 was assumed to reflect the near-incompressibility of PVA cryogel [266].

Table 4.2: First order Ogden and Yeoh constitutive parameters fitted to PVA/gelatin compression data and densities of all PVA/gelatin cryogel compositions in Chapter 3 (mean ± SD).

FIRST ORDER OGDEN CONSTITUTIVE PARAMETERS				
	P_9G_1-A-C	**P_9G_1-A-NC**	**P_9G_1-B-C**	**P_9G_1-B-NC**
μ_1 **(MPa)**	0.0444 ± 0.0060	0.0374 ± 0.0042	0.0276 ± 0.0010	0.0227 ± 0.0025
α_1	7.116 ± 0.528	6.553 ± 0.276	7.765 ± 0.493	7.311 ± 0.581
μ_0 **(MPa)**	0.157 ± 0.016	0.122 ± 0.012	0.107 ± 0.009	0.083 ± 0.011
r^2	0.9994 ± 0.0004	0.9988 ± 0.0008	0.9994 ± 0.0003	0.9988 ± 0.0008
YEOH CONSTITUTIVE PARAMETERS				
	P_9G_1-A-C	**P_9G_1-A-NC**	**P_9G_1-B-C**	**P_9G_1-B-NC**
C_{10} **(MPa)**	0.0205 ± 0.0035	0.0180 ± 0.0024	0.0126 ± 0.0006	0.0108 ± 0.0014
C_{20} **(MPa)**	0.0015 ± 0.0028	−0.0015 ± 0.0019	0.0015 ± 0.0014	−0.0007 ± 0.0007
C_{30} **(MPa)**	0.0042 ± 0.0017	0.0044 ± 0.012	0.0032 ± 0.0006	0.0033 ± 0.0009
μ_0 **(MPa)**	0.0410 ± 0.0070	0.0360 ± 0.0049	0.0252 ± 0.0012	0.0217 ± 0.0027
r^2	0.9994 ± 0.0008	0.9984 ± 0.0009	0.9997 ± 0.0002	0.9985 ± 0.0007
DENSITY				
	P_9G_1-A-C	**P_9G_1-A-NC**	**P_9G_1-B-C**	**P_9G_1-B-NC**
ρ **(kg m^{-3})**	1080 ± 36	1190 ± 16	1070 ± 37	1120 ± 38

4.2.3 Field Variable Extraction for Stress/Strain Analyses

For all models investigated in this study, three outcomes of interest were highlighted for extraction:

- Transmural stress/strain distribution at a set pressure (systolic pressure);
- Transmural stress/strain distribution as a function of pressure;
- The absolute compliance of the graft between systolic and diastolic pressure.

In the first instance, the nodal analysis path depicted in Figure 4.5 was used to extract stress and strain field variables from the step increment corresponding to

systolic pressure. By relating the position of each node in the nodal analysis path to its position in the wall, the stress or strain at that node was plotted with respect to wall thickness, as demonstrated in Figure 4.5.

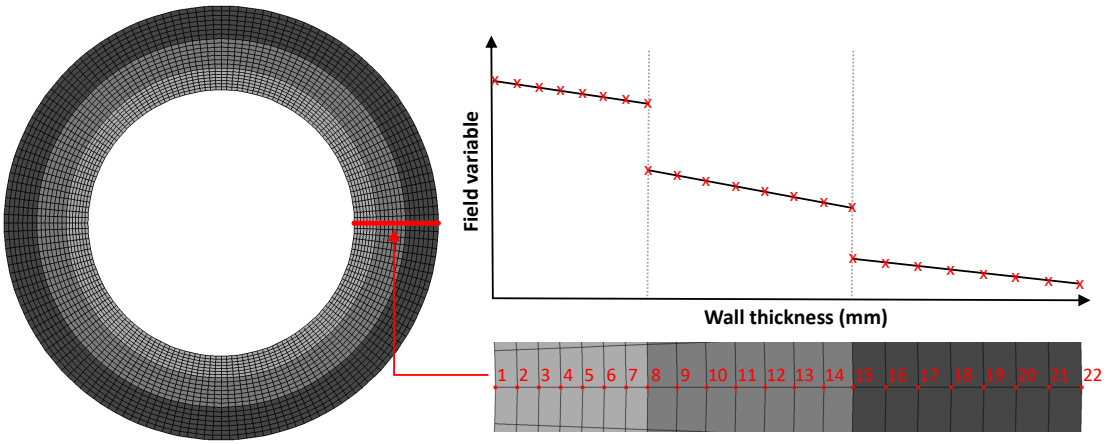


Figure 4.5: Schematic of the nodal analysis path used to extract stress and strain values with respect to wall thickness. Representative node labels are shown in red; dashed lines represent the boundaries between tissue layers.

To obtain transmural stress/strain as a function of pressure, stress and strain were extracted using the same nodal analysis path in Figure 4.5. However, instead of extracting the data at only systolic pressure, the data were extracted at each step increment of the simulation. Depending on the field variable of interest, this generated stress–pressure or strain–pressure curves for each of the nodes along the nodal analysis path. To gain insight into the layer-specific stress/strain distribution under physiological loading, the stress–pressure/strain–pressure curves for all nodes within a given wall layer were averaged to give the mean circumferential stress (σ_θ), mean circumferential strain (ϵ_θ), mean radial stress (σ_r) and mean radial strain (ϵ_r) for the intima, media and adventitia. This process is demonstrated for the mean σ_θ of the medial layer of Ogden-derived coronary artery model in Figure 4.6.

As the lumen volume did not vary in the longitudinal direction, the 2D

cross-sectional compliance (CC, units: $\frac{mm^2}{mmHg}$) was calculated as the absolute change in cross-sectional area A between diastolic (80 mmHg) and systolic (120 mmHg) pressure (Equation 4.1).

$$CC = \frac{\Delta A}{\Delta P} \tag{4.1}$$

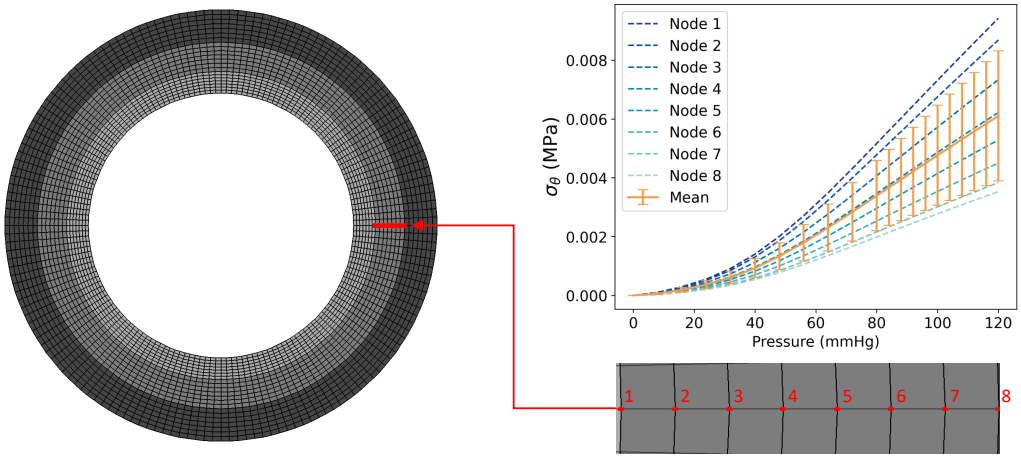


Figure 4.6: Example schematic of the individual and mean stress–pressure curves obtained for the medial layer of the Ogden-derived coronary artery model.

4.2.4 Relative Difference Calculation

The relative differences in transmural stress and strain distribution between the synthetic grafts and arterial models ($\sigma_{\theta,r(diff)}$ and $\epsilon_{\theta,r(diff)}$) at 120 mmHg pressure were calculated using Equation 4.2.

$$\sigma, \epsilon_{\theta,r(diff)} = \frac{\sigma, \epsilon_{\theta,r(PVA/gelatin)} - \sigma, \epsilon_{\theta,r(artery)}}{\sigma, \epsilon_{\theta,r(artery)}} \times 100\% \tag{4.2}$$

4.3 Results

4.3.1 Comparison of Coronary Artery Transmural Biomechanics

The tri-layer FE model was first run using layer-specific hyperelastic material coefficients fitted to coronary artery tissue (Table 4.1). The strain response of each layer of the artery models showed a non-linear relationship with pressure across the 0-–120 mmHg pressure range. Demonstrated for the circumferential strain (ϵ_θ) of the intima in Figure 4.7, this indicates a strain-stiffening response at higher physiological pressures, a phenomenon well documented experimentally [27, 337]. Analogous behaviour was observed for $\epsilon_{(r,intima)}$ (Figure 4.8). To prevent repetition, $\epsilon_{(\theta,media)}/\epsilon_{(r,media)}$ and $\epsilon_{(\theta,adventitia)}/\epsilon_{(r,adventitia)}$ are included in Appendix B (Figures B.1 and B.2). The response was approximately linear between diastole (80 mmHg) and systole (120 mmHg). Furthermore, the difference in ϵ_θ between each model was largest at systolic pressure: for example, $\epsilon_{(\theta,intima)} = 0.14 \pm 0.01$, 0.15 ± 0.01 and 0.19 ± 0.02 MPa in the polynomial, reduced polynomial and Ogden models, respectively. A similar trend was observed for ϵ_r ($\epsilon_{(r,intima)} = 0.13 \pm 0.01$, 0.13 ± 0.01 and 0.15 ± 0.01 MPa, respectively).

The circumferential stress (σ_θ) and radial stress (σ_r) at systolic pressure, as a function of radial wall thickness, are displayed in Figure 4.9. For all three coronary artery models, the distribution of σ_θ was non-uniform across the three tissue layers (Figure 4.9A). Each model demonstrated maximum σ_θ at the luminal surface, followed by a marked decrease at the intima–media interface. Of the three models, the maximum value of σ_θ was lower in the polynomial model ($\sigma_\theta = 0.079$ MPa) than

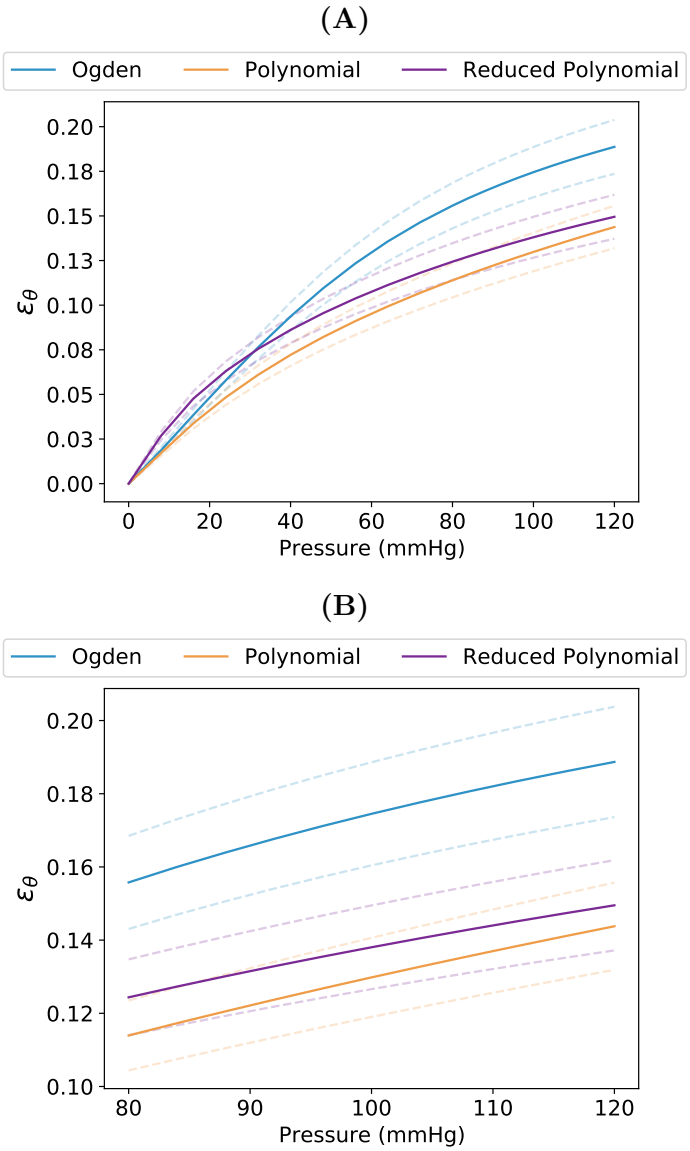


Figure 4.7: Mean ϵ_θ of the coronary intima between **(A)** 0–120 mmHg pressure and **(B)** 80–120 mmHg pressure (dashed lines show the SD for each model).

in the Ogden ($\sigma_\theta = 0.117$ MPa) and reduced polynomial ($\sigma_\theta = 0.126$ MPa) models. Though a further increase in σ_θ was observed between the media and adventitia in the Ogden and polynomial models, the σ_θ transitioned continuously across the media–adventitia interface in the reduced polynomial model.

The effects of compressive stresses through the wall cannot be neglected as the artery has a radius-to-thickness ratio of less than 10, necessitating the thick-walled

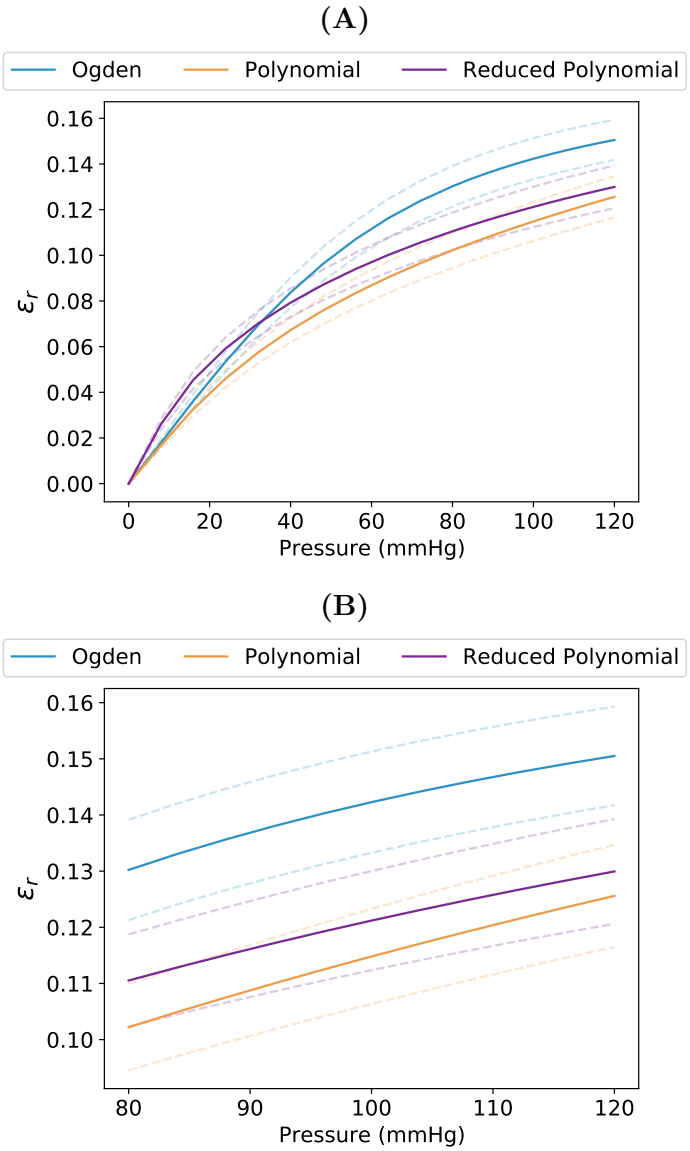


Figure 4.8: Mean ϵ_r of the coronary intima between **(A)** 0–120 mmHg pressure and **(B)** 80–120 mmHg pressure (dashed lines show the SD for each model).

assumption. In all cases, σ_r was an order of magnitude lower than σ_θ and decreased with increasing distance from the luminal surface (Figure 4.9B).

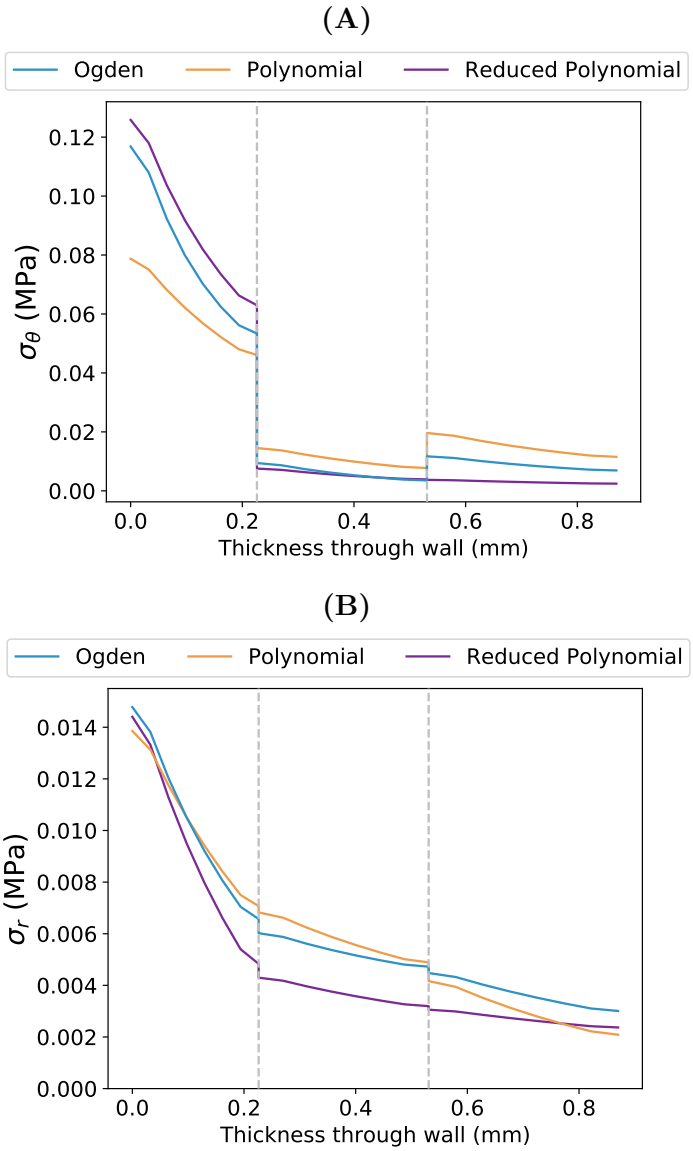


Figure 4.9: **(A)** σ_θ and **(B)** σ_r profiles for each coronary artery model at systolic pressure. Grey dashed lines represent the intima–media and media–adventitia interfaces.

4.3.2 PVA/Gelatin Graft Design Validation

Based on the transmural trends observed from the coronary artery models in Section 4.3.1, the following targets were set for the PVA/gelatin graft constructs:

- for σ_θ, $\sigma_{(\theta,intima)} > \sigma_{(\theta,media)} \leq \sigma_{(\theta,adventitia)}$;

Table 4.3: PVA/gelatin (PG) compositions used in the four iterations of the PVA/gelatin tri-layered FE model.

	PG–1	**PG–2**	**PG–3**	**PG–4**
Intima	P_9G_1-A-C	P_9G_1-A-C	P_9G_1-A-C	P_9G_1-A-C
Media	P_9G_1-B-NC	P_9G_1-B-NC	P_9G_1-B-NC	P_9G_1-B-NC
Adventitia	P_9G_1-A-C	P_9G_1-A-NC	P_9G_1-B-C	P_9G_1-B-NC

- for σ_r, $\sigma_{(r,intima)} > \sigma_{(r,media)} > \sigma_{(r,adventitia)}$;
- for ϵ_θ and ϵ_r, strain-stiffening should occur between 0–120 mmHg pressure.

The original test data of Holzapfel et al. [288] and the results from Section 4.3.1 of this study showed that the coronary intima displays substantial mechanical strength and load-bearing properties. By contrast, the media was the softest of the three tissue layers. The intima was therefore set to the stiffest PVA/gelatin composition (P_9G_1-A-C), and the media was set to the most compliant PVA/gelatin composition (P_9G_1-B-NC), using the Ogden and Yeoh parameters fitted in Section 4.3.1. The adventitia was then varied across the four cryogel compositions tested in the study (Table 4.3).

The distributions of σ_θ, ϵ_θ, σ_r, and ϵ_r demonstrate a qualitative correlation between the histologically derived coronary artery models (Figures 4.7–4.9) and the synthetic graft designs (Figures 4.11 and 4.12). Figure 4.10 shows the σ_θ contour maps of the four PVA/gelatin graft designs outlined in Table 4 at systolic pressure. σ_θ was largest at the luminal surface of all four grafts, comparable to the location of maximum σ_θ in the three coronary artery models. Moreover, σ_θ decreased across the intima—media interface (Figure 4.11).

Grafts PG–1, PG–2 and PG–3 replicate the behaviour of a tri-layered

system, with an increase in circumferential stiffness provided by the adventitial layer. This mimics the behaviour of the Ogden and polynomial coronary artery models (Figure 4.9). The distribution of σ_θ was discontinuous at the media–adventitia interface; $\sigma_{(\theta,adventitia)}$ increased with increasing stiffness of adventitia mimicking material (PG–1 > PG–2 > PG–3). Meanwhile, $\sigma_{(\theta,intima)}$ decreased (Figure 4.11B). This suggests that increasing the stiffness of the adventitia relieved some of the stress from the intima and shifted the distribution of σ_θ from the intima to the adventitia (and, simultaneously, ϵ_θ was reduced across all three tissue layers). On the other hand, PG–4 displayed no discernible change in stiffness between the media and adventitia. Instead, PG–4 behaved like a bi-layered graft consisting of a stiff intima and compliant media–adventitia with biomechanics akin to the reduced polynomial coronary artery model. As the graft with the most compliant adventitia mimic, PG-4 exhibited the highest maximum σ_θ and ϵ_θ of the four designs.

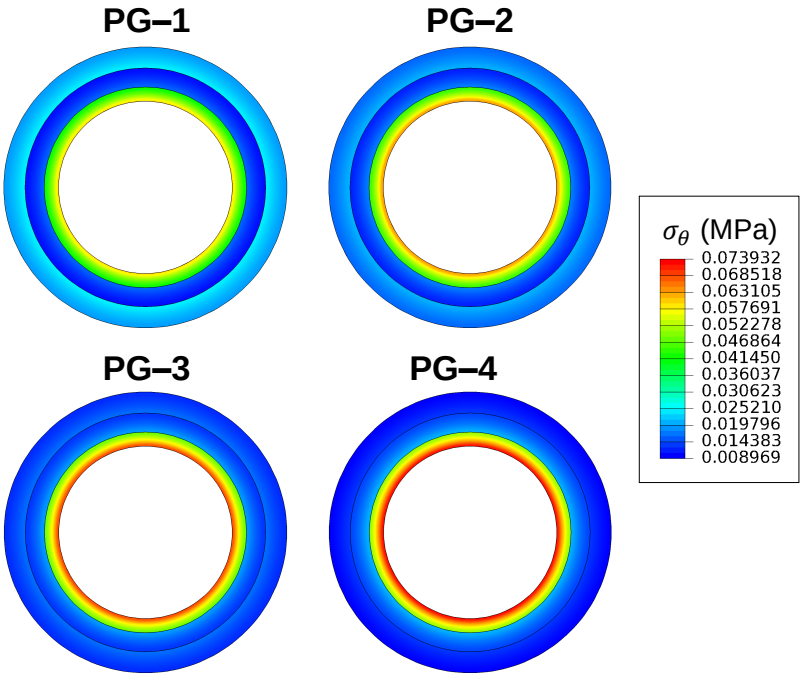


Figure 4.10: σ_θ contour maps of each PVA/gelatin graft using Ogden parameters. Analogous Yeoh σ_θ contour maps are displayed in Figure B.3.

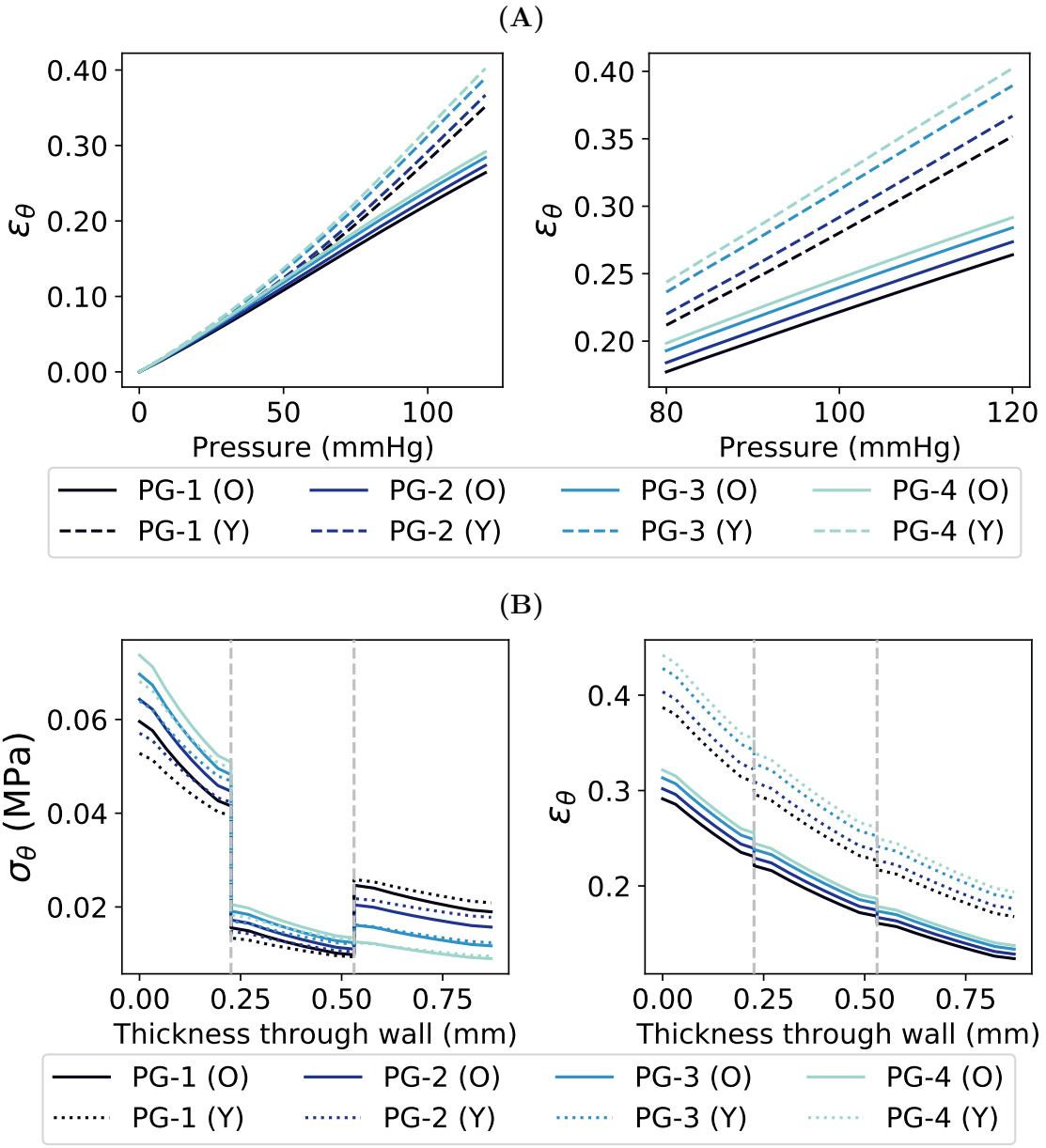


Figure 4.11: The circumferential biomechanics of PVA/gelatin grafts at systolic pressure. **(A)** The mean ϵ_θ of the PVA/gelatin graft intima between 0–120 and 80–120 mmHg pressure (error bars have been omitted for clarity), modelled using Ogden (solid lines) and Yeoh (dashed lines) hyperelastic parameters. **(B)** σ_θ and ϵ_θ profiles through the radial thickness of each PVA/gelatin graft design. Grey dashed lines represent the intima–media and media–adventitia interfaces.

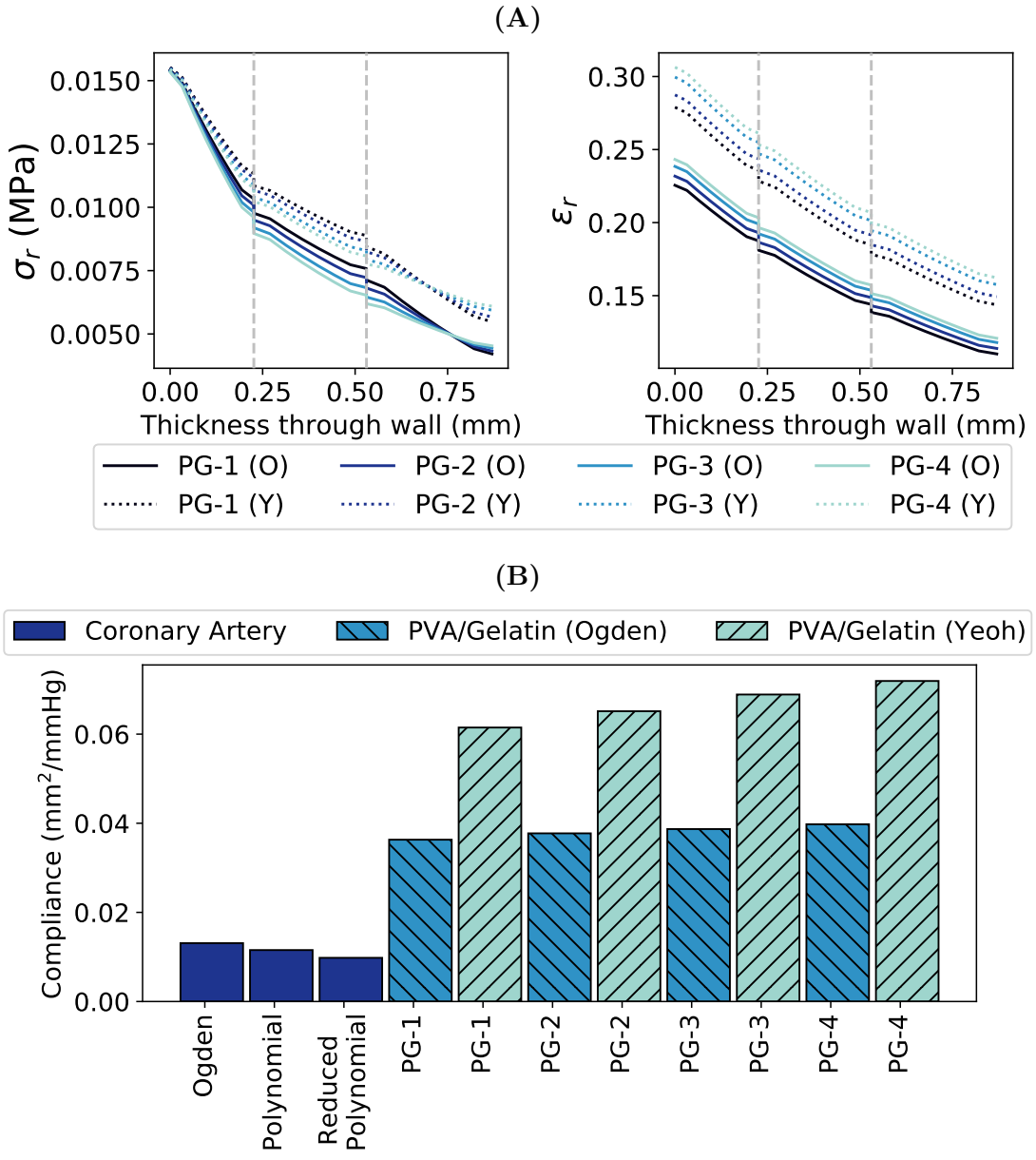


Figure 4.12: The radial biomechanics of PVA/gelatin grafts at systolic pressure. **(A)** σ_r and ϵ_r profiles through the radial thickness of each PVA/gelatin graft design, modelled using Ogden (solid lines) and Yeoh (dashed lines) hyperelastic parameters. Grey dashed lines represent the intima–media and media–adventitia interfaces; **(B)** Compliance of PVA/gelatin grafts compared with coronary artery models.

The mean ϵ_θ of the PVA/gelatin graft intima between 0–120 mmHg is shown in Figure 4.11A. Analagous trends were observed for $\epsilon_{(\theta,media)}$ and $\epsilon_{(\theta,adventitia)}$; for these, the reader is referred to Figures B.4 and B.5.

The radial biomechanics of PG–1, PG–2 and PG–3 mimicked that of the tri-layered coronary artery models. At approximately the same magnitude as the applied pressure (120 mmHg $\approx$ 0.016 MPa), σ_r was highest at the luminal surface of the graft with minor stepwise decreases between each tissue layer (Figure 4.12A). Equally, no change in the gradient of σ_r was observed between the media and adventitia of PG–4, comparable to the bi-layered artery model (Figure 4.9B).

For each bi- and tri-layered graft and its relevant artery model equivalent, stress and strain were on the same order of magnitude. However, there were some notable location-specific quantitative differences which varied in the degree of error. The relative differences in transmural stress and strain distribution between the synthetic grafts and arterial models ($\sigma_{\theta,r(diff)}$ and $\epsilon_{\theta,r(diff)}$) at 120 mmHg pressure are plotted in Figures 4.13–4.15. Key discrepancies were observed at the luminal surface of the grafts and the interfaces between tissue layers. These differences were compounded by the choice of hyperelastic model used to model both PVA/gelatin and the coronary artery. Focusing on σ_θ distribution, the magnitude of σ_θ at the luminal surface of PG–1, PG–2 and PG–3 when modelling the cryogels using Ogden parameters was 40–49% lower than that observed in the Ogden coronary artery model and 12–24% lower than that observed in the polynomial coronary artery model. Using Yeoh cryogel parameters, $\sigma_{\theta(diff)}$ at the same location were 45–55% and 19–33% lower, respectively. The luminal σ_θ of PG–4 closely resembled the reduced polynomial coronary artery model when using both Ogden and Yeoh PVA/gelatin parameters ($\sigma_{\theta(diff)}$ = 6–7%).

The absolute compliance of PVA/gelatin grafts decreased with increasing adventitial stiffness (PG-1 < PG-2 < PG-3 < PG-4, Figure 4.12B). However, the compliance of the PG-1 graft was more than double that observed for all three coronary artery models.

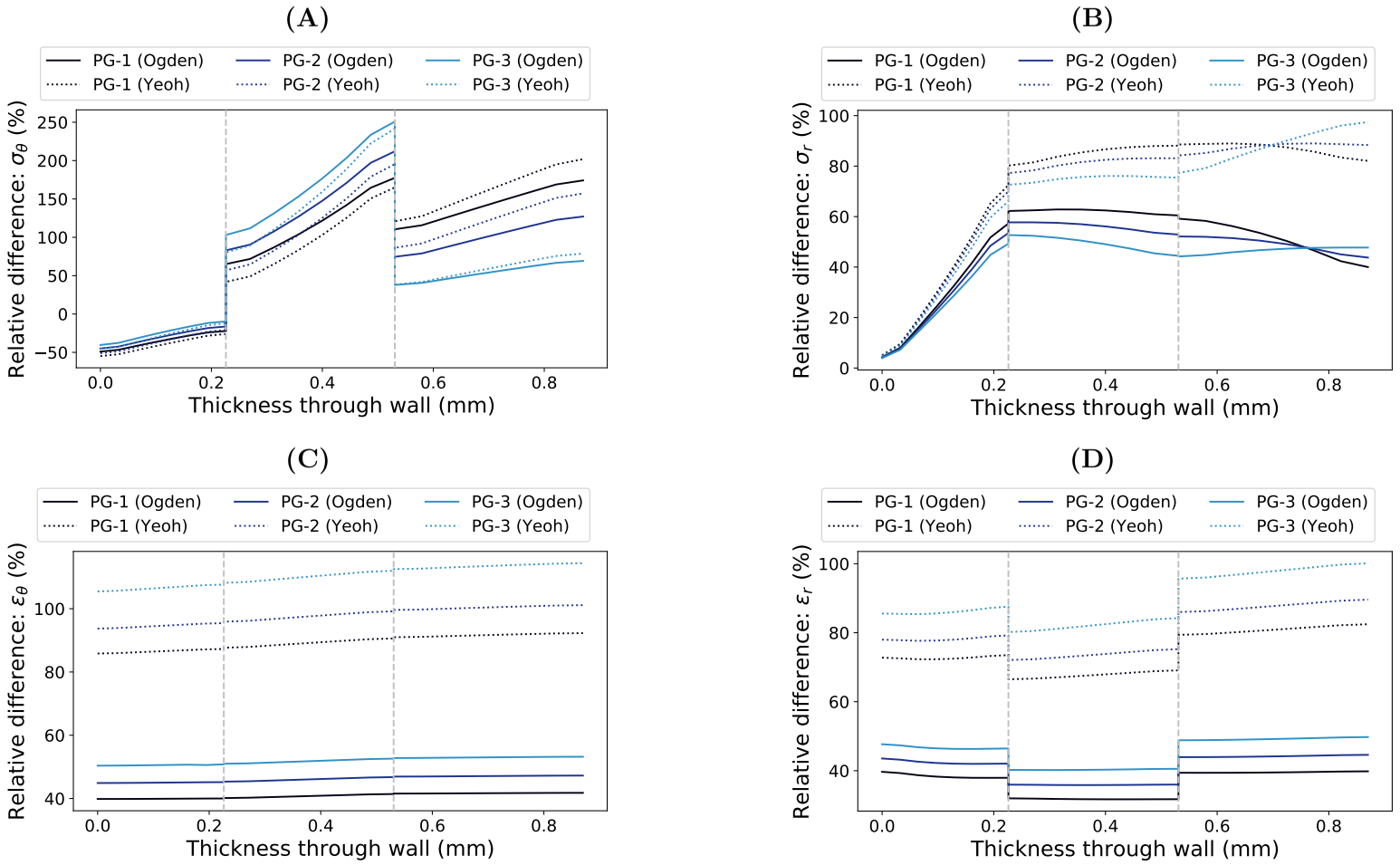


Figure 4.13: The relative difference (%) in **(A)** σ_θ, **(B)** σ_r, **(C)** ϵ_θ and **(D)** ϵ_r between tri-layered PVA/gelatin grafts and the Ogden coronary artery model. The solid and dotted lines represent PVA/gelatin grafts modelled using Ogden and Yeoh hyperelastic parameters, respectively. Grey dashed lines represent the intima—media and media-–adventitia interfaces.

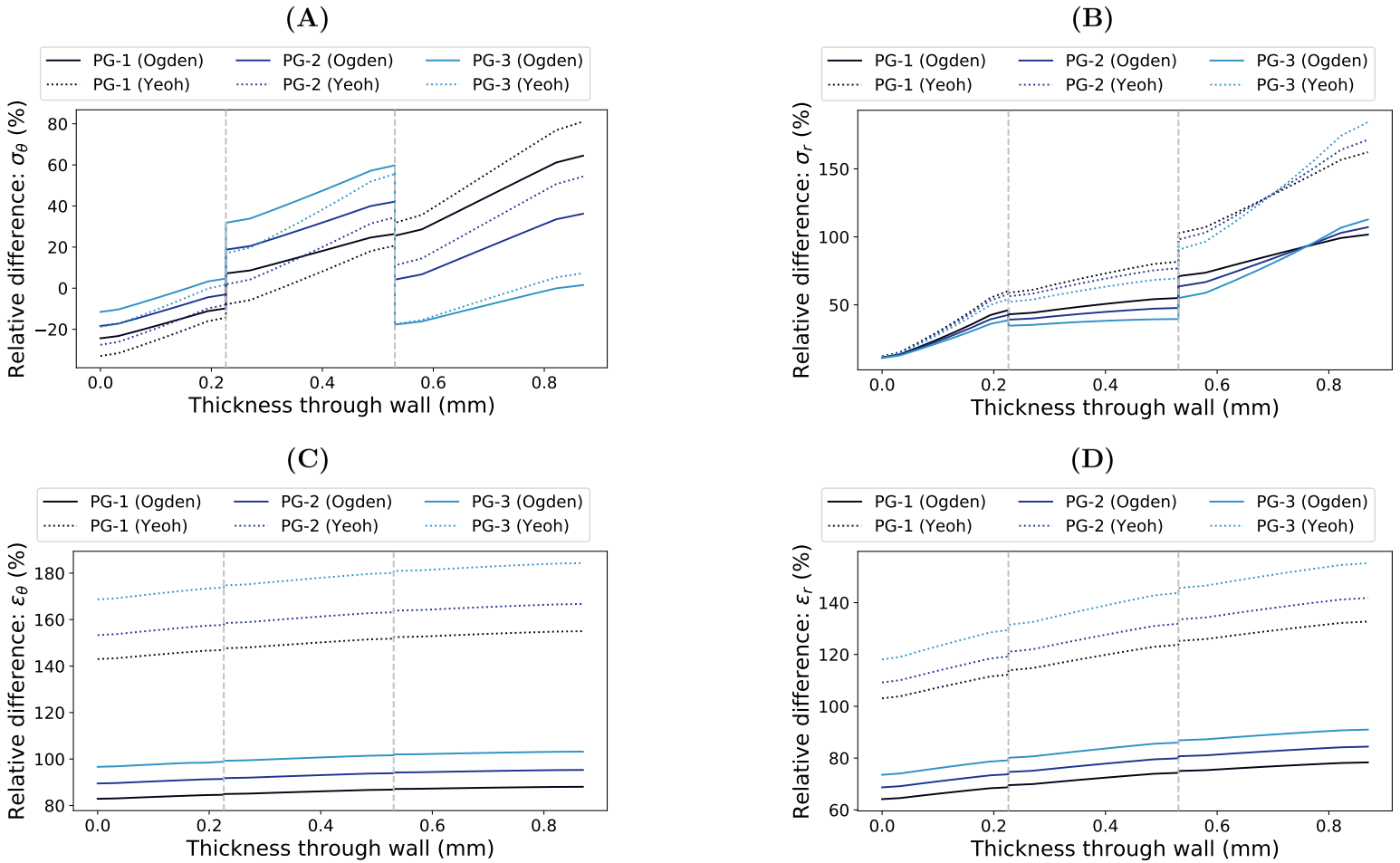


Figure 4.14: The relative difference (%) in **(A)** σ_θ, **(B)** σ_r, **(C)** ϵ_θ and **(D)** ϵ_r between tri-layered PVA/gelatin grafts and the polynomial coronary artery model. The solid and dotted lines represent PVA/gelatin grafts modelled using Ogden and Yeoh hyperelastic parameters, respectively. Grey dashed lines represent the intima—media and media-–adventitia interfaces.

Figure 4.15: The relative difference (%) in **(A)** σ_θ, **(B)** σ_r, **(C)** ϵ_θ and **(D)** ϵ_r between bi-layered PVA/gelatin graft PG–4 and the reduced polynomial coronary artery model. The solid and dotted lines represent PVA/gelatin grafts modelled using Ogden and Yeoh hyperelastic parameters, respectively. Grey dashed lines represent the intima—media and media–-adventitia interfaces.

4.4 Discussion

Tri-layered grafts are gaining traction in small-diameter blood vessel tissue engineering as a strategy to reduce the mechanical incompatibilities associated with homogeneous grafts [150]. In addition, PVA/gelatin cryogel has been highlighted as a haemocompatible VMM whose mechanical properties can not only be tuned to the ranges reported for arterial tissue, but has the potential to be manufactured into tri-layered constructs using casting [267], dip-coating [245, 268] or sub-zero AM [15–17, 271]. FE analysis has the potential to rapidly accelerate the design process for engineering biomimetic synthetic grafts by highlighting the parameters which promote specific mechanical behaviours [23]. However, its use in the design and validation of multi-layered synthetic arterial grafts is relatively uncommon, and was unexplored for PVA/gelatin cryogel grafts prior to this thesis. Section 4.4.1 reviews the key discussion points pertaining to the FEA of the coronary artery wall, while Section 4.4.2 relates the biomechanical behaviours reported for the four PVA/gelatin graft designs to the benchmarks set by the native vessel. Finally, Section 4.4.3 will address study limitations and highlight future steps to increase model complexity and facilitate improvement of coronary artery graft optimisation through experimentally-informed FEA.

4.4.1 Simulating the Biomechanics of the Coronary Artery Wall

Arterial wall stiffness is commonly probed using uniaxial and biaxial testing; for coronary arteries, the values range hugely from 0.9 kPa to 10 MPa [9]. The experimental work of Holzapfel *et al.*, which examined the layer-specific mechanical

properties of human coronary arteries under tension [288], remains the basis of many computational studies where layer-specific wall properties are relevant to the simulation [332–334, 338–341]. In all cases, a phenomenological approach was used to curve fit the experimental test data and extract the hyperelastic coefficients that best capture the "J"-shaped hyperelastic stress–strain curve. The optimal model is the one which provides the best fit across the required strain range. However, these cited studies differ in the material constitutive law used to fit the same experimental data. The rationale behind hyperelastic model choice is not always stated. Furthermore, the impact of hyperelastic model choice on the desired FE outputs is rarely investigated or compared. This study sought to address the variety of hyperelastic models used to model arterial tissue, and in doing so has highlighted the difference in transmural stress and strain, and subsequently compliance, using three isotropic strain energy density constitutive equations based on the same experimental data.

The results indicate that both circumferential (tensile) and radial (compressive) stress and strain primarily act upon the intimal layer of coronary arteries with non-atherosclerotic intimal thickening, regardless of hyperelastic model used. However, while the stiffness of each of the three layers was distinct when using the Ogden and polynomial models, the reduced polynomial model behaved like a bi-layered wall consisting of an intima and combined media–adventitia layer. These results not only have implications in the assessment of synthetic grafts, where arterial wall properties are needed as a benchmark for their performance [275], but for any FE model aiming to replicate the quasi-static biomechanics of the coronary artery wall. This is particularly relevant when modelling (or mimicking) mechanotransduction in the endothelium, as the forces generated by stress and strain within the wall play a concerted role in mediating healthy and disease-related endothelial cell behaviour [114]. For instance, numerical analysis has shown that transmural pressure influences

low-density lipoprotein accumulation across the intima and media, a key process in the progression of atherosclerotic plaques [342]. Yet, the impact of the constitutive model used for these tissue layers was not discussed.

The stress–strain results of all three coronary artery models study aligned with the experimental data from which the hyperelastic parameters were fitted: at physiological pressures, in coronary arteries with non-atherosclerotic thickening, the intima was largely responsible for the mechanical strength of the coronary artery [288]. It displayed the highest stiffness of all three tissue layers and bore the brunt of both circumferential (tensile) and radial (compressive) stresses. At the intima—media interface, σ_θ dropped an order of magnitude while the gradient of σ_r decreased substantially. The contributions of the two layers to the mechanical properties of the wall must therefore be considered separately. This is in contrast to studies performed using porcine coronary artery data, where the intima and media are generally analysed as a combined intima—media layer [323, 324]. These results reflect the limitations associated with using such bi-layered models (i.e. models comprised of intima-–media and adventitia) as the basis to develop functional coronary artery grafts.

4.4.2 Comparison of Coronary Artery and PVA/Gelatin Graft Biomechanics

FE analysis has shown that, by keeping the composition of PVA/gelatin cryogel fixed across the intima and media and varying the stiffness of the adventitia, hyperelastic bi- or tri-layered synthetic grafts of variable mechanical stiffness can be constructed. Qualitatively, PG–4 (where the same cryogel composition is used as both the media and adventitia mimic) captured the behaviour of the bi-layered reduced polynomial

arterial model, while PG–1, –2 and –3 resembled the tri-layered Ogden and polynomial arterial models. Mimicking the additional stiffness provided by the adventitia in the tri-layered models was achieved by choosing a cryogel composition where $\sigma_{(\theta,adventitia)} > \sigma_{(\theta,media)}$; this has been accomplished by increasing the M_w of PVA and/or employing polymer coagulation to increase the crystalline domain of PVA. Crucially, increasing the stiffness of the adventitia mimicking material influenced the transmural distribution of stress and strain in the graft. σ_θ distribution was reduced in the intima and increased in the adventitia. This behaviour matches that reported by McClure *et al.*, who used mathematical modelling to assess the layer-specific σ_θ distribution of electrospun grafts [275]. They determined that an increase in medial or adventitial stiffness (in their case, defined by E) would cause the stress distribution in the respective layer to increase while simultaneously causing a downward shift in the intima [275]. While this study has focused on PVA/gelatin grafts, the importance of layer stiffness is translatable to other hyperelastic VMMs and should be considered when designing any multi-layered graft.

Quantitatively, several differences are observed in the stress—strain behaviour of the synthetic grafts and arterial tissue. Despite strain increasing linearly between diastole and systole in both the artery and synthetic models, the coronary artery exhibited significant strain stiffening at pressures below diastole. PVA/gelatin, however, did not; at systolic pressure, the ϵ_θ and ϵ_r of PVA/gelatin grafts reached up to double that in native tissue. Furthermore, the relative error between graft and artery was highly sensitive to the constitutive models used to describe them.

The compliance of all four synthetic grafts at physiological pressure was notably higher than the compliance of each coronary artery model. Compliance values are lacking in the majority of multi-layered artery graft literature, despite it being a critical parameter in determining graft success [150]. From the perspective

of shear stress exerted at the blood—endothelium interface, mismatched wall compliance changes the cross-sectional area of the vessel and thus flow through the vessel, particularly at anastomoses. As compliance is inversely proportional to the graft diameter [108], overly compliant grafts may generate abnormally low levels of WSS that, once sensed by ECs, may activate signalling cascades (eg increased production of inflammatory cytokines) that drive pathogenic, mechanically-induced vascular remodelling. In addition, excessive circumferential stretch may also trigger inflammatory cascades that, if maintained over a prolonged period of time, lead to EC stiffening [124]. Given the impact that manufacturing parameters have on the mechanical properties of PVA/gelatin cryogel, designing stiffer PVA/gelatin compositions with enhanced strain-stiffening behaviour could reduce the compliance and better fit the requirements of synthetic coronary artery grafts.

4.4.3 Study Limitations and Next Steps

To increase the applicability of experimentally-informed FE models for the computational optimisation of synthetic coronary artery grafts, there are certain study limitations that should be addressed. Firstly, viscoelasticity and anisotropy were not incorporated into any of the constitutive material models used. As the frequency and stress relaxation responses of PVA/gelatin were not measured in this study, viscoelastic effects were neglected. The quasi-static nature of this study rendered this an applicable simplification. If future work seeks to investigate dynamic loads, or the time-dependent stress response of artery and graft, viscoelasticity would need to be represented in the constitutive material model.

Arteries display direction-dependent stress–stretch responses [288]. As longitudinal motion was constrained in this study, isotropic hyperelastic coefficients fitted

to circumferential stress–stretch data were applicable and hence sourced from the literature (Table 4.1). The casting method used to manufacture PVA/gelatin cryogels produced isotropic samples. In future, anisotropy may be engineered into PVA/gelatin cryogels by introducing a freezing gradient during the initial freezing step [198, 343] or through cryogenic 3D printing [16].

The effects of residual stresses (longitudinal, radial and circumferential) were not incorporated into the coronary artery models; that is, when free of external load, the models were assumed to experience a zero-stress state. Residual stresses affect the uniformity of transmural stress in arteries [344], and the magnitude of σ_θ at the luminal surface has been shown to reduce significantly in their presence [94]. Consequently, the disparity in σ_θ at the surface of PVA/gelatin grafts and the coronary artery may be less significant than reported in this study. While future efforts should be made to include the effects of residual stress and strain, the qualitative trends reported here — the relative magnitudes of σ_θ and σ_r, the discontinuity of σ_θ at the media-–adventitia interface and the off-loading of stress from the intima to the adventitia — match those reported when residual stresses are considered [94]. In addition, the perivascular pressure (exemplified here by embedding the artery and graft in a fixed block of surrounding connective tissue) will influence stress and strain distribution through the vessel wall. The properties and boundary conditions associated with this surrounding tissue should thus be explored further in future work.

To allow relative motion between the heterogeneous boundaries of the simulated coronary artery wall and PVA/gelatin grafts, the interfacing surfaces of the mesh were allocated hard penalty contact constraints and a friction coefficient. For this quasi-static study of the transmural biomechanics of a laminated artery and graft, this was an applicable assumption. However, it should be noted that further research

involving dynamic loading conditions requires further research into how to most accurately define the behaviour of these interfacing surfaces. There is negligible literature defining this behaviour. The friction coefficient used between the layers of the artery wall, for example, was taken from the literature [335]. The authors note that a friction coefficient of 0.2 was assumed "for all contact pairs", though they do not explicitly identify which surfaces this applies to. The interactions between two PVA surfaces are even less defined and will be influenced by the manufacturing protocol. Crolla et al. demonstrated that 3D printed PVA cryogel fails at the interfacing boundaries between the printed filaments when tested under tension [16], which suggests that simply tying the surfaces together and constraining translational and rotational motion is unsuitable for representing the contact behaviour. As the model complexity is increased to incorporate the effects of wall viscoelasticity and complex geometries, research into the interfacing behaviour must be undertaken.

4.5 Conclusion

The transmural biomechanics of multi-layered coronary artery grafts is a largely unexplored area of cardiovascular research, despite the important role of wall stress and strain distribution on vascular (dys)function. This chapter aimed to apply the hyperelastic constitutive parameters fitted PVA/gelatin cryogel in Chapter 3 and develop experimentally-informed FE models to evaluate the quasi-static responses of four multi-layered PVA/gelatin graft designs relative to the coronary artery wall. This chapter presented a new cardiovascular tissue engineering approach for designing multi-layered hydrogel grafts that synergised experimental data with computational simulations to enhance understanding of the transmural biomechanics, and their potential impact on EC behaviour, under physiological loading. Importantly,

the proposed method is applicable to the development of other hyperelastic VMMs for cardiovascular tissue engineering. The following conclusions are drawn:

- Despite being fit to the same experimental test data, the coronary artery wall displayed bi-layered biomechanical behaviour when modelled using the reduced polynomial model and tri-layered biomechanical behaviour when modelled using the polynomial and Ogden models. The results highlight the impact of hyperelastic model choice in replicating arterial mechanical behaviour, a finding that has significance across the wider field of cardiovascular FEA;

- Bi- and tri-layered PVA/gelatin grafts were obtained by varying the stiffness of the adventitia mimic relative to the stiffness of the media mimic; increasing the adventitial stiffness reduced the maximal stresses observed at the luminal surface of the graft and decreased graft compliance;

- For both PVA/gelatin and coronary artery models, stress and strain distributions were heavily influenced by the constitutive model used to capture the hyperelastic response of the material;

- While the qualitative trends of stress and strain distribution of PVA/gelatin grafts matched those observed in the coronary artery, hyperelastic model-specific quantitative differences were observed both at the luminal surface and within each tissue layer.

Chapter Five

HETEROGENEOUS DESIGN OF FUNCTIONALLY GRADED CORONARY ARTERY GRAFTS

5.1 Introduction

Arteries, among other biological tissues, achieve multi-functional combinations of strength, stiffness and toughness through a combination of material and geometric heterogeneity [345]. The FEA results presented in Chapter 4 demonstrated the ability to tailor the stiffness gradient of PVA/gelatin coronary artery grafts by varying the radial cryogel composition of the intima, media and adventitia. This chapter aims to build upon these results by investigating the impact of geometric heterogeneity – specifically, the interface geometry between layers – on the biomechanical properties of PVA/gelatin grafts.

For decades, engineers have used bioinspired design principles to manufacture synthetic materials with advanced mechanical properties [346]. Nature uses struc-

tural and hierarchical design elements to meet the strength, toughness and flexibility requirements of a given organ or tissue [345, 346]. Of these design elements, the interfaces between regions of opposing properties play a vital role in determining the mechanical performance of a tissue in its biomechanical environment. For instance, the compliant interface between dentin and enamel in teeth improves the fracture toughness of the otherwise brittle enamel; in the skull, interdigitated suture lines provide both flexibility for growth and strength [347, 348].

In arteries, the interfaces between the three tissue layers are separated by elastic laminae. Not only are the internal (intima–media) and external (media–adventitia) elastic laminae approximately triple the stiffness of the media in healthy coronary arteries [349], but these undulating sheets straighten as they bear load under intraluminal pressure, helping to evenly distribute transmural stresses (Figure 5.1A) [350, 351]. Moreover, the 'waviness' of the elastic lamellae is amplified toward the inner surface of the wall to compensate for increased circumferential stretch at the intima (Figure 5.1B [351]). Thus, many biological tissues use variations in structure and composition to introduce gradated properties along at least one direction throughout their volume. This concept, known as *functional grading*, can be applied to biomaterials to create tissue implants with versatile mechanical and physical properties [233].

The majority of FGBMs are designed for orthopaedic [352, 353] and orthodontic [354] applications. As such, many FGBMs are comprised of thermoplastics, ceramics or metals [352]; comparatively fewer soft FGBMs are reported in the literature, despite the need to replicate the multi-layered structures of soft tissues such as arteries [150]. Mismatching mechanical properties between both hard and soft implants and their host environments result in stress patterns known to contribute to graft failure. Femoral prostheses stiffer than bone fail due to stress shielding

[355]; arterial grafts stiffer than their respective artery (such as Dacron grafts) fail due to intimal hyperplasia induced by compliance mismatch and subsequent turbulent flow [8]. In both cases, interfacing FGBMs could be utilised to alter the stress pattern at the prosthesis–tissue interface or anastamoses, reducing or redistributing stress concentrations when placed under external load [352, 356]. Furthermore, the concept of gradating graft stiffness to generate mechanical stimuli related to tissue remodelling has been applied to orthopaedic plates [357–359]. A similar approach should be investigated for arterial grafts, where EC migration is directed by local rigidity gradients in substrate stiffness [360].

Layered grafts, such as those developed in Chapter 4 of this thesis, are examples of discontinuous FGBMs. The discrete interfaces between each layer create stepwise changes in composition and thus mechanical properties [233]. By contrast, continuous FGBMs use gradual transitions between dissimilar materials to reduce moduli mismatch between interfacing materials [356, 361]. This thesis has provided ample justification for the development of multi-layered PVA/gelatin coronary artery grafts: in addition to literature-documented capacity for endothelialisation [12, 13], the ability to match the mechanical properties of PVA/gelatin to the intima, media and adventitia through simple adjustments in manufacturing and compositional parameters renders it a versatile VMM for mimicking the heterogeneity of the artery wall. Intriguingly, these parameters can also be manipulated to create heterogeneous cryogel constructs with continuous functional grading. Wahab *et al.* created synthetic glenoid labrum implants by casting high- and low-stiffness PVA into a two-chamber mould [362]. By removing the divider between both chambers and allowing diffusion between both solutions, they obtained a continuous FGBM with a stiffness gradient of 0.1–0.4 MPa that was capable of reducing the stress at the glenohumeral joint by ≈50% [362]. Alternatively, gradual directional

freezing methods have been used to manufacture PVA cylinders with longitudinal stiffness gradients between 1–200 kPa [363, 364].

Ultimately, these methods lack control over the resulting gradient. Controlling the diffusion between interfacing solutions to create consistent gradients between batches is inherently difficult; equally, the geometric complexity between interfacing regions of cast cryogels is limited. The design flexibility afforded by technologies such as AM gives engineers the ability to manufacture FGBMs with biomimetic, interlocking interfaces (sutures) on the mesoscale [365–369]. While discontinuous in nature, the suture geometry can be designed to yield a homogeneous stress field and impart optimised load transmission, energy absorption and fatigue behaviour [370].

Sub-zero AM has been used to manufacture PVA-based cryogels with biomimetic gradients through control of the infill density [271] and print toolpath [371]. Though both studies aimed to replicate the gradient structure of cartilage, analogous methods could be used to fabricate cryogel structures that mimic the elastic lamellae of arteries. As such, sub-zero AM has the potential to print PVA/gelatin soft tissue mimics with complex interfaces and stress patterns. Yet, there is little information on the impact of interface design on the resulting stress patterns of soft VMMs – especially in the realm of cardiovascular tissue engineering.

5.1.1 Aims and Objectives

This chapter aims to extend the stress analyses of the laminated coronary artery grafts from Chapter 4 to develop graft designs with increased geometric complexity. Drawing bioinspiration from the macroscale waviness of the elastic lamellae (Figure 5.1) and the microscale crimped waveform of collagen fibres, the impact of a sinusoidal interface on the transmural biomechanics of PVA/gelatin grafts will be

assessed parametrically using FEA. The following objectives were set:

- Develop a Python script that enables full control of a sinusoidal interface geometry in Abaqus;
- Establish an appropriate method for modelling the contact between complex

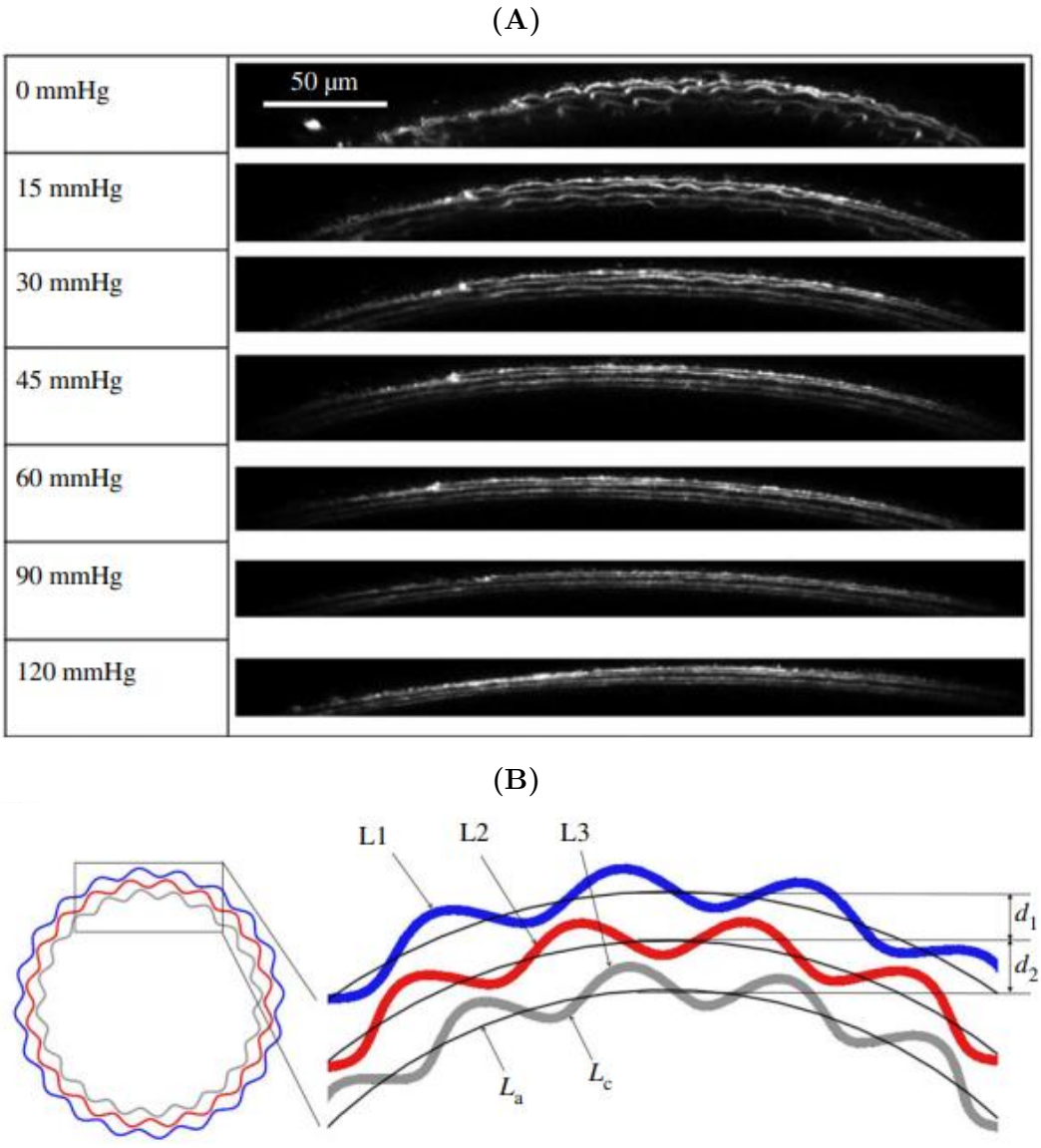


Figure 5.1: Micromechanics of elastic lamellae. **(A)** Transverse cross-sectional images of mouse carotid artery elastic lamellae when loaded up to systolic pressure and **(B)** Schematic of three elastic lamellae layers in the arterial wall. Both figures reprinted from [351] with permission from The Royal Society (UK).

interfaces, and assess the impact of contact formulation on transmural stress distribution;

- Assess the impact of sinusoidal parameters (radius, amplitude and frequency) on the transmural stress distribution of PVA/gelatin grafts under physiological pressure;

- Assess the impact of sinusoidal parameters (radius, amplitude and frequency) on the compliance behaviour of PVA/gelatin grafts under physiological pressure.

It is intended that the findings from this chapter will complement the future development PVA-based grafts using sub-zero AM. Furthermore, while PVA/gelatin has been chosen as the model VMM throughout this thesis, it is anticipated that the approach to interface design presented in this study will translate more widely to the design of biomimetic coronary artery grafts with functionally graded mechanical properties derived from interdigitated interfaces.

5.2 Method

5.2.1 Overview

The impact of a bioinspired sinusoidal waveform interface on the biomechanics of PVA/gelatin grafts was investigated using 2D FEA. All models were constructed in Abaqus/CAE 2021 using quasi-static implicit analyses.

The workflow of this chapter is provided in Figure 5.2. In the first instance, the boundaries between interfacing layers of interdigitated and laminated grafts were

assessed according to three contact formulations, as described in Section 5.2.2.2. These data were then used to inform the interfacing boundary conditions in the main study of this chapter: the evaluation of the impact of the sinusoidal interface parameters, as detailed in Section 5.2.2.1.

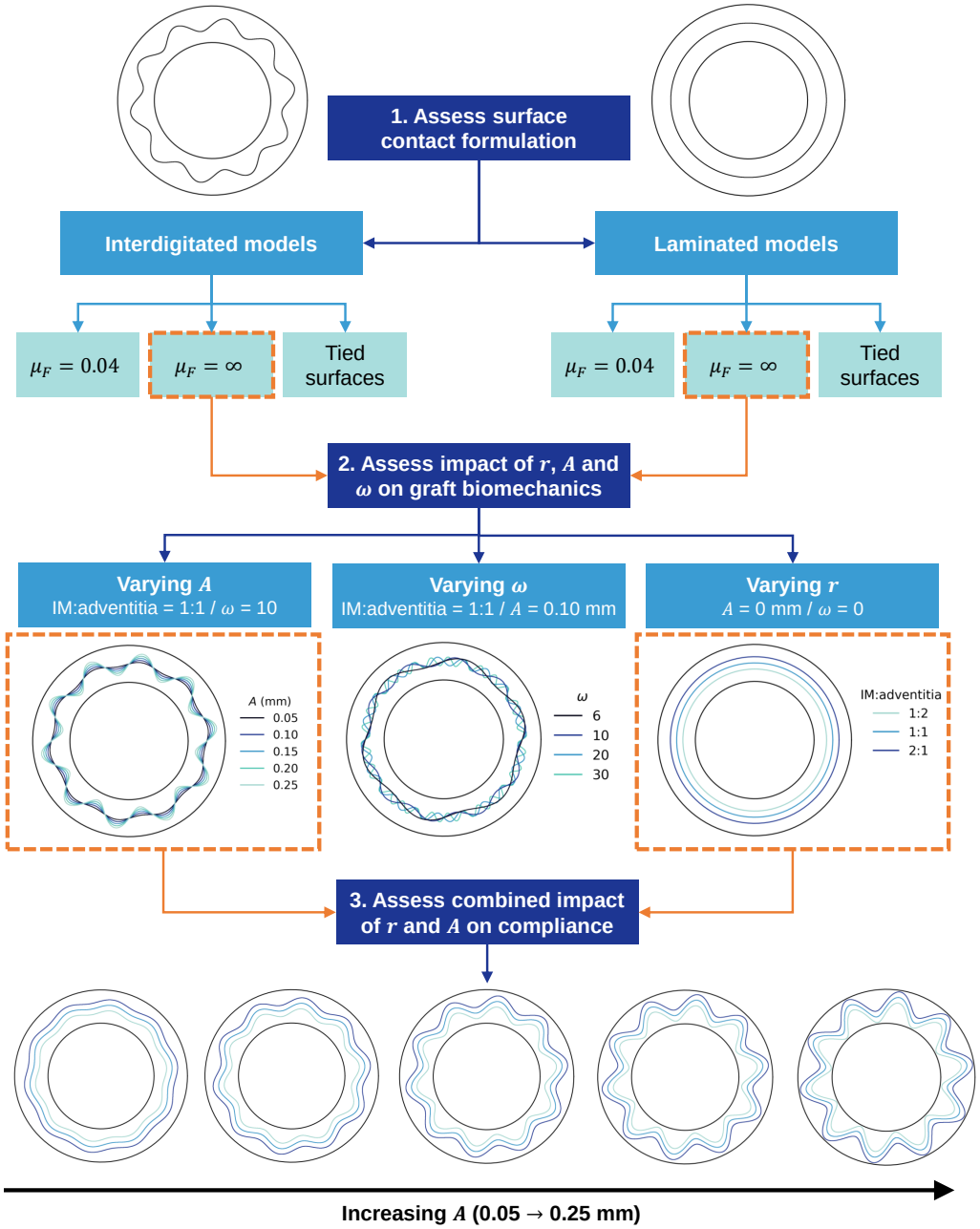


Figure 5.2: Workflow of Chapter 5.

5.2.2 FE Model

5.2.2.1 Geometry

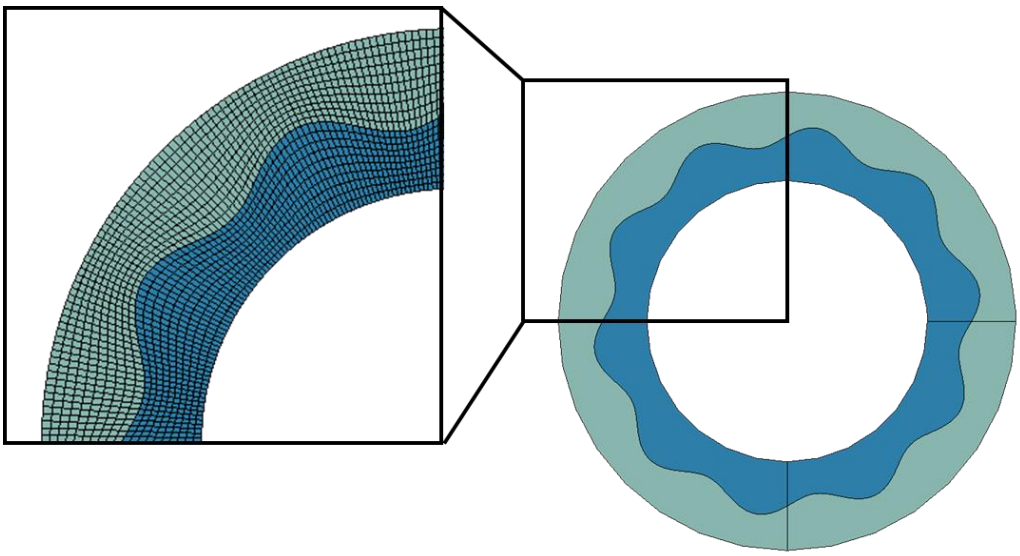


Figure 5.3: Example of a sinusoidally-interdigitated graft model and its mesh.

Bilayered, interdigitated PVA/gelatin grafts were generated in Abaqus/CAE 2021 using a custom Python script. A bilayered model was chosen to reduce the complexity of the graft and allow investigation of the biomechanics of a single interdigitated interface. The innermost layer was representative of a combined intima–media (IM) layer and the outermost layer was representative of the adventitia in line with bilayered coronary artery models from the literature [323, 324].

The full script is given in Appendix C.1. The following parametric equations were used to create a sinusoidal wave following a circular path of radius r (Figure 5.3):

$$\begin{aligned} x &= (r + Asin(\omega\theta)cos(\theta)) + c \\ y &= (r + Asin(\omega\theta)sin(\theta)) + c \end{aligned} \tag{5.1}$$

where c_x and c_y are the central x and y coordinates of the circle, and A and ω are the amplitude and frequency of the sine wave, respectively. The interface geometry was therefore characterised by three independent variables: A, ω (per 360° graft) and r. The total wall thickness of the grafts were set to 0.87 mm to mirror the total thickness of the coronary artery wall, as per Chapter 4 [288]. The impact of r on the compliance and σ_θ distribution of the graft was analysed by setting A and ω to zero and varying the relative thickness of the IM:adventitia (1:2, 1:1 and 2:1). The impact of A on the compliance and σ_θ distribution of the graft was individually assessed by keeping ω and r fixed; similarly, the impact of ω was tested by keeping A and r fixed (Table 5.1). In both cases, r was set such that the relative thickness of the IM:adventitia was 1:1 (r = 1.815 mm).

Table 5.1: Design matrix of sine wave parameters for amplitude and frequency studies. The blue row represents the variation of ω at a fixed A of 0.10 mm; the red column represents the variation in A at a fixed ω of 10; the purple cell represents overlap between the two studies. In all cases, r was fixed to 1.815 mm.

$\omega/360°$ / A (mm)	6	10	20	30
0.05		*		
0.10	*	*	*	*
0.15		*		
0.20		*		
0.25		*		

5.2.2.2 Boundary Conditions

Chapter 4 addressed the limitations associated with modelling the contact behaviour between PVA/gelatin layers. In that study, static friction coefficients

were used to prevent unconstrained sliding between interfacing hydrogel layers. This was an applicable assumption due to the laminated nature of each of the three graft layers. However, it was hypothesised that using estimated friction coefficients may introduce unrealistic stress concentrations when modelling interdigitated interfaces due to tangential sliding. To establish the most appropriate method for modelling contact between complex interfaces, the following contact formulations σ_θ were compared:

- A μ_F of 0.04, as per Pan *et al.* [306] and Chapter 4;
- Rough friction, where $\mu_F = \infty$ and relative sliding between two interfaces was prohibited;
- Tied surfaces, such that the interfaces are fused together and the graft acted as one body.

The impact of the three contact formulations were first compared using a non-interdigitated model ($A = 0$ mm, $\omega = 0$ and $r = 1.815$ mm). The three contact formulations were then compared using an interdigitated model with a sinusoidal interface of $A = 0.15$ mm, $\omega = 10$ and $r = 1.815$ mm. To distinguish between stress patterns relating to the interface and stress patterns relating to the choice of cryogel composition, each contact formulation was tested on a model where the material properties of the IM and adventitia were the same (P_9G_1-A-C) and a model where the IM (P_9G_1-A-C) was stiffer than the adventitia (P_9G_1-B-NC).

5.2.2.3 Mesh

All grafts were partitioned into quarters and discretised using quadrilateral plane stress (CPS4R) elements (Figure 5.3). Both graft layers contained 7200 elements and

had ten layers of elements through the radial thickness. Thanks to the structured mesh, transmural nodal analysis paths were taken as a function of the phase, ϕ, of the sine wave. For example, consider a graft whose interface has a sinusoidal frequency of 10. If the circumference of the graft is seeded with 360 elements, then each period of the sine wave will comprise 36 elements, and the circumferential edge length of each element will correspond to a phase shift of 10°. This is displayed visually in Figure 5.4. In cases where the stress analyses of two or more models were compared and their interfaces were out of phase (such as when varying interface ω, as illustrated in Figure 5.5), transmural analyses were also conducted with respect to arc length or arc angle.

In addition to transmural stress analysis through the radial thickness of the wall, the variation in σ_θ along the interface was calculated using the nodal path highlighted in Figure 5.6. To account for in phase and out of phase interfaces (as determined by variation of A and ω), σ_θ was plotted as a function of ϕ and/or graft arc angle.

5.2.2.4 Material Properties

To ensure the largest difference in mechanical properties between the two layers, the first order Ogden coefficients and densities of the stiffest and most compliant PVA/gelatin compositions, P_9G_1-A-C and P_9G_1-B-NC, were taken from Chapter 3 and are listed in Table 5.2. The IM layer was set to the stiffer composition of PVA/gelatin and the adventitia was set to the more compliant composition. The surrounding soft tissue was modelled as a Hookean linearly elastic material, as per Chapter 4 and Table 5.2, using an average value of density for soft tissue taken from the literature [336].

Table 5.2: Material parameters used in all Chapter 5 experiments (mean ± SD). ν = Poisson's ratio.

MATERIAL PROPERTIES			
	P_9G_1-A-C	**P_9G_1-B-NC**	**Surrounding Tissue**
$\boldsymbol{\mu_1}$ **(MPa)**	0.0444 ± 0.0060	0.0227 ± 0.0025	-
$\boldsymbol{\alpha_1}$	7.116 ± 0.528	7.311 ± 0.581	-
$\boldsymbol{E}$ **(MPa)**	-	-	0.05 [336]
$\boldsymbol{\nu}$	-	-	0.49 [336]
$\boldsymbol{\rho}$ **(kg m^{-3})**	1080 ± 36	1120 ± 38	1040 [336]

5.2.3 Compliance Analysis

As all graft models in this study were modelled in 2D, graft compliance was calculated as the cross-sectional compliance ($CC = \frac{\Delta A}{\Delta P}$, units: mm^2/mmHg). CC may be used in clinical practice if axial vessel movement due to pulse pressure is assumed to be negligible compared with the change in vessel diameter [372, 373]. Understanding the impact of interdigitation on the CC of the graft was therefore determined to be a key measure of graft performance.

The presence of the interdigitated wave yielded non-uniform radial deformation around the lumen. Thus, the lumen diameter – and therefore ΔA – was dependent on where it was measured around the luminal surface. More specifically, the diameter varied as a function of the ϕ of the wave; this is exemplified in Figure C.2. Even-numbered frequencies ($\omega = 6$, 10, 20 or 30 per 360° graft) were chosen to ensure that the phases of the wave on opposite sides of the graft were equivalent, as depicted in Figure 5.7. This symmetry ensured that, for any given diameter, the graft expanded equally on both sides of the central coordinates of the model. For any given model,

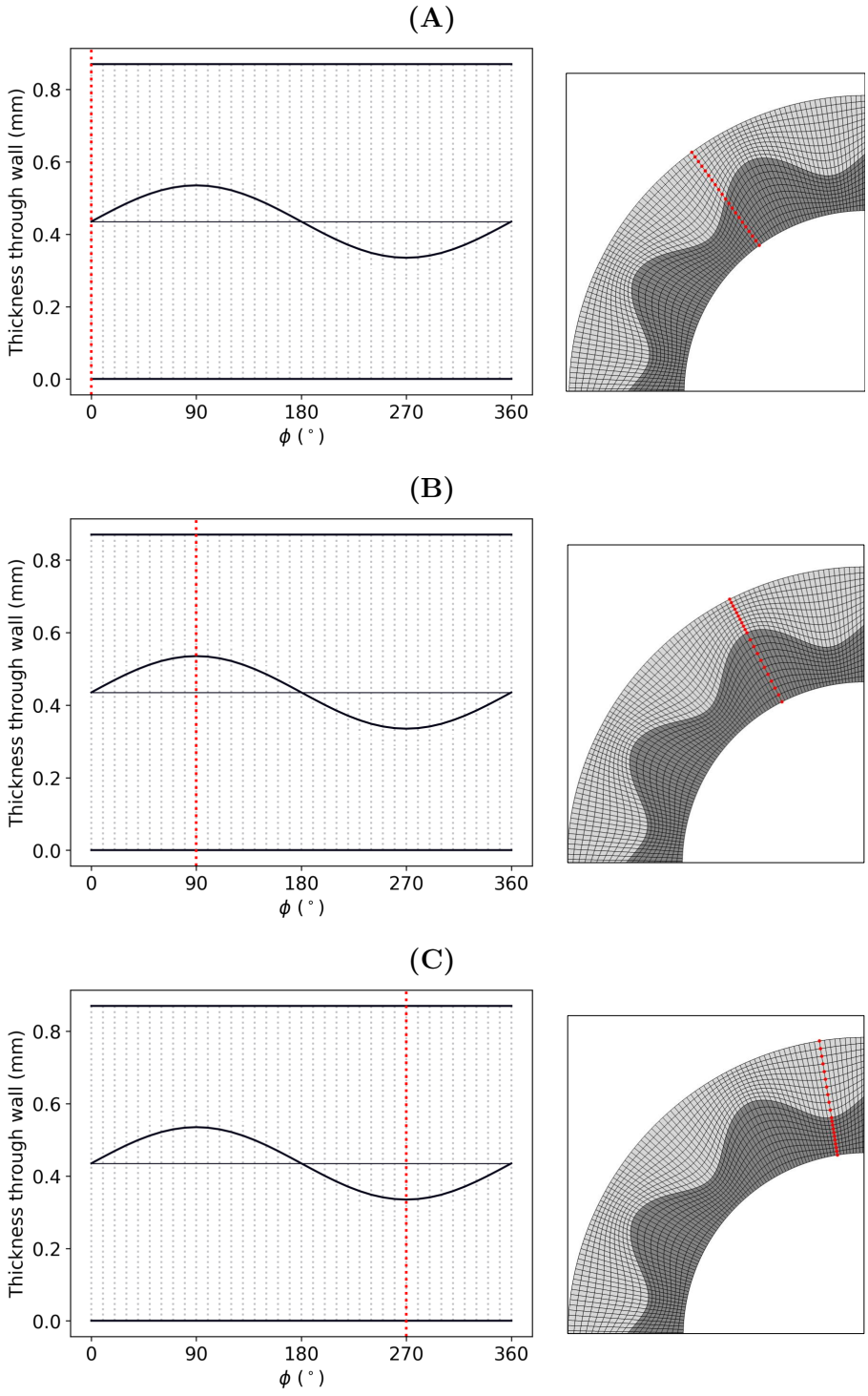


Figure 5.4: Examples of nodal analysis paths (red dotted lines) taken at $\phi =$ **(A)** 0°, **(B)** 90° and **(C)** 270°. In the left panel, grey dotted vertical lines represent a circumferential mesh density of 36 elements/wave.

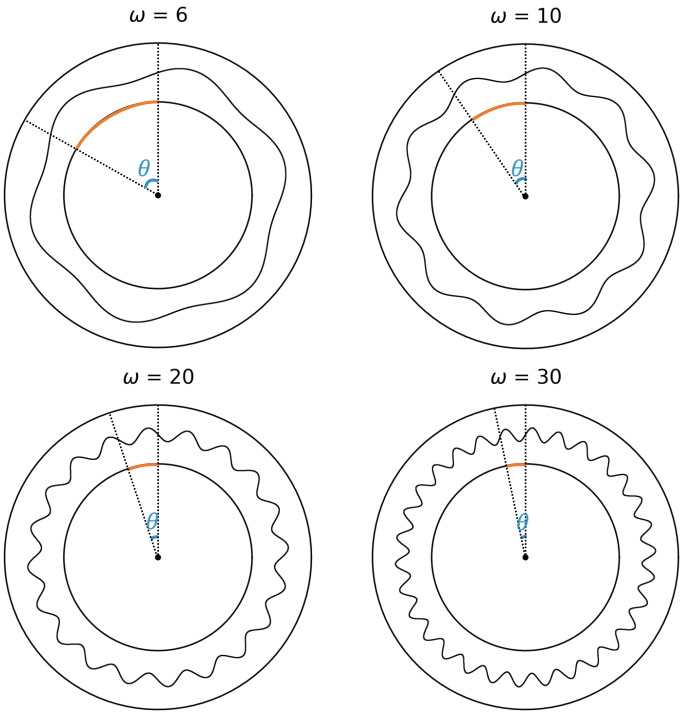


Figure 5.5: Interfaces comprised of different ω were out of phase. Arc lengths are shown in orange and and arc angles are shown in blue.

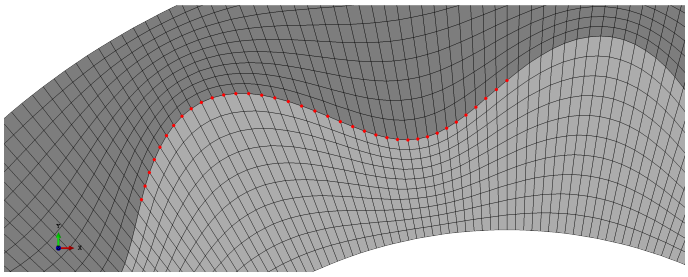


Figure 5.6: Node path corresponding to stress analyses along the interface. The stress at the nodes in red were plotted either as a function of ϕ or as a function of graft arc angle.

the CC was calculated as a function of ϕ; these CC values were then summed to give the mean CC ($\overline{CC}$) of the graft.

For the purpose of comparing the impact of interface parameters on graft compliance, $\overline{CC}$ is presented as the absolute compliance between diastole and

systole (mm^2/mmHg). However, to allow additional comparison of PVA/gelatin graft compliance with the compliance of coronary arteries (as reported in the literature), the compliance was also normalised to the graft diameter at diastolic pressure ($CC = \frac{(D_{sys} - D_{dia}/D_{dia})}{\Delta P} \times 10^4$, units: %/100 mmHg) [157].

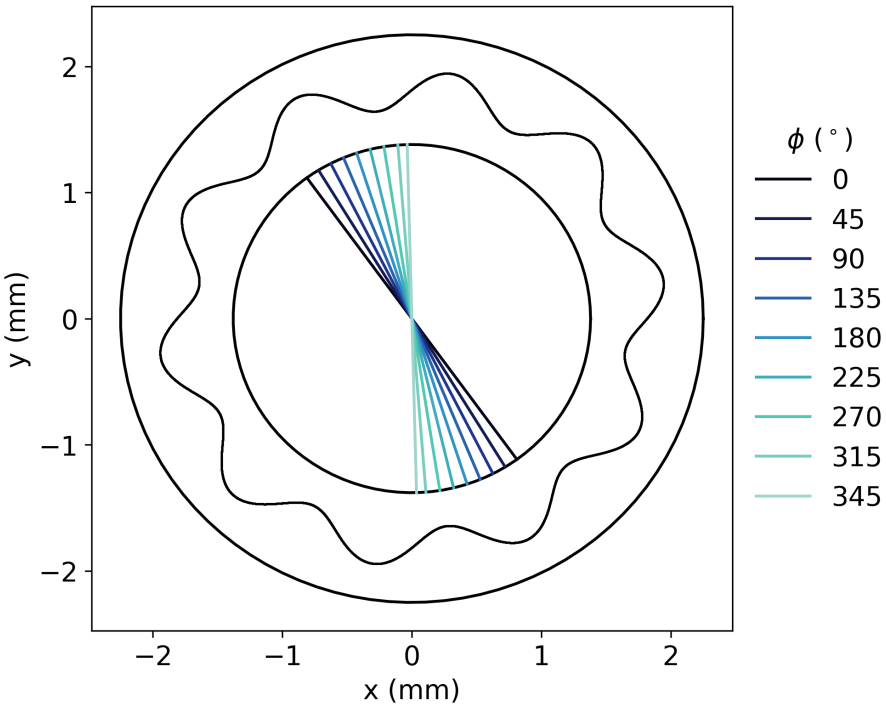


Figure 5.7: The lumen diameter was assessed as a function of ϕ to calculate $\overline{CC}$.

5.2.4 Analysis of the Variation of Lumen Radii

In addition to non-uniform $\overline{CC}$, the presence of non-uniform radial deformation around the lumen with pressure introduced a luminal surface wave. Plotting r_{lumen} as a function of ϕ, graft arc angle or graft arc length at a specified pressure allowed indirect mapping of the lumen surface profile. Due to the sinusoidal interface geometry, the surface height profile of the lumen was calculated by subtracting the minimum r_{lumen} value from the maximum r_{lumen} value (the 'peak-to-trough' height

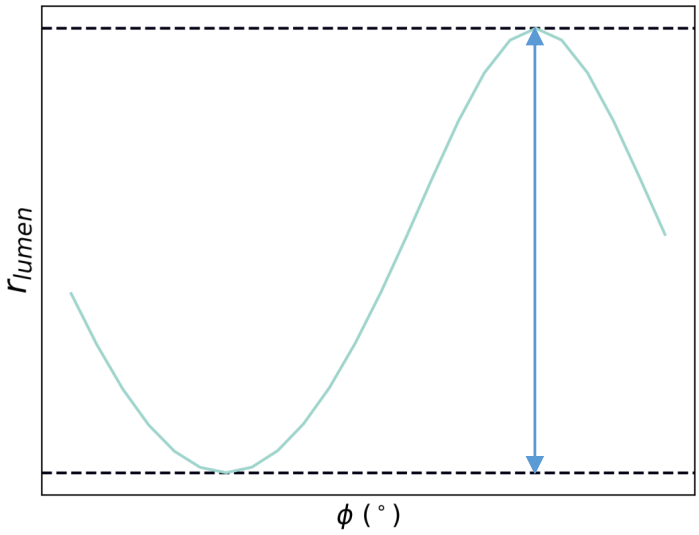


Figure 5.8: r_{lumen} was used to map the surface profile of the lumen; the blue arrow represents the peak-to-trough height profile of the lumen surface. Note that arc angle or arc length can be used in place of ϕ to map the luminal surface profile.

profile, Figure 5.8).

5.2.5 Discretisation Analysis

It was hypothesised that a variation of sine wave parameters would impact the magnitude of $\overline{CC}$ by changing the spatial composition of the IM and adventitia through the graft and hence graft distensibility. Therefore, to investigate the impact of sine wave parameters on the spatial composition of the IM and adventitia, sectors of each graft were reconstructed in Fusion 360, as demonstrated in Figure 5.9. The two radii of the sector were chosen such that the sector contained one complete wave period: $r_1 = \phi = 0°$; and $r_2 = \phi = 360°$. The cartesian coordinates of the nodes corresponding to the outer boundaries of each sector were extracted from their respective Abaqus model and imported into Fusion 360 using the latter's *ImportSplineCSV* script.

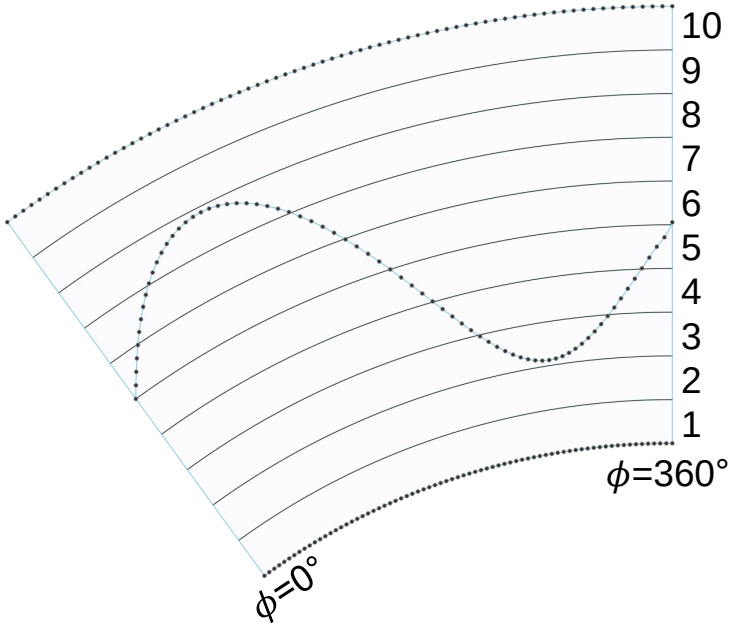


Figure 5.9: Example reconstruction of a graft sector in Fusion 360, shown for an interdigitated graft where $A = 0.25$ mm, $\omega = 10$ and $r = 1.815$ mm. Circumferential segments are numbered from 1–10.

The circumferential variation in IM and adventitial layers was measured through circumferential discretisation of each sector into 10 segments of equal depth (Figure 5.9). For each segment, the areas of the IM and adventitia were measured in Fusion 360 and converted into IM:adventitia ratios using Equation 5.2.

$$IM : adventitia = \frac{[Area\ of\ IM]}{[Area\ of\ segment]} : \frac{[Area\ of\ adventitia]}{[Area\ of\ segment]} \tag{5.2}$$

5.2.6 Data Analysis

The changes in $\overline{CC}$ as a function of A and ω were analysed in SigmaPlot 14.5 using one-way ANOVA. Note that, as only one diameter (and therefore CC) was obtained for each of the laminated models, statistical significance could not be obtained as a function of r.

5.3 Results

5.3.1 Overview

The results from this chapter are presented according to the order depicted in the study overview displayed in Figure 5.2. To help guide the reader through this section, the results have been structured as follows:

- Modelling the **contact** between interdigitated interfaces (Section 5.3.2);
- Evaluation of the impact of interface parameter $\boldsymbol{r}$ on graft biomechanics (Section 5.3.3);
- Evaluation of the impact of interface parameter $\boldsymbol{A}$ on graft biomechanics (Section 5.3.4);
- Evaluation of the impact of interface parameter $\boldsymbol{\omega}$ on graft biomechanics (Section 5.3.5);
- Evaluation of the combined impact of interface parameters $\boldsymbol{r}$ and $\boldsymbol{A}$ on graft compliance (Section 5.3.6).

Due to the number of models developed in this study, some data are presented in Appendix C to prevent repetition.

5.3.2 Modelling the Contact Between Interdigitated Surfaces

Figure 5.10 shows the impact of contact formulation on the transmural σ_θ distribution of bi-layered non-interdigitated grafts ($A = 0$ and $\omega = 0$). No

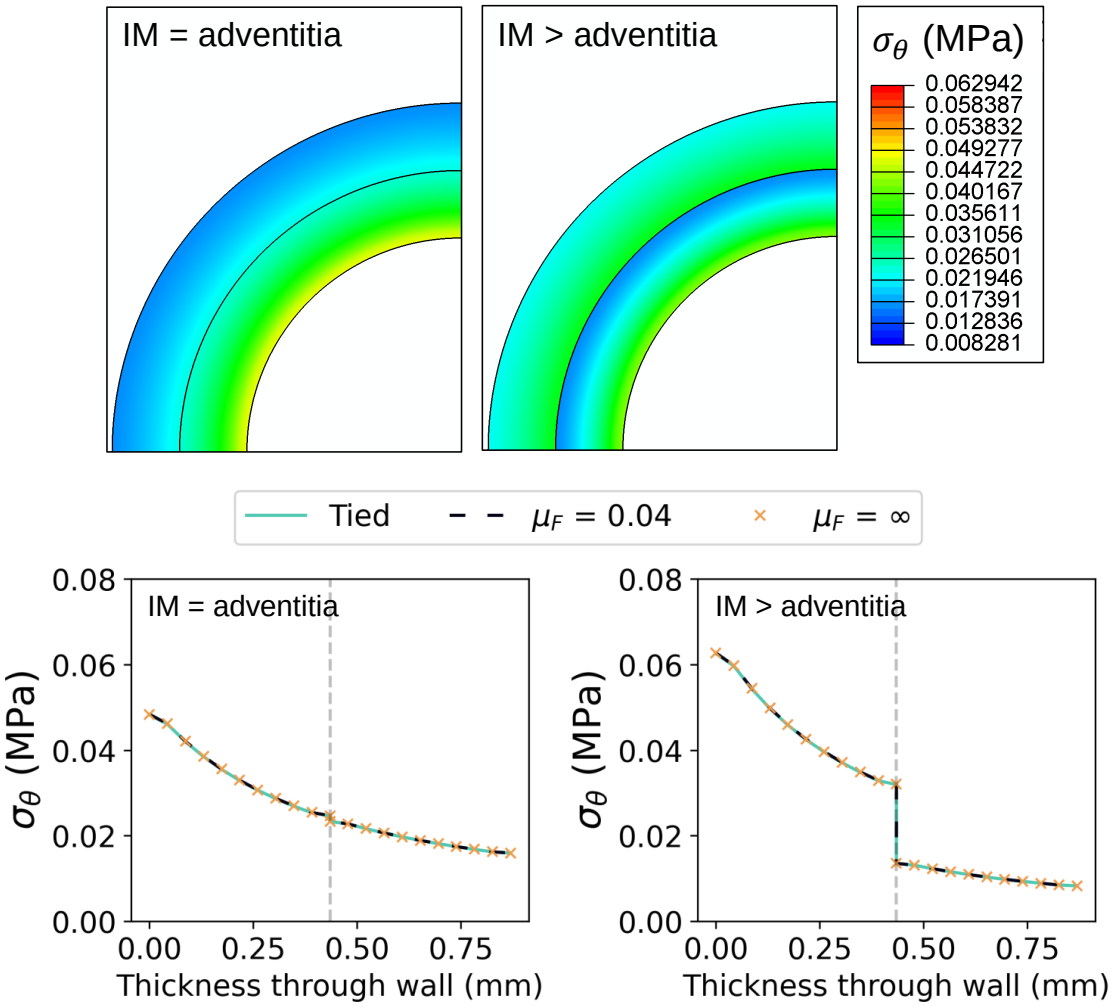


Figure 5.10: Comparison of friction, rough friction and tied contact formulations on a bi-layered non-interdigitated graft, where the IM and adventitia were modelled using the same PVA/gelatin composition (IM = adventitia; P_9G_1-A-C) and different PVA/gelatin compositions (IM > adventitia; IM = P_9G_1-A-C; adventitia = P_9G_1-B-NC).

difference in σ_θ distribution was observed between friction, rough friction and tied contact models; the resulting stress pattern was independent of contact formulation and was instead determined by the overall dimensions of the graft and the material properties of each layer, with heterogeneous material properties amplifying the discontinuity at the interface.

Different σ_θ distributions were observed between contact formulations for the interdigitated model. These differences were observed irrespective of the relative material properties of the IM and adventitia (Figures 5.11 and 5.12). For all contact formulations, σ_θ concentrations were observed in both the IM and adventitia at the peaks ($\phi = 90°$) and troughs ($\phi = 270°$) of the interdigitated wave. Using the rough friction coefficient and tying the two surfaces together yielded equivalent σ_θ distribution patterns. However, the magnitude of the stress concentrations were amplified in the friction coefficient model. For example, when the IM and adventitia layers were modelled using the same PVA/gelatin composition (P_9G_1-A-C), the σ_θ at the interface at $\phi = 270°$ was 0.030 MPa in the rough friction and tied surface models (Figure 5.11). However, at the same location, σ_θ increased to 0.094 MPa in the friction coefficient model. A similar trend was observed when the IM and adventitia were modelled with different PVA/gelatin compositions. When the IM was stiffer than the adventitia (to mimic the relative stiffnesses of the native layers, as per Chapter 4), σ_θ increased from 0.056 MPa in the rough friction model and 0.055 MPa in the tied surface model to 0.188 MPa in the friction model (Figure 5.12).

The amplified stress concentrations observed at the interface of the friction model were accompanied by increased σ_θ discontinuities across the IM–adventitia interface. Using $\phi = 270°$ as the example once more, when the IM and adventitia were modelled using the same PVA/gelatin composition, σ_θ decreased across the interface by 0.003 MPa and 0.002 MPa in the rough friction and tied models, respectively (Figure 5.11). In the friction model, σ_θ decreased by 0.103 MPa. Similarly, when the IM was stiffer than the adventitia, σ_θ decreased across the IM–adventitia interface by 0.030 MPa, 0.028 MPa and 0.195 MPa in the rough friction, tied surface and friction models, respectively (Figure 5.12).

Analysis of the tangential displacement (x_θ) of the IM and adventitia showed the relative movement of the interface under the applied pressure load (Figure 5.13). In the rough friction and tied surface models, tangential slip was constrained. At all phases, the x_θ of the IM and adventitia layers occurred in parallel directions (Figure 5.13A). The direction of x_θ between $\phi = 90$–$270°$ and $\phi = 270$–$90°$ indicate stretching of the interface under loading. These displacements corresponded to regions of high tensile stress in the graft: in the IM layer, for instance, tensile stress concentrations were observed at the troughs ($\phi = 270°$) of the wave (Figure 5.13B). Simultaneously, tensile stress concentrations were observed in the peaks of the adventitia ($\phi = 90°$).

Meanwhile, tangential slip in the 0.04 friction coefficient model caused the IM and adventitia to slip against one another. This was evidenced by the opposing displacement direction (x_θ) of the IM and adventitia at the interface (Figure 5.13C). While high tensile stress (stretching) was still observed at the troughs of the IM layer, compressive stress concentrations were introduced in the peaks of the adventitia (Figure 5.13D). The absolute magnitude of x_θ for the friction coefficient model was also greater (0.038 mm) compared with the rough friction (0.011 mm) and tied (0.010 mm) models (Figures 5.13C and C.3).

While the σ_θ and x_θ outputs from the rough friction and tied surface models were comparable, the rough friction model allowed analysis of the contact pressure at the interface (Figure C.4). This output variable was not available with the tied surface model. Due to the increased capacity to observe stress distribution at the interface of the rough friction model, rough friction was chosen as the contact formulation for all further analyses in this study; for a more detailed justification, the reader is directed to Section 5.4.1.

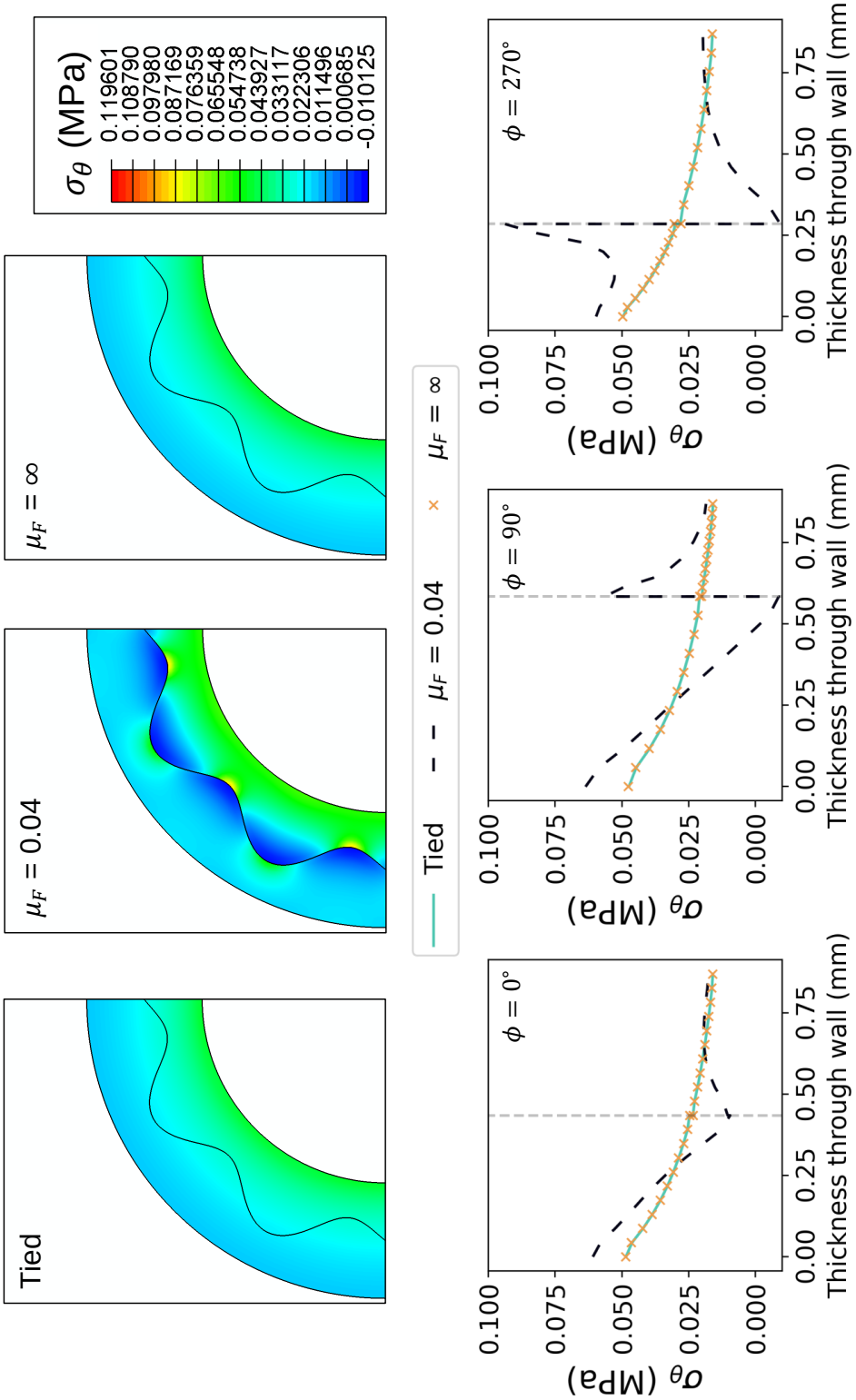


Figure 5.11: σ_θ distributions for three contact formulations (tied / $\mu_F = 0.04$ / $\mu_F = \infty$) when the IM and adventitia were modelled using the same PVA/gelatin composition (P_9G_1-A-C). Layer boundaries are represented by grey dashed lines.

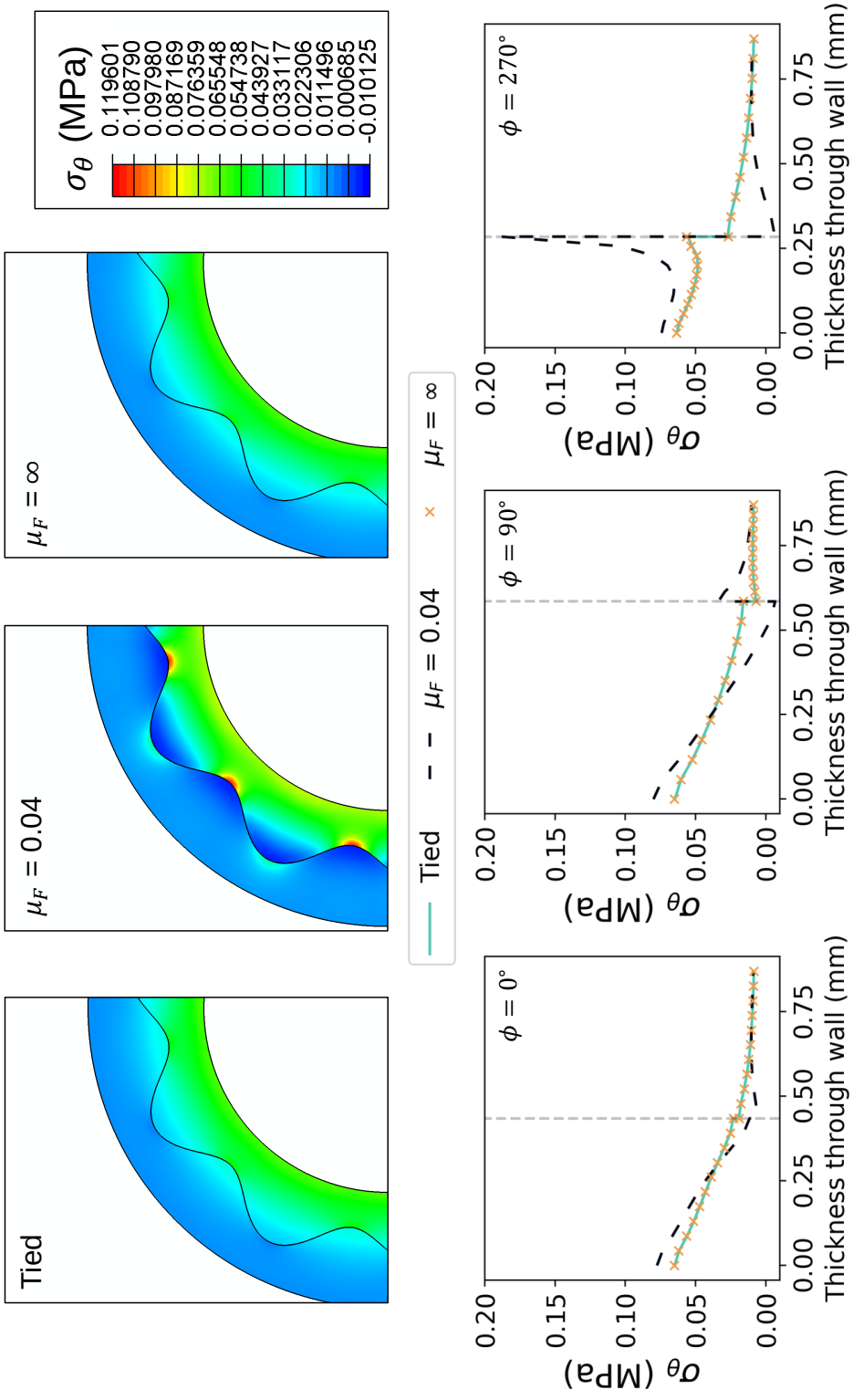


Figure 5.12: σ_θ distributions for three contact formulations (tied / $\mu_F = 0.04$ / $\mu_F = \infty$) when the IM (P_9G_1-A-C) was stiffer than the adventitia (P_9G_1-B-NC). Layer boundaries are represented by grey dashed lines.

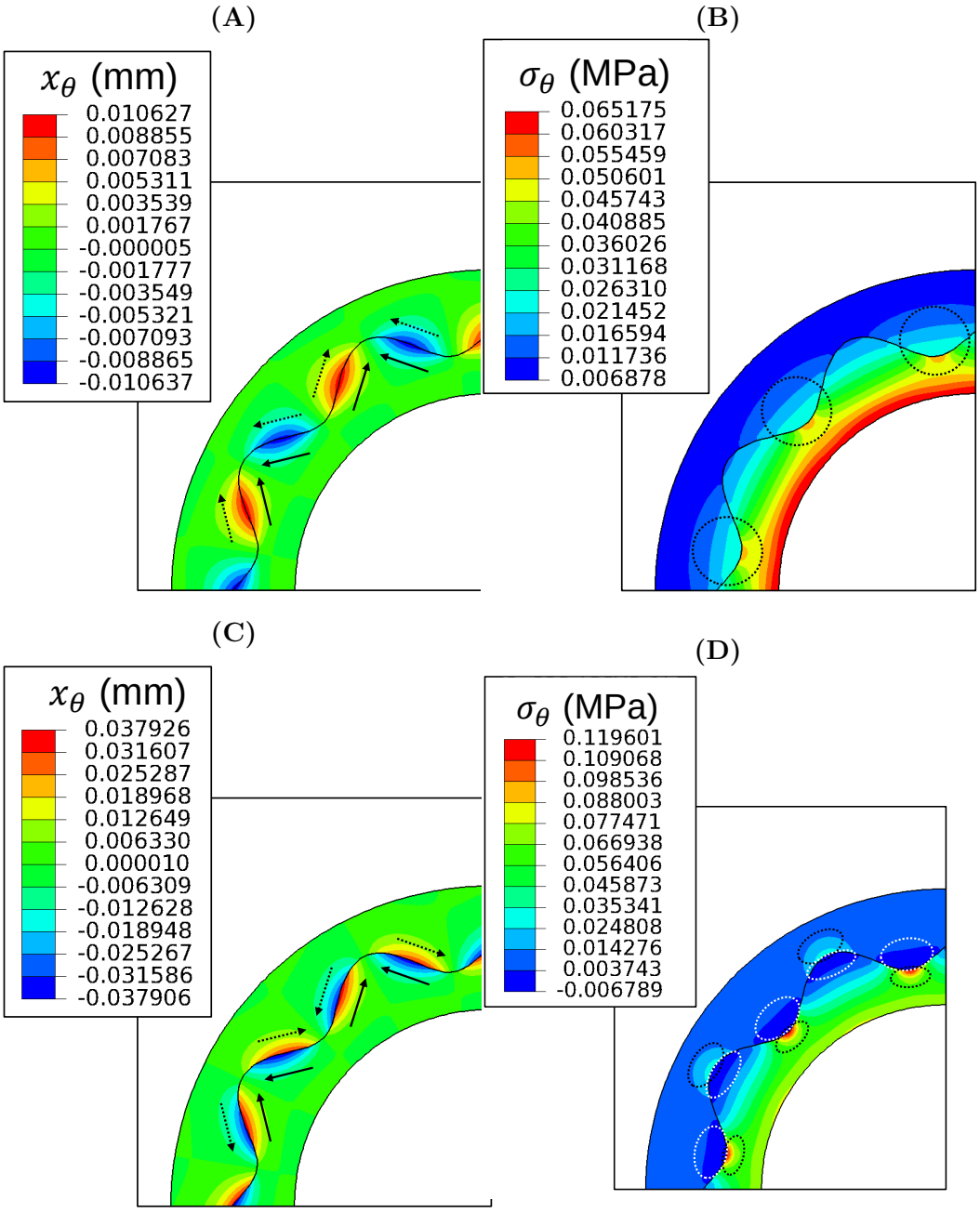


Figure 5.13: **(A)** x_θ and **(B)** σ_θ of the rough friction coefficient model; **(C)** x_θ and **(D)** σ_θ of the 0.04 friction coefficient model (IM = P_9G_1-A-C, adventitia = P_9G_1-B-NC). In the x_θ plots, red and blue signify clockwise and anticlockwise displacement, respectively. In the σ_θ plots, tensile stress concentrations are highlighted by black dotted circles and compressive stress concentrations are highlighted by white dotted circles. Data for the tied model are displayed in Figure C.3.

5.3.3 Impact of Interface Radius on Graft Biomechanics

5.3.3.1 Varying Interface Radius: Stress Distribution

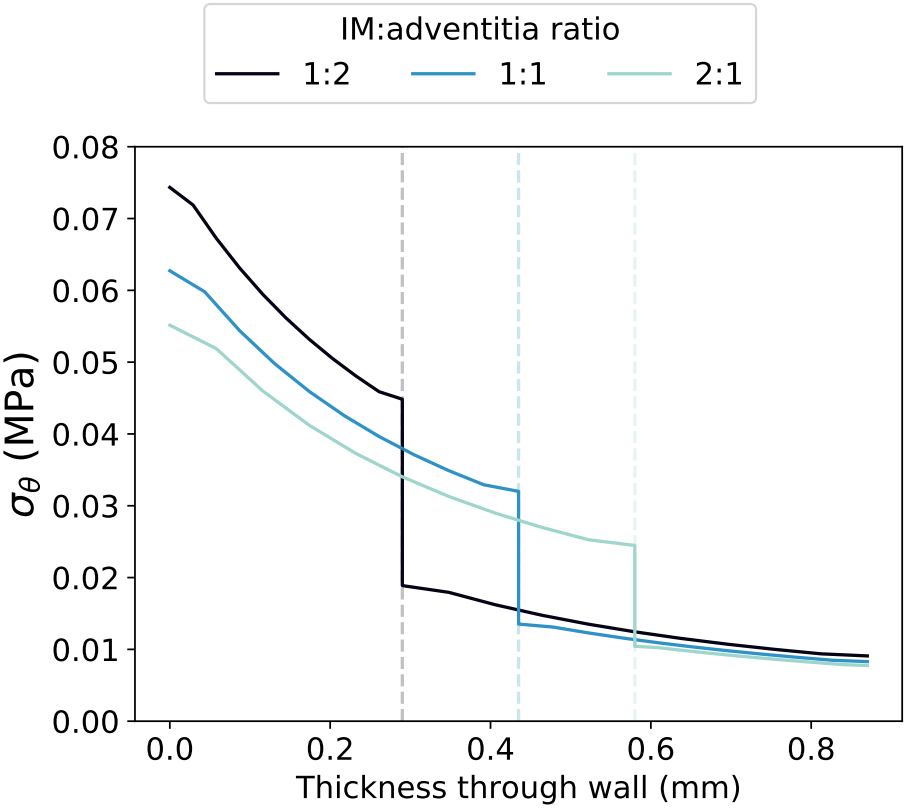


Figure 5.14: σ_θ distribution at systolic pressure at an IM:adventitia ratio of 1:2, 1:1 and 2:1. Dashed lines show the interface boundary (r).

A and ω were set to 0 to investigate the impact of r in isolation. This produced a laminated, non-interdigitated graft, as shown in Figure 5.2. For all models, the maximum σ_θ was observed at the luminal surface (Figure 5.14). A stepwise decrease in σ_θ was observed at the IM–adventitia interface, reflecting the discontinuous nature of the boundary. Increasing the relative volume of the stiffer IM layer increased the distance between the interface and the applied pressure. This influenced the σ_θ distribution in two ways. Firstly, the maximum σ_θ observed at

the lumen decreased: $\sigma_\theta = 0.074$ MPa and 0.055 MPa at IM:adventitia ratios of 1:2 and 2:1, respectively. Secondly, the magnitude of σ_θ reduction at the IM–adventitia interface also decreased: at the same IM:adventitia ratios, σ_θ decreased across the interface by 0.026 MPa and 0.014 MPa.

5.3.3.2 Varying Interface Radius: Compliance

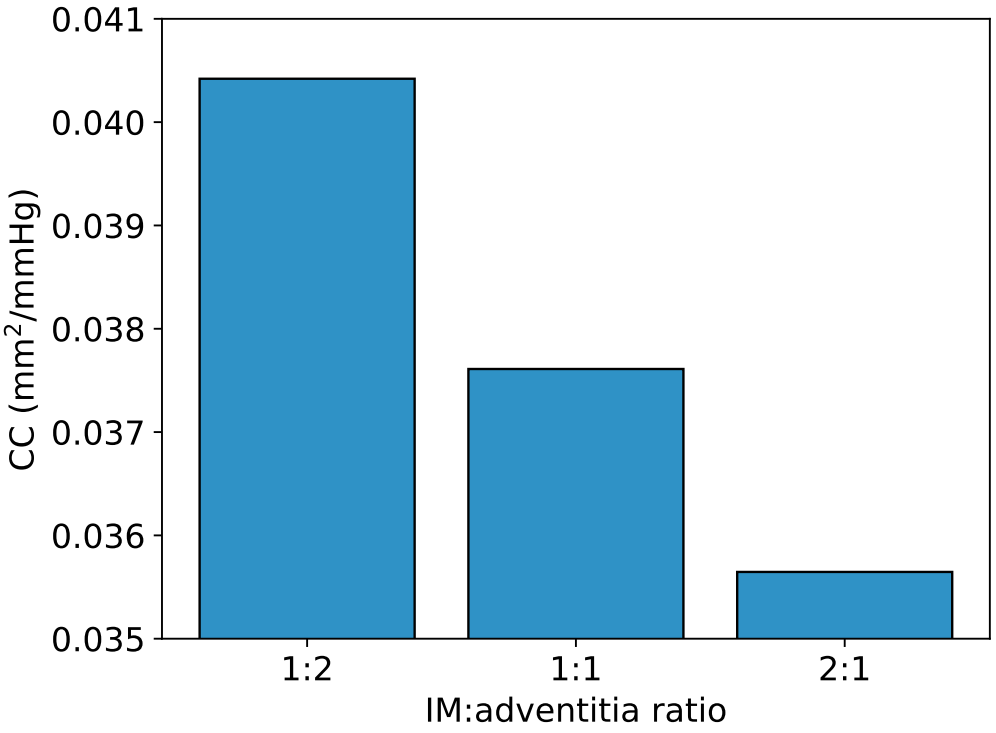


Figure 5.15: The impact of varying the IM:adventitia ratio on the CC of the graft.

Increasing the IM:adventitia ratio decreased the CC of the graft (Figure 5.15). Overall graft stiffness increased with increasing volume of the stiffer IM layer; when IM:adventitia = 2:1, $CC = 0.0356$ mm^2/mmHg. Similarly, the reverse effect was achieved by reducing the volume of the IM; when IM:adventitia = 1:2, $CC = 0.0404$ mm^2/mmHg.

5.3.4 Impact of Interface Amplitude on Graft Biomechanics

5.3.4.1 Varying Interface Amplitude: Stress Distribution

For all phases, the magnitude of σ_θ at the luminal surface increased with increasing A (Figures 5.16 and 5.17). Of the three phases presented in Figure 5.17, the difference in luminal σ_θ between the smallest ($A = 0.05$ mm) and largest ($A = 0.25$ mm) amplitudes ranged from 0.0017 MPa ($\phi = 270°$) to 0.0048 MPa ($\phi = 0°$).

When $A \leq 0.15$ mm, the maximum σ_θ of each model was highest at the luminal surface across all phases and was followed by a marked decrease at the interface (Figure 5.17). The extent of this decrease correlated with increasing A (Figure 5.17). At $\phi = 0°$ and $\phi = 90°$, the magnitude of σ_θ reduction at the interface decreased with increasing A, indicating a smoother transition in transmural stress across the interface at these phases when A was increased. For example, at systolic pressure, when $A = 0.05$ mm, the σ_θ at the interface decreased by 0.015 MPa at $\phi = 0°$ and 0.014 MPa at $\phi = 90°$. When $A = 0.25$ mm, σ_θ decreased by 0.00006 MPa and 0.007 MPa, respectively. However, at $\phi = 270°$, the magnitude of σ_θ reduction at the interface increased with increasing amplitude. The distance between the lumen and the troughs of the wave decreased with increasing A; the IM was placed under higher tension in this region, as demonstrated by the increased stress concentration measured at this phase.

For all models, the highest and lowest interface contact pressures were observed at $\phi = 270°$ and $0°/180°$, respectively (Figure 5.18).

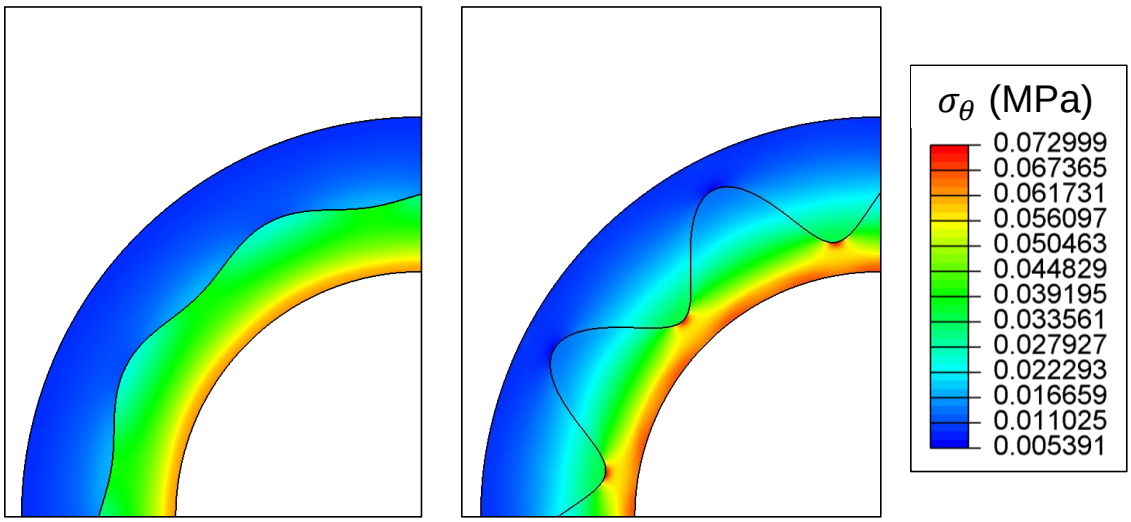


Figure 5.16: σ_θ distribution at $A = 0.05$ mm (left) and $A = 0.25$ mm (right) at systolic pressure.

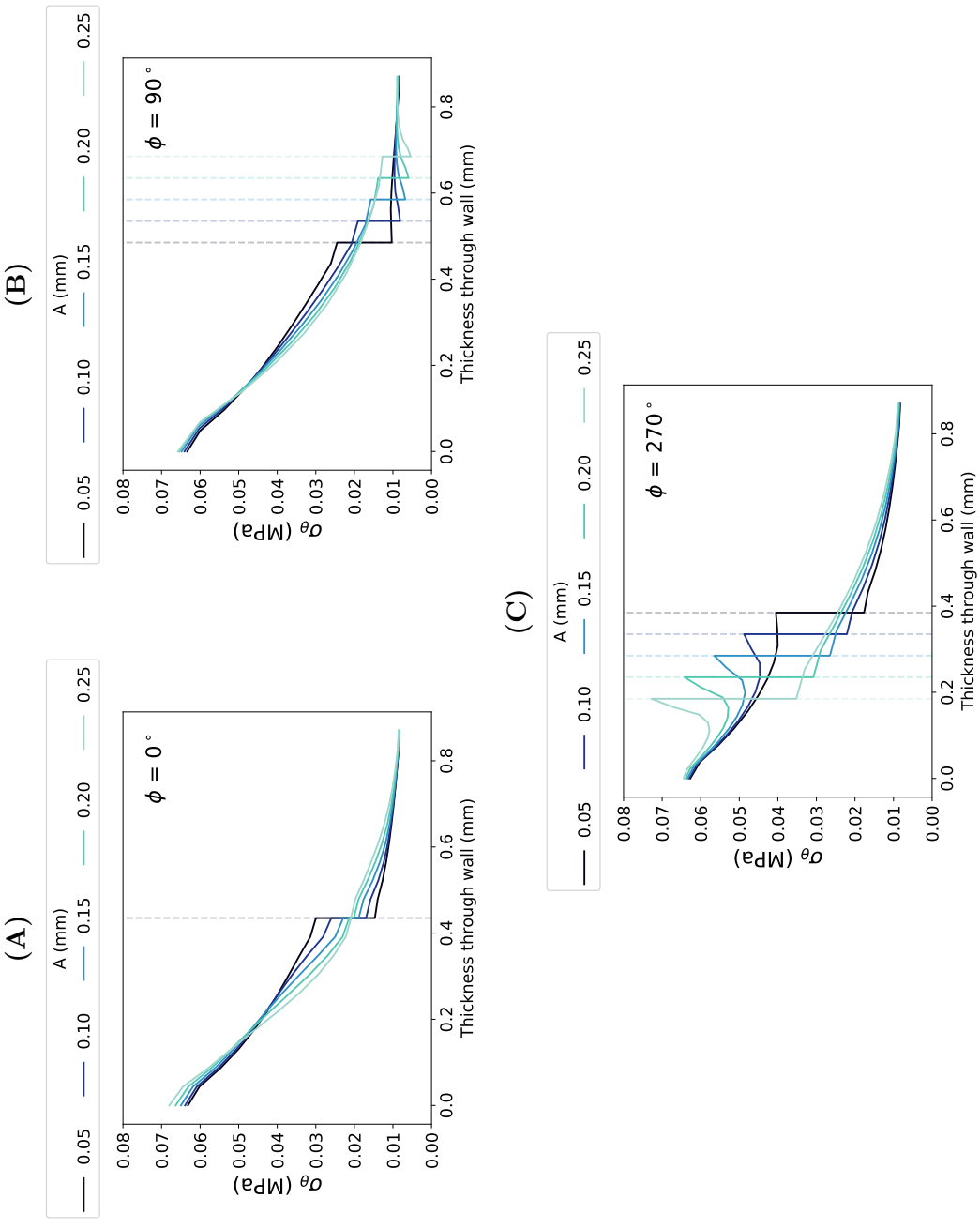


Figure 5.17: Transmural σ_θ distribution at systolic pressure with varying A at **(A)** $\phi = 0°$, **(B)** $\phi = 90°$ and **(C)** $\phi = 270°$. Dashed lines show the interface at each ϕ.

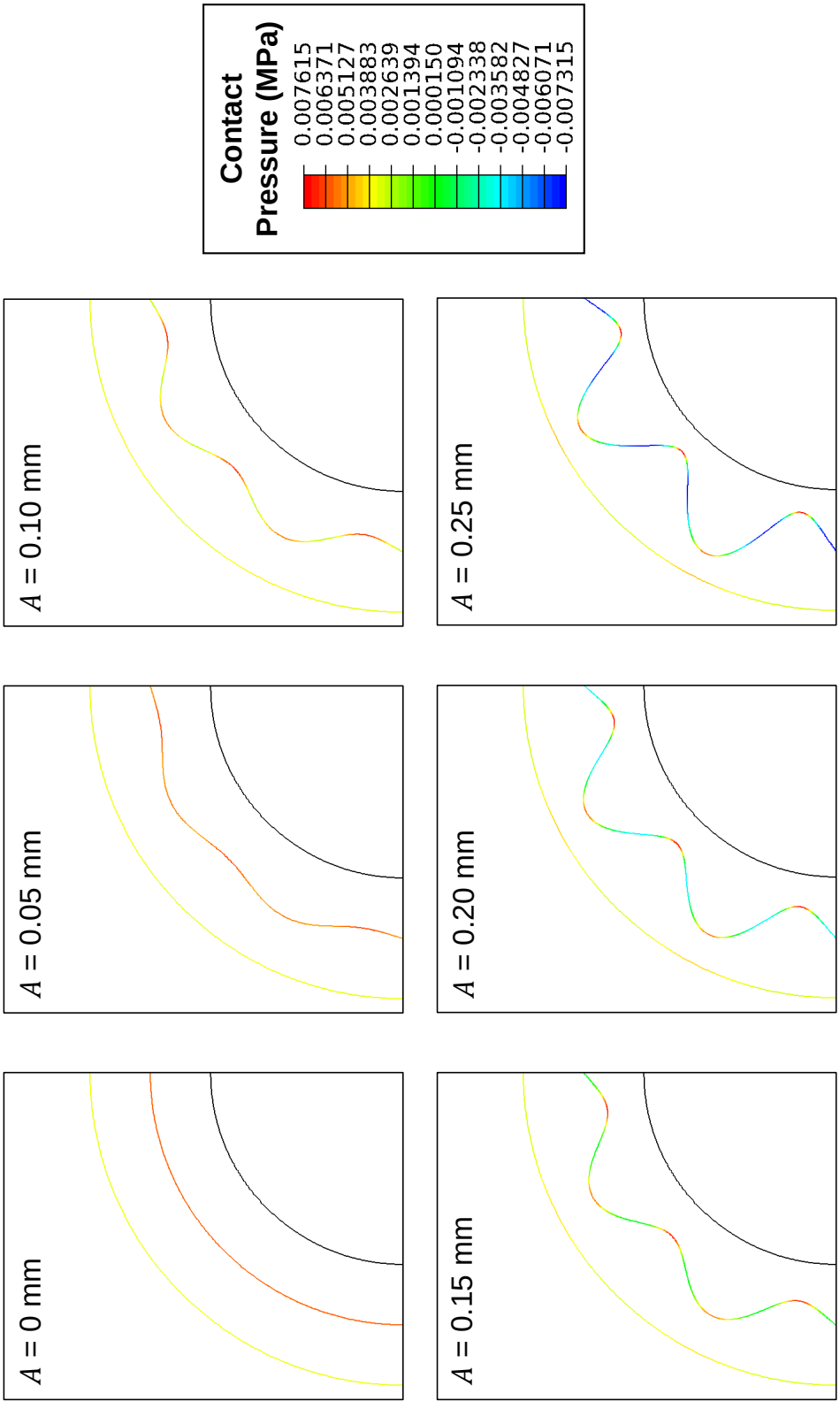


Figure 5.18: Contact pressures observed at the interface of all amplitude models at systolic pressure.

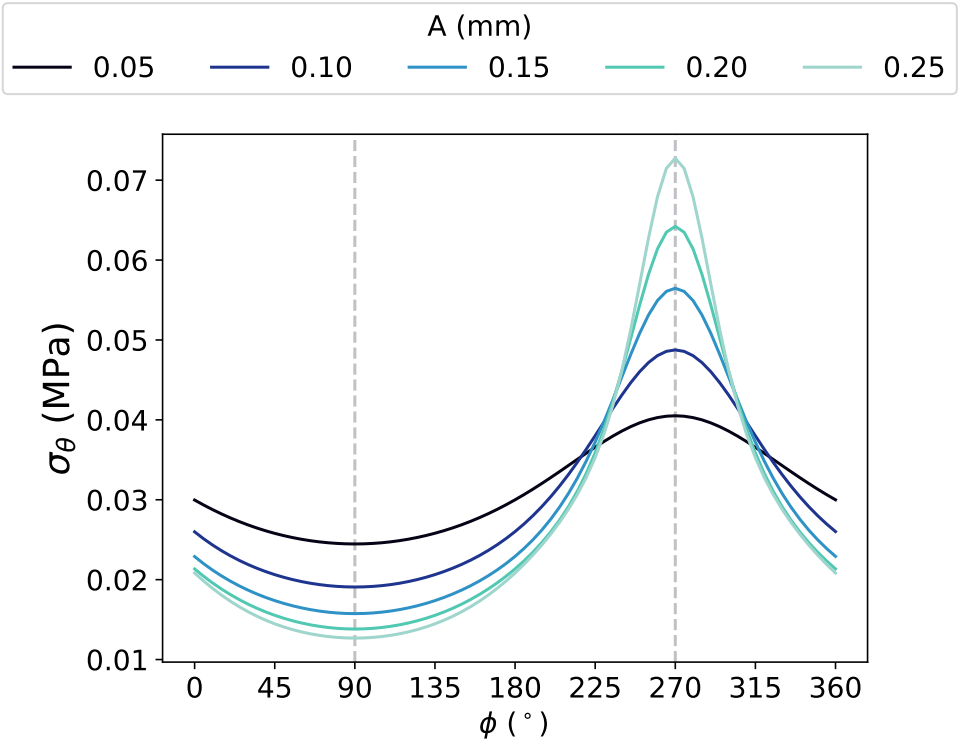


Figure 5.19: σ_θ along the interface as a function of ϕ at systolic pressure. Dashed lines show the locations of minimum and maximum σ_θ.

The variation in σ_θ along the interface as a function of ϕ is shown in Figure 5.19. σ_θ was lowest at the peak of the interface wave ($\phi = 90°$), where the interface was furthest away from the applied pressure load. On the other hand, σ_θ was highest where the interface was closest to the pressure load ($\phi = 270°$). The σ_θ distribution along the interface became more non-uniform with increasing A (Figure 5.19). For instance, the difference in σ_θ at the peak and trough of each wave period increased from 0.016 MPa at $A = 0.05$ mm to 0.060 MPa at $A = 0.25$ mm. The relative decrease and increase in σ_θ at $\phi = 90°$ and $\phi = 270°$ respectively suggests that, as A was increased, the load was shifted from the peaks to the troughs of each wave.

5.3.4.2 Varying Interface Amplitude: Compliance

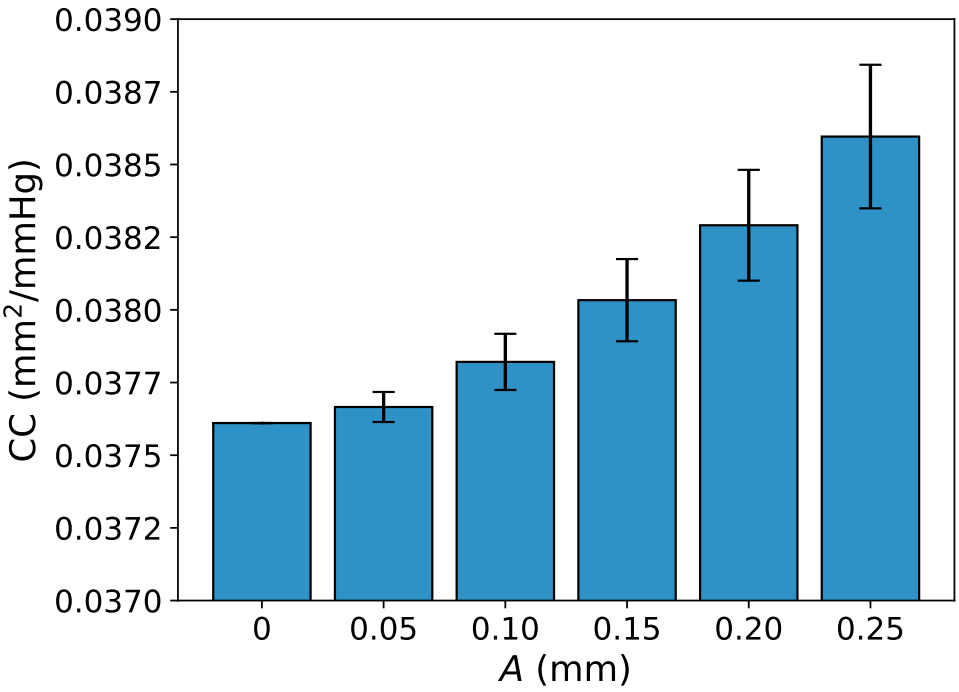


Figure 5.20: The impact of varying A on the $\overline{CC}$ ($\pm$ SD) of PVA/gelatin grafts.

Increasing the amplitude of the sine wave increased the $\overline{CC}$ of the graft (Figure 5.20). When $A = 0$ mm, $\overline{CC} = 0.0376$ mm^2/mmHg. When $A = 0.25$ mm (the largest amplitude tested in this study), $\overline{CC} = 0.0386 \pm 0.0002$ mm^2/mmHg. The increase in $\overline{CC}$ observed between consecutive amplitudes (between $A_{0.05} \rightarrow A_{0.10}$, $A_{0.10} \rightarrow A_{0.15}$, etc) was statistically significant ($P < 0.001$).

To investigate the relationship between the spatial composition of the IM and adventitia as a function of A and the magnitude of $\overline{CC}$, sectors corresponding to one complete period of the interdigitated wave were discretised into ten circumferential segments, as detailed in Section 5.2.5. As A was increased, the total area of the IM increased slightly (and, subsequently, the total area of the adventitia decreased slightly) due to the curvature of the graft (Table C.1). By increasing A,

circumferential segments closer to the lumen contained more of the compliant outer adventitial layer compared with grafts of lower A (Table 5.4). The reverse trend was observed for the circumferential segments furthest away from the lumen; these segments contained more of the stiff inner IM layer compared with grafts of lower A.

Increasing the amplitude of the wave also increased the SD of the $\overline{CC}$ of the graft (Figure 5.20). As A increased, the radial deformation around the lumen became more non-uniform as a function of ϕ. This was reflected in the larger range of lumen radii (r_{lumen}) observed at larger amplitudes (Figure 5.21A). There was a correlation between r_{lumen} (and subsequently CC) and the depth of the interface at each ϕ (Figure 5.21B). r_{lumen} was smallest at phases containing more of the inner IM layer, where the interface was furthest away from the lumen ($\phi = 90°$). Conversely, r_{lumen} was largest at phases containing more of the outer AM layer, where the interface was closest to the lumen ($\phi = 270°$).

Consequently, the presence of a sinusoidal interface – and therefore non-uniform radial deformation – induced a surface wave on the lumen of the graft. In lieu of surface roughness calculations, r_{lumen} was used to indirectly measure the height profile at the lumen surface. The peak-to-trough height profile increased with increasing A, ranging from 2.12 µm when $A = 0.05$ mm at systolic pressure to 11.29 µm when $A = 0.25$ mm at the same pressure (Table 5.3).

Table 5.3: Peak-to-trough height profiles at the lumen surface as a function of A at systolic pressure.

	$\boldsymbol{A = 0.05}$ **mm**	$\boldsymbol{A = 0.10}$ **mm**	$\boldsymbol{A = 0.15}$ **mm**	$\boldsymbol{A = 0.20}$ **mm**	$\boldsymbol{A = 0.25}$ **mm**
Peak-to-trough height profile (µm)	2.12	4.15	6.24	8.56	11.29

Table 5.4: The ratio of IM:adventitia through each circumferential segment as a function of A. The relative areas of the IM and adventitia are normalised to the total area of the corresponding segment. Segment 1 is closest to the lumen, while segment 10 is furthest away from the lumen.

	IM:adventitia ratio				
Circumferential segment	$A = 0.05$ **mm**	$A = 0.10$ **mm**	$A = 0.15$ **mm**	$A = 0.20$ **mm**	$A = 0.25$ **mm**
1	1:0	1:0	1:0	1:0	1:0
2	1:0	1:0	1:0	1:0	1:0
3	1:0	1:0	1:0	0.966:0.034	0.851:0.149
4	1:0	0.978:0.022	0.859:0.141	0.731:0.269	0.674:0.326
5	0.814:0.186	0.649:0.351	0.598:0.402	0.567:0.433	0.557:0.443
6	0.178:0.822	0.347:0.653	0.402:0.598	0.431:0.569	0.441:0.559
7	0:1	0.019:0.981	0.142:0.858	0.274:0.726	0.321:0.679
8	0:1	0:1	0:1	0.036:0.964	0.144:0.856
9	0:1	0:1	0:1	0:1	0:1
10	0:1	0:1	0:1	0:1	0:1

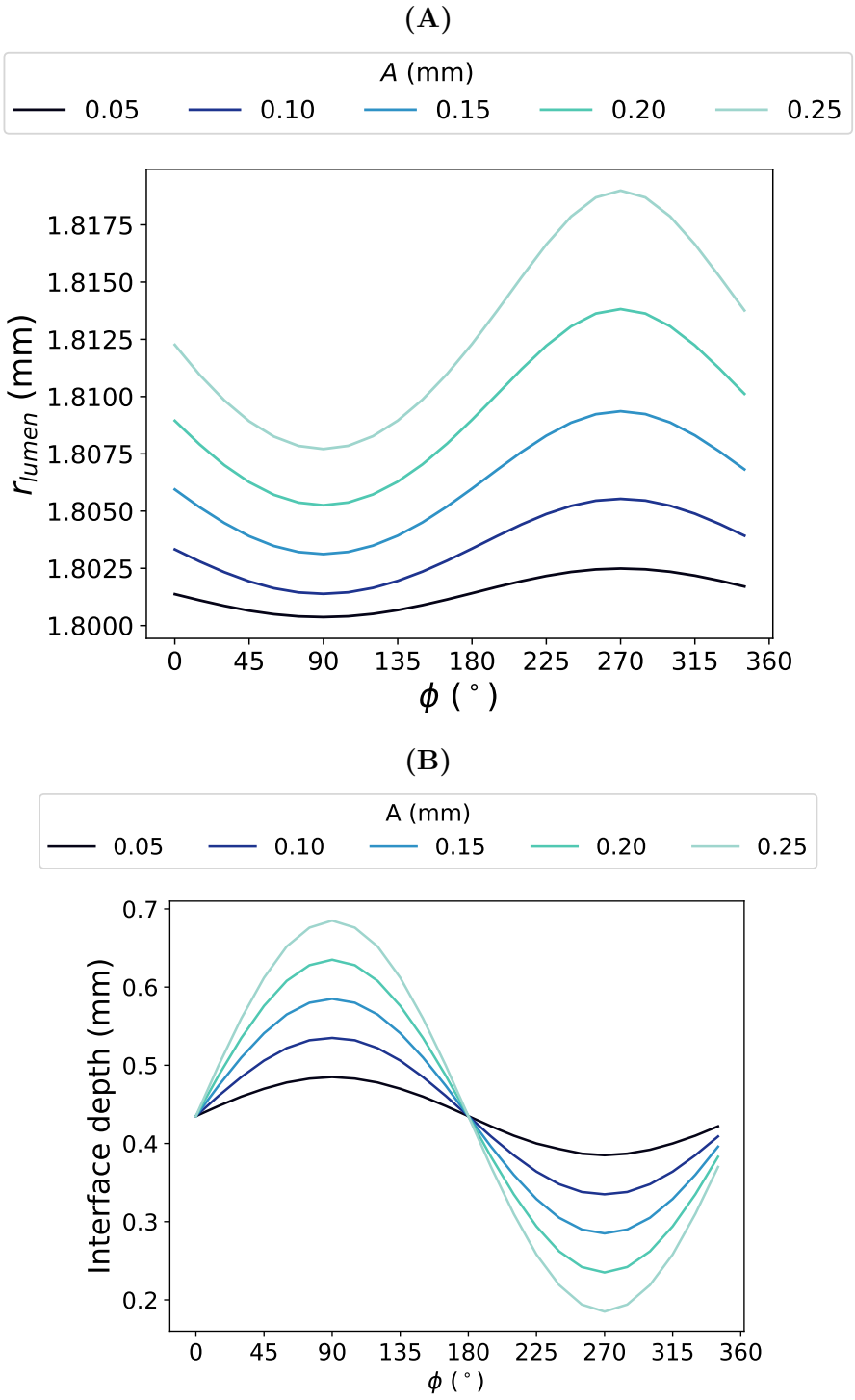


Figure 5.21: The impact of varying A on the **(A)** r_{lumen} at systolic pressure and **(B)** interface depth of PVA/gelatin grafts. Both **(A)** and **(B)** are presented as a function of ϕ.

5.3.5 Impact of Interface Frequency on Graft Biomechanics

5.3.5.1 Varying Interface Frequency: Stress Distribution

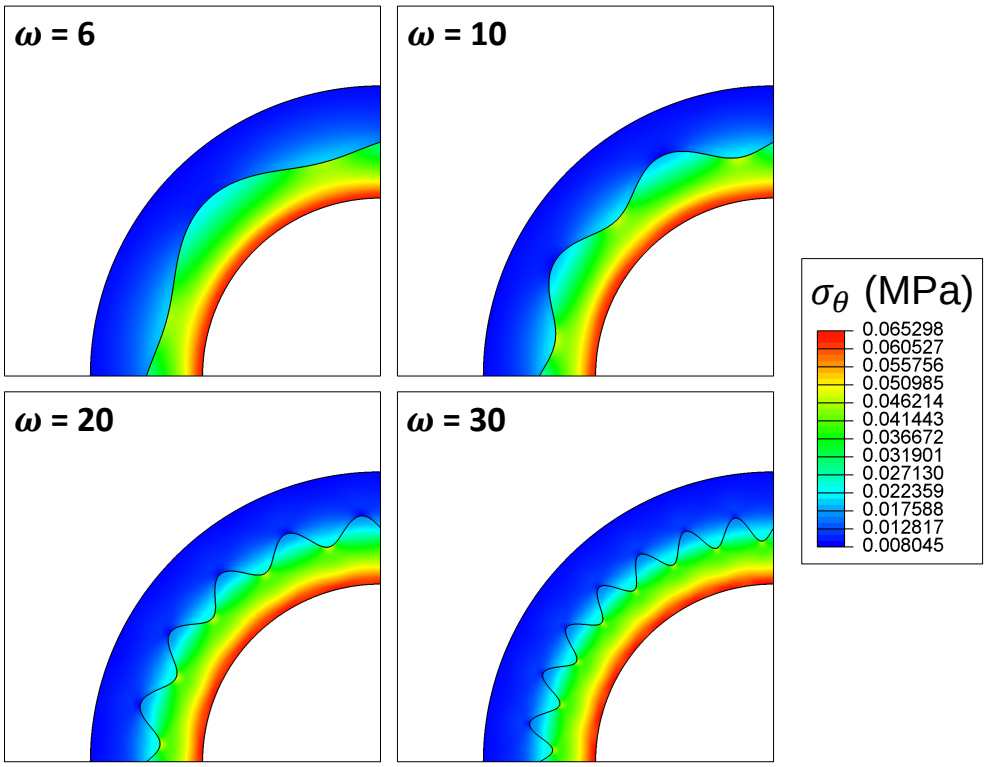


Figure 5.22: σ_θ distribution at systolic pressure when ω = 6, 10, 20 and 30.

The maximum σ_θ of each model was highest at the luminal surface across all phases, irrespective of ω (Figures 5.22 and 5.23). However, the magnitude of σ_θ at the luminal surface with increasing ω was dependent on ϕ (Figure 5.23). For instance, at $\phi = 0°$, the largest difference in luminal σ_θ was observed between the lowest (ω = 6) and highest (ω = 30) frequencies (0.0005 MPa). At $\phi = 270°$, the largest difference was observed between ω = 10 and ω = 30 (0.0016 MPa).

At all values of ϕ, σ_θ decreased across the IM–adventitia interface; increasing ω resulted in a smoother transition across the interface (Figure 5.22).

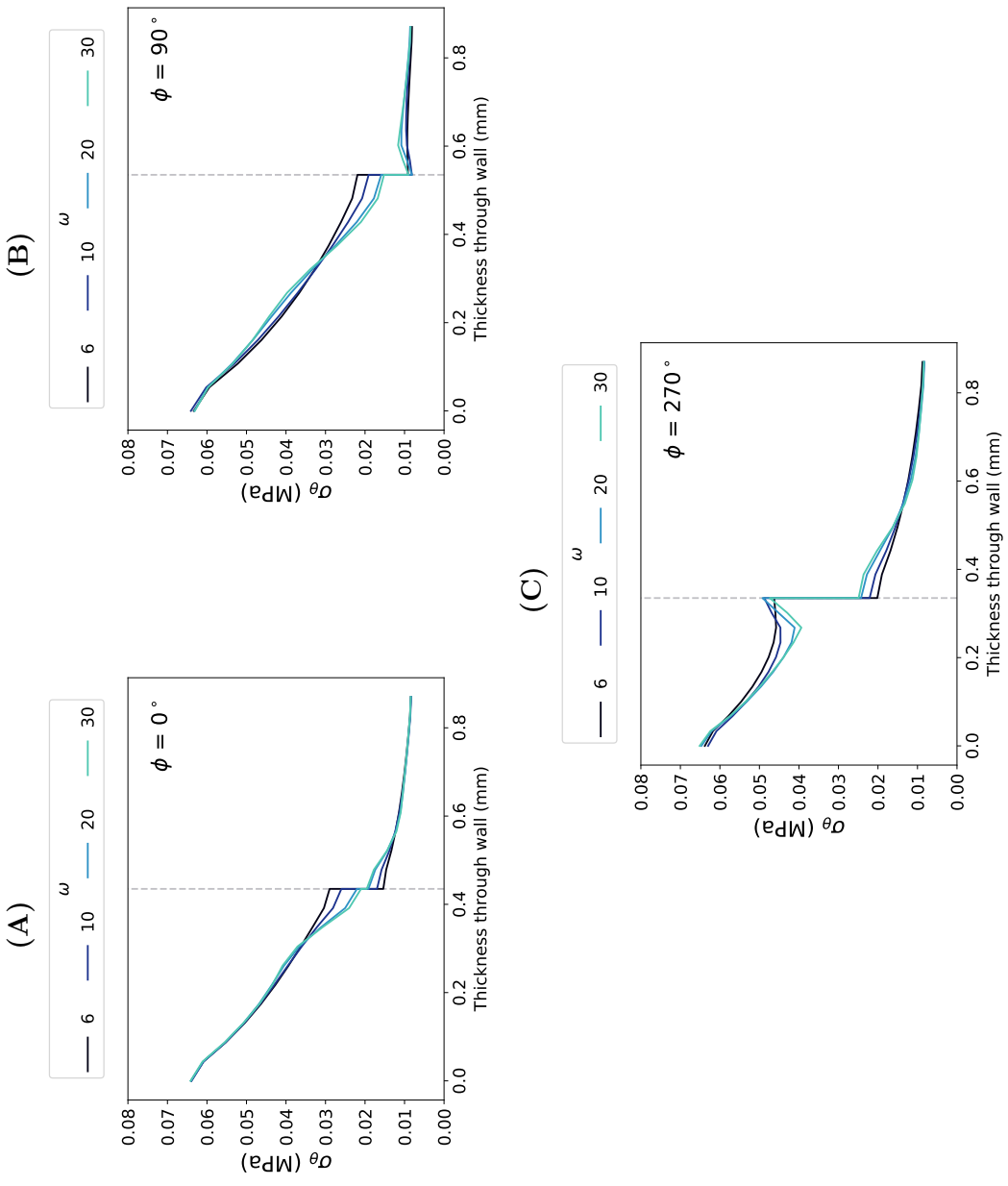


Figure 5.23: Transmural σ_θ distribution at systolic pressure with varying ω at **(A)** $\phi = 0°$, **(B)** $\phi = 90°$ and **(C)** $\phi = 270°$. Dashed lines show the interface at each ϕ.

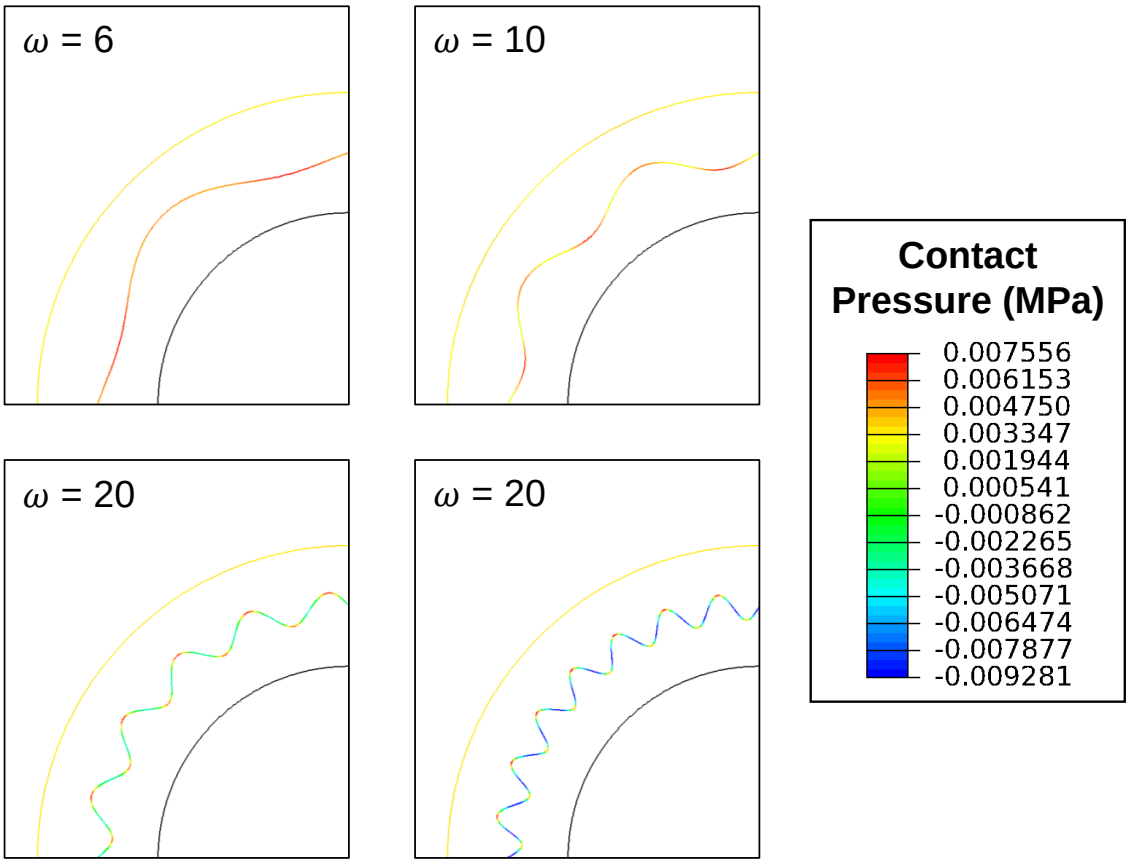


Figure 5.24: Contact pressures observed at the interface of all amplitude models at systolic pressure.

Table 5.5: Magnitude of the decrease in σ_θ across the IM–adventitia interface at the extremes of ϕ (0°, 90° and 270°) and ω (6 and 30) at systolic pressure.

DECREASE IN σ_θ ACROSS THE IM–ADVENTITIA INTERFACE			
ω	**0°**	**90°**	**270°**
6	0.0135 MPa	0.0127 MPa	0.0260 MPa
30	0.0014 MPa	0.0062 MPa	0.0225 MPa

Table 5.5 reports the decrease in σ_θ across the IM–adventitia interface at systolic pressure for the extremes of ϕ (0°, 90° and 270°) and ω (6 and 30).

When $\omega = 6$ and 10, the highest and lowest interface contact pressures were observed at $\phi = 270°$ and 0°, respectively (Figure 5.24). However, when $\omega = 20$ and

30, the highest contact pressure was shifted to $\phi = 90°$.

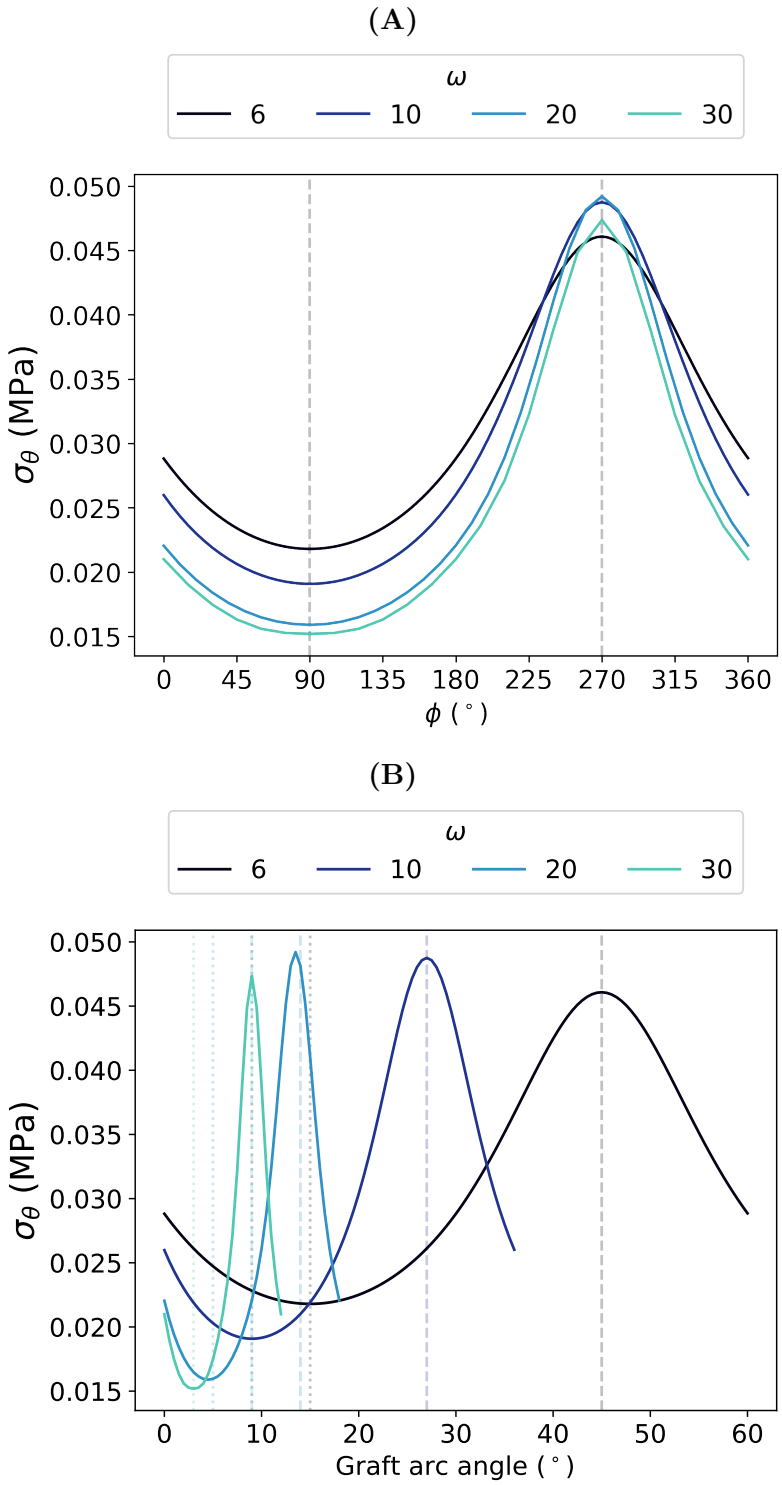


Figure 5.25: σ_θ along the interface at systolic pressure as a function of **(A)** ϕ of the interface and **(B)** graft arc angle. Dotted and dashed lines in **(B)** show arc angles corresponding to $\phi = 90°$ and $\phi = 270°$, respectively.

Figure 5.25A shows the variation in σ_θ along the interface as a function of ϕ for each frequency tested. As per the amplitude results presented in Section 5.3.4.1, σ_θ was lowest at $\phi = 90°$ and highest at $\phi = 270°$, reflecting the increased tension observed at the trough of the interface. The difference in σ_θ between the peak and trough of each wave increased from 0.024 MPa at $\omega = 6$ to 0.032 MPa at $\omega = 30$.

The circumferential properties of the interface, or the length of the interface around the graft circumference (as determined by the distance covered by one complete wavelength of the interface), varied with ω. Each interface was out of phase with each other; higher frequency interfaces had shorter wavelengths and thus corresponded to shorter arc lengths around the luminal circumference of the graft, as demonstrated graphically in Figure 5.5. As the arc length was restricted to the absolute dimensions of the graft investigated in this study, Figure 5.25B instead shows the variation in σ_θ along the interface at systolic pressure as a function of graft arc angle.

The interface resisted the intraluminal pressure load along its length. The impact of ω on this phenomenon was two-fold. First, at high ω, the load acting on one complete wavelength was distributed over a shorter length of interface compared with low ω. Second, the peaks and troughs of the wave became steeper with increasing ω. Figure 5.25B suggests that the latter increased the stress concentration experienced at the troughs of high ω interfaces. Together, these phenomena may explain the increased difference between the minimum and maximum σ_θ values along the interface at higher frequencies, as evidenced by the increased difference in σ_θ at the peaks and troughs of each wave.

5.3.5.2 Varying Interface Frequency: Compliance

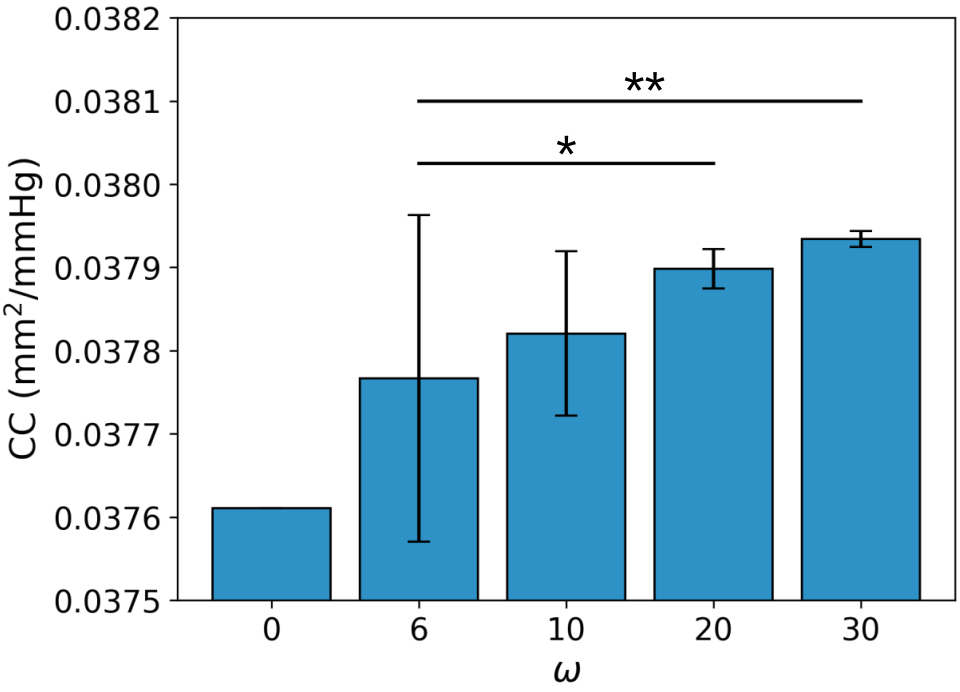


Figure 5.26: The impact of varying ω on the $\overline{CC}$ ($\pm$ SD) of PVA/gelatin grafts. *P<0.05; **P<0.01

Increasing the frequency of the sine wave increased the $\overline{CC}$ of the graft (Figure 5.26). When $\omega = 6$, $\overline{CC} = 0.0378 \pm 0.0002$ mm^2/mmHg. When $\omega = 30$, $\overline{CC} = 0.0379 \pm 9.8\times10^{-6}$ mm^2/mmHg. While the magnitude of $\overline{CC}$ increased with ω, statistical significance was only observed between $\omega = 6$ and $\omega = 20$ (P=0.027) and $\omega = 6$ and $\omega = 30$ (P=0.004).

The radial deformation became more uniform with increasing ω, as evidenced by the decrease in $\overline{CC}$ SD with ω (Figure 5.26). This was further illustrated by the decreased range of r_{lumen} values at higher frequencies. Figure 5.27 demonstrates the variation in r_{lumen} values between the lowest ($\omega = 6$) and highest ($\omega = 30$) frequencies tested. As the interfaces produced by both waves were out of phase with each other, r_{lumen} is plotted as a function of graft arc angle rather than the

phase of the interface. Consequently, the peak-to-trough height profile decreased with increasing ω (Table 5.6).

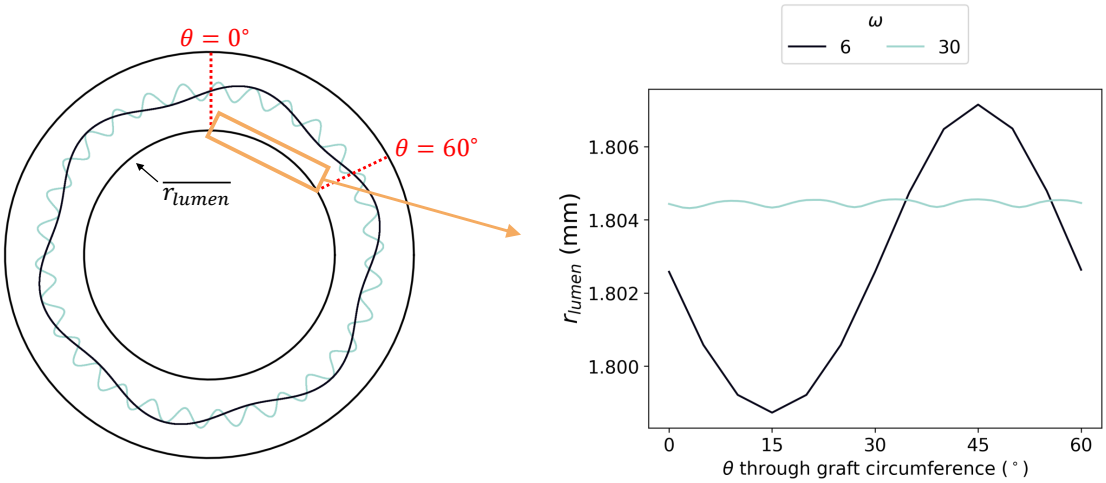


Figure 5.27: The impact of varying ω on r_{lumen} at systolic pressure with respect to graft arc angle.

Table 5.6: Peak-to-trough height profiles at the lumen surface as a function of ω at systolic pressure.

	$\omega = 6$	$\omega = 10$	$\omega = 20$	$\omega = 30$
Peak-to-trough height profile (µm)	8.41	4.15	0.68	0.20

5.3.6 Combining Interface Radius and Amplitude: Compliance

As proof-of-concept for the targeted optimisation of graft mechanical behaviours using multiple interface parameters, the combined effect of varying A (0.05 mm → 0.25 mm) and r (1:2, 1:1 and 2:1) on the $\overline{CC}$ (Figure 5.28A) and r_{lumen} (Figure 5.28B) of PVA/gelatin grafts was assessed. These values were then compared with literature compliance values for the coronary artery (Table 5.8).

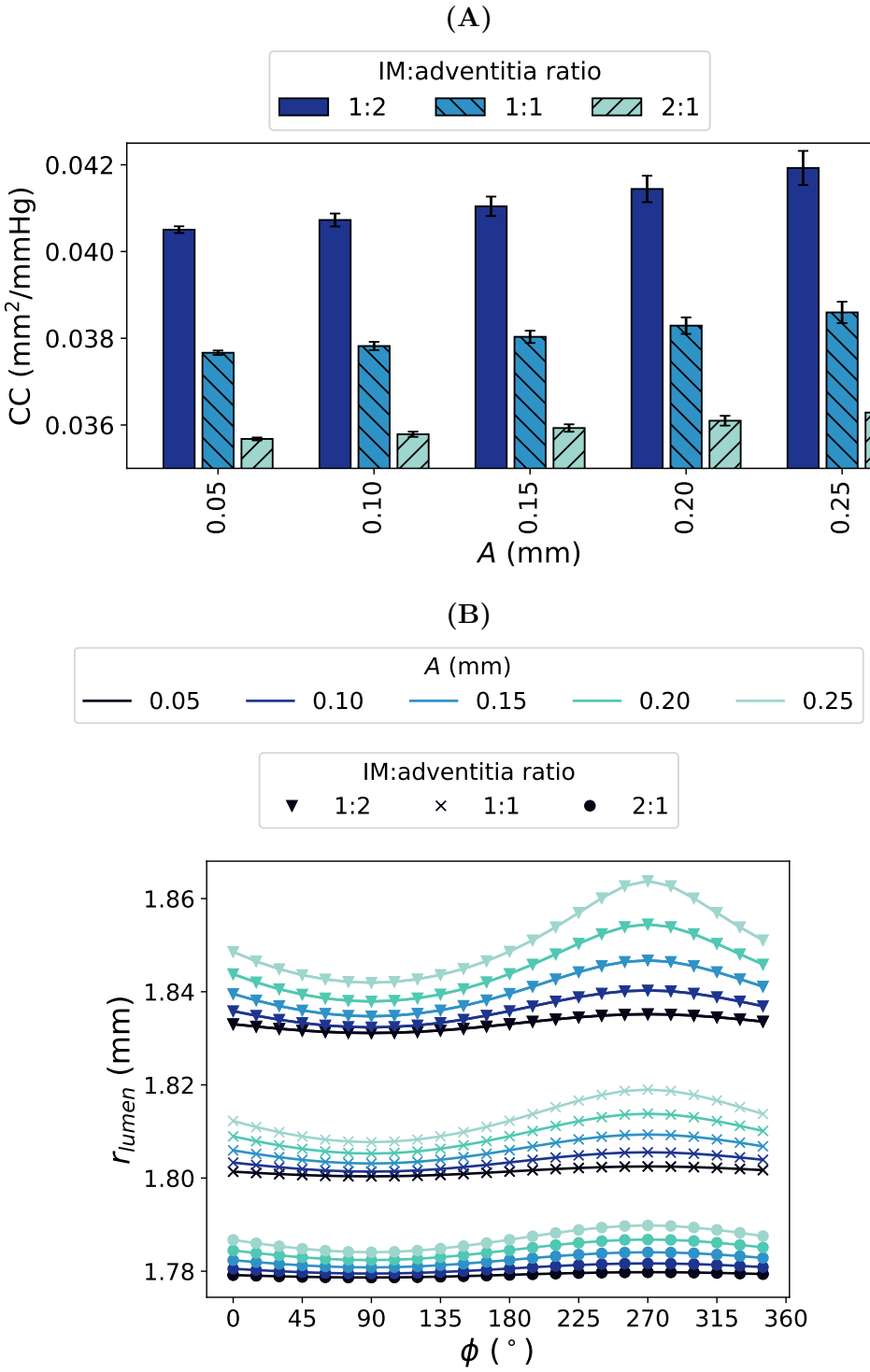


Figure 5.28: The impact of varying the r and A of bi-layered interdigitated PVA/gelatin grafts. (A) $\overline{CC} \pm$ SD; **(B)** r_{lumen} at systolic pressure. In all cases, $\omega = 10$.

The magnitude of $\overline{CC}$ was dominated by the IM:adventitia ratio (Figure 5.28A). Decreasing the relative volume of the stiffer IM layer, for instance, incurred a greater increase in $\overline{CC}$ than increasing A. This was also reflected in the magnitude of r_{lumen}; while increasing A increased the non-uniformity of r_{lumen} with ϕ, Figure 5.28B shows that the overall magnitude of deformation was primarily governed by the IM:adventitia ratio.

The extent to which larger amplitudes increased the non-uniformity of r_{lumen} was reduced by increasing the relative volume of the stiffer IM layer (Figure 5.28B). Consequently, the lumen surface height profiles were also reduced with increasing IM:A ratio. The smallest height profile was obtained when the IM:adventitia ratio was 2:1 and $A = 0.05$ mm (1.13 µm); conversely, the largest height profile was obtained when the IM:adventitia ratio was 1:2 and $A = 0.25$ mm (21.83 µm). When the IM:adventitia ratio was 1:2, the surface height profile ranged from 4.04 µm – 21.83 µm. When the volume of the IM was increased such that the IM:adventitia ratio was 2:1, the surface height profile spanned a smaller range of values (1.13 µm – 5.75 µm). The full list of peak-to-trough height profiles are listed in Table 5.7.

Table 5.7: Peak-to-trough height profiles at the lumen surface as a function of A and IM:adventitia ratio at systolic pressure.

	PEAK-TO-TROUGH HEIGHT PROFILE (µm)				
IM:adventitia ratio	$\boldsymbol{A = 0.05}$ **mm**	$\boldsymbol{A = 0.10}$ **mm**	$\boldsymbol{A = 0.15}$ **mm**	$\boldsymbol{A = 0.20}$ **mm**	$\boldsymbol{A = 0.25}$ **mm**
1:2	4.04	7.94	12.01	16.56	21.83
1:1	2.12	4.15	6.24	8.56	11.29
2:1	1.13	2.18	3.25	4.42	5.75

Table 5.8 shows the degree of compliance match between the bi-layered interdigitated PVA/gelatin grafts in Figure 5.28 and those reported for human and

porcine coronary arteries. Although variation of A and r extended the range of compliance values for PVA/gelatin grafts, both the absolute and normalised $\overline{CC}$ remained ≈100–200% larger compared with the native vessel.

Table 5.8: Compliance of bi-layered interdigitated PVA/gelatin grafts compared with human and porcine coronary arteries.

	Bi-layered interdigitated PVA/gelatin graft	**Human LAD coronary artery** [374]	**Porcine coronary artery** [157]
Systolic pressure (mmHg)	120	126.7 ± 5.8	120
Diastolic pressure (mmHg)	80	81.3 ± 3.8	80
$\overline{CC}$ **(mm²/mmHg)**	0.036–0.042	0.017 ± 3.8	–
$\overline{CC}$ **(%/100mmHg)**	20.12–22.11	–	6.69–8.02

5.4 Discussion

The influence of artery wall heterogeneity on the mechanical and biological functions of coronary arteries has remained a key theme throughout this thesis. Achieving structural biomimicry through the manufacture of multi-layered grafts is gaining traction in the field of small diameter vessel engineering. This is due to the roles that the intima, media and adventitia play in regulating the mechanical environment experienced by the endothelium and the resulting balance between healthy (anti-thrombogenic) and diseased (atherogenic) EC behaviour [150, 226]. Interlayer gradients may be achieved through variation of the material composition to form two or more distinct layers [240, 325–327]. This was the approach taken in Chapter 4, where it was observed that the stress/strain profiles and compliance of PVA/gelatin grafts could be tuned by varying the layer-specific cryogel composition. However, intralayer variations in properties – be they compositional or structural – have been significantly less explored. This is likely due to the limited ability of traditional man-

ufacturing processes (casting, dip-coating and electrospinning) to produce intralayer gradients or grafts with controlled interface geometries.

The advent of sub-zero AM offers a rich design space for the manufacture of functionally graded PVA cryogel-based constructs with optimised complex internal structures [15, 271, 375]. Of these, controlling the interface(s) between adjacent tissue layers through toolpath design presents a compelling parameter in the creation of functionally graded implants [16]. It should be noted that, while sub-zero AM is the intended manufacturing route for functionally-graded grafts, the current resolution of sub-zero AM (0.26 mm [15]) is lower than that required to accurately print the sinusoidal interfaces investigated in this study. Until strategies that increase the resolution of sub-zero AM are reported in the literature, the design of such grafts is limited solely to the computational realm.

In the meantime, there is outstanding need for computational simulations that aim to identify and optimise print parameters such as toolpath that induce gradiated wall stiffnesses and/or circumferential stress profiles that promote anti-pathogenic EC function. FEA is firmly established as an effective platform to accelerate the design and optimisation of graded orthopaedic implants under physiological load [272–274]. Yet, FEA remains a relatively untapped resource in the assessment of novel coronary artery graft designs.

This chapter has used FEA to explore the impact of a bioinspired sinusoidal interface – as has been experimentally manufactured using sub-zero AM in recent work [371] – on the circumferential stress pattern and compliance of bi-layered PVA/gelatin grafts.

5.4.1 Modelling the Contact Between Interdigitated Surfaces

This study modelled the quasi-static expansion of interdigitated PVA/gelatin grafts under intraluminal loading up to systolic pressure. The discussion section of Chapter 4 highlighted the lack of literature defining the contact interactions between two PVA/gelatin surfaces and the importance of accurately defining such interactions when increasing graft design complexity. Thus, before analysing the impact of a complex interface on transmural stress distribution, it was necessary to establish a suitable contact formulation that would emulate the expected movement between graft layers without introducing unrealistic displacements and/or stress concentrations at the interface.

Figure 5.10 demonstrates the stress independency of laminated models when using friction coefficients, implementing rough friction or tying the surfaces together. σ_θ was governed only by the relative material properties and thicknesses of both layers. These data verified the assumptions outlined in Chapter 4 where, in lieu of a friction coefficient between two PVA cryogel surfaces, a friction coefficient of 0.04 was chosen according to the friction coefficient of PVA cryogel and titanium alloy [306]. However, the same friction coefficient caused anti-parallel sliding of the two layers upon introduction of the interdigitated interface. This tangential slip amplified stress concentrations at the peaks and troughs of the interdigitated wave, regardless of the PVA/gelatin composition used to model each layer. While x_θ is presented for systolic pressure in Section 5.3.2, tangential slip occurred from the first step increment of all interdigitated models (8 mmHg).

The adhesive behaviour between interfacing cryogel layers under an applied load (and the magnitude of force responsible for failure) is not well defined for any mode of loading in the literature. Instead, this behaviour must be qualitatively inferred from

existing studies of hydrogel-based FGBMs. This lack of knowledge is further narrowed by the choice of manufacturing method used to fabricate heterogeneous grafts. For instance, the casting method proposed by Wahab *et al.* exploited the diffusion between adjacent PVA solutions to form continuously graded constructs with intermediary zones [362]. In this case, tying adjacent interfaces may be an applicable assumption. Conversely, materials printed using extrusion-based AM techniques are subject to interface formation both between and within successive print layers [16, 376]. When PVA is extruded onto a frozen print bed, physical crosslinks form between adjacent filaments [16]. However, the extent of crosslinking is governed by the freezing process. Interfacing regions may be vulnerable to excessive deformation and delamination when placed under tension [376]; the decreased bond strength between parallel strands of 3D-printed PVA cryogel has been recognised as a potential mechanism of premature sample failure under uniaxial tension [16]. Tied surface constraints likely oversimplify the local deformations and displacements that may occur between adjacent printed regions under physiological loading; on the other hand, static friction coefficients are unable to model the expected delamination failure mechanism.

Caution should therefore be exercised when using friction coefficients to model the contact between interdigitated or interlocking hydrogel layers. For the purpose of this thesis, a rough (infinite) friction constraint was implemented to prohibit relative slip between the two graft layers while allowing analysis of the contact pressure at the interface. This simplification assumes the two layers remain adhered when the graft is pressurised to systolic pressure. To validate this assumption, experimental data quantifying the local displacement of interdigitated interfaces under physiologically-relevant loading (eg tracking local strains through digital image correlation [376]) are needed.

The conclusions derived from these simulations further reinforce the need to adequately report and/or explore the contact between interfacing layers in the FEA of multi-layered vascular grafts. In a study of a composite vascular scaffold comprised of a knitted wire mesh embedded in a polyurethane scaffold, Sirry *et al.* used static friction coefficients between 0.2–0.55 to model the tangential surface interactions between the two components [377]. Meanwhile, Byrne *et al.* tied separate material sections of their fibre-reinforced graft using a tie constrant [23]. Though both studies developed grafts using alternative VMMs, the inclusion of complex geometrical elements – and thus more complex stress–strain behaviour – warrants further exploration of contact properties of VMMs in interfacing regions.

5.4.2 Analysis of Sine Wave Parameters on Graft Biomechanics

Sinusoidal waveforms are attractive design components in cardiovascular tissue engineering as they mimic the crimping (and subsequent stiffening under increasing pressure) behaviour exhibited by collagen fibres [371] and elastic lamellae. For instance, Byrne *et al.* embedded sinusoidal polyurethane fibres in a soft silicone matrix to provide hyperelastic reinforcement to composite medium-large vascular grafts [23]. Sinusoidal filament networks have also been explored in the wider context of soft tissue engineering; by varying the filament period and amplitude-to-period ratio, Meng *et al.* demonstrated how the mechanical properties of PCL scaffolds can be tuned between 27–1944 kPa [378]. Importantly, the ability to create mathematically-driven toolpaths using AM enables printing of sinusoidal PVA/gelatin cryogel fibres using sub-zero AM [371]. A bioinspired sinusoid was therefore explored as the complex interface in this study.

The custom Python script developed to create the sinusoidal interface granted control over three key sine wave parameters: r, A and ω. Variations in r and A at fixed ω predominantly altered the radial composition of the IM and adventitia. By contrast, variations in ω at fixed r and A predominantly altered the circumferential composition of the two layers. Subsequently, this study determined that the transmural σ_θ distribution, luminal displacement and CC of bi-layered interdigitated PVA/gelatin grafts subjected to physiological pressures were dependent on the phase and/or graft angle at which they were measured. This was an important finding as it emphasised the need to evaluate stress patterns (including concentrations) and lumen displacement with respect to the interface waveform.

The ability to vary the radial and circumferential composition of the IM and adventitia through the amplitude and frequency of a sinusoidal interface around the graft circumference presents a compelling method to manufacture functionally graded vascular grafts. Compared with non-interdigitated interfaces, the transmural σ_θ gradients at $\phi = 0°$ and $\phi = 180°$ (which have the same radial depth as the non-interdigitated interface) were 'phased' (the stress distribution was more continuous). Moreover, the degree of phasing increased with increasing A. This behaviour mimics the role of residual stresses in native coronary arteries, which minimise intramural σ_θ gradients derived from blood pressure [379]. However, this phased behaviour was achieved at the expense of increased σ_θ at the luminal surface (which residual stresses have been found to decrease [380]) and intramural σ_θ concentrations at $\phi = 270°$, both of which were exacerbated at higher amplitudes.

Troughs are an intrinsic property of sinusoidal waveforms. High intramural stress concentrations alter EC morphology and are associated with decreased turnover of ECM proteins [381, 382]. Furthermore, based on studies of coronary arteries [383, 384], it is speculated that increased stretching at the troughs of the

interface may increase EC permeability and facilitate LDL accumulation in the IM layer of the graft. Together, these data suggest that sinusoidal interfaces may provide both atheroprotective and atherogenic cues to the endothelium. Experimental validation of these graft designs should therefore aim to investigate the impact of interface variables on EC expression of cyclic stretch-mediated mechanosensitive genes.

Intriguingly, the phased behaviour at $\phi = 0°$ – as yielded at higher amplitudes – was achievable at lower amplitudes by increasing ω. This was achieved without significantly increasing σ_θ at the luminal surface; moreover, as A was kept constant for each frequency simulation, σ_θ concentrations at $\phi = 270°$ were comparatively lower than at higher A. It is hypothesised that the phased behaviour of σ_θ with increasing A and ω are caused by the bifurcation of behaviour as a direct consequence of the interface. Bifurcation theory is a deeply mathematical concept that describes the way that a system varies under parametric changes [385]. In the context of this research, it could explain how σ_θ behaves relative to the interface until a theshold A and ω, upon which is acts independently. For instance, consider the σ_θ contour maps in Figure 5.22: when $\omega = 6$, the distribution of σ_θ was dependent on the interface geometry; when $\omega = 20$, it became independent of the interface geometry. This behaviour may be attributed to an assumption related to the FE model (eg mesh density) or may be representative of physical phenomena. Chapter 6, Section 6.3 will address the implications of this hypothesis in more detail. Nevertheless, it is hypothesised that the combination of A and ω may be tuned to maximise atheroprotective σ_θ-derived cues. Future work should therefore look to evaluate a combined amplitude/frequency parameter sweep on transmural σ_θ patterns using both *in silico* and *in vitro* testing.

In addition to mediating σ_θ distribution, the magnitude and range of CC

increased with increasing r, A and ω. Of the three sinusoidal parameters, r and A had the biggest impact on the magnitude of $\overline{CC}$. This was unsurprising given the reliance of lumen deformation and compliance on radial composition. Increasing r increased the relative amount of stiff IM layer, decreasing CC. As A was increased, the relative amount of compliant outer adventitial layer in circumferential segments closer to the lumen increased. Thus, in grafts with larger A, the compliant adventitia bore more of the pressure load compared with grafts of lower A. This resulted in larger $\overline{CC}$ as a function of A, as shown in Figure 5.20. This trend is in agreement with the study by Byrne *et al.*, where grafts designed with the largest fibre amplitude yielded the highest compliance across mean pressures of 0–130 mmHg [23].

Furthermore, as A was increased, the radial deformation around the lumen became more non-uniform as a function of ϕ. This was reflected in the larger range of lumen radii observed at larger amplitudes (Figure 5.21A). r_{lumen} was smallest at phases containing more of the inner IM layer, where the interface was furthest away from the lumen ($\phi = 90°$). The increased stiffness at these phases resulted in decreased radial deformation, yielding lower CC values. On the other hand, r_{lumen} was largest at phases containing more of the outer adventitial layer ($\phi = 90°$). The decreased stiffness at these phases resulted in increased radial deformation and larger CC values.

The ability to control graft compliance through interface design has exciting consequences for the development of coronary artery tissue replacements. Synthetic grafts are often developed according to an idealised isotropic or orthotropic tubular geometry, yet coronary arteries exhibit location-specific compliance along their length [157]. Extending the parametrically-driven toolpath developed in this study into a third dimension could allow for graded compliance along the length

of the graft. Graded compliance could also help to reduce compliance mismatch at anastamoses or even mediate disrupted flow patterns experienced near bifurcations [386, 387], which could in theory be used to minimise turbulent flow patterns that promote an atherogenic EC phenotype, drive endothelial damage and trigger inflammatory signalling cascades [108].

While this thesis has focused on the manufacture of haemocompatible PVA/gelatin grafts, the ability to control graft compliance through interface design may also find use in the design of coronary artery phantoms. Synthetic tissue phantoms are important tools in the diagnostic field, as they present an efficient and cost-effective method of developing and validating novel imaging techniques by simulating the coronary artery without the use of biological tissue and/or animal models [388, 389]. Varying the compliance around the circumference, such as may be expected when modelling a stenosed artery, could be achieved by increasing the relative volume of stiff IM:adventitia (shifting r) and/or increasing the amplitude to reflect regions with neointimal hyperplasia or plaque formation. Together, these data suggest that interface design could provide an effective avenue for manufacturing a variety of physiologically-relevant coronary artery graft constructs.

Irrespective of application, it is evident that the $\overline{CC}$ of the PVA/gelatin graft designs evaluated in this study were more compliant between diastolic and systolic pressure than the native coronary artery wall. This finding matches the conclusions drawn from the tri-layered non-interdigitated grafts in Chapter 4. Given that the interdigitated waveform increases compliance relative to a non-interdigitated graft, this chapter further highlights the need for cryogel compositions with sufficient strain-stiffening behaviour over physiological pressure. To achieve a closer compliance match in terms of magnitude, stiffer compositions of PVA/gelatin cryogel are required. While this could be achieved by increasing the cryogel concentration [103],

decreased viscosity and subsequent loss of geometric fidelity presents a problem for extrusion-based sub-zero AM [10]. Alternatively, the stiffness of PVA/gelatin cryogel could be improved through fibre reinforcement, either through direct addition of fibres to the polymer solution [390–392] or through the combination of sub-zero AM and electrospinning [269]. For instance, the compliance of PVA/gelatin cyrogel has been shown to decrease when the lumen is reinforced with an electrospun mat of PVA-SbQ (PVA modified with styrylpyridinium pendant groups) fibres [269]. In all cases, the FE models developed within this thesis could be used as tools to help validate the compliance of grafts made from additional PVA/gelatin compositions.

An interesting consequence of the interdigitated interface was the introduction of pressure-induced luminal surface waviness due to non-uniform radial expansion when loaded to systole. If a VMM is to be used in endothelium-contacting and blood-interfacing graft constructs, it is imperative to understand the impact that its surface topography has on its haemocompatibility. For instance, VMMs with microscale surface roughness have higher thromobogenic potential than those with nanoscale roughness due to the increased surface area for platelet activation and adhesion [393]. On the other hand, incorporating sub-micron ridges into the VMM surface (0.05–2 µm) may attenuate thromobogenicity by limiting platelet adhesion to the peaks of the grooves, where the surface area is minimised [393, 394]. Furthermore, compared with smooth surfaces, increased endothelialisation rates and EC alignment have been observed on VMMs with structured anisotropic nano- and microscale ridged topographies [395, 396]. It must be emphasised that the *in silico* expansion behaviour of the interdigitated grafts reported in this study did not consider the initial surface roughness and require experimental validation. However, the results presented in this thesis suggest that interface design may be a viable target toward the generation of surface topographies that are representative of the native

intima under physiological loading.

For each graft design, the peak-to-trough height of the lumen at systolic pressure was reported to quantify the maximum deviation in the lumen height profile. Of the three sinusoidal interface parameters explored in this study, the luminal height profile was most susceptible to variations in amplitude and radius; the largest height profile (21.83 µm) was obtained for the largest amplitude when the IM:adventitia ratio was set to 1:2. The surface topographies of the grafts in this study met the standard reported for porcine LAD coronary arteries, where circumferential and longitudinal height profiles span ≈10 µm [102, 397]. While sub-micron features elicit desirable surface characteristics compared with smooth surfaces, there is a growing body of evidence associating increased intimal surface roughness with the onset and progression of atherosclerosis [398]. Computational fluid dynamics models have indicated that local minima in the surface height profile of porcine LAD coronary arteries correspond to regions of atherogenic WSS [397]. As the sinusoidal interfaces formed sinusoidal surface features, these findings suggest scope for research into alternative interface waveforms that promote haemocompatible topographies while minimising atherogenic trough formation.

5.5 Conclusion

This chapter aimed to increase the geometric complexity of the heterogeneous tri-layered PVA/gelatin graft designs in Chapter 4 through the inclusion of a bioinspired sinusoidal interface between graft layers. It was hypothesised that a sinusoidal interface could be used to alter the stress pattern across interfacing tissue layers and induce gradual changes in transmural stress – a physiologically relevant yet critically underexplored concept in the field of cardiovascular tissue engineering

that has the potential to reduce atherogenic stress concentrations linked to graft failure. Recent studies have demonstrated the potential to fabricate functionally-graded PVA cryogel-based lattice structures using sub-zero AM. On the basis that such grafts could one day become viable through sub-zero AM, the study presented in this chapter sought to explore the impact of interface design on graft biomechanics using FEA. To summarise, this study has:

- Presented a method to generate a 2D sinusoidal waveform interface using Abaqus' Scripting Interface that grants the user parametric control over three key interface parameters: r, A and ω;
- Evaluated the impact that friction coefficients and tied surface constraints have on modelling the relative displacement and transmural stress of laminated and complex interdigitated interfaces. Notably, a static friction coefficient was unable to model the expected displacement of a complex interface; setting $\mu = \infty$ is suggested until such time that experimental data are available;
- Demonstrated that the inclusion of an interdigitated interface decreases graft compliance with respect to a laminated interface, that compliance was dependent upon the phase of the interface, and that compliance was predominantly influenced by variations in r and A;
- Demonstrated that the inclusion of an interdigitated interface 'phases' transmural σ_θ to decrease the discontinuity of stress across the interface; this behaviour was observed with increasing A and ω and was dependent upon the phase of the interface wave or the graft arc angle;
- Uncovered the formation of lumen 'waviness' as a result of non-uniform radial expansion, the magnitude of which was determined by r, A and ω.

Chapter Six

GENERAL DISCUSSION AND CONCLUSIONS

6.1 Thesis Summary

After almost four decades of tissue engineering research, the search for clinically viable, small-diameter tissue-engineered grafts remains limited by a lack of suitable VMMs for implantation. Despite substantial research into the *in vitro* biomechanical behaviour of VMMs, small-diameter grafts – including those designed for CABG – are often associated with poor patency and implant failure. PVA/gelatin cryogels are prospective VMMs thanks to their composition- and manufacturing-specific mechanical behaviours and documented capacity for endothelialisation. Compared with their homogeneous counterparts, heterogeneous, multi-layered grafts better meet the extensive design requirements needed to replicate the structure and function of coronary arteries. Thus, this thesis hypothesised that PVA/gelatin cryogel can be used to manufacture heterogeneous, biomimetic coronary artery grafts with layer-specific biomechanical properties representative of the artery wall. The

thesis objectives were completed as follows:

- The linear elastic, dynamic viscoelastic and hyperelastic properties of PVA/gelatin cryogel were quantitatively characterised according to variations in M_w PVA and use of polymer coagulation treatment;
- Experimental hyperelastic test data were integrated with computational FE models, enabling the *in silico* assessment of four heterogeneous laminated graft designs under physiological pressure relative to the coronary artery wall. The results not only highlighted the impact of layer composition on matching the quasi-static biomechanical response of PVA/gelatin grafts with native tissue, but also the impact of hyperelastic constitutive model choice on modelling these responses;
- A parametrically-controlled, bioinspired sinusoidal interface was incorporated into a bi-layered graft *in silico* to investigate the impact of complex interface design on the transmural biomechanics of PVA/gelatin grafts. The ability to introduce graded intramural mechanical properties through variation of interface design parameters was demonstrated, representing a novel approach to achieving functionally graded coronary artery grafts.

6.2 Impact, Novelty and Contribution to the Field

To date, the basic mechanical properties [13, 199, 297, 298] and endothelialisation [12, 13, 172, 174, 207] of PVA/gelatin hydrogels have been reported, highlighting their potential as homogeneous VMMs. However, the link between the mechanical behaviour of PVA/gelatin grafts when subjected to a dynamic haemodynamic environment and the resulting mechanotransductive behaviours of ECs is critically

underresearched. This thesis combined experimental and computational methods to not only characterise the viscoelasticity and hyperelasticity of PVA/gelatin cryogel, but to model the stress and compliance of *heterogeneous* PVA/gelatin grafts under physiological pressure for the first time. By matching the biomechanical response of multi-layered PVA/gelatin grafts with that of the native wall and assessing the impact this may have on atheroprotective versus atherogenic EC behaviour, this thesis has taken a novel and important step towards bridging the gap between the mechanical and biological characterisation of PVA/gelatin grafts.

Chapter 3 quantified the linear elastic, dynamic viscoelastic and hyperelastic properties of PVA/gelatin cryogel as a function of two key formulation parameters: the M_w of PVA and the use of polymer coagulation treatment. The research implications of the data presented in this chapter are two-fold. First, the data extend current understanding of the mechanical behaviour of PVA/gelatin cryogel – largely limited to linear elastic moduli – under physiologically relevant loading conditions. Notably, these parameters can be varied to yield quasi-static and dynamic stiffnesses resembling those reported in the literature for coronary arteries; these findings further support the potential of PVA/gelatin as a mechanically-relevant VMM. Second, the constitutive parameters generated from each mechanical test facilitate the development of computational models of PVA/gelatin-based coronary artery grafts. Such computational models could be used to supplement experimental data by allowing prediction of physiological graft behaviours that are not readily observed *in vitro*, such as the transmural stress distribution or dynamic viscoelastic response under physiological loading. Thus, the dynamic viscoelastic and hyperelastic constitutive parameters quantified in this thesis contribute to the field of cardiovascular tissue engineering research by enabling computational research into complex biomechanical behaviours relevant to arterial tissue.

Chapter 4 successfully developed a framework for designing multi-layered PVA/gelatin cryogel grafts informed by the hyperelastic data produced in Chapter 3. For the first time, FEA has been used to probe these behaviours in PVA/gelatin coronary artery grafts. Exemplified using four tri-layered laminated PVA/gelatin graft designs, it was shown that layer composition impacts the transmural stress and strain distribution when loaded to systolic pressure. Furthermore, it was demonstrated that the layer composition could be varied to yield grafts with transmural biomechanics that qualitatively match those observed through the coronary artery wall. Building upon a study that modelled the impact of layer-specific elastic moduli on the circumferential stress of electrospun vascular grafts, [275] the simulations presented in this chapter reinforce the inadequacy of homogeneous grafts to replicate the biomechanics of the native wall and provide further justification for biomimetic, multi-layered graft designs. Importantly, while the PVA/gelatin grafts studied in this thesis were more compliant than the coronary artery wall, the framework developed in this thesis provides a useful design aid for the development of other hyperelastic VMMs intended for CABG.

Finally, Chapter 5 demonstrated the impact of a geometrically complex interface on the compliance and transmural stress distributions of heterogeneous bi-layered PVA/gelatin grafts. Despite the functionally-graded nature of the artery wall, the development of FGBMs thus far has been restricted to the arena of hard tissue engineering. The data obtained in this chapter address this untapped area of research by demonstrating the potential of interface design to engineer functionally-graded coronary artery grafts. It was not only demonstrated that surface contact interactions have a significant role on the radial expansion behaviour of interdigitated grafts, but that a homogenenised ('phased') stress field – a physiologically relevant concept that is achieved in native arteries through the existence of residual stresses

– can be theoretically obtained as a function of interface amplitude and frequency. Specifically, interface amplitude and radius can be used to produce subtle changes in graft compliance and lumen surface characteristics, while interface frequency can be used to reduce intramural circumferential stress concentrations as a function of the phase of the interface. The implications of these results paves the way for an exciting yet unexplored research theme in cardiovascular tissue engineering: the ability to incorporate functionally graded biomechanics through biomimetic interface design, and the impact that interface design may have on generating atheroprotective or atherogenic cues for ECs.

6.3 Limitations

There are several limitations associated with the research presented in this thesis; these can be broadly categorised as limitations pertaining to the collection of experimental data, or limitations concerning the computational assumptions adopted during FEA. It is imperative to address prominent limitations and suggest potential routes to overcome them.

First, the casting method used to manufacture PVA and PVA/gelatin cryogel samples in Chapter 3 yielded isotropic samples. While arteries may be considered incrementally isotropic at low physiological strain [399, 400], the layer-specific orientation and dispersion of elastin and collagen fibres throughout the wall imparts direction-specific, or anisotropic, mechanical properties when subject to high physiological load [400]. Fibre orientation provides resistance to stretch and thus contributes to arterial compliance at physiological pressure. Recapitulating the anisotropic properties of coronary arteries in VMMs may improve graft patency and help to maintain vessel function *in vivo* [401].

Orthotropic PVA cryogel can be obtained using the FT under drawing method, whereby a uniaxial stress/strain is applied during the freezing step to induce fibre alignment parallel to the applied stress/strain [179, 402]. Due to the extrusion of PVA fibres during sub-zero AM, sub-zero AM PVA cryogel also exhibits orthotropic mechanical properties relative to the print direction and nozzle size [16]. As sub-zero AM is the expected route of manufacture for the interdigitated PVA/gelatin graft designs in Chapter 5, it is imperative that future work characterises the constitutive material properties of sub-zero PVA/gelatin cryogel such that FE models can accurately reflect their mechanical behaviour under pressure.

While compression testing is relevant in the characterisation of VMMs [291], the mechanical testing performed in this thesis was limited to uniaxial loading. Pressurised arteries, and therefore implanted grafts, experience multi-axial physiological load states (uniaxial tension, uniaxial compression and biaxial tension [291]) that cannot be completely captured by uniaxial loading. Future work should therefore look to obtain mechanical test data across multiple deformation modes to help improve the accuracy of the FE model. For instance, the accuracy of the Ogden model can be increased when data from multiple loading modes are available, as this would allow higher order models to be fitted [93, 98].

All mechanical testing was performed in air (ie dry test conditions) and at room temperature due to the setup of the mechanical testing machine. While the DMA of coronary arteries has been performed under similar conditions [102], the preferred approach is to test the sample in the wet state and at 37 °C [286, 288, 291, 292, 302]. The latter conditions are more representative of the *in vivo* environment and therefore allow better prediction of material behaviour under physiological conditions [403]. Both the quasi-static [403, 404] and dynamic [405] mechanical properties of biological tissues and biomaterials can change depending on the relative humidity

and/or hydration. Therefore, to aid translation of PVA/gelatin cryogel as a viable VMM, additional mechanical characterisation tests are needed (eg immersion DMA) to approximate its mechanical properties *in vivo*.

The FEA results presented in this thesis demonstrated that the compliance of PVA/gelatin grafts was higher than the coronary artery wall. Weaknesses in the graft wall may lead to bulging when exposed to haemodynamic stresses post-implantation. It is likely that stiffer compositions of PVA/gelatin would be needed to provide reinforcement under physiological loads. These may be obtained using additional formulation or manufacturing parameters: cryogel concentration is perhaps the simplest method of increasing bulk stiffness [103]. However, highly concentrated PVA solutions have poor flowability due to their increased viscosity [10]; alternative parameters may need targeting to ensure compability with sub-zero AM. An alternative approach would be to look at increasing the anisotropic and strain stiffening behaviour of PVA/gelatin within the physiological pressure range experienced by coronary arteries. In their quest to develop synthetic tendons, Hua *et al.* used a combination of directional freezing and polymer coagulation to increase the micro- and nano-alignment of PVA/gelatin cryogel networks [198]. Incorporating a similar network structure in the adventitia could be an effective way of decreasing graft compliance. Future work should look to characterise PVA/gelatin over a broader spectrum of formulation and manufacturing parameters and simulate their distensibility using the FEA approach developed in Chapters 4 and 5.

The FE models developed in this thesis represent a crucial tool toward the design and validation of functionally graded coronary artery grafts and selecting candidates for manufacture. Nevertheless, certain assumptions were applied to decrease model complexity. Notably, residual stresses were not incorporated into the coronary artery models in Chapter 4. Modelling the layer-specific residual stresses

of arteries is complex; it is not uncommon for FE studies to neglect their contribution to arterial biomechanics [406]. Yet, compressive residual stresses in the inner wall and tensile residual stresses in the outer wall reduce stress concentrations both transmurally and at the luminal surface [380]. Recent studies have demonstrated the impact of neglecting residual stresses in tri-layered models of the artery wall on exaggerating stress contributions, especially within the intima [406]. If these coronary artery FE models are to provide a benchmark for synthetic grafts, future work must aim to incorporate layer-specific residual stresses.

From the data presented in Chapter 5, the root cause of the phased behaviour of interdigitated grafts could not be ascertained. The circumferential stress behaved relative to the interface up until a threshold amplitude or frequency, upon which it acted independently ('phased'). The behaviour of a system can change once a threshold point is met; this behaviour is analogous to a vibrating cantilever beam that changes mode shape as the vibration frequency changes [385]. This behaviour could be caused by methodological choice (such as mesh density relative to the interface wavelength or contact definition), or it could be created by a bifurcation in the real-world, physical behaviour of the system.

To assess the former, a much broader parameter sweep of FE variables is needed to ensure that phased behaviour is not a direct consequence of the FE system. To assess the latter requires a deep understanding of the mathematical concepts behind bifurcation theory [385], which falls outside of the scope of this thesis. As the physical system has not been investigated experimentally, there is no previous research to confirm or reject either hypothesis. Research investigating the role of geometry in governing the mechanical behaviour of triangular suture joints reported a similar homogeneous stress distribution [370]. The computational nature of the study raises similar questions to this research. As such, this interesting and promising result will

require investigation through future research trajectories.

6.4 Future Work

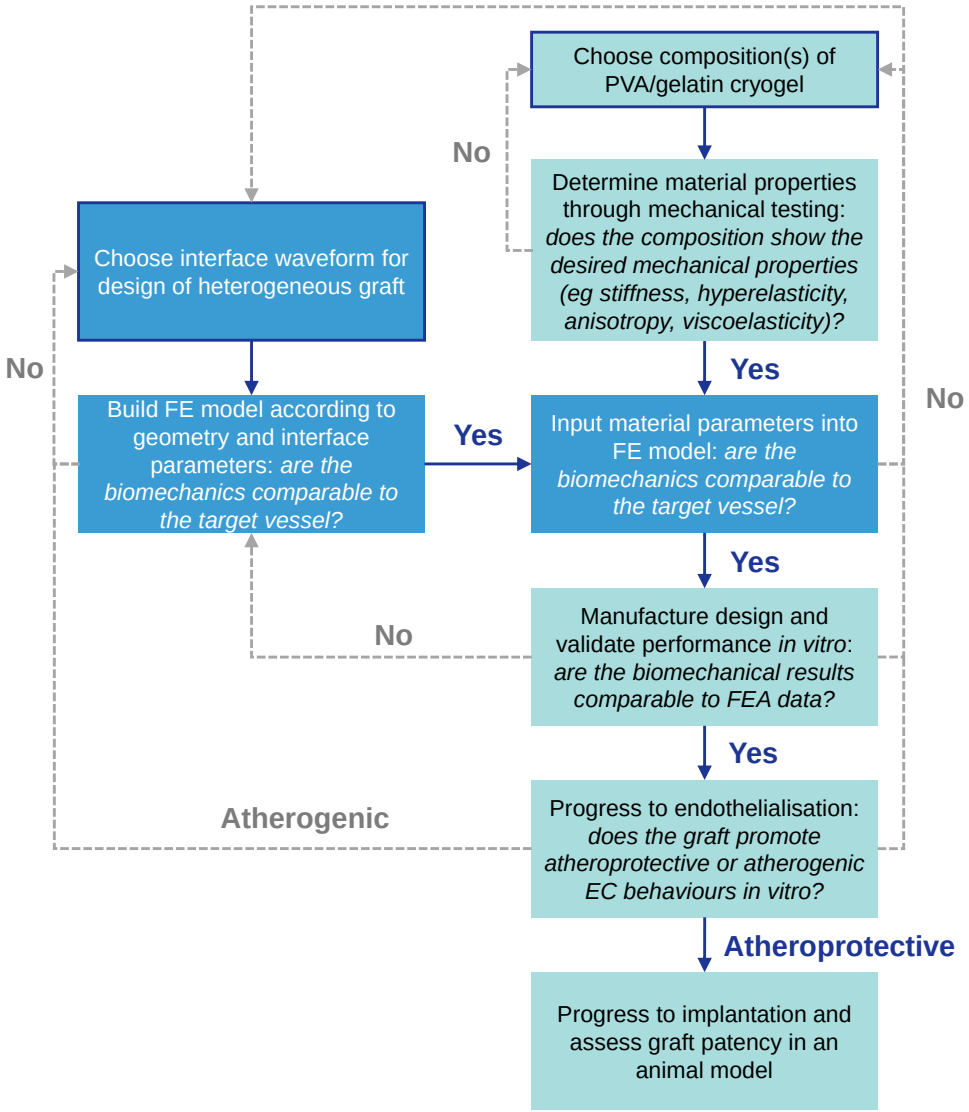


Figure 6.1: Anticipated future trajectory of this thesis. The boxes with solid outlines represent the starting points for the experimental (aqua) and computational (blue) workstreams; if at any point undesirable biomechanical or haemocompatible behaviours surface, the research should circle back to both starting points.

This thesis has laid the groundwork for designing multi-layered coronary artery grafts. Future work should aim to characterise the hyperelasticity of additional PVA/gelatin compositions and use the FEA framework to obtain grafts that more closely match the layer-specific biomechanics and compliance of the native wall. An additional avenue of research should look at extending the FE model to incorporate the dynamic viscoelastic behaviour reported in Chapter 3, as this would allow investigation into the nature of elastic recoil and energy dissipation of synthetic grafts under dynamic loading and how this compares to the native wall. Such models would also complement an emerging area of fundamental cardiovascular research: understanding the impact of matrix viscosity on EC mechanotransduction [407].

The common denominator between many of the limitations discussed in Section 6.3 is the need for experimental validation of the simulated graft designs. A pivotal next step in the development of heterogeneous, functionally graded coronary artery grafts will be to assess whether the biomechanical metrics observed *in silico* (eg compliance) match those observed *in vitro*. Sub-zero AM has demonstrated promise

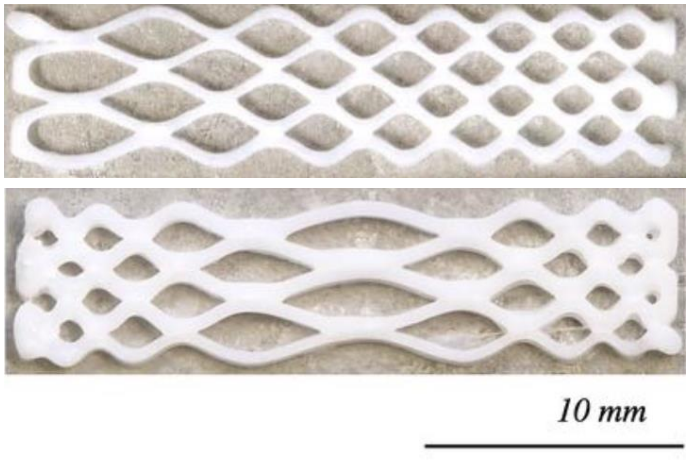


Figure 6.2: Sub-zero AM has been used to fabricate functionally graded PVA cryogel lattice structures with variable sinusoidal wavelengths. Reprinted from [371] with permission from the author.

toward the complex design of functionally graded PVA cryogel lattice structures (Figure 6.2), [371]) and is the predicted method for future functionally graded graft manufacture. While FEA has been successfully used to parametrically expand the design space made available by sub-zero AM, it is clear that the latter technique needs further refinement before it can be used to create functionally graded small diameter grafts. Most notably, print replicability and resolution remain key drawbacks to the approach. Once these practical issues have been addressed, the link between the biomechanical behaviours of different heterogeneous graft designs and EC behaviour must also be determined. For this validation, the author suggests quantifying the expression of mechanosensitive genes seeded to tubular grafts using polymerase chain reaction analysis. Figure 6.1 summarises the anticipated future trajectory of this thesis and the steps that are needed to take heterogeneous grafts from computational simulations to functional and potentially implantable grafts.

References

1. *Global Heart Circulatory Diseases Factsheet* (British Heart Foundation, 2023).
2. Wilkins, E. *et al. European Cardiovascular Disease Statistics 2017* (European Heart Network, Brussels, 2017).
3. Roth, G. A. *et al.* Global burden of cardiovascular diseases and risk factors, 1990–2019: Update from the GBD 2019 study. *Journal of the American College of Cardiology* **76,** 2982–3021 (2020).
4. *United Nations Sustainable Development Goal 3: Good health and well-being* https://www.un.org/sustainabledevelopment/health/ (2022).
5. *World health statistics 2021: monitoring health for the SDGs, sustainable development goals* (Geneva: World Health Organization, 2021).
6. Eschenhagen, T. & Zimmermann, W. H. Engineering myocardial tissue. *Circulation Research* **97,** 1220–1231 (2005).
7. Wu, J. *et al.* Tissue-engineered vascular grafts: balance of the four major requirements. *Colloid and Interface Science Communications* **23,** 34–44 (2018).
8. Salacinski, H. J., Goldner, S., Giudiceandrea, A., Hamilton, G. & Seifalian, A. M. The mechanical behavior of vascular grafts: a review. *Journal of Biomaterials Applications* **15,** 241–278 (2001).
9. Miramini, S. *et al.* The status and challenges of replicating the mechanical properties of connective tissues using additive manufacturing. *Journal of the Mechanical Behavior of Biomedical Materials* **103,** 103544 (2020).
10. Adelnia, H. *et al.* Freeze/thawed polyvinyl alcohol hydrogels: present, past and future. *European Polymer Journal* **164,** 110974 (2022).
11. Kumar, A. & Han, S. S. PVA-based hydrogels for tissue engineering: a review. *International Journal of Polymeric Materials and Polymeric Biomaterials* **66,** 159–182 (2017).
12. Vrana, N. E., Cahill, P. A. & McGuinness, G. B. Endothelialization of PVA/gelatin cryogels for vascular tissue engineering: effect of disturbed shear stress conditions. *Journal of Biomedical Materials Research Part A* **94,** 1080–1090 (2010).

13. Liu, Y., Vrana, N., Cahill, P. & McGuinness, G. Physically crosslinked composite hydrogels of PVA with natural macromolecules: structure, mechanical properties, and endothelial cell compatibility. *Journal of Biomedical Materials Research Part B: Applied Biomaterials: An Official Journal of The Society for Biomaterials, The Japanese Society for Biomaterials, and The Australian Society for Biomaterials and the Korean Society for Biomaterials* **90,** 492–502 (2009).

14. Pompe, W. *et al.* Functionally graded materials for biomedical applications. *Materials Science and Engineering: A* **362,** 40–60 (2003).

15. Tan, Z., Parisi, C., Di Silvio, L. & Forte, A. E. Cryogenic 3D printing of super soft hydrogels. *Scientific Reports* **7,** 16293–16304 (2017).

16. Crolla, J., Britton, M., Espino, D. & Thomas-Seale, L. The orthotropic viscoelastic characterisation of sub-zero 3D-printed poly(vinyl alcohol) cryogel. *MRS Advances* **6,** 467–471 (2021).

17. Kim, H., Yang, G. H., Choi, C. H., Cho, Y. S. & Kim, G. Gelatin/PVA scaffolds fabricated using a 3D-printing process employed with a low-temperature plate for hard tissue regeneration: fabrication and characterizations. *International Journal of Biological Macromolecules* **120,** 119–127 (2018).

18. Karimi, A., Navidbakhsh, M., Faghihi, S., Shojaei, A. & Hassani, K. A finite element investigation on plaque vulnerability in realistic healthy and atherosclerotic human coronary arteries. *Proceedings of the Institution of Mechanical Engineers, Part H: Journal of Engineering in Medicine* **227,** 148–161 (2012).

19. Lally, C., Dolan, F. & Prendergast, P. Cardiovascular stent design and vessel stresses: a finite element analysis. *Journal of Biomechanics* **38,** 1574–1581 (2005).

20. Schiavone, A., Zhao, L. & Abdel-Wahab, A. Effects of material, coating, design and plaque composition on stent deployment inside a stenotic artery–finite element simulation. *Materials Science and Engineering: C* **42,** 479–488 (2014).

21. Migliavacca, F., Petrini, L., Colombo, M., Auricchio, F. & Pietrabissa, R. Mechanical behavior of coronary stents investigated through the finite element method. *Journal of Biomechanics* **35,** 803–811 (2002).

22. Rogers, C., Tseng, D. Y., Squire, J. C. & Edelman, E. R. Balloon-artery interactions during stent placement: a finite element analysis approach to pressure, compliance and stent design as contributors to vascular injury. *Circulation Research* **84,** 378–383 (1999).

23. Byrne, O., Coulter, F., Roche, E. T. & O'Cearbhaill, E. D. In silico design of additively manufacturable composite synthetic vascular conduits and grafts with tuneable compliance. *Biomaterials Science* **9,** 4343–4355 (2021).

24. Drake, R., Vogl, A. W. & Mitchell, A. *Gray's Anatomy for Students, Fourth Edition* (Elsevier, 2019).

25. Aaronson, P. I., Ward, J. P. & Connolly, M. J. *The Cardiovascular System at a Glance, 5th Edition* (John Wiley & Sons, 2020).

26. Traore, M. A. & George, S. C. Tissue engineering in the vascular tree. *Tissue Engineering: Part B* **23,** 505–514 (2017).

27. Gasser, T. C., Ogden, R. W. & Holzapfel, G. A. Hyperelastic modelling of arterial layers with distributed collagen fibre orientations. *Journal of the Royal Society Interface* **3,** 15–35 (2006).

28. Wagenseil, J. E. & Mecham, R. P. Vascular extracellular matrix and arterial mechanics. *Physiological Reviews* **89,** 957–989 (2009).

29. Barallobre-Barreiro, J. *et al.* Extracellular matrix in vascular disease, part 2/4: JACC focus seminar. *Journal of the American College of Cardiology* **75,** 2189–2203 (2020).

30. Félétou, M. *The endothelium, Part I: Multiple functions of the endothelial cells–focus on endothelium-derived vasoactive mediators* (Morgan Claypool Life Sciences, 2011).

31. Chistiakov, D. A., Orekhov, A. N. & Bobryshev, Y. V. Endothelial barrier and its abnormalities in cardiovascular disease. *Frontiers in Physiology* **6,** 365 (2015).

32. Van Hinsbergh, V. V. Endothelial permeability for macromolecules. *Arteriosclerosis, Thrombosis, and Vascular Biology* **17,** 1018–1023 (1997).

33. Yau, J. W., Teoh, H. & Verma, S. Endothelial cell control of thrombosis. *BMC Cardiovascular Disorders* **15,** 1–11 (2015).

34. Wang, M., Hao, H., Leeper, N. J. & Zhu, L. Thrombotic regulation from the endothelial cell perspectives. *Arteriosclerosis, Thrombosis, and Vascular Biology* **38,** e90–e95 (2018).

35. Cook-Mills, J. M. & Deem, T. L. Active participation of endothelial cells in inflammation. *Journal of Leukocyte Biology* **77,** 487–495 (2005).

36. Wettschureck, N., Strilic, B. & Offermanns, S. Passing the vascular barrier: endothelial signaling processes controlling extravasation. *Physiological Reviews* **99,** 1467–1525 (2019).

37. Mas, M. A close look at the endothelium: its role in the regulation of vasomotor tone. *European Urology Supplements* **8,** 48–57 (2009).

38. Tang, E. H. & Vanhoutte, P. Endothelial dysfunction: a strategic target in the treatment of hypertension? *Pflügers Archiv-European Journal of Physiology* **459,** 995–1004 (2010).

39. Muñoz-Chápuli, R., Quesada, A. & Ángel Medina, M. Angiogenesis and signal transduction in endothelial cells. *Cellular and Molecular Life Sciences CMLS* **61,** 2224–2243 (2004).

40. Michiels, C. Endothelial cell functions. *Journal of Cellular Physiology* **196,** 430–443 (2003).

41. Ricard, N., Bailly, S., Guignabert, C. & Simons, M. The quiescent endothelium: signalling pathways regulating organ-specific endothelial normalcy. *Nature Reviews Cardiology* **18,** 565–580 (2021).

42. Dawson, A., Wang, Y., Li, Y., LeMaire, S. A. & Shen, Y. H. New technologies with increased precision improve understanding of endothelial cell heterogeneity in cardiovascular health and disease. *Frontiers in Cell and Developmental Biology* **9,** 1–12 (2021).

43. Rajendran, P. *et al.* The vascular endothelium and human diseases. *International Journal of Biological Sciences* **9,** 1057–1069 (2013).

44. Dela Paz, N. G. & D'Amore, P. A. Arterial versus venous endothelial cells. *Cell and Tissue Research* **335,** 5–16 (2009).

45. Aird, W. C. Phenotypic heterogeneity of the endothelium: II. representative vascular beds. *Circulation Research* **100,** 174–190 (2007).

46. Peng, Z., Shu, B., Zhang, Y. & Wang, M. Endothelial response to pathophysiological stress. *Arteriosclerosis, Thrombosis, and Vascular Biology* **39,** e233–e243 (2019).

47. Jana, S., Hu, M., Shen, M. & Kassiri, Z. Extracellular matrix, regional heterogeneity of the aorta, and aortic aneurysm. *Experimental Molecular Medicine* **51,** 1–15 (2019).

48. Patil, M. S., Cartland, S. P. & Kavurma, M. M. TRAIL signals, extracellular matrix and vessel remodelling. *Vascular Biology* **2,** R73–R84 (2020).

49. Ma, Z., Mao, C., Jia, Y., Fu, Y. & Kong, W. Extracellular matrix dynamics in vascular remodeling. *American Journal of Physiology-Cell Physiology* **319,** C481–C499 (2020).

50. Hoskins, P. R., Lawford, P. V. & Doyle, B. J. *Cardiovascular Biomechanics* (Springer, 2017).

51. Chow, M.-J., Turcotte, R., Lin, C. P. & Zhang, Y. Arterial extracellular matrix: a mechanobiological study of the contributions and interactions of elastin and collagen. *Biophysical Journal* **106,** 2684–2692 (2014).

52. Chen, H. *et al.* Biaxial deformation of collagen and elastin fibers in coronary adventitia. *Journal of Applied Physiology* **115,** 1683–1693 (2013).

53. Chen, H. Y. *et al.* Mis-sizing of stent promotes intimal hyperplasia: impact of endothelial shear and intramural stress. *American Journal of Physiology-Heart and Circulatory Physiology* **301,** H2254–H2263 (2011).

54. Abbott, W. M. *et al.* The glycocalyx: a central regulator of vascular function. *American Journal of Physiology–Regulatory, Integrative and Comparative Physiology* **320,** R508–R518 (2021).

55. Florian, J. A. *et al.* Heparan sulfate proteoglycan is a mechanosensor on endothelial cells. *Circulation Research* **93,** e136–e142 (2003).

56. Mitra, R. *et al.* Glycocalyx in atherosclerosis-relevant endothelium function and as a therapeutic target. *Current Atherosclerosis Reports* **19,** 1–13 (2017).

57. Mattson, J. M., Turcotte, R. & Zhang, Y. Glycosaminoglycans contribute to extracellular matrix fiber recruitment and arterial wall mechanics. *Biomechanics and Modeling in Mechanobiology* **16,** 213–225 (2017).

58. Cavalcante, F. S. *et al.* Mechanical interactions between collagen and proteoglycans: implications for the stability of lung tissue. *Journal of Applied Physiology* **98,** 672–679 (2005).

59. Steucke, K. E., Tracy, P. V., Hald, E. S., Hall, J. L. & Alford, P. W. Vascular smooth muscle cell functional contractility depends on extracellular mechanical properties. *Journal of Biomechanics* **48,** 3044–3051 (2015).

60. Wang, G., Jacquet, L., Karamariti, E. & Xu, Q. Origin and differentiation of vascular smooth muscle cells. *Journal of Physiology* **593,** 3013–3030 (2015).

61. Cao, G. *et al.* How vascular smooth muscle cell phenotype switching contributes to vascular disease. *Cell Communication and Signaling* **20,** 180–202 (2022).

62. Shadwick, R. E. Mechanical design in arteries. *The Journal of Experimental Biology* **202,** 3305–3313 (1999).

63. Leloup, A. J. *et al.* Elastic and muscular arteries differ in structure, basal NO production and voltage-gated Ca^{2+}- channels. *Frontiers in Physiology* **6,** 375 (2015).

64. Akyildiz, A. C., Barrett, H. E. & Gijsen, F. J. *Chapter 18 – Identification of coronary plaque mechanical properties from ex vivo testing* (Academic Press, 2021).

65. Ostadfar, A. *Chapter 2 – Macrocirculation system* (Academic Press, 2016).

66. Nelson, J., Wani, O., May, H. & Budoff, M. Potential benefits of eicosapentaenoic acid on atherosclerotic plaques. *Vascular Pharmacology* **91,** 1–9 (2017).

67. Van Trier, T. *et al.* Lifestyle management to prevent atherosclerotic cardiovascular disease: evidence and challenges. *Netherlands Heart Journal* **30,** 3–14 (2022).

68. Mundi, S. *et al.* Endothelial permeability, LDL deposition, and cardiovascular risk factors–a review. *Cardiovascular Research* **114,** 35–52 (2018).

69. Tabas, I. & Bornfeldt, K. E. Macrophage phenotype and function in different stages of atherosclerosis. *Circulation Research* **118,** 653–667 (2016).

70. Wen, Y. & Leake, D. S. Low density lipoprotein undergoes oxidation within lysosomes in cells. *Circulation Research* **100,** 1337–1343 (2007).

71. Poznyak, A. V. *et al.* Overview of oxLDL and its impact on cardiovascular health: focus on atherosclerosis. *Frontiers in Pharmacology* **11,** 613780 (2021).

72. Obermayer, G., Afonyushkin, T. & Binder, C. Oxidized low-density lipoprotein in inflammation-driven thrombosis. *Journal of Thrombosis and Haemostasis* **16,** 418–428 (2018).

73. Poston, R. N. Atherosclerosis: integration of its pathogenesis as a self perpetuating propagating inflammation: a review. *Cardiovascular Endocrinology Metabolism* **8,** 51–61 (2019).

74. Hegyi, L., Skepper, J. N., Cary, N. R. & Mitchinson, M. J. Foam cell apoptosis and the development of the lipid core of human atherosclerosis. *The Journal of Pathology* **180,** 423–429 (1996).

75. Basatemur, G. L., Jørgensen, H. F., Clarke, M. C., Bennett, M. R. & Mallat, Z. Vascular smooth muscle cells in atherosclerosis. *Nature Reviews Cardiology* **16,** 727–744 (2019).

76. Rosano, G. M. C., Fini, M., Caminiti, G. & Barbaro, G. Cardiac metabolism in myocardial ischemia. *Current Pharmaceutical Design* **14,** 2551–2562 (2008).

77. *Global Heart Circulatory Diseases Factsheet* (British Heart Foundation, 2022).

78. Tsao, C. W. *et al.* Heart disease and stroke statistics–2022 update: a report from the American Heart Association. *Circulation* **145,** e153–e639 (2022).

79. Melly, L., Torregrossa, G., Lee, T., Jansens, J.-L. & Puskas, J. D. Fifty years of coronary artery bypass grafting. *Journal of Thoracic Disease* **10,** 1960–1967 (2018).

80. Mangiacapra, F., De Bruyne, B., Wijns, W. & Bartunek, J. Optimizing revascularization strategies in coronary artery disease for optimal benefit to patients. *Clinical Pharmacology and Therapeutics* **90,** 630–633 (2011).

81. Serruys, P. W. *et al.* Percutaneous coronary intervention versus coronary-artery bypass grafting for severe coronary artery disease. *New England Journal of Medicine* **360,** 961–972 (2009).

82. Lee, S. E. *et al.* Coronary artery bypass graft versus percutaneous coronary intervention in acute heart failure. *Heart* **106,** 50–57 (2020).

83. Canver, C. C. Conduit options in coronary artery bypass surgery. *Chest* **108,** 1150–1155 (1995).

84. Subbu, V., Boey, F. & Lao, L. L. Implanted cardiovascular polymers: natural, synthetic and bio-inspired. *Progress in Polymer Science* **33,** 853–874 (2008).

85. Goldman, S. *et al.* Long-term patency of saphenous vein and left internal mammary artery grafts after coronary artery bypass surgery: results from a Department of Veterans Affairs Cooperative Study. *Journal of the American College of Cardiology* **44,** 2149–2156 (2004).

86. Hisayoshi, S. Arterial grafts in coronary bypass surgery. *Annals of Thoracic and Cardiovascular Surgery: Official journal of the Association of Thoracic and Cardiovascular Surgeons of Asia* **5,** 141–145 (1999).

87. Jashari, R., Van Hoeck, B., Ngakam, R., Goffin, Y. & Fan, Y. Banking of cryopreserved arterial allografts in Europe: 20 years of operation in the European Homograft Bank (EHB) in Brussels. *Cell Tissue Bank* **14,** 589–599 (2013).

88. Friedman, S. G., Lazzaro, R. S., Spier, L. N., Moccio, C. & Tortolani, A. J. A prospective randomized comparison of Dacron and polytetrafluoroethylene aortic bifurcation grafts. *Surgery* **117,** 7–10 (1995).

89. Mallis, P., Kostakis, A., Stavropoulos-Giokas, C. & Michalopoulos, E. Future perspectives in small-diameter vascular graft engineering. *Bioengineering* **7,** 160–200 (2020).

90. Isenberg, B. C., Williams, C. & Tranquillo, R. T. Small-diameter artificial arteries engineered in vitro. *Circulation Research* **98,** 25–35 (2006).

91. Hibbeler, R. *Mechanics of Materials, tenth edition* (Hoboken, NJ: Pearson, 2015).

92. Mihai, A. L. & Goriely, A. How to characterize a nonlinear elastic material? A review on nonlinear constitutive parameters in isotropic finite elasticity. *Proceedings of the Royal Society A: Mathematical, Physical and Engineering Sciences* **473,** 20170607 (2017).

93. Melly, S. K., Liu, L., Liu, Y. & Leng, J. A review on material models for isotropic hyperelasticity. *International Journal of Mechanical System Dynamics* **1,** 71–88 (2021).

94. Holzapfel, G. A., Gasser, T. C. & Ogden, R. W. A new constitutive framework for arterial wall mechanics and a comparative study of material models. *Journal of Elasticity* **61,** 1–48 (2000).

95. Nolan, D., Gower, A., Destrade, M., Ogden, R. & Mcgarry, J. A robust anisotropic hyperelastic formulation for the modelling of soft tissue. *Journal of the Mechanical Behavior of Biomedical Materials* **39,** 48–60 (2014).

96. Vahapoğlu, V. & Karadeniz, S. Constitutive equations for isotropic rubber-like materials using phenomenological approach: a bibliography (1930–2003). *Rubber Chemistry and Technology* **79,** 489–499 (2006).

97. Bahreman, M., Darijani, H. & Fooladi, M. Constitutive modeling of isotropic hyperelastic materials using proposed phenomenological models in terms of strain invariants. *Polymer Engineering and Science* **56,** 249–370 (2016).

98. Ali, A., Hosseini, M. & Sahari, B. A review of constitutive models for rubber-like materials. *American Journal of Engineering and Applied Sciences* **3,** 232–239 (2010).

99. Wex, C., Arndt, S., Stoll, A., Bruns, C. & Kupriyanova, Y. Isotropic incompressible hyperelastic models for modelling the mechanical behaviour of biological tissues: a review. *Biomedical Engineering/Biomedizinische Technik* **60,** 577–592 (2015).

100. Brighenti, R., Artoni, F. & Cosma, M. P. Viscous and failure mechanisms in polymer networks: a theoretical micromechanical approach. *Materials* **12,** 1576–1593 (2019).

101. Roylance, D. *Engineering viscoelasticity* (Department of Materials Science and Engineering–Massachusetts Institute of Technology, Cambridge MA, 2001), 1–37.

102. Burton, H. E., Freij, J. M. & Espino, D. M. Dynamic viscoelasticity and surface properties of porcine left anterior descending coronary arteries. *Cardiovascular Engineering and Technology* **8,** 41–56 (2017).

103. Crolla, J., Britton, M., Espino, D. & Thomas-Seale, L. The dynamic viscoelastic characterisation and magnetic resonance imaging of poly(vinyl alcohol) cryogel: identifying new attributes and opportunities. *Materials Science and Engineering: C* **129,** 112383–112396 (2021).

104. Li, W., Shepherd, D. E. & Espino, D. M. Frequency dependent viscoelastic properties of porcine brain tissue. *Journal of the Mechanical Behavior of Biomedical Materials* **102,** 103460 (2020).

105. Fulcher, G. R., Hukins, D. W. & Shepherd, D. E. Viscoelastic properties of bovine articular cartilage attached to subchrondral bone at high frequencies. *BMC Musculoskeletal Disorders* **10,** 61–68 (2009).

106. Charbonier, F. W., Zamani, M. & Huang, N. F. Endothelial cell mechanotransduction in the dynamic vascular environment. *Advanced Biosystems* **3,** 1800252 (2019).

107. James, B. D. & Allen, J. B. Vascular endothelial cell behavior in complex mechanical microenvironments. *ACS Biomaterials Science and Engineering* **4,** 3818–3842 (2018).

108. Chatterjee, S. Endothelial mechanotransduction, redox signaling and the regulation of vascular inflammatory pathways. *Frontiers in Physiology* **9,** 524 (2018).

109. Katranas, S. A., Kelekis, A. L., Antoniadis, A. P., Ziakas, A. G. & Giannoglou, G. D. Differences in stress forces and geometry between left and right coronary artery: a pathophysiological aspect of atherosclerosis heterogeneity. *Hellenic Journal of Cardiology* **56,** 217–223 (2015).

110. Ding, Z., Zhu, H. & Friedman, M. H. Coronary artery dynamics in vivo. *Annals of Biomedical Engineering* **30,** 419–429 (2002).

111. Hartman, E. M. *et al.* The definition of low wall shear stress and its effect on plaque progression estimation in human coronary arteries. *Scientific Reports* **11,** 22086 (2021).

112. Gijsen, F. *et al.* Expert recommendations on the assessment of wall shear stress in human coronary arteries: existing methodologies, technical considerations, and clinical applications. *European Heart Journal* **40,** 3421–3433 (2019).

113. Samady, H. *et al.* Coronary artery wall shear stress is associated with progression and transformation of atherosclerotic plaque and arterial remodeling in patients with coronary artery disease. *Circulation* **124,** 779–788 (2011).

114. Califano, J. P. & Reinhart-King, C. A. Exogenous and endogenous force regulation of endothelial cell behavior. *Journal of Biomechanics* **43,** 79–86 (2010).

115. Ando, J. & Yamamoto, K. Hemodynamic forces, endothelial mechanotransduction and vascular diseases. *Magnetic Resonance in Medical Sciences* **21,** 258–266 (2022).

116. Lehoux, S. *Chapter 2 – molecular mechanisms of the vascular responses to hemodynamic forces* (Academic Press, 2021).

117. Dhawan, S. S. *et al.* Shear stress and plaque development. *Expert Review of Cardiovascular Therapy* **8,** 545–556 (2010).

118. Thondapu, V. *et al.* Biomechanical stress in coronary atherosclerosis: emerging insights from computational modelling. *European Heart Journal* **38,** 81–92 (2016).

119. Hatami, J., Tafazzoli-Shadpour, M., Haghighipour, N. & Shokrgozar, M. A. Influence of cyclic stretch on mechanical properties of endothelial cells. *Experimental Mechanics* **53,** 1–8 (2013).

120. Lacolley, P. Mechanical influence of cyclic stretch on vascular endothelial cells. *Cardiovascular Research* **63,** 577–579 (2004).

121. Williams, B. Mechanical influences on vascular smooth muscle cell function. *Journal of Hypertension* **16,** 1921–1929 (1998).

122. Humphrey, J., Eberth, J., Dye, W. & Gleason, R. Fundamental role of axial stress in compensatory adaptations by arteries. *Journal of Biomechanics* **42,** 1–8 (2009).

123. Lai, M. W. *et al.* Systems biology analysis of temporal dynamics that govern endothelial response to cyclic stretch. *Biomolecules* **12,** 1837–1858 (2022).

124. Jufri, N. F., Mohamedali, A., Avolio, A. & Baker, M. S. Mechanical stretch: physiological and pathological implications for human vascular endothelial cells. *Vascular Cell* **7,** 1–12 (2015).

125. Naruse, K., Yamada, T. & Sokabe, M. Involvement of SA channels in orienting response of cultured endothelial cells to cyclic stretch. *Vascular Physiology* **274,** H1532–H1538 (1998).

126. Chuong, C. & Fung, Y. On residual stresses in arteries. *Journal of Biomedical Engineering* **108,** 189–192 (1986).

127. Kassab, G. S. Biomechanics of the cardiovascular system: the aorta as an illustratory example. *Journal of the Royal Society Interface* **3,** 719–740 (2006).

128. Schmid, H. *et al.* Impact of transmural heterogeneities on arterial adapatation. *Biomechanics and Modeling in Mechanobiology* **9,** 295–315 (2010).

129. Thubrikar, M. J. & Robicsek, F. Pressure-induced arterial wall stress and atherosclerosis. *The Annals of Thoracic Surgery* **59,** 1594–1603 (1995).

130. Ohayon, J., Finet, G., Treyve, F., Rioufol, G. & Dubreuil, O. A three dimensional finite element analysis of stress distribution in a coronary atherosclerotic plaque: in-vivo prediction of plaque rupture location. *Biomechanics Applied to Computer Assisted Surgery* **37,** 225–241 (2005).

131. Athaide, C. E., Spronck, B. & Au, J. S. Physiological basis for longitudinal motion of the arterial wall. *American Journal of Physiology Heart and Circulatory Physiology* **322,** H689–H701 (2022).

132. Doriot, P.-A., Dorsaz, P.-A. & Nobel, J. Could increased axial wall stress be responsible for the development of atheroma in the proximal segment of myocardial bridges? *Theoretical Biology and Medical Modelling* **4,** 29–40 (2007).

133. Persson, M. *et al.* A new non-invasive ultrasonic method for simultaneous measurements of longitudinal and radial wall movements: first in vivo trial. *Clinical Physiology and Functional Imaging* **23,** 247–251 (2003).

134. Dessalles, C. A., Leclech, C., Castagnino, A. & Barakat, A. I. Integration of substrate-and flow-derived stresses in endothelial cell mechanobiology. *Communications Biology* **4,** 763 (2021).

135. Banerjee, S. & Marchetti, M. C. Contractile stresses in cohesive cell layers on finite-thickness substrates. *Physical Review Letters* **109,** 108101 (2012).

136. Tusan, C. G. *et al.* Collective cell behavior in mechanosensing of substrate thickness. *Biophysical Journal* **114,** 2743–2755 (2018).

137. Namba, T., Masaki, N., Takase, B. & Adachi, T. Arterial stiffness assessed by cardio-ankle vascular index. *International Journal of Molecular Sciences* **20,** 3664 (2019).

138. Fang, Y., Wu, D. & Birukov, K. G. Mechanosensing and mechanoregulation of endothelial cell functions. *Comprehensive Physiology* **9,** 873–904 (2019).

139. Chien, S. Mechanotransduction and endothelial cell homeostasis: the wisdom of the cell. *American Journal of Physiology-Heart and Circulatory Physiology* **292,** H1209–H1224 (2007).

140. Givens, C. & Tzima, E. Endothelial mechanosignaling: does one sensor fit all? *Antioxidants and Redox Signaling* **25,** 373–388 (2016).

141. Tzima, E. *et al.* A mechanosensory complex that mediates the endothelial cell response to fluid shear stress. *Nature* **437,** 426–431 (2005).

142. Zhou, T. *et al.* Endothelial mechanotransduction mechanisms for vascular physiology and atherosclerosis. *Journal of Mechanics in Medicine and Biology* **14,** 143006 (2014).

143. Zang, H., Mathew, R. O. & Cui, T. The dark side of Nrf2 in the heart. *Frontiers in Physiology* **11,** 722 (2020).

144. Shen, L. *et al.* Prediction of mechanosensitive genes in vascular endothelial cells under high wall shear stress. *Frontiers in Genetics* **12,** 796812 (2022).

145. Yamashiro, Y. & Yanagisawa, H. The molecular mechanism of mechanotransduction in vascular homeostasis and disease. *Clinical Science* **134,** 2399–2418 (2020).

146. Piterina, A. V. *et al.* ECM-based materials in cardiovascular applications: inherent healing potential and augmentation of native regenerative processes. *International Journal of Molecular Sciences* **10,** 4375–4417 (2009).

147. YeJin, J., Yao, Y. & Kim, E. K. Current understanding of intimal hyperplasia and effect of compliance in synthetic small diameter vascular grafts. *Biomaterials Science* **8,** 4383–4395 (2020).

148. Yao, Y. *et al.* In vivo evaluation of compliance mismatch on intimal hyperplasia formation in small diameter vascular grafts. *Biomaterials Science* **11,** 3297–3307 (2023).

149. Huynh, J. *et al.* Age-related intimal stiffening enhances endothelial permeability and leukocyte transmigration. *Cell Biomechanics* **3,** 112ra122 (2011).

150. Goins, A., Webb, A. R. & Allen, J. B. Multi-layer approaches to scaffold-based small diameter vessel engineering: a review. *Materials Science and Engineering C* **97,** 896–912 (2019).

151. Carrabba, M. & Madeddu, P. Current strategies for the manufacture of small size tissue engineering vascular grafts. *Frontiers in Bioengineering and Biotechnology* **6,** 41 (2018).

152. Pashneh-Tala, S., MacNeil, S. & Claeyssens, F. The tissue-engineered vascular graft–past, present, and future. *Tissue Engineering: Part B* **22,** 68–100 (2016).

153. Seifu, D. G., Purnama, A., Mequanint, K. & Mantovani, D. Small-diameter vascular tissue engineering. *Nature Reviews Cardiology* **10,** 410–421 (2013).

154. Jørgensen, C. & Paaske, W. Physical and mechanical properties of ePTFE stretch vascular grafts determined by time-resolved scanning acoustic microscopy. *European Journal of Vascular and Endovascular Surgery* **15,** 416–422 (1998).

155. Faturechi, R., Hashemi, A., Abolfathi, N. & Solouk, A. Mechanical guidelines on the properties of human healthy arteries in the design and fabrication of vascular grafts: experimental tests and quasi-linear viscoelastic model. *Acta of Bioengineering and Biomechanics* **21,** 1–9 (2019).

156. Castillo-Cruz, O. *et al.* Prediction of circumferential compliance and burst strength of polymeric vascular grafts. *Journal of the Mechanical Behavior of Biomedical Materials* **79,** 332–340 (2018).

157. Brandt-Wunderlich, C. *et al.* A method to determine the radial compliance of porcine coronary arteries ex vivo via optical coherence tomography. *Current Directions in Biomedical Engineering* **6,** 20203013 (2020).

158. Dondoni, F. *et al.* Patient-specific, multi-scale modeling of neointimal hyperplasia in vein grafts. *Frontiers in Physiology* **8,** 226 (2017).

159. Zilla, P., Bezuidenhout, D. & Human, P. Prosthetic vascular grafts: wrong models, wrong questions and no healing. *Biomaterials* **28,** 5009–5027 (2007).

160. Ott, M. J. & Ballermann, B. J. Shear stress-conditioned endothelial cell-seeded vascular grafts: improved cell adherence in response to in vitro shear stress. *Surgery* **117,** 334–339 (1995).

161. Sarkar, S., Sales, K. M., Hamilton, G. & Seifalian, A. M. Addressing thrombogenicity in vascular graft construction. *Journal of Biomedical Materials Research Part B: Applied Biomaterials* **82B,** 100–108 (2007).

162. Bird, R. l. R., Hall, B., Hobbs, K. & Chapman, D. New haemocompatible polymers assessed by thrombelastography. *Journal of Biomedical Engineering* **11,** 231–234 (1988).

163. Kottke-Marchant, K., Anderson, J. M., Umemura, Y. & Marchant, R. E. Effect of albumin coating on the in vitro blood compatibility of Dacron arterial prostheses. *Biomaterials* **10,** 147–155 (1989).

164. Heyligers, J. M. *et al.* Heparin immobilization reduces thrombogenicity of small-caliber expanded polytetrafluoroethylene grafts. *Journal of Vascular Surgery* **43,** 587–591 (2006).

165. El-Sherbiny, I. M. & Yacoub, M. H. Hydrogel scaffolds for tissue engineering: progress and challenges. *Global Cardiology Science and Practice* **38,** 1–27 (2013).

166. Hu, W., Wang, Z., Xiao, Y., Zhang, S. & Wang, J. Advances in crosslinking strategies of biomedical hydrogels. *Biomaterials Science* **7,** 843–855 (2019).

167. Ahmed, E. M. Hydrogel: Preparation, characterization, and applications: a review. *Journal of Advanced Research* **6,** 105–121 (2015).

168. Varaprasad, K., Raghavendra, G. M., Jayaramudu, T., Yallapu, M. M. & Sadiku, R. A mini review on hydrogels classification and recent developments in miscellaneous applications. *Materials Science and Engineering: C* **79,** 958–971 (2017).

169. Ren, T., Gan, J., Zhou, L. & Chen, H. Physically crosslinked hydrogels based on poly (vinyl alcohol) and fish gelatin for wound dressing application: fabrication and characterization. *Polymers* **12,** 1729–1742 (2020).

170. Zhao, Z. *et al.* Composite hydrogels in three-dimensional in vitro models. *Frontiers in Bioengineering and Biotechnology* **8,** 611 (2020).

171. Jeong, Y., Yao, Y., Mekonnen, T. H. & Yim, E. K. Changing compliance of poly(vinyl alcohol) tubular scaffold for vascular graft applications through modifying interlayer adhesion and crosslinking density. *Frontiers in Materials* **7,** 595295 (2021).

172. Rizwan, M. *et al.* One-pot covalent grafting of gelatin on poly (vinyl alcohol) hydrogel to enhance endothelialization and hemocompatibility for synthetic vascular graft applications. *ACS Applied Bio Materials* **3,** 693–703 (2019).

173. Cutiongco, M. F., Anderson, D. E., Hinds, M. T. & Yim, E. K. In vitro and ex vivo hemocompatibility of off-the-shelf modified poly(vinyl alcohol) vascular grafts. *Acta Biomaterialia* **25,** 97–108 (2015).

174. Ino, J. M. *et al.* Evaluation of hemocompatibility and endothelialization of hybrid poly(vinyl alcohol) (PVA)/gelatin polymer films. *Journal of Biomedical Materials Research Part B: Applied Biomaterials* **101,** 1549–1559 (2013).

175. Chaouat, M. *et al.* A novel cross-linked poly(vinyl alcohol) (PVA) for vascular grafts. *Advanced Functional Materials* **18,** 2855–2861 (2008).

176. Malone, A. J., Cournane, S., Naydenova, I. G., Fagan, A. J. & Browne, J. E. Polyvinyl alcohol cryogel based vessel mimicking material for modelling the progression of atherosclerosis. *Physica Medica* **69,** 1–8 (2020).

177. Conconi, M. T. *et al.* Evaluation of vascular grafts based on polyvinyl alcohol cryogels. *Molecular Medicine Reports* **10,** 1329–1334 (2020).

178. Mohammadi, H., Boughner, D. & Wan, W. Design and simulation of a poly (vinyl alcohol)–bacterial cellulose nanocomposite mechanical aortic heart valve prosthesis. *Proceedings of the Institution of Mechanical Engineers, Part H: Journal of Engineering in Medicine* **223,** 697–711 (2009).

179. Millon, L., Mohammadi, H. & Wan, W. Anisotropic polyvinyl alcohol hydrogel for cardiovascular applications. *Journal of Biomedical Materials Research Part B: Applied Biomaterials: An Official Journal of The Society for Biomaterials, The Japanese Society for Biomaterials, and The Australian Society for Biomaterials and the Korean Society for Biomaterials* **79,** 305–311 (2006).

180. Wan, W., Campbell, G., Zhang, Z., Hui, A. & Boughner, D. Optimizing the tensile properties of polyvinyl alcohol hydrogel for the construction of a bioprosthetic heart valve stent. *Journal of Biomedical Materials Research: Applied Biomaterials: An Official Journal of The Society for Biomaterials, The Japanese Society for Biomaterials, and The Australian Society for Biomaterials and the Korean Society for Biomaterials* **63,** 854–861 (2002).

181. Bates, N. M., Puy, C., Jurney, P. L., McCarty, O. J. & Hinds, M. T. Evaluation of the effect of crosslinking method of poly(vinyl alcohol) hydrogels on thrombogenicity. *Cardiovascular Engineering and Technology* **11,** 448–455 (2020).

182. Yokoyama, F., Masada, I., Shimamura, K., Ikawa, T. & Monobe, K. Morphology and structure of highly elastic poly(vinyl alcohol) hydrogel prepared by repeated freezing-and-melting. *Colloid and Polymer Science* **264,** 595–601 (1986).

183. Holloway, J. L., Lowman, A. M. & Palmese, G. R. The role of crystallization and phase separation in the formation of physically cross-linked PVA hydrogels. *Soft Matter* **9,** 826–833 (2013).

184. Gonzalez, J. S. & Alvarez, V. A. Mechanical properties of polyvinylalcohol/hydroxyapatite cryogel as potential artificial cartilage. *Journal of the Mechanical Behavior of Biomedical Materials* **34,** 47–56 (2014).

185. Holloway, J. L., Lowman, A. M., VanLandingham, M. R. & Palmese, G. R. Interfacial optimization of fiber-reinforced hydrogel composites for soft fibrous tissue applications. *Acta Biomaterialia* **10,** 3581–3589 (2014).

186. Wang, B. H. & Campbell, G. Formulations of polyvinyl alcohol cryogel that mimic the biomechanical properties of soft tissues in the natural lumbar intervertebral disc. *Spine* **34,** 2745–2753 (2009).

187. Wang, J., Gao, C., Zhang, Y. & Wan, Y. Preparation and in vitro characterization of BC/PVA hydrogel composite for its potential use as artificial cornea biomaterial. *Materials Science and Engineering: C* **30,** 214–218 (2010).

188. Chaturvedi, A., Bajpai, A. K., Bajpai, J. & Singh, S. K. Evaluation of poly (vinyl alcohol) based cryogel–zinc oxide nanocomposites for possible applications as wound dressing materials. *Materials Science and Engineering: C* **65,** 408–418 (2016).

189. Górska, A. *et al.* Poly(vinyl alcohol) cryogel membranes loaded with resveratrol as potential active wound dressings. *AAPS PharmSciTech* **22,** 109 (2021).

190. Nugent, M. J. & Higginbotham, C. L. Preparation of a novel freeze thawed poly(vinyl alcohol) composite hydrogel for drug delivery applications. *European Journal of Pharmaceutics and Biopharmaceutics* **67,** 377–386 (2007).

191. Takamura, A., Ishii, F. & Hidaka, H. Drug release from poly(vinyl alcohol) gel prepared by freeze-thaw procedure. *Journal of Controlled Release* **20,** 21–28 (1992).

192. Kosukegawa, H. *et al.* Measurements of dynamic viscoelasticity of poly (vinyl alcohol) hydrogel for the development of blood vessel biomodeling. *Journal of Fluid Science and Technology* **3,** 533–543 (2008).

193. Hassan, C. M. & Peppas, N. A. Structure and morphology of freeze/thawed PVA hydrogels. *Macromolecules* **33,** 2472–2479 (2000).

194. Gupta, S., Goswami, S. & Sinha, A. A combined effect of freeze–thaw cycles and polymer concentration on the structure and mechanical properties of transparent PVA gels. *Biomedical Materials* **7,** 015006 (2012).

195. Pazos, V., Mongrain, R. & Tardif, J. Polyvinyl alcohol cryogel: optimizing the parameters of cryogenic treatment using hyperelastic models. *Journal of the Mechanical Behavior of Biomedical Materials* **2,** 542–549 (2009).

196. Jiang, S., Liu, S. & Feng, W. PVA hydrogel properties for biomedical application. *Journal of the Mechanical Behavior of Biomedical Materials* **4,** 1228–1233 (2011).

197. Nakano, T. & Nakaoki, T. Coagulation size of freezable water in poly(vinyl alcohol) hydrogels formed by different freeze/thaw cycle periods. *Polymer Journal* **43,** 875–880 (2011).

198. Hua, M. *et al.* Strong tough hydrogels via the synergy of freeze-casting and salting out. *Nature* **590,** 594–600 (2021).

199. Liu, Y. *et al.* Thermal behavior and mechanical properties of physically crosslinked PVA/gelatin hydrogels. *Journal of Mechanical Behavior of Biomedical Materials* **3,** 203–209 (2010).

200. Patachia, S., Florea, C., Friedrich, C. & Thomann, Y. Tailoring of poly(vinyl alcohol) cryogels properties by salts addition. *eXPRESS Polymer Letters* **3,** 320–331 (2009).

201. Khajavi, R. & Damerchely, R. Effect of polyvinyl alcohol concentration in spinning dope on diameter, beads and HHS of produced nanofibers. *Pakistan Journal of Biological Sciences* **10,** 314–317 (2007).

202. Nagakawa, Y., Kato, M., Suye, S.-i. & Fujita, S. Fabrication of tough, anisotropic, chemical-crosslinker-free poly(vinyl alcohol) nanofibrous cryogels via electrospinning. *RSC Advances* **10,** 38045–38054 (2020).

203. Nuttelman, C. R., Mortisen, D. J., Henry, S. M. & Anseth, K. S. Attachment of fibronectin to poly(vinyl alcohol) hydrogels promotes NIH3T3 cell adhesion, proliferation, and migration. *Journal of Biomedical Materials Research: An Official Journal of The Society for Biomaterials, The Japanese Society for Biomaterials, and The Australian Society for Biomaterials and the Korean Society for Biomaterials* **57,** 217–223 (2001).

204. Jurney, P. L., Anderson, D. E., Pohan, G., Yim, E. K. & Hinds, M. T. Reactive ion plasma modification of poly(vinyl-alcohol) increases primary endothelial cell affinity and reduces thrombogenicity. *Macromolecular Bioscience* **18,** 1800132 (2018).

205. Firoozi, M., Entezam, M., Masaeli, E., Ejeian, F. & Nasr-Esfahani, M. H. Physical modification approaches to enhance cell supporting potential of poly (vinyl alcohol)-based hydrogels. *Journal of Applied Polymer Science* **139,** 51485 (2022).

206. Chen, L., Yan, C. & Zheng, Z. Functional polymer surfaces for controlling cell behaviors. *Materials Today* **21,** 38–59 (2018).

207. Atlan, M. *et al.* Design, characterization and in vivo performance of synthetic 2 mm-diameter vessel grafts made of PVA-gelatin blends. *Scientific Reports* **8,** 7417 (2018).

208. Mathews, D., Birney, Y., Cahill, P. & McGuinness, G. Vascular cell viability on polyvinyl alcohol hydrogels modified with water-soluble and -insoluble chitosan. *Journal of Biomedical Materials Research Part B: Applied Biomaterials: An Official Journal of The Society for Biomaterials, The Japanese Society for Biomaterials, and The Australian Society for Biomaterials and the Korean Society for Biomaterials* **84,** 531–540 (2008).

209. Vrana, N. E., Liu, Y., McGuinness, G. B. & Cahill, P. A. Characterization of poly(vinyl alcohol)/chitosan hydrogels as vascular tissue engineering scaffolds. *Macromolecular Symposia* **269,** 106–110 (2008).

210. Rodriguez-Rodriguez, R., Espinosa-Andrews, H., Velasquillo-Martnez, C. & Garca-Carvajal, Z. Y. Composite hydrogels based on gelatin, chitosan and polyvinyl alcohol to biomedical applications: a review. *Journal of Biomedical Materials Research Part B: Applied Biomaterials: An Official Journal of The Society for Biomaterials, The Japanese Society for Biomaterials, and The Australian Society for Biomaterials and the Korean Society for Biomaterials* **84,** 531–540 (2008).

211. Ino, J. M., Chevallier, P., Letourneur, D., Mantovani, D. & Le Visage, C. Plasma functionalization of poly(vinyl alcohol) hydrogel for cell adhesion enhancement. *Biomatter* **3,** e25414 (2013).

212. Cutiongco, M. F. *et al.* Planar and tubular patterning of micro and nanotopographies on poly(vinyl alcohol) hydrogel for improved endothelial cell responses. *Biomaterials* **84,** 184–195 (2016).

213. Chong, S.-F., Smith, A. A. & Zelikin, A. N. Microstructured, functional PVA hydrogels through bioconjugation with oligopeptides under physiological conditions. *Small* **9,** 942–950 (2013).

214. Rafat, M., Rotenstein, L. S., You, J.-O. & Auguste, D. T. Dual functionalized PVA hydrogels that adhere endothelial cells synergistically. *Biomaterials* **33,** 3880–3886 (2012).

215. Post, A., Wang, E. & Cosgriff-Hernandez, E. A review of integrin-mediated endothelial cell phenotype in the design of cardiovascular devices. *Annals of Biomedical Engineering* **47,** 366–380 (2019).

216. Davidenko, N. *et al.* Evaluation of cell binding to collagen and gelatin: a study of the effect of 2D and 3D architecture and surface chemistry. *Journal of Materials Science: Materials in Medicine* **27,** 1–14 (2016).

217. Xing, Q. *et al.* Increasing mechanical strength of gelatin hydrogels by divalent metal ion removal. *Scientific Reports* **4,** 1–10 (2014).

218. Bello, A. B., Kim, D., Kim, D., Park, H. & Lee, S.-H. Engineering and functionalization of gelatin biomaterials: from cell culture to medical applications. *Tissue Engineering: Part B* **26,** 164–180 (2020).

219. Baydin, T., Aarstad, O. A., Dille Morten J Hattrem, M. N. & Draget, K. I. Long-term storage stability of type A and type B gelatin gels: the effect of Bloom strength and co-solutes. *Food Hydrocolloids* **127,** 107535 (2022).

220. Ceylan, S., Göktürk, D. & Bölgen, N. Effect of crosslinking methods on the structure and biocompatibility of polyvinyl alcohol/gelatin cryogels. *Bio-Medical Materials and Engineering* **27,** 327–340 (2016).

221. Yue, K. *et al.* Synthesis, properties, and biomedical applications of gelatin methacryloyl (GelMA) hydrogels. *Biomaterials* **73,** 254–271 (2015).

222. Parikh, V. *et al.* Small diameter helical vascular scaffolds support endothelial cell survival. *Nanomedicine: Nanotechnology, Biology, and Medicine* **14,** 2598–2608 (2018).

223. Chlupáč, J., Filova, E. & Bačáková, L. Blood vessel replacement: 50 years of development and tissue engineering paradigms in vascular surgery. *Physiological Research* **58,** S119–S139 (2009).

224. Stonebridge, P. & Brophy, C. Spiral laminar flow in arteries? *The Lancet* **338,** 1360–1361 (1991).

225. Holzapfel, G. A. & Ogden, R. W. Constitutive modelling of arteries. *Proceedings of The Royal Society A* **466,** 1551–1597 (2010).

226. Zia, A. W., Liu, R. & Wu, X. Structural design and mechanical performance of composite vascular grafts. *Bio-Design and Manufacturing* **5,** 757–785 (2022).

227. Chen, H. & Kassab, G. S. Microstructure-based biomechanics of coronary arteries in health and disease. *Journal of Biomechanics* **49,** 2548–2559 (2016).

228. Zhang, C. *et al.* Additive manufacturing of functionally graded materials: a review. *Materials Science and Engineering A* **764,** 138209 (2019).

229. Chen, H., Slipchenko, M. N., Zhao, X., Cheng, J.-X. & Kassab, G. S. The layered structure of coronary adventitia under mechanical load. *Biophysical Journal* **101,** 2555–2562 (2011).

230. Milutinović, A., Šuput, D. & Zorc-Pleskovič, R. Pathogenesis of atherosclerosis in the tunica intima, media, and adventitia of coronary arteries: an updated review. *Bosnian Journal of Basic Medical Sciences* **20,** 21–30 (2020).

231. Subbotin, V. M. Excessive intimal hyperplasia in human coronary arteries before intimal lipid depositions is the initiation of coronary atherosclerosis and constitutes a therapeutic target. *Drug Discovery Today* **21,** 1578–1595 (2016).

232. Scaffaro, R., Lopresti, F., Maio, A., Sutera, F. & Botta, L. Development of polymeric functionally graded scaffolds: a brief review. *Journal of Applied Biomaterials and Functional Materials* **15,** e107–e121 (2017).

233. Lowen, J. M. & Leach, J. K. Functionally graded biomaterials for use as model systems and replacement tissues. *Advanced Functional Materials* **30,** 1909089 (2020).

234. Mahmoud, D. & Elbestawi, M. A. Lattice structures and functionally graded materials applications in additive manufacturing of orthopedic implants: a review. *Journal of Manufacturing and Materials Processing* **1,** 13 (2017).

235. Wang, D., Xu, Y., Li, Q. & Turng, L.-S. Artificial small-diameter blood vessels: materials, fabrication, surface modification, mechanical properties, and bioactive functionalities. *Journal of Materials Chemistry B* **8,** 1801–1822 (2020).

236. Song, Y. *et al.* Dynamic culturing of smooth muscle cells in tubular poly(trimethylene carbonate) scaffolds for vascular tissue engineering. *Tissue Engineering Part A* **17,** 381–387 (2010).

237. Rickel, A. P., Deng, X., Engebretson, D. & Hong, Z. Electrospun nanofiber scaffold for vascular tissue engineering. *Materials Science and Engineering C* **129,** 112373 (2021).

238. Thomas, V., Zhang, X., Catledge, S. A. & Vohra, Y. K. Functionally graded electrospun scaffolds with tunable mechanical properties for vascular tissue regeneration. *Biomedical Materials* **2,** 224–232 (2007).

239. Best, C. *et al.* Toward a patient-specific tissue engineered vascular graft. *Journal of Tissue Engineering* **9,** 1–9 (2018).

240. Wang, C., Li, Z., Zhang, L., Sun, W. & Zhou, J. Long-term results of triple-layered small diameter vascular grafts in sheep carotid arteries. *Medical Engineering and Physics* **85,** 1–6 (2020).

241. Jiang, Y., Wang, H., Wang, X. & Li, Q. Surface modification with hydrophilic and heparain-loaded coating for endothelialization and anticoagulation promotion of vascular scaffold. *International Journal of Biological Macromolecules* **219,** 1146–1154 (2022).

242. Zheng, W. *et al.* Mussel-inspired triblock functional protein coating with endothelial cell selectivity for endothelialization. *Journal of Colloid and Interface Science* **576,** 68–78 (2020).

243. De Valence, S. *et al.* Advantages of bilayered vascular grafts for surgical applicability and tissue regeneration. *Acta Biomaterialia* **8,** 3914–3920 (2012).

244. Grey, C. P., Newton, S. T., Bowlin, G. L., Haas, T. W. & Simpson, D. G. Gradient fiber electrospinning of layered scaffolds using controlled transitions in fiber diameter. *Biomaterials* **34,** 4993–5006 (2013).

245. Shimizu, Y. *et al.* Development of a stereo dip-coating system for fabrication of tube-shaped blood vessel models. *Scientific Reports* **10,** 1–10 (2020).

246. Livingston, M. & Tan, A. Coating techniques and release kinetics of drug-eluting stents. *Journal of Medical Devices* **10** (2019).

247. Enis, I. Y. & Sakikogly, T. G. Design parameters for electrospun biodegradable vascular grafts. *Journal of Industrial Textiles* **47,** 2205–2227 (2018).

248. Devillard, C. D. & Marquette, C. A. Vascular tissue engineering: challenges and requirements for an ideal large scale blood vessel. *Frontiers in Bioengineering and Biotechnology* **9,** 931 (2021).

249. Smith, J. A. & Mele, E. Electrospinning and additive manufacturing: adding three-dimensionality to electrospun scaffolds for tissue engineering. *Frontiers in Bioengineering and Biotechnology* **9,** 1238 (2021).

250. Hong, J., Yeo, M., Yang, G. H. & Kim, G. Cell-electrospinning and its application for tissue engineering. *International Journal of Molecular Sciences* **20,** 6208 (2019).

251. Dahlin Rebecca L Kasper, F. K. & Mikos, A. G. Polymeric nanofibers in tissue engineering. *Tissue Engineering Part B: Reviews* **17,** 349–364 (2011).

252. Vyas, C. *et al.* Three-dimensional printing and electrospinning dual-scale polycaprolactone scaffolds with low-density and oriented fibers to promote cell alignment. *3D Printing and Additive Manufacturing* **7,** 105–113 (2020).

253. Wang, P. *et al.* 3D printing of tissue engineering scaffolds: a focus on vascular regeneration. *Bio-Design and Manufacturing* **4,** 344–378 (2021).

254. Du, F. *et al.* Gradient nanofibrous chitosan/poly e-caprolactone scaffolds as extracellular microenvironments for vascular tissue engineering. *Biomaterials* **33,** 762–770 (2012).

255. Ferroni, L., Tremoli, E., Leo, S., Zavan, B. & Mortelaro, C. Last technological advancement in additive manufacturing for cardiovascular applications. *European Review for Medical and Pharmacological Sciences* **26,** 1–10 (2022).

256. Ngo, T. D., Kashani, A., Imbalzano, G., Nguyen, K. T. & Hui, D. Last technological advancement in additive manufacturing for cardiovascular applications. *Composites Part B* **143,** 172–196 (2018).

257. Chimene, D., Kaunas, R. & Gaharwar, A. K. Hydrogel bioink reinforcement for additive manufacturing: a focused review of emerging strategies. *Advanced Materials* **32,** 1902026 (2020).

258. Schöneberg, J. *et al.* Engineering biofunctional in vitro vessel models using a multilayer bioprinting technique. *Scientific Reports* **8,** 10430 (2018).

259. Cicha, I. *et al.* Biofabrication of vessel grafts based on natural hydrogels. *Current Opinion in Biomedical Engineering* **2,** 83–89 (2017).

260. Yang, D.-L., Faraz, F., Wang, J.-X. & Radacsi, N. Combination of 3D printing and electrospinning techniques for biofabrication. *Advanced Materials Technologies* **7,** 2101309 (2022).

261. M, C. *et al.* Combining electrospinning and fused deposition modeling for the fabrication of a hybrid vascular graft. *Biofabrication* **2,** 014102 (2010).

262. Guerra, A. J., de Marie, C., Ceretti, E. & Ciurana, J. Real bifurcated vascular grafts manufacturing for tissue engineering. *Procedia CIRP* **89,** 92–97 (2020).

263. Hu, Q. *et al.* Designed and fabrication of triple-layered vascular scaffold with microchannels. *Journal of Biomaterials Science, Polymer Edition* **32,** 714–734 (2021).

264. Huang, R. *et al.* Triple-layer vascular grafts fabricated by combined E-jet 3D printing and electrospinning. *Annals of Biomedical Engineering* **46,** 1254–1266 (2018).

265. Arabul, M. U., Rutten, M., van de Vosse, F. & Lopata, R. Optical and acoustic characterization of freeze-thawed polyvinyl alcohol gels. *IEEE International Ultrasonics Symposium Proceedings,* 2410–2413 (2014).

266. Fromageau, J. *et al.* Estimation of polyvinyl alcohol cryogel mechanical properties with four ultrasound elastography methods and comparison with gold standard testings. *IEEE Transactions on Ultrasonics, Ferroelectrics, and Frequency Control* **54,** 498–509 (2007).

267. Bisaillon, C.-É., Campbell, G., Pazos, V. & Lamouche, G. Poly (vinyl alcohol) cryogel, multi-layer artery phantoms for optical coherence tomography. *Proceedings of SPIE* **7906,** 79060 (2011).

268. Kosukegawa, H., Kiyomitsu, C. & Ohta, M. Control of wall thickness of blood vessel biomodel made of poly (vinyl alcohol) hydrogel by a three-dimensional-rotating spin dip-coating method. *ASME International Mechanical Engineering Congress and Exposition* **54884,** 221–228 (2011).

269. Liu, Y., Zahedmanesh, H., Lally, C., Cahill, P. & McGuinness, G. Compliance properties of a composite electrospun fibre–hydrogel blood vessel scaffold. *Materials Letters* **178,** 296–299 (2016).

270. Ravanbakhsh, H. *et al.* Freeform cell-laden cryobioprinting for shelf-ready tissue fabrication and storage. *Matter* **5,** 573–593 (2022).

271. Meng, Y., Cao, J., Chen, Y., Yu, Y. & Ye, L. 3D printing of poly(vinyl alcohol)-based nano-composite hydrogel as an artificial cartilage replacement and the improvement mechanism of printing accuracy. *Journal of Materials Chemistry B* **8,** 677 (2020).

272. Geringer, J., Imbert, L. & Kim, K. *Computational Modeling of Hip Implants* 389–416 (Woodhead Publishing Limited, 2014).

273. Kladovasilakis, N., Tsongas, K. & Tzetzis, D. Finite element analysis of orthopedic hip implant with functionally graded bioinspired lattice structures. *Biomimetics* **5,** 44–60 (2020).

274. Levadnyi, I., Awrejcewicz, J., Gubaua, J. E. & Pereira, J. T. Numerical evaluation of bone remodelling and adaptation considering different hip prosthesis designs. *Clinical Biomechanics* **50,** 122–129 (2017).

275. McClure, M. J., Sell, S. A., Simpson, D. G., Walpoth, B. H. & Bowlin, G. L. A three-layered electrospun matrix to mimic native arterial architecture using polycaprolactone, elastin, and collagen: a preliminary study. *Acta Biomaterialia* **6,** 2422–2433 (2010).

276. GR, L. & SS, Q. *The Finite Element Method: A Practical Course, Second Edition* (Elsevier Science, 2013).

277. Pavlou, D. G. *Essentials of the Finite Element Method for Mechanical and Structural Engineers* (Elsevier Science, 2015).

278. Zienkiewicz, O., Taylor, R. & Zhu, J. *Chapter 1 – The standard discrete system and origins of the finite element method* 1–20 (Elsevier Ltd, 2013).

279. Veress, A. *et al.* Vascular mechanics of the coronary artery. *Zeitschrift für Kardiologie* **89,** S092–S100 (2000).

280. Chandran, K., Gao, D., Han, G., Baraniewski, H. & Corson, J. Finite-element analysis of arterial anastomoses with vein, Dacron and PTFE graffs. *Medical and Biological Engineering and Computing* **30,** 413–418 (1992).

281. Mitchell, S. L. & Niklason, L. E. Requirements for growing tissue-engineered vascular grafts. *Cardiovascular Pathology* **12,** 59–64 (2003).

282. Abbott, W. M. *et al.* Evaluation and performance standards for arterial prostheses. *Journal of Vascular Surgery* **17,** 746–756 (1993).

283. Desai, M. & Hamilton, G. *Graft Materials Past and Future* (University of Adelaide Press, 2011).

284. Devine, C. & McCollum, C. Heparin-bonded Dacron or polytetrafluorethylene for femoropopliteal bypass: five-year results of a prospective randomized multicenter clinical trial. *Journal of Vascular Surgery* **40,** 924–931 (2004).

285. Azevedo, E. P., Retarekar, R., Raghavan, M. L. & Kumar, V. Mechanical properties of cellulose: chitosan blends for potential use as a coronary artery bypass graft. *Journal of Biomaterials Science, Polymer Edition* **17,** 239–252 (2013).

286. Karimi, A., Navidbakhsh, M., Shojaei, A. & Faghihi, S. Measurement of the uniaxial mechanical properties of healthy and atherosclerotic human coronary arteries. *Materials Science and Engineering C* **33,** 2550–2554 (2013).

287. Ozolanta, I., Tetere, G., Purinya, B. & Kasyanov, V. Changes in the mechanical properties, biochemical contents and wall structure of the human coronary arteries with age and sex. *Materials Science and Physics* **20,** 523–533 (1998).

288. Holzapfel, G. A., Sommer, G., Gasser, C. T. & Regitnig, P. Determination of layer-specific mechanical properties of human coronary arteries with nonatherosclerotic intimal thickening and related constitutive modeling. *American Journal of Physiology-Heart and Circulatory Physiology* **289,** H2048–H2058 (2005).

289. Karimi, A., Navidbakhsh, M. & Shojaei, A. A combination of histological analyses and uniaxial tensile tests to determine the material coefficients of the healthy and atherosclerotic human coronary arteries. *Tissue and Cell* **47,** 152–158 (2015).

290. Kural, M. H. *et al.* Planar biaxial characterization of diseased human coronary and carotid arteries for computational modeling. *Journal of Biomechanics* **45,** 790–798 (2012).

291. Lally, C., Reid, A. & Prendergast, P. Elastic behavior of porcine coronary artery tissue under uniaxial and equibiaxial tension. *Annals of Biomedical Engineering* **32,** 1355–1364 (2004).

292. Claes, E. *et al.* Mechanical properties of human coronary arteries. *2010 Annual International Conference of the IEEE Engineering in Medicine and Biology,* 3792–3795 (2010).

293. Freij, J. M., Burton, H. E. & Espino, D. M. Objective uniaxial identification of transition points in non-linear materials: sample application to porcine coronary arteries and the dependency of their pre- and post-transitional moduli with position. *Cardiovascular Engineering and Technology* **10,** 61–68 (2019).

294. Holzapfel, G., Gasser, T. & Stadler, M. A structural model for the viscoelastic behavior of arterial walls: continuum formulation and finite element analysis. *European Journal of Mechanics A-Solids* **21,** 441–463 (2002).

295. McGuinness, G. B., Vrana, N. E. & Liu, Y. Polyvinvyl alcohol-based cryogels: tissue engineering and regenerative medicine. *Encyclopedia of Biomedical Polymers and Polymeric Biomaterials* **11,** 6743–6753 (2015).

296. Zhuang, Y. *et al.* Challenges and strategies for in situ endothelialization and long-term lumen patency of vascular grafts. *Bioactive Materials* **6,** 1791–1809 (2021).

297. Charron, P. N., Jacobs, J. I., Yao, S. X. & Oldinski, R. A. Effects of cryoprocessing on the mechanical and biological properties of poly(vinyl alcohol)-gelatin theta-gels. *Biointerphases* **15,** 051004 (2020).

298. Charron, P. N., Braddish, T. A. & Oldinski, R. A. PVA-gelatin hydrogels formed using combined theta-gel and cryo-gel fabrication techniques. *Journal of the Mechanical Behavior of Biomedical Materials* **92,** 90–96 (2019).

299. Zhang, Y. & Cremer, P. S. Interactions between macromolecules and ions: the Hofmeister series. *Current Opinion in Chemical Biology* **10,** 658–663 (2006).

300. Diani, J., Fayolle, B. & Gilormini, P. A review on the Mullins effect. *European Polymer Journal* **45,** 601–612 (2009).

301. Mavrilas, D. *et al.* Dynamic mechanical properties of arterial and venous grafts used in coronary bypass surgery. *Journal of Mechanics in Medicine and Biology* **2,** 329–337 (2002).

302. Stepniak, K., Ursani, A., Paul, N. & Naguib, H. Development of a phantom network for optimization of coronary artery disease imaging using computed tomography. *Biomedical Physics and Engineering Express* **5,** 045019 (2019).

303. Drucker, D. C. A definition of a stable inelastic material. **26,** 101–106 (1959).

304. Phothiphatcha, J. & Puttapitukporn, T. Determination of material parameters of PDMS material models by MATLAB. *Engineering Journal* **25,** 11–28 (2021).

305. Bergström, J. *Elasticity/hyperelasticity* 394–400 (Norwich, NY: William Andrew Publishing, 2015).

306. Pan, Y.-S., Xiong, D.-S. & Ma, R.-Y. A study on the friction properties of poly(vinyl alcohol) hydrogel as articular cartilage against titanium alloy. *Wear* **262,** 1021–1025 (2007).

307. Yeoh, O. *Phenomenological theory of rubber elasticity* (Pergamon Press, 1989).

308. Miao, T., Miller, E. J., McKenzie, C. & Oldinski, R. A. Physically crosslinked polyvinyl alcohol and gelatin interpenetrating polymer network theta-gels for cartilage regeneration. *Journal of Materials Chemistry B* **3,** 9242–9249 (2015).

309. Lozinsky, V. *et al.* Study of cryostructuring of polymer systems: 27. physicochemical properties of poly(vinyl alcohol) cryogels and specific features of their macroporous morphology. *Colloid Journal* **69,** 747–764 (2007).

310. Hassan, C. M. & Peppas, N. A. Structure and applications of poly(vinyl alcohol) hydrogels produced by conventional crosslinking or by freezing/thawing methods. *Advances in Polymer Science* **153,** 37–65 (2000).

311. Camasão, D. & Mantovani, D. The mechanical characterization of blood vessels and their substitutes in the continuous quest for physiological-relevant performances. a critical review. *Materials Today Bio* **10,** 100106 (2021).

312. Millon, L. E., Oates, C. J. & Wan, W. Compression properties of polyvinyl alcohol–bacterial cellulose nanocomposite. *Journal of Biomedical Materials Research Part B: Applied Biomaterials: An Official Journal of The Society for Biomaterials, The Japanese Society for Biomaterials, and The Australian Society for Biomaterials and the Korean Society for Biomaterials* **90,** 922–929 (2009).

313. Liu, K. & Ovaert, T. C. Poro-viscoelastic consitutive modeling of unconfined creep of hydrogels using finite element analysis with integrated optimization method. *Journal of Mechanical Behavior of Biomedical Materials* **4,** 440–450 (2011).

314. Nazouri, M., Seifzadeh, A. & Masaeli, E. Characterization of polyvinyl alcohol hydrogels as tissue-engineered cartilage scaffolds using a coupled finite element-optimization algorithm. *Journal of Biomechanics* **99,** 109525 (2020).

315. Święszkowski, W., Ku, D. N., Bersee, H. E. & Kurzydlowski, K. J. An elastic material for cartilage replacement in an arthritic shoulder joint. *Biomaterials* **27,** 1534–1541 (2006).

316. Nafo, W. & Al-Mayah, A. Characterization of PVA hydrogels' hyperelastic properties by uniaxial tension and cavity expansion tests. *International Journal of Non-Linear Mechanics* **124,** 103515 (2020).

317. Szurgott, P. & Jarzębski, Ł. Selection of a hyper-elastic model-a case study for a polyurethane component. *Latin American Journal of Solids and Structures* **16,** 1–16 (2019).

318. Czerner, M., Sanchez Fellay, L., Suárez, M. P., Frontini, P. M. & Fasce, L. A. Determination of elastic modulus of gelatin gels by indentation experiments. *Procedia Materials Science* **8,** 287–296 (2015).

319. Sanchez Fellay, L., Fasce, L., Czerner, M., Pardo, E. & Frontini, P. On the feasibility of identifying first order Ogden constitutive parameters of gelatin gels from flat punch indentation tests. *Soft Materials* **13,** 188–200 (2015).

320. Ravi, S. & Chaikof, E. L. Biomaterials for vascular tissue engineering. *Regenerative Medicine* **5,** 107–120 (2010).

321. Chistiakov, D., Orekhov, A. & Bobryshev, Y. Effects of shear stress on endothelial cells: go with the flow. *Acta Physiologica* **219,** 382–408 (2017).

322. Wang, Z., Golob, M. J. & Chesler, N. C. *Chapter 7: Viscoelastic properties of cardiovascular tissues* 141–163 (IntechOpen, 2016).

323. Lu, X., Pandit, A. & Kassab, G. S. Biaxial incremental homeostatic elastic moduli of coronary artery: two-layer model. *American Journal of Physiology-Heart and Circulatory Physiology* **287,** H1663–H1669 (2004).

324. Lu, Y. *et al.* Passive and active triaxial wall mechanics in a two-layer model of porcine coronary artery. *Scientific Reports* **7,** 1–12 (2017).

325. Chen, X., Yao, Y., Liu, S. & Hu, Q. An integrated strategy for designing and fabricating triple-layer vascular graft with oriented microgrooves to promote endothelialization. *Journal of Biomaterials Applications* **36,** 297–310 (2021).

326. Han, F. *et al.* Performance of a multilayered small-diameter vascular scaffold dual-loaded with VEGF and PDGF. *Biomaterials* **34,** 7302–7313 (2013).

327. Jia, W., Li, M., Weng, H., Gu, G. & Chen, Z. Design and comprehensive assessment of a biomimetic tri-layer tubular scaffold via biodegradable polymers for vascular tissue engineering applications. *Materials Science and Engineering C* **110,** 110717 (2020).

328. Javanmardi, Y. *et al.* Endothelium and subendothelial matrix mechanics modulate cancer cell transmission migration. *Advanced Science* **10,** 2206554 (2023).

329. Ma, X. *et al.* Fibers in the extracellular matrix enable long-range stress transmission between cells. *Biophysical Journal* **104,** 1410–1418 (2013).

330. Tamimi, E. A., Ardila, D. C., Ensley, B. D., Kellar, R. S. & Vande Geest, J. P. Computationally optimizing the compliance of multilayered biomimetic tissue engineered vascular grafts. *Journal of Biomechanical Engineering* **141,** 061003 (2019).

331. Harrison, S., Tamimi, E., Uhlorn, J., Leach, T. & Vande Geest, J. P. Computationally optimizing the compliance of a biopolymer based tissue engineered vascular graft. *Journal of Biomechanical Engineering* **138,** 014505 (2016).

332. Gholipour, A., Ghayesh, M. H., Zander, A. & Mahajan, R. Three-dimensional biomechanics of coronary arteries. *International Journal of Engineering Science* **130,** 93–114 (2018).

333. Gervaso, F. *et al.* On the effects of different strategies in modelling balloon-expandable stenting by means of finite element method. *Journal of Biomechanics* **41,** 1206–1212 (2008).

334. Martin, D. & Boyle, F. Finite element analysis of balloon-expandable coronary stent deployment: influence of angioplasty balloon configuration. *International Journal For Numerical Methods In Biomedical Engineering* **29,** 1161–1175 (2013).

335. Mortier, P. *et al.* A novel simulation strategy for stent insertion and deployment in curved coronary bifurcations: comparison of three drug-eluting stents. *Annals of Biomedical Engineering* **38,** 88–99 (2010).

336. Thomas-Seale, L. E. *et al.* A simulation of the magnetic resonance elastography steady state wave response through idealised atherosclerotic plaques. *IAENG International Journal of Computer Science* **38,** 394–400 (2011).

337. Dobrin, P. B. Mechanical properties of arteries. *Physiological Reviews* **58,** 397–360 (1978).

338. Nolan, D. R. & Lally, C. An investigation of damage mechanisms in mechanobiological models of in-stent restenosis. *Journal of Computational Science* **24,** 132–142 (2018).

339. Qiu, T., He, R., Abunassar, C., Hossainy, S. & Zhao, L. Effect of two-year degradation on mechanical interaction between a bioresorbable scaffold and blood vessel. *Journal of the Mechanical Behavior of Biomedical Materials* **78,** 254–265 (2018).

340. Wei, L., Chen, Q. & Li, Z. Influences of plaque eccentricity and composition on the stent–plaque–artery interaction during stent implantation. *Biomechanics and Modeling in Mechanobiology* **18,** 45–56 (2019).

341. Gholipour, A., Ghayesh, M. H., Zander, A. C. & Psaltis, P. J. In vivo based biomechanics of right and left coronary arteries. *International Journal of Engineering Science* **154,** 103281 (2020).

342. Sun, N., Wood, N. B., Hughes, A. D., Thom, S. A. & Xu, X. Y. Effects of transmural pressure and wall shear stress on LDL accumulation in the arterial wall: a numerical study using a multilayered model. *American Journal of Physiology-Heart and Circulatory Physiology* **292,** H3148–H3157 (2007).

343. Zhang, L., Zhao, J., Zhu, J., He, C. & Wang, H. Anisotropic tough poly(vinyl alcohol) hydrogels. *Soft Matter* **8,** 10439–10447 (2012).

344. Huang, W. & Yen, R. Zero-stress states of human pulmonary arteries and veins. *Journal of Applied Physiology* **85,** 867–873 (1998).

345. Barthelat, F. Architectured materials in engineering and biology: fabrication, structure, mechanics and performance. *International Materials Reviews* **60,** 413–430 (2017).

346. Libonati, F. & Buehler, M. J. Advanced structural materials by bioinspiration. *Advanced Engineering Materials* **19,** 1600787 (2017).

347. Naleway, S. E., Porter, M. M., McKittrick, J. & Meyers, M. A. Structural design elements in biological materials: application to bioinspiration. *Advanced Materials* **27,** 5455–5476 (2015).

348. Malik, I. A. & Barthelat, F. Bioinspired sutured materials for strength and toughness: pullout mechanisms and geometric enrichments. *International Journal of Solids and Structures* **138,** 118–133 (2018).

349. Rezvani-Sharif, A., Tafazzoli-Shadpour, M. & Avolio, A. Progressive changes of elastic moduli of arterial wall and atherosclerotic plaque components during plaque development in human coronary arteries. *Medical and Biological Engineering and Computing* **57,** 731–740 (2019).

350. Wagenseil, J. E. & Mecham, R. P. Elastin in large artery stiffness and hypertension. *Journal of Cardiovascular Tissue Research* **5,** 264–273 (2012).

351. Yu, X., Turcotte, R., Seta, F. & Zhang, Y. Micromechanics of elastic lamellae: unravelling the role of structural inhomogeneity in multi-scale arterial mechanics. *Journal of the Royal Society Interface* **15,** 20180492 (2018).

352. Rouf, S. *et al.* Functionally graded additive manufacturing for orthopedic applications. *Journal of Orthopaedics* **33,** 70–80 (2022).

353. Sola, A., Bellucci, D. & Cannillo, V. Functionally graded materials for orthopedic applications – an update on design and manufacturing. *Biotechnology Advances* **34,** 504–531 (2016).

354. Bakar, W. Z., Basri, S., Jamaludin, S. N. & Sajjad, A. Functionally graded materials: an overview of dental applications. *World Journal of Dentistry* **9,** 137–144 (2018).

355. Chashmi, M. J. *et al.* Design and analysis of porous functionally graded femoral prostheses with improved stress shielding. *Designs* **4,** 1–15 (2020).

356. Shirazi, H. A., Ayatollahi, M. & Asnafi, A. To reduce the maximum stress and stress shielding effect around a dental implant–bone interface using radial functionally graded biomaterials. *Computer Methods in Biomechanics and Biomedical Engineering* **20,** 750–759 (2017).

357. Verma, V. & Pal, K. A finite element investigation on the design of mechanically compatible functionally graded orthopaedic plate for diaphyseal tibia. *Composites Part C: Open Access* **7,** 100228 (2022).

358. Mehboob, H. & Chang, S.-H. Effect of structural stiffness of composite bone plate–scaffold assembly on tibial fracture with large fracture gap. *Composite Structures* **124,** 327–336 (2015).

359. Ganesh, V., Ramakrishna, K. & Ghista, D. N. Biomechanics of bone-fracture fixation by stiffness-graded plates in comparison with stainless-steel plates. *Biomedical Engineering Online* **4,** 1–15 (2005).

360. Van Oers, R. F., Rens, E. G., LaValley, D. J., Reinhart-King, C. A. & Merks, R. M. Mechanical cell-matrix feedback explains pairwise and collective endothelial cell behavior in vitro. *PLoS Computational Biology* **10,** e1003774 (2014).

361. Ahirwar, H., Sahu, A., Gupta, V. K., Kumar, P. & Nanda, H. S. Design and finite element analysis of femoral stem prosthesis using functional graded materials. *Computer Methods in Biomechanics and Biomedical Engineering* **25,** 1262–1275 (2022).

362. Wahab, A. H. A. *et al.* Developing functionally graded PVA hydrogel using simple freeze-thaw method for artificial glenoid labrum. *Journal of the Mechanical Behavior of Biomedical Materials* **91,** 406–415 (2019).

363. Ho, K. T. *et al.* Creating stiffness gradient polyvinyl alcohol hydrogel using a simple gradual freezing–thawing method to investigate stem cell differentiation behaviors. *Biomaterials* **40,** 51–60 (2015).

364. Heang, O. S., Bi, A. D., Ho, K. T. & Ho, L. J. Wide-range stiffness gradient PVA/HA hydrogel to investigate stem cell differentiation behavior. *Acta Biomaterialia* **35,** 23–31 (2016).

365. Lin, E., Li, Y., Weaver, J. C., Ortiz, C. & Boyce, M. C. Tunability and enhancement of mechanical behavior with additively manufactured bio-inspired hierarchical suture interfaces. *Journal of Materials Research* **29,** 1867–1875 (2014).

366. Lin, E., Li, Y., Ortiz, C. & Boyce, M. C. 3D printed, bio-inspired prototypes and analytical models for structured suture interfaces with geometrically-tuned deformation and failure behavior. *Journal of the Mechanics and Physics of Solids* **73,** 166–182 (2014).

367. Mirkhalaf, M. & Barthelat, F. Design, 3D printing and testing of architectured materials with bistable interlocks. *Extreme Mechanics Letters* **11,** 1–7 (2017).

368. Liu, L. *et al.* The effects of morphological irregularity on the mechanical behavior of interdigitated biological sutures under tension. *Journal of Biomechanics* **58,** 71–78 (2017).

369. Liu, L. & Li, Y. Failure mechanism transition of 3D-printed biomimetic sutures. *Engineering Fracture Mechanics* **199,** 372–379 (2018).

370. Li, Y., Ortiz, C. & Boyce, M. C. Stiffness and strength of suture joints in nature. *Physical Review E* **84,** 062904 (2011).

371. Crolla, J. P. *Replicating the intrinsic biomechanical characteristics of connective tissue: an exploration into the design and manufacture of PVA cryogel* (University of Birmingham, 2022).

372. Tozzi, P., Corno, A. & Hayoz, D. Definition of arterial compliance. *Physiology-Heart and Circulatory Physiology* **278,** H1407 (2000).

373. Tozzi, P., Corno, A. & Hayoz, D. Age-related changes in the mechanical properties of arteries. *Physiology-Heart and Circulatory Physiology* **278,** H1407 (2000).

374. Shaw, J. A. *et al.* Determinants of coronary artery compliance in subjects with and without angiographic coronary artery disease. *Journal of the American College of Cardiology* **39,** 1637–1643 (2002).

375. Li, Z., Xu, M., Wang, J. & Zhang, F. Recent advances in cryogenic 3D printing technologies. *Advanced Engineering Materials* **24,** 2200245 (2022).

376. Christensen, K., Davis, B., Jin, Y. & Huang, Y. Effects of printing-induced interfaces on localized strain within 3D printed hydrogel structures. *Materials Science and Engineering C* **89,** 65–74 (2018).

377. Sirry, M. S., Zilla, P. & Franz, T. A computational study of structural designs for a small-diameter composite vascular graft promoting tissue regeneration. *Cardiovascular Engineering and Technology* **1,** 269–281 (2010).

378. Meng, Z. *et al.* Design and additive manufacturing of flexible polycaprolactone scaffolds with highly-tunable mechanical properties for soft tissue engineering. *Materials and Design* **189,** 108508 (2020).

379. Chaudhry, H., Bukiet, B., Davis, A., Ritter, A. & Findley, T. Residual stresses in oscillating thoracic arteries reduce circumferential stresses and stress gradients. *Journal of Biomechanics* **30,** 57–62 (1997).

380. Niinomi, M., Naurshima, T. & Nakai, M. *Advances in Metallic Biomaterials: Tissues, Materials and Biological Reactions* (Springer Berlin Heidelberg, 2016).

381. Thubrikar, M. J., Roskelley, S. K. & Eppink, R. T. Study of stress conentration in the walls of the bovine coronary arterial branch. *Journal of Biomechanics* **23,** 15–17 (1990).

382. Taylor, C. & Humphrey, J. Open problems in computational vascular biomechanics: hemodynamics and arterial wall mechanics. *Computer Methods in Applied Mechanics and Engineering* **198,** 3514–3523 (2009).

383. Meyer, G., Merval, R. & Tedgui, A. Effects of pressure-induced stretch and convection on low-density lipoprotein and albumin uptake in the rabbit aortic wall. *Circulation Research* **79,** 532–540 (1996).

384. Chen, H. Y., Koo, B.-K., Bhatt, D. L. & Kassab, G. S. Impact of stent missizing and mis-positioning on coronary fluid wall shear and intramural stress. *Journal of Applied Physiology* **115,** 285–292 (2013).

385. Glendinning, P. *Stability, Instability and Chaos: an Introduction to the Theory of Nonlinear Differential Equations* (Cambridge University Press, 1994).

386. Weston, M. W., Rhee, K. & Tarbell, J. M. Compliance and diameter mismatch affect the wall shear rate distribution near an end-to-end anastomosis. *Journal of Biomechanics* **29,** 187–198 (1996).

387. Huo, Y., Choy, J. S., Svendsen, M., Sinha, A. K. & Kassab, G. S. Effects of vessel compliance on flow pattern in porcine epicardial right coronary arterial tree. *Journal of Biomechanics* **42,** 594–602 (2009).

388. Osawa, M., Kondo, K., Hisaya, S. & Kato, K. Development of a dynamic blood vessel phantom for evaluation of moving images. *Journal of Applied Clinical Medical Physics* **20,** 193–203 (2019).

389. Brunette, J., Mongrain, R. & Tardif, J. A realistic coronary artery phantom for particle image velocimetry. *Journal of Visualization* **7,** 241–248 (2004).

390. Mohammadi, H., Goode, D., Fradet, G. & Mequanint, K. Proposed percutaneous aortic valve prosthesis made of cryogel. *Proceedings of the Institution of Mechanical Engineers, Part H: Journal of Engineering in Medicine* **233,** 515–524 (2019).

391. Holloway, J. L., Lowman, A. M. & Palmese, G. R. Mechanical evaluation of poly(vinyl alcohol)-based fibrous composites as biomaterials for meniscal tissue replacement. *Acta Biomaterialia* **6,** 4716–4724 (2010).

392. Kong, I., Shang, J. T. B. & Tshai, K. Y. Study of properties of coconut fibre reinforced poly(vinyl alcohol) as biodegradable composites. *ARPN Journal of Engineering and Applied Sciences* **11,** 135–143 (2016).

393. Radke, D. *et al.* Tissue egineering at the blood-contacting surface: a review of challenges and strategies in vascular graft development. *Advanced Healthcare Materials* **7,** 1701461 (2018).

394. Liu, R. *et al.* The in vivo blood compatibility of bio-inspired small diameter vascular graft: effect of submicron longitudinally aligned topography. *BMC Cardiovascular Disorders* **13,** 79 (2013).

395. Lu, J., Rao, M. P., MacDonald, N. C., Khang, D. & Webster, T. J. Improved endothelial cell adhesion and proliferation on patterned titanium surfaces with rationally designed, micrometer to nanometer features. *Acta Biomaterialia* **4,** 192–201 (2008).

396. Liliensiek, S. J. *et al.* Modulation of human vascular endothelial cell behaviors by nanotopographic cues. *Biomaterials* **31,** 5418–5426 (2010).

397. Owen, D. G., Schenkel, T., Shepherd, D. E. & Espino, D. M. Assessment of surface roughness and blood rheology on local coronary haemodynamics: a multi-scale computational fluid dynamics study. *Journal of The Royal Society Interface* **17,** 20200327 (2020).

398. Nagai, Y., Hasegawa, H. & Kanai, H. Improvement of accuracy in ultrasonic measurement of luminal surface roughness of carotid arterial wall by deconvolution filtering. *Japanese Journal of Applied Physics* **53,** 07KF19 (2014).

399. Weizsacker, H. W. & Pinto, J. G. Isotropy and anisotropy of the arterial wall. *Journal of Biomechanics* **21,** 477–487 (1988).

400. Karlsson, J., Stålhand, J., Carlhäll, C.-J., Länne, T. & Engvall, J. An in vivo study of isotropic and anisotropic wall stress in a hyperelastic Holzapfel-Gasser-Ogden model in the human abdominal aorta: effects of age and sex. *Frontiers in Physiology* **14,** 286 (2023).

401. Xing, Q. *et al.* Aligned nanofibrous cell-derived extracellular matrix for anisotropic vascular graft construction. *Advanced Healthcare Materials* **6,** 1601333 (2017).

402. Chen, Y. *et al.* Biomimetic anisotropic poly(vinyl alcohol hydrogels with significantly enhanced mechanical properties by freezing–thawing under drawing. *Journal of Materials Chemistry B* **7,** 3243 (2019).

403. Arbeiter, D., Oschatz, S., Lebahn, K., Illner, S. & Grabow, N. Dry vs. wet testing: quasi-static tensile experiment setup for polymer based biomaterials. *Current Directions in Biomedical Engineering* **7,** 627–639 (2021).

404. Harding, S. *et al.* Engineering and cell attachment properties of human fibronectin–fibrinogen scaffolds for use in tissue engineered blood vessels. *Bioprocess and Biosystems Engineering* **25,** 53–59 (2002).

405. Bose, S., Li, S., Mele, E. & Silberschmidt, V. V. Dry vs. wet: properties and performance of collagen films. Part II. Cyclic and time-dependent behaviours. *Journal of the Mechanical Behavior of Biomedical Materials* **112,** 104040 (2020).

406. Giudici, A. & Spronck, B. The role of layer-specific residual stresses in arterial mechanics: analysis via a novel modelling framework. *Artery Research* **28,** 41–54 (2022).

407. Cantini, M., Donnelly, H., Dalby, M. J. & Salmeron-Sanchez, M. The plot thickens: the emerging role of matrix viscosity in cell mechanotransduction. *Advanced Healthcare Materials* **9,** 1901259 (2020).

Appendix A

Appendix A includes supplementary data for Chapter 3 of this thesis. Listed in order of appearance throughout 3, these include:

- First order Ogden parameters for individual PVA/gelatin samples (Table A.1);
- Complete DMA data for all compositions of PVA and PVA/gelatin cryogel at all frequencies tested (Tables A.2–A.7);
- Hyperelastic test data for all PVA/gelatin cryogel compositions (Figure A.1);
- Hyperelastic curve fitting coefficients for all stable hyperelastic models (Table A.8).

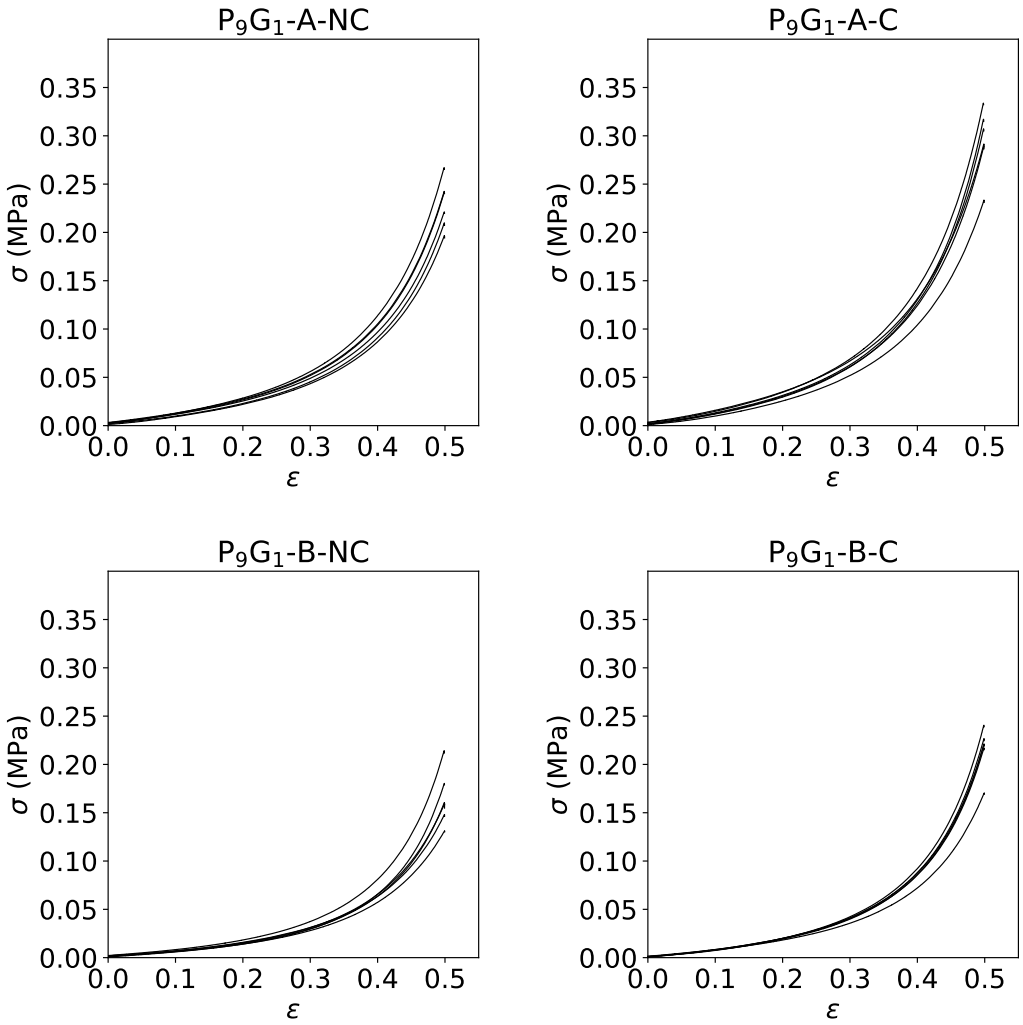


Figure A.1: Individual stress–strain curves (test data) for P_9G_1-A-NC, P_9G_1-A-C, P_9G_1-B-NC and P_9G_1-B-C.

Table A.1: First order Ogden parameters and r^2 values for individual PVA/gelatin samples. For P_9G_1-B-C, samples marked with $**$ yielded $\alpha_1 < 0$ and were excluded to allow averaging of α_1. For P_9G_1-A-C, P_9G_1-A-NC and P_9G_1-B-NC, samples marked with $**$ were excluded to keep the sample size consistent between compositions ($n = 6$). The $n = 6$ mean values were the hyperelastic constants used in subsequent FE models.

P_9G_1-A-C			
Sample	**μ_1 (MPa)**	**α_1**	**r^2**
1	0.0448	7.330	0.9993
2	0.0433	7.169	0.9999
3	0.0502	7.065	0.9995
4	0.0416	7.672	0.9998
5	0.0516	6.122	0.9988
6	0.0352	7.337	0.9993
7**	0.0460	6.718	0.9998
8**	0.0475	6.461	0.9984
Average ($n = 8$)	0.0450 ± 0.0052	6.984 ± 0.513	0.9994 ± 0.0004
Average ($n = 6$)	0.0444 ± 0.0060	7.116 ± 0.528	0.9994 ± 0.0004
P_9G_1-A-NC			
Sample	**μ_1 (MPa)**	**α_1**	**r^2**
1	0.0409	6.261	0.9978
2	0.0417	6.782	0.9991
3	0.0335	6.725	0.9995
4	0.0379	6.207	0.9981
5	0.0313	6.854	0.9999
6	0.0394	6.488	0.9986
7**	0.0370	6.807	0.9991
8**	0.0355	6.968	0.9996
Average ($n = 8$)	0.0371 ± 0.0036	6.636 ± 0.283	0.9989 ± 0.0008
Average ($n = 6$)	0.0374 ± 0.0042	6.553 ± 0.276	0.9988 ± 0.0008
P_9G_1-B-C			
Sample	**μ_1 (MPa)**	**α_1**	**r^2**
1	0.0260	6.923	0.9995
2	0.0274	7.903	0.9995
3	0.0288	7.516	0.9989
4	0.0279	8.308	0.9997
5**	0.0167	−3.470	0.9980
6**	0.0176	−2.944	0.9946
7	0.0271	8.120	0.9997
8	0.0285	7.819	0.9992
Average ($n = 8$)	0.0250 ± 0.0049	5.022 ± 5.098	0.9986 ± 0.0017
Average ($n = 6$)	0.0276 ± 0.0010	7.765 ± 0.493	0.9994 ± 0.0003
P_9G_1-B-NC			
Sample	**μ_1 (MPa)**	**α_1**	**r^2**
1	0.0229	7.172	0.9992
2	0.0235	6.680	0.9990
3	0.0201	8.252	0.9987
4	0.0209	6.760	0.9996
5	0.0216	7.421	0.9988
6	0.0271	7.580	0.9973
7**	0.0198	7.225	0.9995
8**	0.0197	7.385	0.9999
Average ($n = 8$)	0.0220 ± 0.0025	7.309 ± 0.493	0.9990 ± 0.0008
Average ($n = 6$)	0.0227 ± 0.0025	7.311 ± 0.581	0.9988 ± 0.0008

Table A.2: E' (mean ± SD) for all PVA(/gelatin) compositions tested between 0.5 Hz and 10 Hz.

	E' (kPa)			
Frequency (Hz)	**$P_{10}G_0$-A-C**	**$P_{10}G_0$-A-NC**	**$P_{10}G_0$-B-C**	**$P_{10}G_0$-B-NC**
0.5	378.3 ± 28.1	272.4 ± 24.9	271.2 ± 18.4	167.4 ± 20.0
1	378.0 ± 27.6	273.9 ± 24.8	271.4 ± 18.3	168.9 ± 19.9
2	386.2 ± 28.3	279.6 ± 24.9	276.2 ± 19.2	172.6 ± 20.0
3	390.2 ± 28.6	282.2 ± 25.1	278.5 ± 19.4	174.4 ± 20.3
4	392.9 ± 28.9	284.0 ± 25.2	280.0 ± 19.6	175.6 ± 20.5
6	397.2 ± 29.4	286.4 ± 25.4	282.8 ± 20.1	177.6 ± 20.7
8	399.8 ± 29.6	287.8 ± 25.6	284.6 ± 20.3	178.7 ± 20.8
10	401.4 ± 29.7	288.9 ± 25.7	286.0 ± 20.5	179.8 ± 20.9
Frequency (Hz)	**P_9G_1-A-C**	**P_9G_1-A-NC**	**P_9G_1-B-C**	**P_9G_1-B-NC**
0.5	424.0 ± 46.3	313.2 ± 39.7	259.5 ± 26.0	182.9 ± 20.0
1	425.8 ± 46.3	313.6 ± 39.6	259.7 ± 26.2	183.9 ± 20.3
2	432.3 ± 47.0	318.9 ± 39.8	264.4 ± 26.6	188.2 ± 20.6
3	435.6 ± 47.3	321.8 ± 39.9	266.8 ± 26.8	190.4 ± 20.6
4	437.8 ± 47.6	323.7 ± 39.8	268.4 ± 26.9	191.9 ± 20.8
6	441.0 ± 47.9	327.2 ± 40.0	271.2 ± 27.0	194.5 ± 20.8
8	442.8 ± 48.1	329.2 ± 40.1	272.9 ± 27.2	196.0 ± 20.6
10	444.4 ± 48.3	330.9 ± 40.2	274.6 ± 27.2	197.5 ± 20.6

Table A.3: E'' (mean ± SD) for all PVA(/gelatin) compositions tested between 0.5 Hz and 10 Hz.

	E'' (kPa)			
Frequency (Hz)	**$P_{10}G_0$-A-C**	**$P_{10}G_0$-A-NC**	**$P_{10}G_0$-B-C**	**$P_{10}G_0$-B-NC**
0.5	48.8 ± 7.2	29.8 ± 3.6	31.9 ± 6.3	20.2 ± 2.9
1	46.9 ± 7.0	29.2 ± 4.2	30.4 ± 5.7	19.8 ± 2.6
2	43.8 ± 6.5	26.7 ± 4.3	29.6 ± 5.5	19.2 ± 2.6
3	42.2 ± 6.3	25.8 ± 4.4	29.5 ± 5.5	19.2 ± 2.6
4	41.3 ± 6.1	25.6 ± 4.5	29.7 ± 5.5	19.4 ± 2.5
6	40.7 ± 5.7	26.0 ± 4.6	30.8 ± 5.5	20.0 ± 2.5
8	41.1 ± 5.4	27.1 ± 4.7	32.1 ± 5.5	20.8 ± 2.5
10	42.4 ± 5.3	28.5 ± 4.8	33.7 ± 5.6	21.7 ± 2.6
Frequency (Hz)	**P_9G_1-A-C**	**P_9G_1-A-NC**	**P_9G_1-B-C**	**P_9G_1-B-NC**
0.5	34.0 ± 5.0	26.6 ± 4.1	31.0 ± 4.6	24.8 ± 2.8
1	33.1 ± 4.8	28.2 ± 4.3	31.4 ± 4.5	24.9 ± 2.8
2	32.2 ± 4.5	28.4 ± 4.3	31.9 ± 4.8	24.9 ± 3.1
3	32.2 ± 4.3	29.0 ± 4.2	32.6 ± 5.1	25.2 ± 3.3
4	32.7 ± 4.3	29.7 ± 4.2	33.5 ± 5.3	25.7 ± 3.5
6	34.7 ± 4.3	31.3 ± 4.2	35.3 ± 5.6	26.7 ± 3.6
8	37.0 ± 4.4	33.0 ± 4.2	37.2 ± 5.9	27.9 ± 3.7
10	39.5 ± 4.6	34.9 ± 4.3	38.9 ± 6.1	29.0 ± 3.7

Table A.4: The relative difference in E' of PVA cryogel between frequencies of 0.5–10 Hz as a function of M_w PVA (top) and coagulation treatment (bottom), calculated as the percentage difference between two compositions of interest.

INCREASING M_w: PVA						
Frequency (Hz)	**Mean E' (kPa) $P_{10}G_0$-B-NC**	**Mean E' (kPa) $P_{10}G_0$-A-NC**	**Relative Difference (%)**	**Mean E' (kPa) $P_{10}G_0$-B-C**	**Mean E' (kPa) $P_{10}G_0$-A-C**	**Relative Difference (%)**
0.5	167.4	272.4	62.7	271.2	378.3	39.5
1	168.9	273.9	62.2	271.4	378.0	39.3
2	172.6	279.6	62.0	276.2	386.2	39.8
3	174.4	282.2	61.8	278.5	390.2	40.1
4	175.6	284.0	61.7	280.0	392.9	40.3
6	177.6	286.4	61.3	282.8	397.2	40.5
8	178.7	287.8	61.1	284.6	399.8	40.5
10	179.8	288.9	60.7	286.0	401.4	40.4
Mean ± S.D.	-	-	61.7 ± 0.6	-	-	40.0 ± 0.5
USE OF COAGULATION TREATMENT: PVA						
Frequency (Hz)	**Mean E' (kPa) $P_{10}G_0$-B-NC**	**Mean E' (kPa) $P_{10}G_0$-B-C**	**Relative Difference (%)**	**Mean E' (kPa) $P_{10}G_0$-A-NC**	**Mean E' (kPa) $P_{10}G_0$-A-C**	**Relative Difference (%)**
0.5	167.4	271.2	61.9	272.4	378.3	38.9
1	168.9	271.4	60.7	273.9	378.0	38.0
2	172.6	276.2	60.0	279.6	386.2	38.1
3	174.4	278.5	59.7	282.2	390.2	38.3
4	175.6	280.0	59.5	284.0	392.9	38.4
6	177.6	282.8	59.3	286.4	397.2	38.7
8	178.7	284.6	59.2	287.8	399.8	38.9
10	179.8	286.0	59.1	288.9	401.4	39.0
Mean ± S.D.	-	-	59.9 ± 1.0	-	-	38.5 ± 0.4

Table A.5: The relative difference in E' of PVA/gelatin cryogel between frequencies of 0.5–10 Hz as a function of M_w PVA (top) and coagulation treatment (bottom), calculated as the percentage difference between two compositions of interest.

INCREASING M_w: PVA/GELATIN						
Frequency (Hz)	**Mean E' (kPa) P_9G_1-B-NC**	**Mean E' (kPa) P_9G_1-A-NC**	**Relative Difference (%)**	**Mean E' (kPa) P_9G_1-B-C**	**Mean E' (kPa) P_9G_1-A-C**	**Relative Difference (%)**
0.5	182.9	313.2	71.3	259.5	424.0	63.4
1	183.9	313.6	70.5	259.7	425.8	64.0
2	188.2	318.9	69.4	264.4	432.3	63.5
3	190.4	321.8	69.0	266.8	435.6	63.2
4	191.9	323.7	68.7	268.4	437.8	63.1
6	194.5	327.2	68.2	271.2	441.0	62.6
8	196.0	329.2	67.9	272.9	442.8	62.3
10	197.5	330.9	67.6	274.6	444.4	61.8
Mean ± S.D.	-	-	69.1 ± 1.3	-	-	63.0 ± 0.7
USE OF COAGULATION TREATMENT: PVA/GELATIN						
Frequency (Hz)	**Mean E' (kPa) P_9G_1-B-NC**	**Mean E' (kPa) P_9G_1-B-C**	**Relative Difference (%)**	**Mean E' (kPa) P_9G_1-A-NC**	**Mean E' (kPa) P_9G_1-A-C**	**Relative Difference (%)**
0.5	182.9	259.5	41.9	313.2	424.0	35.3
1	183.9	259.7	41.2	313.6	425.8	35.8
2	188.2	264.4	40.5	318.9	432.3	35.6
3	190.4	266.8	40.1	321.8	435.6	35.4
4	191.9	268.4	39.8	323.7	437.8	35.2
6	194.5	271.2	39.4	327.2	441.0	34.8
8	196.0	272.9	39.2	329.2	442.8	34.5
10	197.5	274.6	39.1	330.9	444.4	34.3
Mean ± S.D.	-	-	40.2 ± 1.0	-	-	35.1 ± 0.5

Table A.6: The relative difference in E'' of PVA cryogel between frequencies of 0.5–10 Hz as a function of M_w PVA (top) and coagulation treatment (bottom), calculated as the percentage difference between two compositions of interest.

INCREASING M_w: PVA						
Frequency (Hz)	**Mean E'' (kPa) $P_{10}G_0$-B-NC**	**Mean E'' (kPa) $P_{10}G_0$-A-NC**	**Relative Difference (%)**	**Mean E'' (kPa) $P_{10}G_0$-B-C**	**Mean E'' (kPa) $P_{10}G_0$-A-C**	**Relative Difference (%)**
0.5	20.2	29.8	47.5	31.9	48.8	52.9
1	19.8	29.2	47.7	30.4	46.9	54.2
2	19.2	26.7	39.0	29.6	43.8	48.0
3	19.2	25.8	34.6	29.5	42.2	42.8
4	19.4	25.6	32.0	29.7	41.3	38.8
6	20.0	26.0	30.2	30.8	40.7	32.2
8	20.8	27.1	30.1	32.1	41.1	27.8
10	21.7	28.5	31.5	33.7	42.4	25.9
Mean ± S.D.	-	-	36.6 ± 7.4	-	-	40.3 ± 11.0
USE OF COAGULATION TREATMENT: PVA						
Frequency (Hz)	**Mean E'' (kPa) $P_{10}G_0$-B-NC**	**Mean E'' (kPa) $P_{10}G_0$-B-C**	**Relative Difference (%)**	**Mean E'' (kPa) $P_{10}G_0$-A-NC**	**Mean E'' (kPa) $P_{10}G_0$-A-C**	**Relative Difference (%)**
0.5	20.2	31.9	58.0	29.8	48.8	63.8
1	19.8	30.4	53.7	29.2	46.9	60.4
2	19.2	29.6	54.1	26.7	43.8	64.0
3	19.2	29.5	54.1	25.8	42.2	63.5
4	19.4	29.7	53.6	25.6	41.3	61.5
6	20.0	30.8	54.3	26.0	40.7	56.7
8	20.8	32.1	54.4	27.1	41.1	51.7
10	21.7	33.7	55.3	28.5	42.4	48.6
Mean ± S.D.	-	-	54.7 ± 1.4	-	-	58.8 ± 5.9

Table A.7: The relative difference in E'' of PVA/gelatin cryogel between frequencies of 0.5–10 Hz as a function of M_w PVA (top) and coagulation treatment (bottom), calculated as the percentage difference between two compositions of interest.

INCREASING M_w: PVA/GELATIN						
Frequency (Hz)	**Mean E'' (kPa) P_9G_1-B-NC**	**Mean E'' (kPa) P_9G_1-A-NC**	**Relative Change (%)**	**Mean E'' (kPa) P_9G_1-B-C**	**Mean E'' (kPa) P_9G_1-A-C**	**Relative Change (%)**
0.5	24.8	26.6	7.2	31.0	34.0	9.7
1	24.9	28.2	13.3	31.4	33.1	5.4
2	24.9	28.4	14.2	31.9	32.2	0.9
3	25.2	29.0	14.9	32.6	32.2	−1.2
4	25.7	29.7	15.6	33.5	32.7	−2.3
6	26.7	31.3	16.9	35.3	34.7	−1.8
8	27.9	33.0	18.1	37.2	37.0	−0.4
10	29.0	34.9	20.1	38.9	39.5	1.6
Mean ± S.D.	-	-	15.0 ± 3.9	-	-	1.5 ± 4.1
USE OF COAGULATION TREATMENT: PVA/GELATIN						
Frequency (Hz)	**Mean E'' (kPa) P_9G_1-B-NC**	**Mean E'' (kPa) P_9G_1-B-C**	**Relative Difference (%)**	**Mean E'' (kPa) P_9G_1-A-NC**	**Mean E'' (kPa) P_9G_1-A-C**	**Relative Difference (%)**
0.5	24.8	31.0	25.0	26.6	34.0	28.0
1	24.9	31.4	26.4	28.2	33.1	17.7
2	24.9	31.9	28.3	28.4	32.2	13.3
3	25.2	32.6	29.2	29.0	32.2	11.1
4	25.7	33.5	30.3	29.7	32.7	10.2
6	26.7	35.3	32.1	31.3	34.7	11.0
8	27.9	37.2	33.3	33.0	37.0	12.3
10	29.0	38.9	34.0	34.9	39.5	13.3
Mean ± S.D.	-	-	29.8 ± 3.2	-	-	14.6 ± 5.9

Table A.8: Constitutive parameters of stable hyperelastic models fitted to PVA/gelatin compression data for all PVA/gelatin cryogel compositions (mean ± SD)

FIRST ORDER OGDEN CONSTITUTIVE PARAMETERS				
	P_9G_1-A-C	**P_9G_1-A-NC**	**P_9G_1-B-C**	**P_9G_1-B-NC**
μ_1 (MPa)	0.0444 ± 0.0060	0.0374 ± 0.0042	0.0276 ± 0.0010	0.0227 ± 0.0025
α_1	7.116 ± 0.528	6.553 ± 0.276	7.765 ± 0.493	7.311 ± 0.581
μ_0 (MPa)	0.157 ± 0.016	0.122 ± 0.012	0.107 ± 0.009	0.083 ± 0.011
r^2	0.9994 ± 0.0004	0.9988 ± 0.0008	0.9994 ± 0.0003	0.9988 ± 0.0008
NEO-HOOKEAN CONSTITUTIVE PARAMETERS				
	P_9G_1-A-C	**P_9G_1-A-NC**	**P_9G_1-B-C**	**P_9G_1-B-NC**
C_{10} (MPa)	0.0239 ± 0.0029	0.0198 ± 0.0021	0.0152 ± 0.0007	0.0123 ± 0.0014
μ_0 (MPa)	0.0479 ± 0.0059	0.0396 ± 0.0043	0.0304 ± 0.0014	0.0247 ± 0.0027
r^2	0.9483 ± 0.0083	0.9505 ± 0.0032	0.9319 ± 0.0080	0.9329 ± 0.0151
SECOND ORDER REDUCED POLYNOMIAL CONSTITUTIVE PARAMETERS				
	P_9G_1-A-C	**P_9G_1-A-NC**	**P_9G_1-B-C**	**P_9G_1-B-NC**
C_{10} (MPa)	0.0190 ± 0.0028	0.0162 ± 0.0019	0.0116 ± 0.0004	0.0096 ± 0.0011
C_{20} (MPa)	0.0076 ± 0.0012	0.0050 ± 0.0006	0.0060 ± 0.0011	0.0042 ± 0.0009
μ_0 (MPa)	0.0380 ± 0.0056	0.0325 ± 0.0038	0.0231 ± 0.0008	0.0176 ± 0.0044
r^2	0.9951 ± 0.0022	0.9929 ± 0.0023	0.9929 ± 0.0014	0.9912 ± 0.0030
YEOH CONSTITUTIVE PARAMETERS				
	P_9G_1-A-C	**P_9G_1-A-NC**	**P_9G_1-B-C**	**P_9G_1-B-NC**
C_{10} (MPa)	0.0205 ± 0.0035	0.0180 ± 0.0024	0.0126 ± 0.0006	0.0108 ± 0.0014
C_{20} (MPa)	0.0015 ± 0.0028	−0.0015 ± 0.0019	0.0015 ± 0.0014	−0.0007 ± 0.0007
C_{30} (MPa)	0.0042 ± 0.0017	0.0044 ± 0.012	0.0032 ± 0.0006	0.0033 ± 0.0009
μ_0 (MPa)	0.0410 ± 0.0070	0.0360 ± 0.0049	0.0252 ± 0.0012	0.0217 ± 0.0027
r^2	0.9994 ± 0.0008	0.9984 ± 0.0009	0.9997 ± 0.0002	0.9985 ± 0.0007
FIFTH ORDER REDUCED POLYNOMIAL CONSTITUTIVE PARAMETERS				
	P_9G_1-A-C	**P_9G_1-A-NC**	**P_9G_1-B-C**	**P_9G_1-B-NC**
C_{10} (MPa)	0.0218 ± 0.0044	0.0198 ± 0.0031	0.0133 ± 0.0008	0.0121 ± 0.0017
C_{20} (MPa)	−0.0123 ± 0.0110	−0.0192 ± 0.0085	−0.0064 ± 0.0035	−0.0133 ± 0.0038
C_{30} (MPa)	0.0402 ± 0.0212	0.0484 ± 0.0168	0.0251 ± 0.0068	0.0355 ± 0.0083
C_{40} (MPa)	−0.0343 ± 0.0174	−0.0407 ± 0.0140	−0.0217 ± 0.0058	−0.0303 ± 0.0071
C_{50} (MPa)	0.0110 ± 0.0052	0.0126 ± 0.0043	0.0072 ± 0.0019	0.0095 ± 0.0023
μ_0 (MPa)	0.0435 ± 0.0087	0.0396 ± 0.0062	0.0265 ± 0.0017	0.0241 ± 0.0034
r^2	0.9992 ± 0.0006	0.9985 ± 0.0007	0.9993 ± 0.0003	0.9981 ± 0.0005

Appendix B

Appendix B includes supplementary data for Chapter 4 of this thesis. Listed in order of appearance throughout Chapter 4, these include:

- The mean ϵ_θ and ϵ_r of the coronary media (Figure B.1) and coronary adventitia (Figure B.2);
- σ_θ contour maps for Yeoh-modelled PVA/gelatin grafts (Figure B.3);
- The mean ϵ_θ and ϵ_r of PVA/gelatin graft media (Figure B.4) and PVA/gelatin graft adventitia (Figure B.5).

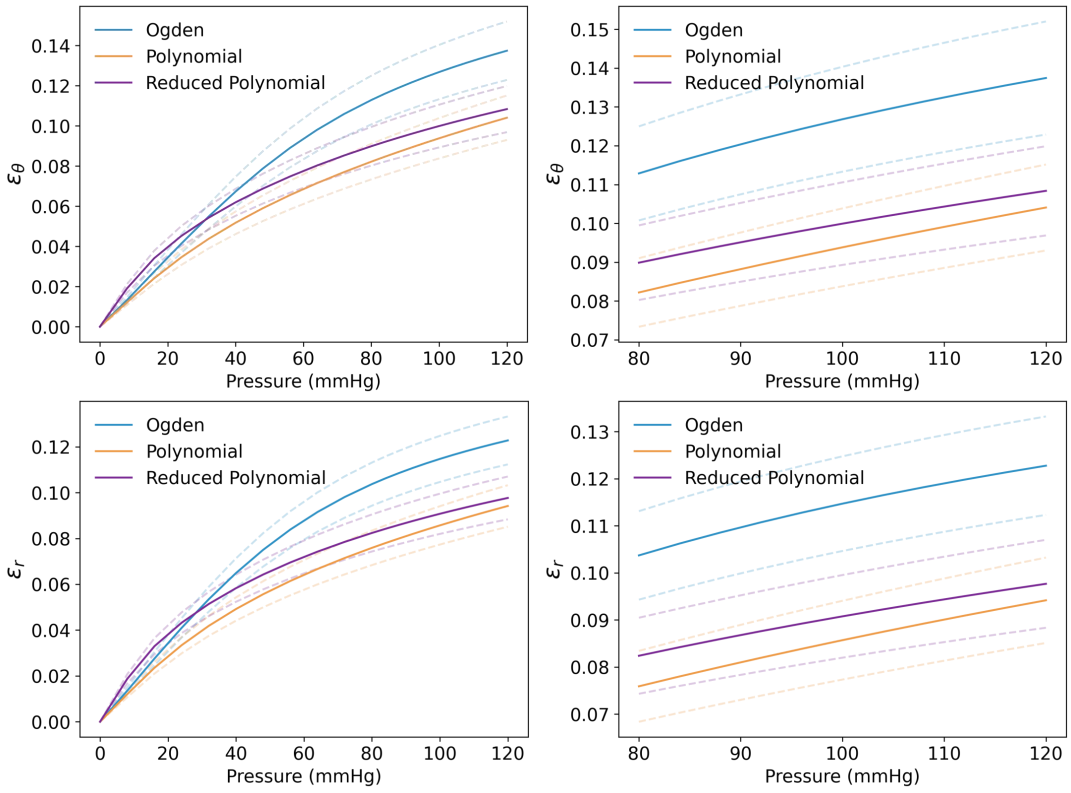


Figure B.1: The mean ϵ_θ (top row) and ϵ_r (bottom row) of the coronary media between 0–120 and 80–120 mmHg pressure. Dashed lines show the SD of each model.

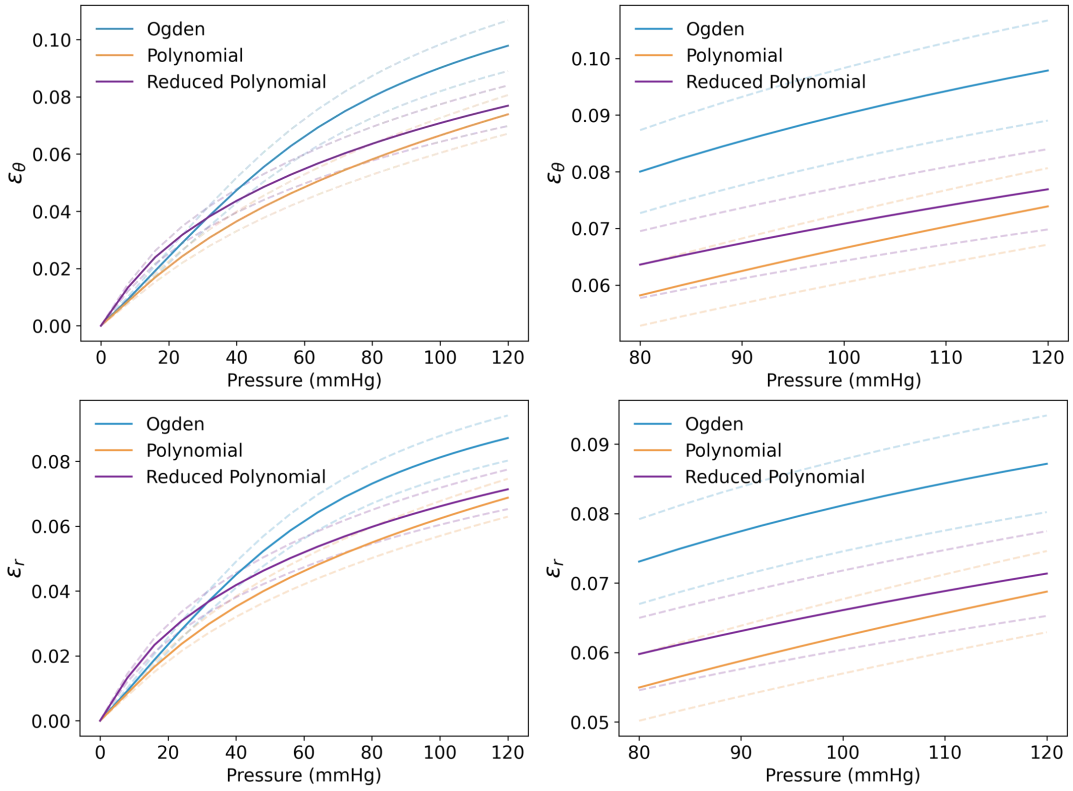


Figure B.2: The mean ϵ_θ (top row) and ϵ_r (bottom row) of the coronary adventitia between 0–120 and 80–120 mmHg pressure. Dashed lines show the SD of each model.

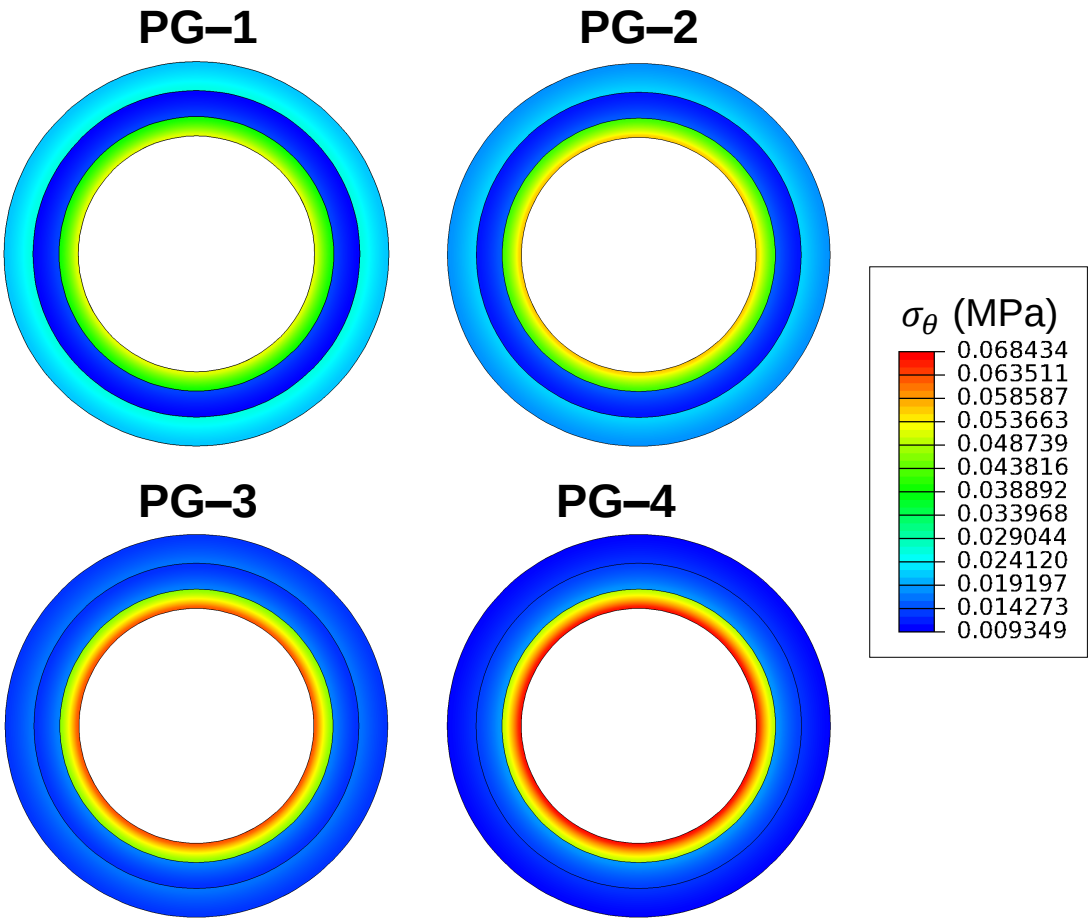


Figure B.3: σ_θ contour maps of each PVA/gelatin graft using Yeoh parameters.

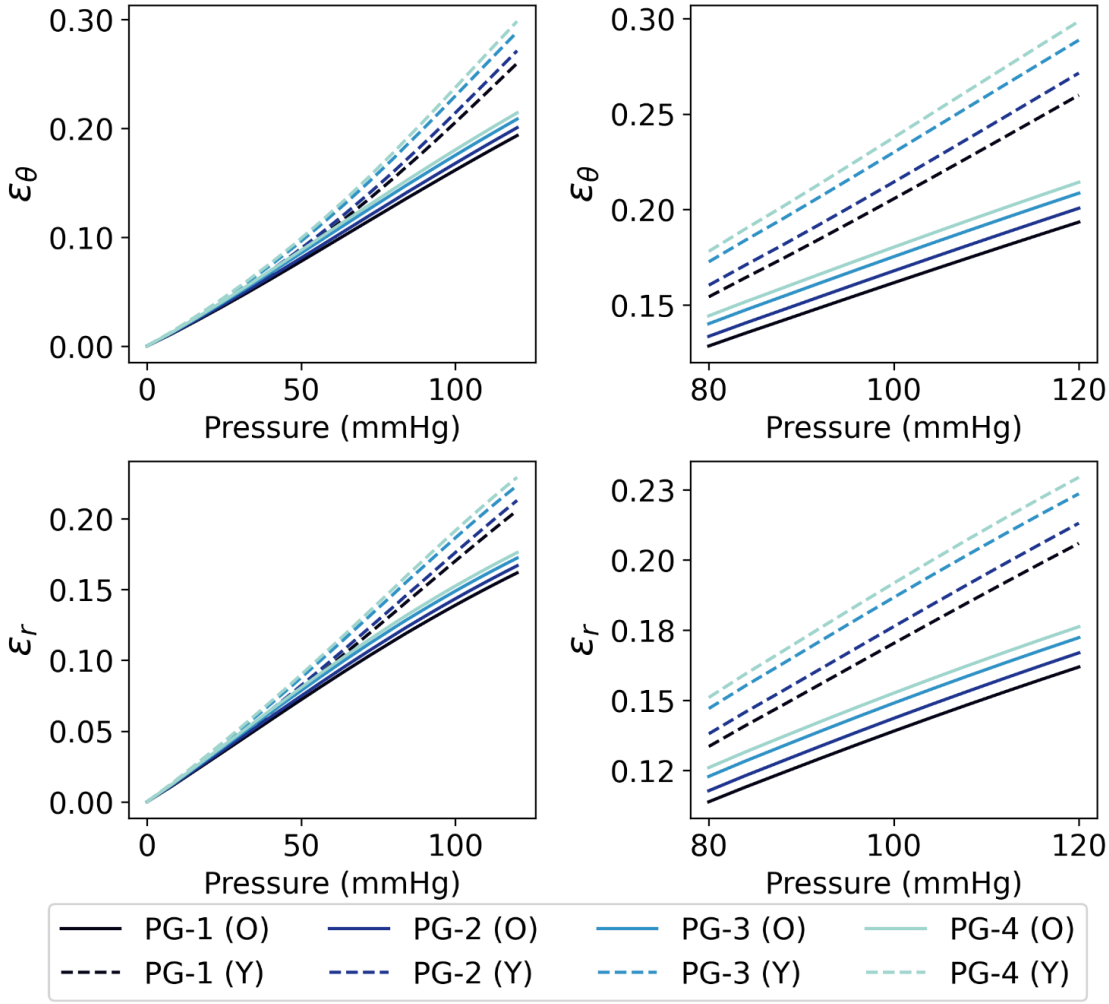


Figure B.4: The mean ϵ_θ (top row) and ϵ_r (bottom row) of PVA/gelatin graft media between 0–120 and 80–120 mmHg pressure, modelled using Ogden (solid lines) and Yeoh (dashed lines) hyperelastic parameters. Error bars have been omitted for clarity.

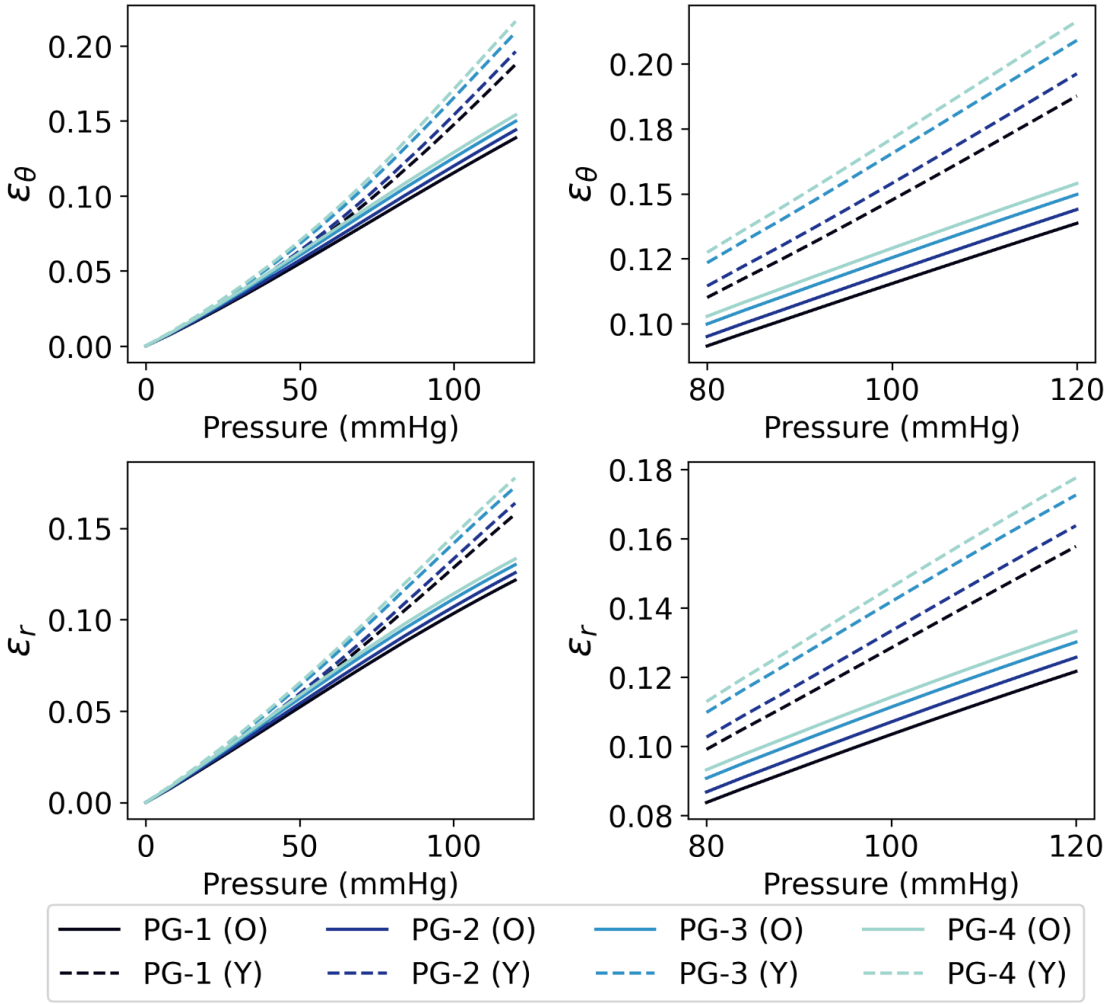


Figure B.5: The mean ϵ_θ (top row) and ϵ_r (bottom row) of PVA/gelatin graft adventitia between 0–120 and 80–120 mmHg pressure, modelled using Ogden (solid lines) and Yeoh (dashed lines) hyperelastic parameters. Error bars have been omitted for clarity.

Appendix C

Appendix C includes supplementary data for Chapter 5 of this thesis. Listed in order of appearance throughout Chapter 5, these include:

- The Python script used to generate sinusoidal interfaces in Abaqus (Figure C.1);
- Example variation of lumen diameter with ϕ (Figure C.2);
- The circumferential displacement and stress profile of the tied surface model at systolic pressure (Figure C.3);
- The contact pressure observed at the interface of rough friction and friction coefficient models (Figure C.4);
- The circumferential composition of the IM and adventitia as a function of A (Table C.1).

```
from abaqus import *
from abaqusConstants import *
import numpy as np
import math

s = mdb.models['Model-1'].ConstrainedSketch(name='Sketch-1',
                                    sheetSize=20.0)
g, v, d, c = s.geometry, s.vertices, s.dimensions, s.constraints
s.setPrimaryObject(option=STANDALONE)

class Point:
    def __init__(self, x=0, y=0):
        self.x = x
        self.y = y

def SineAroundCircle(cx,cy,r,A,f,theta):
        p = Point()
        p.x = cx+(r+A*np.sin(f*theta))*np.cos(theta)
        p.y = cy+(r+A*np.sin(f*theta))*np.sin(theta)
        return p

cx = 0
cy = 0
r = 1.815 # units mm
A = 0.1 # units mm
f = 10 # number of sine wave periods per 360 degree circle

pt= Point()
x,y = [],[]

for i in np.arange(1,361,0.5): # (start,stop,step); decrease step
                                    value to increase number of
                                    points/resolution of sine wave
  theta = i*math.pi/180
  pt = SineAroundCircle(cx,cy,r,A,f,theta)
  x.append(pt.x), y.append(pt.y)

for i in range(len(x)-1):
    if i == 0:
        s.Line(point1=(x[0],y[0]), point2=(x[-1],y[-1]))
    if i == 722: #Change i to the total number of points around the
                                        circle (e.g. (1,361,0.5) =
                                    722 points total)
        s.Line(point=1(x[722],y[722]), point2=(x[0],y[0]))
    else:
        s.Line(point1=(x[i],y[i]),point2=(x[i+1],y[i+1]))

s.unsetPrimaryObject()
```

Figure C.1: Custom Python script used to create a sinusoidal interface in Abaqus. In this example, $r = 1.815$ mm, $A = 0.10$ mm and $\omega = 10$.

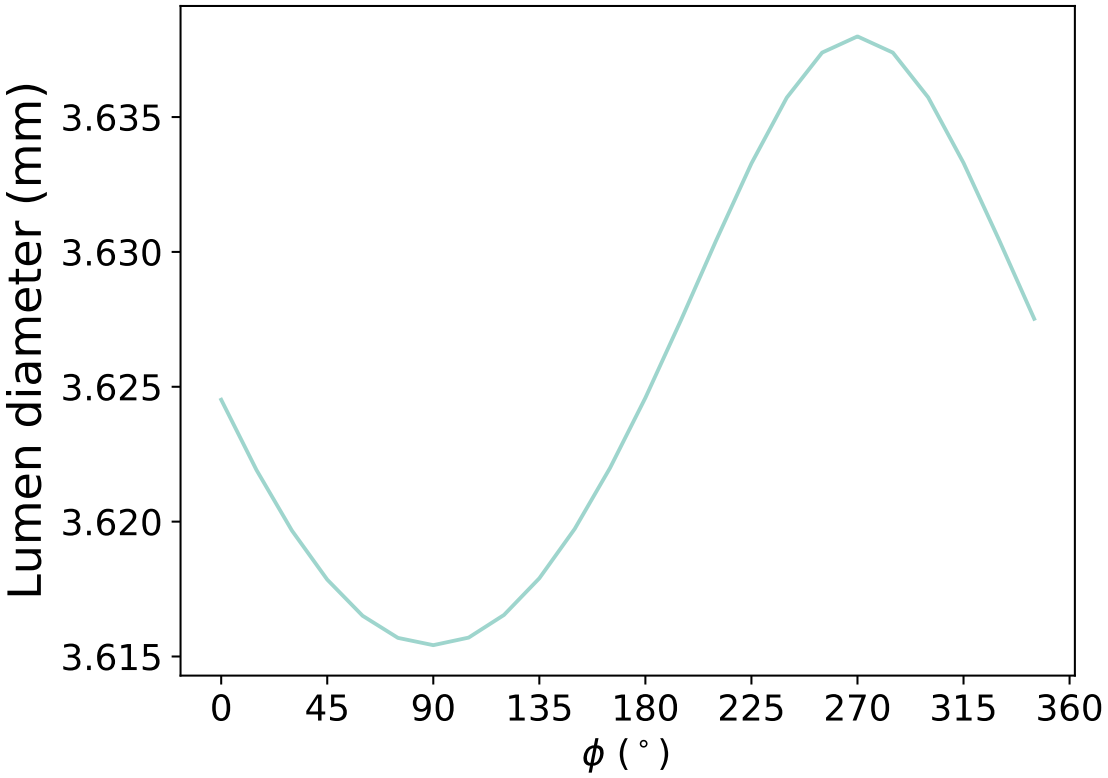


Figure C.2: Lumen diameter varies as a function of ϕ. In this example, $r = 1.815$ mm, $A = 0.25$ mm and $\omega = 10$.

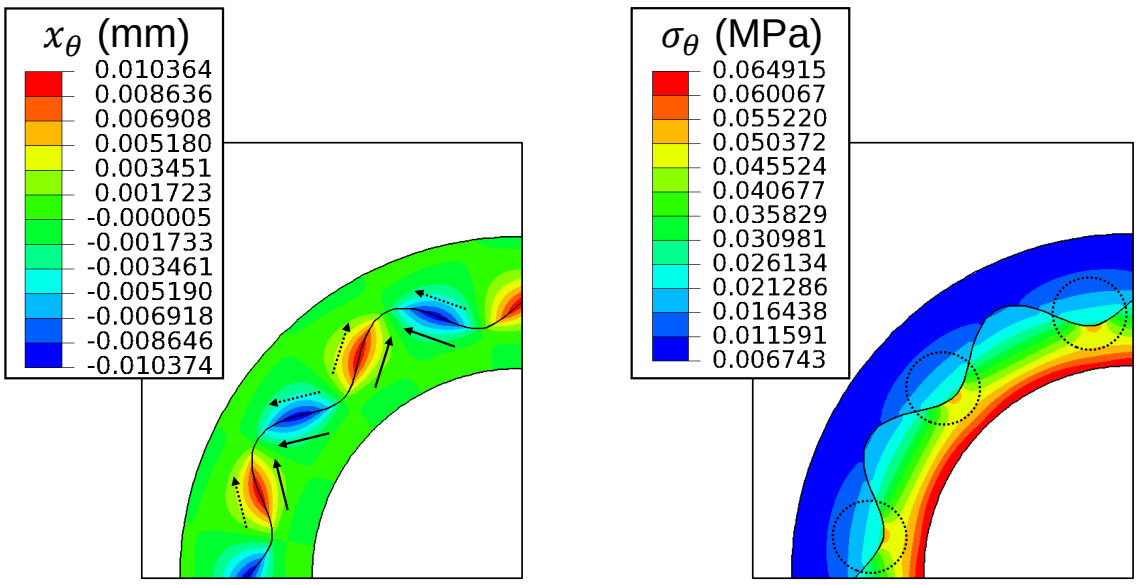


Figure C.3: x_θ (left) and σ_θ (right) in the tied surface model (IM = P_9G_1-A-C, adventitia = P_9G_1-B-NC) at systolic pressure. In the x_θ plots, red and blue signify clockwise and anticlockwise displacement, respectively. In the σ_θ plots, tensile stress concentrations are highlighted by black dotted circles and compressive stress concentrations are highlighted by white dotted circles.

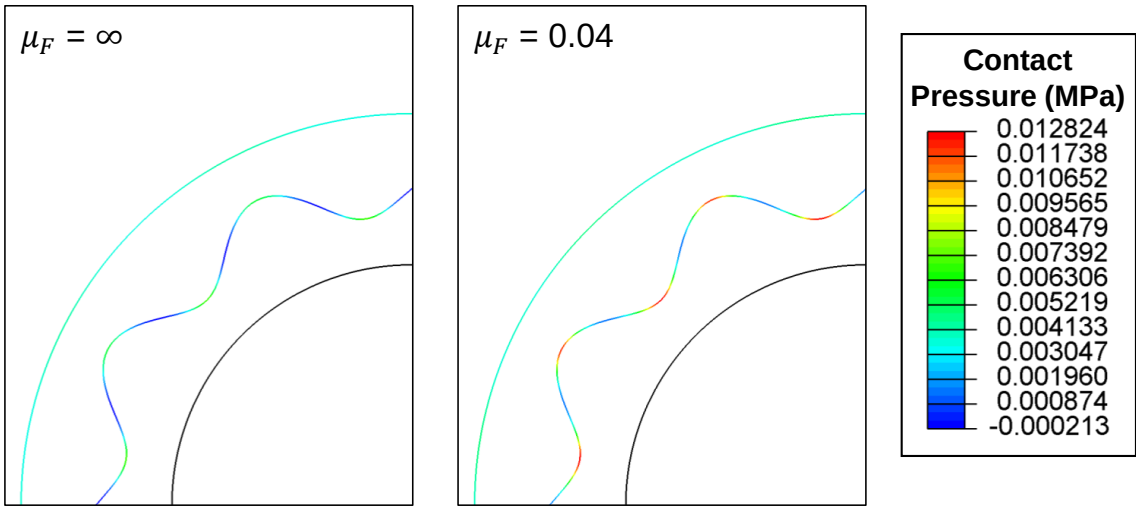


Figure C.4: Contact pressures observed at the interface at systolic pressure for rough friction and friction coefficient models.

Table C.1: The areas of the IM and adventitia through circumferential segments 1–10 as a function of A.

A = 0.05 mm		
Segment	**Total area of the IM (mm²)**	**Total area of the adventitia (mm²)**
1	0.078	0
2	0.083	0
3	0.087	0
4	0.092	0
5	0.079	0.018
6	0.018	0.083
7	0	0.106
8	0	0.111
9	0	0.116
10	0	0.121
1–10 (total)	**0.437**	**0.555**
A = 0.10 mm		
Segment	**Total area of the IM (mm²)**	**Total area of the adventitia (mm²)**
1	0.078	0
2	0.083	0
3	0.087	0
4	0.091	0.002
5	0.063	0.034
6	0.035	0.066
7	0.002	0.105
8	0	0.111
9	0	0.116
10	0	0.121
1–10 (total)	**0.439**	**0.555**
A = 0.15 mm		
Segment	**Total area of the IM (mm²)**	**Total area of the adventitia (mm²)**
1	0.078	0
2	0.083	0
3	0.087	0
4	0.079	0.013
5	0.058	0.039
6	0.041	0.061
7	0.015	0.091
8	0	0.111
9	0	0.116
10	0	0.121
1–10 (total)	**0.441**	**0.552**
A = 0.20 mm		
Segment	**Total area of the IM (mm²)**	**Total area of the adventitia (mm²)**
1	0.078	0
2	0.083	0
3	0.084	0.003
4	0.068	0.025
5	0.055	0.042
6	0.044	0.058
7	0.029	0.077
8	0.004	0.108
9	0	0.116
10	0	0.121
1–10 (total)	**0.445**	**0.550**
A = 0.25 mm		
Segment	**Total area the IM (mm²)**	**Total area of the adventitia (mm²)**
1	0.078	0
2	0.083	0
3	0.074	0.013
4	0.062	0.030
5	0.054	0.043
6	0.045	0.057
7	0.034	0.072
8	0.016	0.095
9	0	0.116
10	0	0.121
1–10 (total)	**0.446**	**0.547**